# Properties of the neutral gas in isolated galaxies

Daniel Espada Fernández

May 10, 2006

Editor: Editorial de la Universidad de Granada
Autor: Daniel Espada Fernández
D.L.: Gr. 1105- 2006
ISBN: 84-338-3857-1

# Contents

# Chapter 0

# Resumen

## 0.1 Título de la Tesis Doctoral

**"Propiedades del gas neutro en galaxias aisladas"**

## 0.2 Problema planteado

La finalidad de esta tesis es la de caracterizar las propiedades del gas neutro (gas atómico y gas molecular) de una muestra de galaxias aisladas, que servirá como referencia para determinar la influencia de las interacciones en la evolución de galaxias. En particular se estudiarán los siguientes puntos: caracterización del contenido y asimetrías del HI en galaxias aisladas, estudio sobre galaxias aisladas de tipo temprano y en especial aquellas detectadas en HI, y por último la caracterización del gas molecular para una submuestra de galaxias aisladas.

## 0.3 Motivación

### Caracterización del contenido de HI en galaxias aisladas

El gas atómico es una componente ligera del medio interestelar que domina en galaxias de tipos tardíos, y que se extiende típicamente hasta el doble del disco óptico (Cayatte et al. 1994). Ello hace que sea especialmente sensible a las interacciones. Haynes & Giovanelli (1984) caracterizaron el contenido de HI de una muestra de 324 galaxias del catálogo CIG (Karachentseva 1973) en función del tipo morfológico y la luminosidad o el diámetro óptico, y que ha servido de referencia para posteriores estudios del contenido de HI de galaxias en diferentes entornos. En particular, las galaxias espirales de los cúmulos parecen presentar una deficiencia de HI, especialmente en las cercanías del centro del cúmulo, donde domina el medio intracúmulo caliente emisor en rayos X (Van Gorkom 1996). Del mismo modo en los grupos compactos de galaxias se observa un nivel de deficiencia de hasta el 90% aunque gran parte de los grupos se encuentran inmersos en las barras de error de las relaciones encontradas por Haynes & Giovanelli (1984) que llegan hasta 0.5 mag (Verdes-Montenegro et al. 2001). Por el contrario, Zasov & Sulentic (1994) estudian 50 pares de galaxias E+S y los comparan con respecto a la muestra considerada por Haynes & Giovanelli, y no encuentran desviación de la normalidad en las espirales de los pares, a pesar de haber un aumento en la formación estelar. La muestra de HG84 considerada en la mayoría de los estudios sobre deficiencias es pequeña estadísticamente (en particular en función de los tipos morfológicos), por lo que es especialmente interesante realizar una revisión y ampliación de ésta.

### Asimetrías en el HI de galaxias aisladas espirales

La forma de los perfiles de HI es una herramienta importante para determinar la existencia de una determinada perturbación en el HI de la galaxia, aunque no podemos distinguir entre una asimetría

en el campo de velocidades o en la distribución de HI, dado que no tenemos información espacial.

Una cuestión interesante es que en muestras pequeñas de galaxias aisladas hay un porcentaje de perfiles asimétricos del 50% aproximadamente (104 galaxias en Haynes et al. 1998; 30 galaxias in Matthews et al. 1998). Sorprendentemte, otras muestras de galaxias en entornos más densos muestran sólo un leve incremento de perfiles asimétricos, alrededor del 50-75% (Swaters et al. 2002; Richter & Sancisi 1994; Sulentic & Arp 1983).

No hay una respuesta globalmente aceptada sobre el posible origen de esta alta tasa de asimetrías en galaxias aisladas. Algunas de las preguntas a responder son las siguientes: ¿las asimetrías están inducidas siempre por la presencia de compañeras?, ¿cuál es la influencia de capturas recientes?, ¿cuanto tiempo tarda la galaxia primaria a volver simétrica después de la perturbación? ¿algunas de estas asimetrías podrían ser explicadas por inestabilidades dinámicas internas de larga duración, que todavía no están bien estudiadas (e.g. Baldwin et al. 1980)?. Para entender la alta tasa de galaxias con perfiles asimétricos, diversas respuestas han sido propuestas, las cuales pueden ser agrupadas como sigue:

1. La perturbación es más duradera de lo que se pensaba anteriormente. Esto puede ser debido a que: a) el "winding out" por precesión diferencial es muy duradera en las regiones externas de las galaxias (Baldwin et al. 1980), b) modos débiles pero considerablemente duraderos (Weinberg 1994), c) amplificación de ondas de densidad (Shu et al. 1990; Syer & Tremaine 1996), o d) el disco es distribuido de forma irregular debido a un halo asimétrico (Levine & Sparke 1998; Noordermeer et al. 2001).

2. La perturbación podría estar forzada por interacciones de marea (e.g. Kornreich et al. 2002), fusiones menores (Zaritsky & Rix 1997) o acreción de gas externo a través de filamentos cosmológicos externos (Bournaud et al. 2005). Estas perturbaciones podrían ser de corta duración pero el efecto podría ser visto dependiendo del número de interacciones que puede sufrir una galaxia (fusiones menores podría ser una explicación porque una galaxia puede sufrir una algo número de posibles interacciones). A través de simulaciones de N-cuerpos de galaxias perturbadas por fusiones menores, Walker et al. (1996) sugiere que las asimetrías pueden durar entorno a 1 Gyr. Por el contrario, según (Wilcots & Prescott 2004) parece que no hay correlación entre la existencia de compañeras y asimetrías.

Por tanto sería especialmente interesante cuantificar las posibles asimetrías de los perfiles de HI, calcular el porcentaje de galaxias con perfiles asimétricos, así como poder decidir el posible origen de estas asimetrías para una muestra bien definida de galaxias aisladas.

### HI en galaxias aisladas de tipo temprano (elípticas y lenticulares)

La mayoría de las galaxias de tipo temprano (elípticas y lenticulares) son sistemas pobres en gas frio pero a veces algunas de éstas poseen una considerable cantidad de dicho gas. Normalmente se acepta que las fusiones entre galaxias espirales ricas en gas pueden crear como producto ETIGs como remanentes (Toomre & Toomre 1972). El HI de estas galaxias podría ser eyectado en colas de marea que en principio podrían volver a caer (e.g. Hibbard 2000 y referencias allí). Algunos procesos han sido estudiados para explicar como muchos remanentes de estas fusiones se mantienen pobres en gas frio en presencia del retorno de dicho gas, tales como por ejemplo posibles super vientos o la ionización por formación estelar continuada (Hibbard 2000). Asumiendo que el escenario de las fusiones es el principal mecanismo para producir galaxias de tipo temprano, podemos imaginar que diferentes tipos de fusiones pueden producir diferentes productos, dependiendo de las características de los impactos y de las propias propiedades de los objetos. Por tanto la presencia de HI en estas galaxias está directamente conectada con el entorno.

Entender el origen de las galaxias de tipo temprano en una muestra de galaxias aisladas, en particular aquellas ricas de HI, puede ayudarnos a entender la naturaleza de estos objetos.

**Caracterización del gas molecular en galaxias aisladas**

En cuanto al gas molecular, hay muy pocos trabajos realizados sobre muestras de galaxias aisladas con un criterio de aislamiento bien definido, y por tanto el sistema de referencia podría ser mejorado. Se ha atribuido a las interacciones un aumento en el contenido molecular de las galaxias, aunque en base a muestras sesgadas hacia las galaxias más brillantes en FIR (Braine & Combes 1993; Combes et al. 1994), y en base al cociente $M_{H_2}/L_B$, que aumenta con $L_B$, y por tanto posee valores mayores en cualquier caso para las galaxias más brillantes. Cuando este efecto se elimina (Perea et al. 1997; Verdes-Montenegro et al. 1998; Leon et al. 1998) el contenido de gas molecular de todas las muestras analizadas parece ser indistinguible del de las galaxias aisladas. Sauty et al. (2003a) estudia 99 galaxias CIG, pero su muestra no es completa porque considera galaxias con velocidades hasta v $<$ 15000 km $s^{-1}$

Tener una referencia de $M_{H_2}$ para galaxias aisladas tan completa como sea posible y bien definida es necesario para caracterizar dicho $M_{H_2}$, lo cual permitirá la revisión de los trabajos anteriores que estudian el $M_{H_2}$ en función del entorno.

## 0.4 Objetivos científicos

Los principales objetivos que han motivado esta Tesis Doctoral son los siguientes:

- Obtener y estudiar la correlación global entre los contenidos de gas atómico, gas molecular, en relación con propiedades de la componente estelar (morfología, diámetro óptico y luminosidad azul).
- Estudiar la tasa de asimetrías en galaxias aisladas a través de un estudio de los perfiles de HI para toda la muestra, así como estudiar el origen de las asimetrías para una submuestra con mapas interferométricos del VLA en la línea de 21 cm.
- Analizar galaxias de tipos tempranos que son ricas en HI.
- Analizar de forma estadística la emisión de CO(1-0) para una submuestra de 278 galaxias aisladas, con el fin de caracterizar el contenido de $H_2$ en galaxias aisladas.

## 0.5 Resumen de las aportaciones de la Tesis al campo científico

**Proyecto AMIGA (Capítulo 2)**

Este trabajo se centra dentro del marco del proyecto "Análisis del Medio Interestelar de Galaxias Aisladas" (AMIGA), el cual tiene como objetivo realizar un estudio cuantitativo de las propiedades físicas del medio interestelar así como de la actividad nuclear y el nivel de formación estelar de galaxias aisladas. Nuestra muestra se basa en una mejora del catálogo CIG, que es una muestra de N $\simeq$ 1000 galaxias en entornos muy poco densos. Para estudiar las distintas componentes, estamos observando y recopilando información para estas galaxias en el óptico (B y H$\alpha$), infrarrojo (FIR y NIR) y emisión de radiocontinuo más las líneas de HI y CO(1-0) (Leon & Verdes-Montenegro 2003; Verdes-Montenegro et al. 2005; Espada et al. 2005; Sulentic et al. 2006; Lisenfeld et al. 2006; Leon et al. 2006). Para ello estamos construyendo y analizando una base de datos multifrecuencia para una muestra de galaxias aisladas, que es significativa estadísticamente y bien definida. En particular, en esta Tesis caracterizamos el gas atómico (HI) observado a partir de la línea de 21 cm, que es la fase del gas neutro más sensible ante cualquier tipo de interacción puesto que su extensión duplica generalmente a la óptica, y el gas molecular ($H_2$), a partir de la línea de CO(1-0), en cuyas regiones tiene lugar la formación estelar.

En este Capítulo incluímos tanto un resumen de las consecuciones de dicho proyecto hasta algunas nuevas aportaciones al mismo, tales como las correcciones a las magnitudes aparentes azules, cálculo de los diámetros lineales, así como las inclinaciones.

### Datos de HI para la muestra AMIGA (Capítulo 3)

En este Capítulo presentamos el gas atómico (HI) para una muestra grande de galaxias aisladas, formando parte del proyecto AMIGA, y que incluye datos para 910 galaxias. El número de galaxias aisladas en nuestro estudio es tres veces mayor que otros estudios de este tipo, y conduce a una mejora sustancial en las estadísticas en función del tipo morfológico por ejemplo. Nuestra base de datos incluye datos de la bibliografía así como nuevas observaciones en diferentes antenas: Green Bank, Nancay, Arecibo y Effelsberg. Se han calculado distintos parámetros de interés, a saber: densidad de flujo integrado, velocidades heliocéntricas, anchos de velocidades a diferentes niveles de altura, así como diferentes parámetros de asimetría. Hemos calculado correcciones para la densidad de flujo integrado teniendo en cuenta la atenuación debida a la propia respuesta del telescopio y deficiencias en el apuntado. Las velocidades heliocéntricas y anchos de velocidades han sido corregidos también por efectos instrumentales y por la propia inclinación de la galaxia.

### Caracterización del contenido de HI (Capítulo 4)

Una vez que disponemos de las densidades de flujo integrados, hemos calculado los contenidos de HI ($M_{HI}$) para todas las galaxias que fueron detectadas, o límites superiores para aquellas galaxias que no lo fueron. En total tenemos datos para N = 910 galaxias. Hemos calculado los $M_{HI}$ tanto para la muestra de HI como una submuestra de ésta conteniendo todas las galaxias con dato de HI en la muestra completa según el óptico (Verdes-Montenegro et al. 2005). Hemos calculado correlaciones lineales entre $M_{HI}$, $L_B$, $a^2$ y los tipos morfológicos, y hemos comparado con las correspondientes de Haynes & Giovanelli (1984) utilizando una muestra de N = 287 galaxias aisladas (HG84). Nuestros ajustes revisados pueden ser utilizados en un futuro para comparar con el correspondiente contenido de HI en galaxias localizadas en entornos densos.

El acuerdo entre los ajustes de HG84 y los nuestros para la muestra de HI y la submuestra completa de HI son razonablemente buenos. Sin embargo, es relevante notar que encontramos varias mejoras con respecto a los ajustes de HG84, principalmente porque consideramos un mayor número de puntos y porque cubrimos un mayor rango en $L_B$ y $M_{HI}$ que ellos. Por tanto son más significativos desde un punto de vista estadístico. Encontramos otra pequeña diferencia entre los ajustes $M_{HI}$ - $L_B$ de HG84 y los nuestros, en cuanto a que nuestros fits parecen estar ligeramente por debajo. Esto es así no sólo cuando consideramos todos los puntos, sino que también ocurre cuando muestreamos por tipos morfológicos. Esto es debido a que nuestras correcciones a la densidad de flujo integrada son menores que los de HG84.

Cuando muestreamos por tipo morfológico, los ajustes $M_{HI}$ - $L_B$ en HG84 con respecto a los nuestros muestran algunas diferencias mientras que los correspondientes a $M_{HI}$ - $a^2$ son casi identicos, incluso considerando análisis de supervivencia para considerar la información contenida en los límites superiores. Vemos que nuestras pendientes decrecen sistemáticamente conforme los tipos morfológicos son mayores, pero sin embargo esta dependencia no está presente en HG84.

Los ajustes para galaxias de tipo temprano (T = -5, -3, -2 y 0) no son fiables ($M_{HI}$ frente a $L_B$ o $a^2$) puesto que existen muchos límites superiores (alrededor de dos terceras partes). En cualquier caso, mejoramos considerablemente la situación con respecto a HG84.

Los ajustes lineales tanto para la muestra de HI como para la submuestra completa de HI muestra las mismas tendencias, pero nosotros utilizaremos esta última porque minimizamos posibles sesgos.

También hemos calculado los residuales de $M_{HI}$ para la muestra de HI, utilizando los ajustes $M_{HI}$ vs $L_B$ para la muestra completa de HI. Hemos obtenido un valor igual a 0.33 para el error típico del ajuste, que es similar al valor dado por HG84.

### Asimetrías en la componente de HI de galaxias aisladas (Capítulo 5)

En este Capítulo estudiamos la tasa de perfiles de HI asimétricos en nuestra muestra de galaxias aisladas. Hemos inspeccionado visualmente todos nuestros perfiles y hemos seleccionado 338 de ellos que no presentaban ningún tipo de irregularidades en la línea de base o interferencias, y con buena

relación señal a ruido, de la misma forma que hicieron Richter & Sancisi (1996) para una muestra de 1371 galaxias. Clasificamos los perfiles de acuerdo con sus criterios y según tres clases: simétricos, casi simétricos y asimétricos. Nosotros encontramos tasas de perfiles simétricos mayores que las obtenidas por Richter & Sancisi (1994): 66% a 50% respectivamente. Aplicamos el coeficiente de asimetría más usado en la bibliografía, $A_{flux\ ratio}$, que básicamente es la relación de flujo a la izquierda y a la derecha de la velocidad media. Hemos calculado las distribuciones de $A_{flux\ ratio}$ para las tres clases (simétrica, casi simétrica y asimétrica). La distribución de perfiles simétricos y casi simétricos son muy parecidos, con la media de esta última un poco mayor que la primera. La distribución para los perfiles asimétricos tiene una dispersión mayor junto con una media esperada más grande. Hemos decidido considerar sólamente dos grupos (simétrico y asimétrico) en el resto del estudio, puesto que las distribuciones de los perfiles simétricos y casi simétricos son muy diferentes con respecto a los asimétricos. Los simétricos y asimétricos no se pueden distinguir muy bien porque los errores en el coeficiente $A_{flux\ ratio}$ se espera que sea de $\pm$ 0.1, y no sabríamos separarlos muy bien cuantitativamente. Hemos considerado un límite entre el grupo simétrico y asimétrico de 1.15 (15% más flujo integrado en uno de los picos que en el otro).

Mostramos que usando el valor esperado $A^{expected}_{flux\ ratio}$ puede ser especialmente útil para limpiar las posibles observaciones que están afectadas por errores de apuntado o con atenuación del haz. Cuando tomamos en cuenta $A^{expected}_{flux\ ratio} < 1.05$ incrementamos la tasa de detección de un 66 % a un 79 %.

También comparamos con otros estudios en la bibliografía que realizan estudios cuantitativos atendiendo a asimetrías para otras muestras de galaxias. Para ello hemos recopilado y convertido sus coeficientes de asimetría de relación de flujos para que sean directamente comparables con los nuestros. Una vez hecho esto, y considerando el mismo límite entre simétricos y asimétricos (1.15), vemos que tienen un porcentaje de 70% para la muestra de galaxias normales de Haynes et al. (1998) y una tasa inferior para otras muestras de galaxias que en principio están interactuando (por ejemplo, Bournaud et al. 2005). Nuestra tasa de simetría global es más grande que cualquier otra encontrada en la bibliografía, sugiriendo que efectivamente nuestra muestra contiene galaxias que son considerablemente aisladas con respecto al resto de muestras.

Discutimos el posible origen del resto de perfiles de HI en nuestra muestra de galaxias aisladas. Nosotros minimizamos la opción de interacciones de marea porque consideramos un criterio de aislamiento estricto y por tanto no vemos galaxias de tamaño similar en los alrededores. La contribución en la asimetría de los perfiles por compañeras ricas en gas no parece ser importante puesto que los perfiles de HI de las galaxias no presentan picos individuales. En la mayoría de los casos vemos que hay diferencias entre el flujo integrado en la parte que se aproxima de la galaxia y la que se aleja, que pensamos pueden provenir de irregularidades en el campo de velocidades o en la distribución del HI (como es el caso de CIG 96, cuyo estudio interferométrico se detalla en el Capítulo 7).

Bournaud et al (2005) sugiere que la acreción de gas cosmológico es necesario para poder explicar la alta tasa de perfiles asimétricos incluso en galaxias aisladas y el hecho de que las asimetrías aumentan con el tipo morfológico de Hubble. Nosotros encontramos una tasa más pequeña de perfiles asimétricos para galaxias aisladas que para otras muestras (que en principio incluyen galaxias en entornos más densos), y probablemente la tasa podría ser más alta si reducimos más cualquier contribución artificial que pudiera contribuir a la forma de los perfiles (atenuación del haz, errores en el apuntado, mala sustracción de la línea de base, etc.). En cuanto a la tasa de asimetrías en función de la morfología, nosotros no vemos ningún aumento en HI. Por lo tanto parece que el alto porcentaje de perfiles asimétricos puede ser explicado en gran parte por el entorno (por ejemplo el escenario de fusiones menores), y por tanto no vemos que sea necesario en primer orden la utilización de acreción de gas.

En el Capítulo 6 estudiamos las imágenes de síntesis obtenidas con el VLA para una submuestra de 12 galaxias con los perfiles más asimétricos, así como 4 con perfiles simétricos para comparación.

**Asimetrías: submuestra de HI del VLA (Capítulo 6)**

Para estudiar el origen de las asimetrías hemos hecho uso del estudio estadístico realizado anteriormente para seleccionar una muestra de galaxias en densidades del entorno bajas con perfiles de HI

asimétricos y con una probabilidad minimizada de contaminación por compañeras. Puesto que no podemos estudiar este problema con nuestros datos, asumiremos desde ahora que el entorno juega el papel fundamental. Hemos observado un total de 12 galaxias aisladas en el VLA en su configuración más compacta (configuración D) para discriminar si las asimetrías se encuentra en la distribución de HI, en el campo de velocidades o es debido a compañeras ricas en HI. La muestra engloba 8 galaxias con perfiles asimétricos y 4 con perfiles simétricos para comparar. En este capítulo presentamos las observaciones así como la distribución de HI, campos de velocidades y mapas de canales. El principal fin es el de introducir y describir dichas imágenes, pero el análisis pormenorizada tal y como se hace para CIG 96 en el Capítulo 7 será presentado más adelante.

La mayoría de los perfiles asimétricos puede ser explicado por irregularidades en el campo de velocidades, y sólamente en algunos casos la distribución de HI se encuentra perturbado. Las galaxias normales (N = 41) incluidas en Pisano et al. (2002) presentan en general distribuciones más irregulares de HI que en nuestra muestra. Esto es con toda probabilidad debido a nuestro mejor criterio de aislamiento para la selección.

Las galaxias en nuestra muestra no tienen compañeras de tamaño comparable, pero normalmente se piensa que las galaxias espirales están rodeadas por satélites. Vemos un reducido número de compañeras muy pequeñas en el óptico, pero casi con toda probabilidad se encuentran proyectadas y no son compañeras reales (este es el caso por ejemplo de CIG 551). De hecho, aunque el límite de flujo de HI is típicamente $5 \times 10^6$ M$\odot$ (detectaríamos galaxias con masas de tipo nubes de magallanes), nosotros sólo vemos tres pequeñas compañeras ricas en gas. En cualquier caso, estos satélites no son lo suficientemente masivos como para haber producido las asimetrías en las galaxias primarias. Si acreción de gas (o nubes de alta velocidad) es la solución (Bournaud et al. 2005), el contenido de HI sería menor que nuestro límite de detección, o alomejor se encuentra muy extendido y presenta densidades muy bajas.

Además, no se encuentran presentes en nuestras galaxias ningún signo de colas de marea que pudiera indicar una interacción mayor, y en la mayoría de los casos el HI se encuentra relajado, excepto en el caso de CIG 96. En nuestra submuestra, si una galaxia presenta irregularidades en la distribución de HI entonces su campo de velocidades también sufre de algún tipo de irregularidad, pero el contrario no es siempre cierto. Entonces el suceso que produjo la asimetría todavía permanece visible en el campo de velocidades por un periodo de tiempo más largo que en su distribución de HI, y esto es lo que principalmente mantiene la asimetría en el perfil global de HI. Este es probablemente la razón de los perfiles asimétricos que encontramos en nuestra muestra de galaxias aisladas.

Desde una inspección visual, vemos que la curva de rotación de las galaxias parece caer más rápido al final de uno de los lados con respecto al otro. Este es el caso por ejemplo de CIG 96, 123, 736, 744 y 812. Las asimetrías en sus campos de velocidades podrían deberse a un origen común. Probablemente estamos viendo el resultado de una captura de un satélite ya completado, y con el HI que todavía muestra algunos indicios de irregularidades en el campo de velocidades (y algunas veces en su distribución de HI), especialmente en las regiones más externas del disco de HI. Las diferencias en forma de las asimetrías de los campos de velocidades podrían ser debidos a los diferentes grados de intensidad de las perturbaciones, o quizás estamos viendo objetos similares en diferentes estados de relajamiento después de un mismo tipo de perturbación, o quizás ambos.

### Análisis de observaciones VLA: CIG 96 (Capítulo 7)

Presentamos en este Capítulo el estudio interferométrico de NGC 864 (CIG 96), una galaxia espiral bien aislada de compañeras de tamaño similar, pero que presenta una gran asimetría en su perfil global de HI. Su distribución de HI presenta dos características principales: un pseudo-anillo de HI justo en la zona donde se acaba el óptico, y una estructura de HI de tipo anillo externa. Detectamos una pequeña galaxia ($M_{HI} = 5 \times 10^6$ M$_\odot$) con una contrapartida óptica muy débil, que se encuentra a at $\sim$ 80 kpc proyectada en distacia de NGC 864.

El perfil de HI es simétrico en velocidad, pero asimétrico en intensidad. Sin embargo, la cinemática 2D de NGC 864 muestra asimetrías a gran escala: hay un alabeo, y en la parte del sur encontramos

una caida muy fuerte en la curva de rotación. El gas atómico en esta región parece más desligado de la galaxia debido a la diferencia en la cinemática. Esto es evidente puesto que vemos un pico secundario en el diagrama posición - velocidad a un radio $\sim 400''$ al SO. Esta región tiene una extensión física de unos $3' \times 4'$ en las direcciones del eje mayor y eje menor respectivamente. Un simple análisis del perfil integrado concluiría que las regiones centrales de NGC 864 son prácticamente simétricas, con un valor de $W_{20}$ correlacionado con la luminosidad de la galaxia, puesto que cae en la relación Tully-Fisher. Son la regiones más externas las que son sorprendentemente más asimétricas, que se manifiestan en una más alta amplitud en el pico corrido al azul del perfil de HI.

La región externa de HI es grande, masiva, muy asimétrica y presenta mucha estructura. Su masa de HI tiene sobre $4.5 \times 10^9$ $M_\odot$, y la masa de HI asociada con la caida en la curva de rotación es sobre $2.3 \times 10^8$ $M_\odot$. No encontramos contrapartida en el óptico asociada con el HI perturbado. Aunque los alabeos en las regiones externas del HI de las galaxias son comunes, pocas tienen tanta estructura y asimetrías como esta galaxia.

La galaxia es aislada con respecto a otras galaxias de tamaño parecido, pero encontramos cinco pequeñas compañeras dentro de una distancia proyectada de 500 kpc. La más proxima, detectada en nuestros mapas, tiene una fuerza de interacción gravitacional (Dahari 1984) de $4 \times 10^{-4}$ (no dimensional), mientras que para otras este parámetro se encuentra entre $1 \times 10^{-5}$ y $8 \times 10^{-7}$. Por lo tanto son demasiado pequeñas en masa para haber causado las perturbaciones tan fuertes en las regiones externas de NGC 864.

Hemos considerado varias posibilidades para explicar el origen de estas asimetrías en el HI. Una perturbación auto inducida parece improbable: mientras que el pseudo anillo es una característica que se ve en muchas galaxias, la estructura de HI tipo anillo externa es demasiado grande para ser un anillo producido por una resonancia rota, puesto que la resonancia Lindblad más externa se encuentra normalmente a dos veces el final de la barra (Athanassoula et al. 1982). Una perturbación externa con una compañera, que podría haber interaccionado o incluso haber sido acretado, parece la causa probable del desligamiento de las regiones del SO y la estructura de HI tipo anillo. De todas formas, podemos excluir un encuentro con una distancia al pericentro grande puesto que necesitaría una compañera muy masiva, que simplemente no está presente. Si fuera debido a una compañera pequeña, entonces necesitaría estar muy cerca de NGC 864 para poder haber producido estas asimetrías, o mejor aún, atravesar la galaxia. Sin embargo, este pasaje no podría ser central porque el resultado no sería parecido a la morfología de NGC 864 (Athanassoula et al. 1997; Berentzen et al. 2003). La alternativa es que la compañera haya cruzado el plano ecuatorial de la galaxia primaria a una distancia intermedia, esto es, justo fuera del disco óptico y dentro del disco de HI extendido. Tal pasaje podría haber inducido el alabeo, y el gas de la compañera podría haber contribuido a la región del SO.

### Galaxias de tipo temprano ricas en HI (Capítulo 8)

El número de ETIGs depende del entorno. De hecho, la población de ETIGs en la muestra AMIGA es de sólo un 14 % (N = 138), porcentaje que está por debajo de la tasa de ETIGs en entornos más densos. Esto puede ser interpretado en el sentido de que nuestra muestra de galaxias minimiza el número de interacciones mayores. En este Capítulo estudiamos la naturaleza de las ETIGs en nuestra muestra. Para hacerlo consideramos toda la información relevante que hemos obtenido, esto es: $M_B$ para todas las ETIGs, colores (B-V) para 19, datos HI para 116 y FIR para 137 de ellas. Detectamos 31 ETIGs en HI (12 E, 3 E/S0 y 16 S0 galaxies; Sulentic et al. 2006) que corresponde a un $\sim$ 27 % de las 116 galaxias de tipo temprano observadas de la muestra AMIGA (y con v > 1500 km $s^{-1}$). Un número parecido de galaxias han sido detectadas en FIR, habiendo una coincidencia entre detecciones de FIR y HI de la mitad aproximadamente.

Teniendo en cuenta las luminosidades encontramos que ninguna de las galaxias en nuestra muestra se espera que sea un grupo fósil, puesto que el valor típico de $M_B$ para galaxias de tipo temprano es sobre $M_B$ = -20.5. Hay una baja probabilidad de que dos galaxias espirales en nuestra muestra (con $M_B$ = -20.8 de valor medio entre tipos Sa - Sc) produzcan una galaxia de tipo temprano puesto que resultaría en un sistema más luminoso.

Nuestra tasa de detección es similar tanto para elípticas como para lenticulares, resultado que está en desacuerdo con otras muestras de ETIGs en la bibliografía, y que sugiere que la naturaleza de nuestras ETIGs podría ser diferente a las correspondientes en otras muestras. Tenemos que notar que en nuestra muestra de galaxias aisladas no tenemos galaxias de tipo temprano muy luminosas (Sulentic et al. 2006), pero por el contrario es probable que otras muestras contengan galaxias elípticas muy luminosas características de entornos densos. Estas últimas son normalmente especialmente pobres en gas y pueden hacer que su tasa de detección disminuya.

La forma de los perfiles puede darnos información sobre el posible origen de las ETIGs ricas en gas: la mitad de las galaxias presentan perfiles de doble pico (incluso galaxias elípticas), que en principio es típico de galaxias con disco. La existencia de discos de gas está de acuerdo con las simulaciones numéricas de fusiones de dos espirales ricas en gas realizadas por Barnes (2002). Parte del gas pierde momento angular debido a choques y cae al núcleo, pero alrededor de la mitad del gas contenido en los progenitores pueden formar un disco estable con rotación. En nuestra muestra un tercio de las ETIGs ricas en HI presentan perfiles asimétricos o algún tipo de peculiaridad (por ejemplo CIG 870), y solamente un 20% presentan perfiles simétricos. Para el resto la baja señal a ruido no nos permite clasificar los perfiles.

De acuerdo con la información de HI, nuestras galaxias dentro de las ETIGs ricas en gas pueden ser clasificadas dentro de tres grandes grupos: 1) perfiles con un solo pico (e.g. CIG 164, 338, 352, 870 y 877), si ningún disco de gas en principio; 2) perfiles de HI asimétricos con dos picos (e.g. CIG 134, 332, 1025 y 1029), donde el gas podría proceder de fusiones menores y cuyo HI no está relajado totalmente; y 3) perfiles simétricos de HI simétricos (e.g. 128 y 393), que probablemente provengan del grupo anterior pero cuyo disco de HI ya está relajado.

Otra posibilidad es que los perfiles simétricos y asimétricos tengan diferentes orígenes: teniendo en cuenta que los perfiles asimétricos son 1 mag más brillantes que los simétricos ($M_B$ -19.8 frente a -18.9), los primeros podrían haber sido originados por fusiones de espirales de baja luminosidad mientras que los últimos podrían ser debidos a acreciones menores.

También discutimos las propiedades de las 6 galaxias para las que tenemos información completa, esto es, color $(B-V)$, peculiaridades en las imágenes ópticas, información HI y luminosidades FIR para chequear su origen. De este conjunto de galaxias hemos detectado HI en dos elípticas (CIG 164 y 870), con colores más azules que los normales encontrados en este tipo de galaxias, con pecularidades morfológicas y con los valores más grandes en luminosidad FIR. Por tanto podrían haber sido formado como un resultado de una fusión menor pasada (o una fusión de galaxias espirales de baja luminosidad). CIG 393 y CIG 481 son también más azules (pero más rojas que el grupo anterior), con valores de luminosidades FIR más pequeñas que CIG 164 y 870 y con algunas peculiaridades (asimetrías en el centro y región de alta densidad de polvo central, respectivamente). Para las galaxias con colores normales, encontramos límites superiores en FIR, ninguna con peculiaridades morfológicas importantes, y encontramos galaxias de tipo temprano con o sin HI. Por ejemplo, detectamos una ETIG: CIG 128, y otra no: CIG 684 (aunque el límite superior es grande). CIG 128 podría ser una galaxia elíptica primordial cuyo ISM ha estado evolucionando relativamente aislado desde el tiempo de formación protogaláctica, o probablemente ha obtenido su HI via acreción de gas desde el medio intergaláctico.

### Gas molecular (Capítulo 9)

Hemos utilizado la transición rotacional J = 1-0 de la molécula de CO para trazar la componente del gas molecular, que es el material fundamental para la formación estelar. Presentamos información CO(1-0) para 278 galaxias dentro de la muestra AMIGA, observados por nosotros en FCRAO, IRAM 30m o Nobeyama (201 galaxias en total); y/o compilados directamente de la bibliografía. Consideramos un submuestra limitada entre 1500 < v <5000 (N = 204 galaxies), con el fin de que sea tan completa como sea posible.

En primer lugar hemos calculado el $M_{H_2}$ (o límites superiores para aquellas galaxias no detectadas), incluyendo una corrección de apertura por atenuación del haz. Después hemos usado esta

submuestra para realizar una caracterización estadística del $M_{H_2}$ para nuestra muestra, y hemos hecho una inspección de las relaciones entre $M_{H_2}$, luminosidad óptica ($L_B$), diámetro lineal óptico ($a$), tipo de Hubble y contenido de HI ($M_{HI}$). Por último vemos la influencia que el entorno ejerce sobre el $M_{H_2}$ en galaxias. La distribución de puntos $M_{H_2}$ frente a $L_B$ para nuestras galaxias aisladas es similar a aquellas utilizadas por Perea et al. (1997). Los ajustes que presentan ellos son diferentes con respecto a los nuestros puesto que utilizamos $M_{H_2}$ como variable dependiente en vez de dependiente. Encontramos que en general no parece que haya un exceso o deficiencia en el $M_{H_2}$ de galaxias en interacción débil o fuerte, como sugería Verdes-Montenegro et al. (1998).

También hemos estudiado los ratios entre $L_B$, $M_{H_2}$, $M_{HI}$, y $M_{gas}$, y comparado con los resultados encontrados principalmente por Young & Knezek (1989) para una muestra conteniendo galaxias en interacción. Parece que el contenido total de gas es un componente fundamental de las galaxias que principalmente depende del tipo morfológico, y que se ve afectado sólo en segundo orden por el entorno. Además, como sugería Young & Knezek (1989), el contenido relativo de gas neutro en las diferentes fases (atómico y molecular) cambia cuando una galaxia sufre una determinada perturbación. Por lo tanto vemos que en galaxias aisladas el contenido relativo de gas atómico es más grande con respecto al contenido de gas molecular, mientras que en galaxias en interacción parece ocurrir lo contrario.

### Apéndices

Incluímos 4 apéndices donde se trata en detalle las diversas correcciones a las magnitudes azules, los diámetros ópticos, casos peculiares en la selección de los datos de HI, correcciones a flujo integrado de HI y anchos de velocidades, así como el análisis estadístico bidimensional haciendo hincapié en análisis de supervivencia y las diversas correlaciones que podemos considerar.

# Part I

# Introduction

# Chapter 1

# Introduction

A major and long-lasting debate in astronomy involves the relative roles of "nature" and "nurture" in galaxy formation and evolution. Although much is known about the effects caused by the environment, much uncertainty still exists to properly quantify them. The observational evidence is sometimes weak or unclear. For example, some studies find enhancements of star formation (SF) in interacting galaxies (Bushouse 1987; Xu & Sulentic 1991) whereas other find a marginal enhancement (Bergvall et al. 1996). Enhancements of the molecular gas ($H_2$) mass (traced by the CO emission line) would be expected for interacting systems, but surprisingly no trend as a function of the isolation level is seen (Perea et al. 1997; Verdes-Montenegro et al. 1998).

Interaction-driven secular evolutionary effects are also found in interacting galaxies. Relationships between density (or distance to the centre in the case of clusters) and morphological type have been widely studied (55 rich clusters by Dressler 1980 and groups by Postman & Geller 1984). Clusters can be classified in three groups: 1) spiral rich clusters, which are irregular in appearance, with low mean density, no concentration and no apparent segregation by morphological type; 2) clusters dominated by central giant elliptical galaxies (cD), dense and centrally concentrated, with morphological segregation and no many spirals; and 3) spiral poor clusters, that could be classified intermediate between 1) and 2) types above, with predominance of S0s and with morphological segregation. Most nearby clusters have a higher ratio of ellipticals and lenticulars, especially in the central regions (Oemler 1974). The morphology-density relationship for higher-redshift ($z \sim 0.5$) clusters was studied by Dressler et al. (1997), finding that the fraction of lenticulars was lower by 2 - 3 times than in nearby clusters, with a proportional increase of the spiral fraction (elliptical fraction remains the same). It seems reasonable to think then that a fraction of spirals could have been transformed into lenticulars after the cluster virialization, while ellipticals could have been formed in the loose-group phase or even earlier. The most studied groups are probably Hickson Compact Groups (HCGs), which are characterised by a small number of members (4 to 10) with a low velocity dispersion ($< \sigma > = 200$ km s$^{-1}$, Hickson et al. 1992) and with a projected galaxy density similar to the cores of dense clusters (Huchtmeier 1997; Verdes-Montenegro et al. 2001a). The mean fraction of spiral galaxies in HCGs is also lower than in the field.

Atomic gas (HI) is the most affected component due to interactions since its extent is usually twice the optical size. Therefore, asymmetries in the HI distribution and in the velocity field of interacting galaxies is the rule more than the exception. The HI can give insight into the dynamics and evolution of a system of galaxies (e.g. VLA HI map of the nearest interacting group of galaxies, the group dominated by M81, by Yun et al. 1994). HI deficiencies in galaxies residing in high density environments are well studied. Several physical mechanisms are present for the removal of HI, like ram pressure stripping in clusters (hot intra-cluster gas producing X-rays), tidal interactions, etc. Two-thirds of the 18 clusters studied by Solanes et al. (2001) show a low content of neutral gas in their inner regions, and the HI deficiencies in their spiral galaxies increases continuously towards their centre. Deficiencies are also seen in groups. An evolutionary model for HCGs is presented by Verdes-Montenegro et al. (2001a), ranging from groups with no obvious signs of interactions in the HI to systems where the HI is totally stripped.

No suitable control samples to which interacting sample properties can be compared exist up to date. Ideally this would involve samples of isolated galaxies. Samples of isolated pairs and compact groups provide the parameters to quantify effects of 2 and n-body interactions. Isolated galaxy samples should provide the baseline for interpreting the strength and properties of interaction-induced effects. Awareness of these two effects (one-on-one vs. local over-density) is important in compiling isolated galaxy samples. In the currently popular theoretical paradigm of hierarchical structure formation and evolution, the concept of "isolated galaxy" does not exist in the strictest sense. Yet it remains a valid concept in terms of understanding the evolution of galaxies in the low density environment and over the dynamical timescale of disk rotation and halo crossing time. They are extremely interesting laboratories for studying and understanding galactic dynamics and disk evolution, and they may prove a testing ground for the ΛCDM substructure problem (i.e., presence of abundant satellite dark matter halos).

The most common reference or control samples found in the literature can be described as either "field" or "normal". The former refers to the most isolated galaxies while the latter refers to galaxies which show none of the generally accepted signs of interaction-induced activity. A field sample (e.g. Kennicutt & Kent 1983) might include any galaxy not belonging to a cluster, so galaxies in pairs, triplets and loose/compact groups would not necessarily be excluded. Normal galaxy samples would be defined in terms of specific parameters such as HI content (Boselli et al. 2001) or a given level of nuclear activity. Study of a selected quantity as a function of the environment is then one way to quantify the level of environmentally induced activity.

The alternative approach involves sample selection using an isolation criterion. Studies of isolated galaxies usually involve from 10s to 100-200 objects (e.g. Huchra & Thuan 1977; Vettolani et al. 1986; Márquez & Moles 1999; Márquez et al. 2000; Colbert et al. 2001;Pisano et al. 2002; Varela et al. 2004). The largest samples of isolated galaxies in the literature involve, in most cases, monochromatic observations of subsamples from the Catalogue of Isolated Galaxies (CIG: Karachentseva 1973, also referred as K73 in SIMBAD and KIG in NED databases) (Adams et al. 1980; Haynes & Giovanelli 1980, 1984; Young et al. 1986; Sulentic 1989; Xu & Sulentic 1991; Hernández Toledo 1999; Perea et al. 1997; Sauty et al. 2003b).

Previous works suggest that small samples of isolated galaxies have limited statistical value. This motivated us to use the CIG as the basis for a large, well-defined and statistically significant multi-wavelength database that can serve as a comparison template for the study of galaxies in denser environments. A large sample like CIG can be refined and quantified in terms of degree of isolation. It can then be correlated with multi-wavelength interstellar medium (ISM) properties. The result can be a sample large enough to characterise the low density tail of the two-point correlation function. This study constitutes the AMIGA project (Analysis of the interstellar Medium of Isolated GAlaxies), that will be explained in detail in the next chapter. AMIGA is compiling data that will characterise all phases of the ISM. All the information gathered will be publicly released at the web page of the project http://www.iaa.csic.es/AMIGA.html.

In this Thesis work the main topic under study is the analysis of the neutral gas properties of the CIG sample. The neutral gas is mostly composed by atomic gas, traced by the HI line, and molecular gas, traced by the 1-0 rotational emission line of the CO molecule. The main objectives of this Thesis can be summarised as follows:

- To build a reference sample of isolated galaxies with HI and CO observations, either performed by us, or compiled from the bibliography, providing relevant HI and $H_2$ information (shape of the spectra and mass content), as well as the total neutral gas.

- To study the correlations between the HI and $H_2$ masses, optical luminosities and sizes for a sample of isolated galaxies, and to compare them with previous works (e.g. Haynes & Giovanelli 1984, Perea et al. 1997)

- To study the rate of isolated galaxies with HI lopsidedness (both in its distribution and/or velocity field),

- To study the origin of HI lopsidedness in isolated galaxies: are they found in the HI distribution and/or the velocity field? Do we find companion galaxies or HI clouds optically invisible around the galaxy that can explain them?,
- To understand the origin of HI-rich early type galaxies (minor/major merger scenario or primordial early type galaxies) and compare with other samples of early types in denser environments.

The outline of the Thesis is as follows. It is divided into three parts: In Part I we introduce the main results of the AMIGA project up to date (Chapter 1). In Part II we study the HI properties of the isolated galaxies, distributed in seven chapters: HI single-dish data (observed by us or compiled from the bibliography) are presented in Chapter 2 together with a general statistics related to the HI properties of the sample. The HI content as a function of the optical luminosity, linear optical diameter and morphology, are presented in Chapter 3. In Chapter 4 and Chapter 5 we study HI lopsidedness from two different approaches, the former using the statistics of HI single-dish profile asymmetries in order to see the typical rate of lopsidedness in isolated spiral galaxies, and the latter to study their origin by using VLA synthesis imaging of a reduced subsample of some of the galaxies showing the most asymmetric profiles. The detailed analysis of the most interesting galaxy of this subsample (CIG 96) is presented in Chapter 6. In Chapter 7 we study the properties of those isolated early-type galaxies (ellipticals or lenticulars) which have been detected in HI in order to understand what their origin is. Part III includes the study of the molecular gas for a subsample of 200 galaxies (Chapter 8), with a structure similar to that of the HI. We present the observations performed by us and the compilation of data, and we study the properties of the $H_2$ content as a function of the optical luminosities, size, HI content, total neutral gas and morphology. The summary of the results and final conclusions are presented in Chapter 9.

A number of appendices are also included in order to give more detailed information about the work performed in this Thesis: A) Corrections to the apparent magnitudes, B) Calculation of optical diameters, C) Selection of the HI data, D) Corrections to the HI integrated flux density and line-width, E) presentation of the HI single-dish profiles, F) presentation of the CO(1-0) profiles and G) Revision of bivariate analysis.

# Chapter 2

# AMIGA project

The AMIGA project (Analysis of the interstellar Medium of Isolated GAlaxies) is building and analysing a multi-wavelength database for a well-defined and statistically significant sample of isolated galaxies in order to study the interplay between star formation, interstellar medium, nuclear activity and environment. Our sample is based on a refinement of the Catalogue of Isolated Galaxies (Karachentseva 1973, CIG), which is a sample of N $\simeq$ 1000 galaxies located in low density environments. To trace the different components, we have gathered information in optical (B and H$\alpha$), infrared (FIR and NIR) and radio emission (continuum plus HI and CO lines) for these galaxies (Leon & Verdes-Montenegro 2003; Verdes-Montenegro et al. 2005; Espada et al. 2005; Sulentic et al. 2006; Lisenfeld et al. 2006; Leon et al. 2006).

## 2.1 Introduction

The main aims of the AMIGA project are:

- to compare and quantify the properties of different phases of the interstellar medium (ISM) in this sample, as well as the level of star formation (SF) and nuclear activity.
- to use this control sample as template in the study of SF and galaxy evolution with respect to denser environments.
- to quantify the role of nature versus nurture, distinguishing between environmental density and one-on-one interactions

In the following sections we summarise the main results of the AMIGA project. In § 2.2 the selection criteria used by Karachentseva (1973) to select the CIG galaxies are explained. The refinements that the AMIGA group has performed over the CIG sample are presented in § 2.3 (positions, redshifts, morphology, isolation and completeness of the sample). An overview of the multi-wavelength studies performed up to now are summarised in § 2.4.

This project is an international collaboration coordinated by Dr. Lourdes Verdes-Montenegro (Instituto de Astrofísica de Andalucía - IAA, CSIC, Granada, Spain). The core of the group is located in Granada, including: Dr. Gilles Bergond (IAA), Daniel Espada (Ph.D. candidate, IAA), Emilio J. García (System Manager, IAA), Dr. Stéphane Leon (IRAM), Dr. Ute Lisenfeld (Universidad de Granada), José Sabater (Ph.D. candidate, IAA), Juan de Dios Santander (Ph.D. candidate, IAA), Dr. Simon Verley (Ph.D. IAA and Observatoire de Paris, currently Post-Doc Oss. Astr. de Arcetri, Italy). Other collaborators in particular aspects of the project are: Dr. Jack Sulentic (Professor at University of Alabama, USA), Dr. Walter Huchtmeier (Staff-Astronomer at Max Planck Institute of Bonn, Germany), Dr. Steven Odewahn (Staff-Astronomer at Mc Donald Observatory, USA), Dr. Min S. Yun (Associate professor at University of Massachusetts, USA), Dr. Françoise Combes (Professor

Observatoire de Paris, France), Dr. Albert Bosma and Dr. Evangelie Athanassoula (Staff-Astronomer Observatoire de Marseille, France).

Next we list the main contributions by D. Espada to this project:

1) Refinements to the sample:

- calculation of optical luminosity, including correction to the apparent blue magnitudes (see § 2.3.5).

- optical geometry: compilation of optical apparent diameters, axis ratios and position angles of the galaxies, as well as re-computation of linear diameters and inclinations (see § 2.3.5).

2) Multi-wavelength study:

- HI: main responsible for the observations (both single dish and synthesis imaging), reduction and analysis of the data (see § 2.4.3), both single-dish and interferometric.

- CO: co-responsible (together with Dr. Ute Lisenfeld) for the observations, reduction and analysis of the data (see § 2.4.4).

All these items are explained in detail along this Ph.D. Thesis work. They have been done under the supervision of Dr. L. Verdes-Montenegro and other members of the team and collaborators. At the same time, D. Espada has actively participated in discussions and publications focused on other parts of the project. More details about the rest of the project can be found in the references listed above.

## 2.2 CIG sample

AMIGA is trying to avoid two forms of "nurture": one-on-one interaction and galaxy environmental density. Our reference sample is drawn from the Catalogue of Isolated Galaxies, which originally included N = 1050 nearby galaxies in the northern hemisphere, which corresponds to 3% of the galaxies included in the CGCG (Catalogue of Galaxies and Clusters of Galaxies, Zwicky et al. 1961) with $m_{pg}<$ 15.7 and $\delta >$ -3°. The main properties and strengths of this sample are explained in detail in Verdes-Montenegro et al. (2005) and Sulentic et al. (2006).

The CIG sample was assembled by Karachentseva (1973) with the requirement that no similar sized galaxies with angular diameter $D_i$ between 1/4 and 4 times diameter $D_P$ of the CIG galaxy lie within 20 × $D_i$:

$$R_{ip} \geq 20 \times D_i \tag{2.1}$$

$$\frac{1}{4} \times D_P \leq D_i \leq 4 \times D_P \tag{2.2}$$

where $R_{ip}$ is the angular separation between the primary and the companion galaxy.

CIG is complemented by catalogues of galaxy pairs (CPG, Catalogue of Paired Galaxies; Karachentsev 1972), triplets (Karachentseva et al. 1979) and compact groups (Hickson catalogue of Compact Groups, HCG; Hickson 1982). All of these interacting comparison samples were visually compiled using an isolation criterion.

## 2.3 Refinement to the CIG sample

We have performed several improvements to the CIG sample, being among the most relevant ones the reevaluation of the positions, redshifts, morphologies, isolation degree and optical properties of the galaxies. The completeness of the sample has been also evaluated.

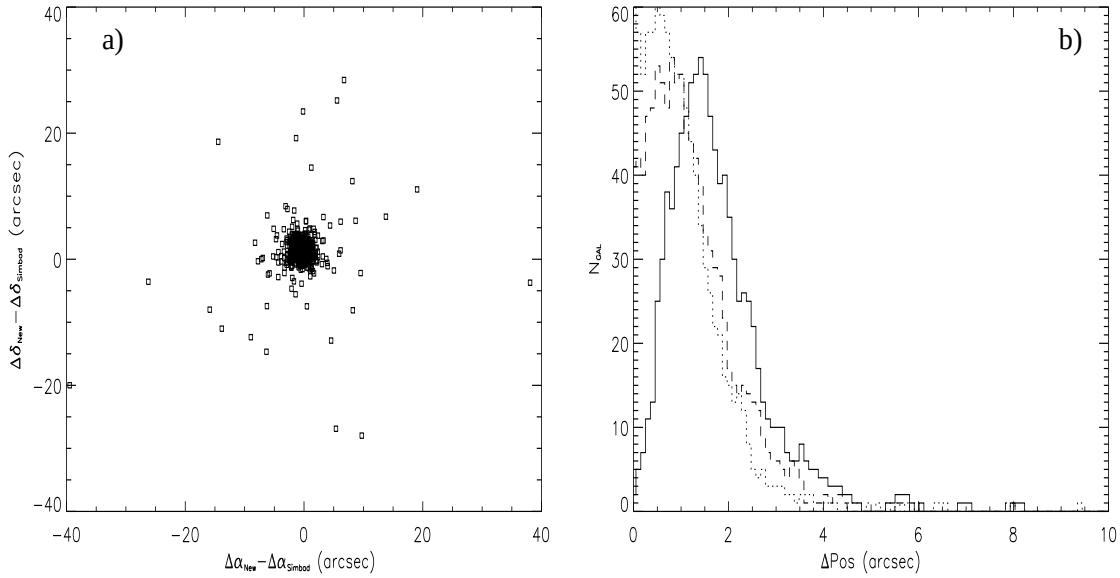


Figure 2.1: a) Differences between our measured positions and those retrieved from SIMBAD for the CIG galaxies. b) Histogram of the difference between the new positions and the SIMBAD positions for the $\alpha$ (dotted line), $\delta$ (dashed line) coordinates and the total distance (solid line) in arcsec. The plotted range is restricted to $10''$ for clarity of the plot (Leon & Verdes-Montenegro 2003).

### 2.3.1 Positions

In a comparison of the CIG positions in the SIMBAD database and the Updated Zwicky Catalogue (UZC; Falco et al. 1999), Leon & Verdes-Montenegro (2003) found differences of up to several tens of arcsec for some galaxies, large enough to make accurate telescope pointings or cross correlations with on-line databases problematic (see Fig 2.1). This is especially relevant for radio single-dish observations since an offset in the pointing can result in a loss of flux and an artificial lopsidedness of the profile. This motivated them to systematically revise all of the CIG positions using SExtractor (Bertin & Arnouts 1996) on the DSS images and checking visually the results, finding differences between old and new positions of up to $38.9''$ with a mean value of $2.4''$ for both SIMBAD and UZC. They provided new positions with a typical uncertainty of the order of $1''$.

### 2.3.2 Redshifts and distances

The archival and bibliographic search carried out by Verdes-Montenegro et al. (2005) reveals redshift data for almost the entire sample from NED (50% of the sample) and 41 other different sources. This includes 10 new redshifts obtained from HI observations performed by us at the Nançay and Green Bank (GBT) radio-telescopes. Redshift distances were derived there for all galaxies with $V > 1000$ km s$^{-1}$ assuming $H_0 = 75$ km s$^{-1}$ Mpc$^{-1}$. Redshift-independent distance estimates were provided when available in the literature for galaxies with $V < 1000$ km s$^{-1}$.

The redshift distribution for the CIG galaxies re-enforces the evidence for a bimodal structure seen earlier in smaller samples (Fig. 2.2). The peaks at redshift near 1500 and 6000 km s$^{-1}$ correspond respectively to galaxies in the local supercluster and those in more distant large-scale components (particularly Perseus-Pisces). The two peaks in the redshift distribution are superimposed on a 50% or more of the sample distributed in a much more homogeneous way. The CIG probably represents one of the most homogeneous local field example that has ever been compiled.

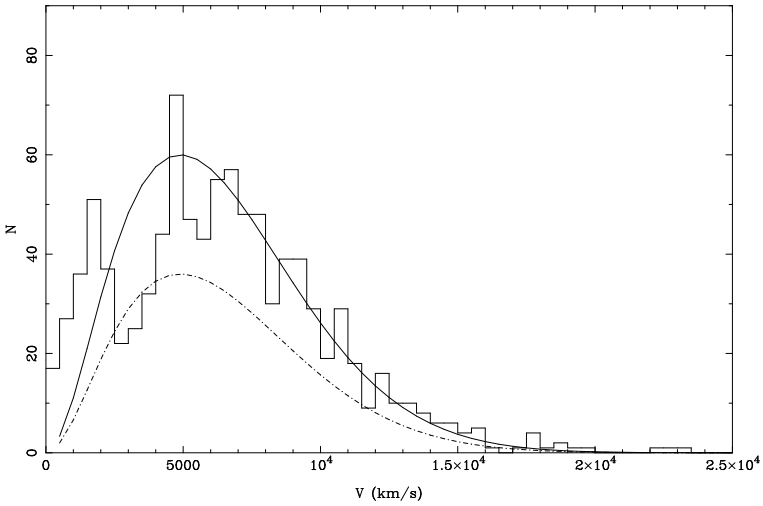


Figure 2.2: Histogram of the optical heliocentric velocities of the 988 CIG galaxies with redshift data (Verdes-Montenegro et al. 2005). The solid line corresponds to a homogeneous redshift distribution of the same sample size, velocity distribution and Schechter function. The dashed line has been obtained by scaling down the previous distribution by a factor of 0.6.

### 2.3.3 Morphology

All morphological types are found in the CIG catalogue, and the CIG sample is large enough to permit discrimination on the basis of galaxy type. Compilation of the types given by several databases was obtained (NED[1] and LEDA[2], but in many cases contradictions were found. This motivated Sulentic et al. (2006) to revise the morphologies for the whole sample using the POSSII images ($\simeq$ 80% of the sample), archival data (SDSS and images in James et al. 2004, accounting for $\simeq$ 20 % of the sample), and new CCD images observed mainly at the 1.5m Observatorio de Sierra Nevada in Granada, Spain). These images improve the sensitivity achieved by POSSI images and allowed us to obtain more accurate morphological classifications.

The results of the morphological reevaluation of the CIG galaxies with $V_{\rm R} > 1000$ km s$^{-1}$ (N = 1018) are listed in Tab. 2.1. This most isolated sample of galaxies in the local Universe is dominated by two populations: 1) 82% spirals (Sa–Sd) with the bulk being luminous systems with small bulges (63% between types Sb–Sc) and 2) a significant population of early-type E–S0 galaxies (14%). Most of the types later than Sd are low luminosity galaxies concentrated in the local supercluster where isolation is difficult to evaluate. The late-type spiral majority of the sample spans a luminosity range $M_{B-\rm corr} = -18$ to $-22$ mag. Few of the E/S0 population are more luminous than $-21.0$ marking an absence of, an often sought, super $L^*$ merger (e.g. fossil elliptical) population.

We show in Fig. 2.3 the morphological type distribution for the CIG sample as a function of recession velocity (Sulentic et al. 2006).

### 2.3.4 Isolation

A total of N = 1050 galaxy members of the CGCG catalogue were selected using the criteria in Eq. 2.1 and Eq. 2.2. After revision, Adams et al. (1980) and Karachentseva (1986) assigned codes to the galaxies that were seen to violate these criteria: 902 galaxies remained as isolated (code=0), 85 as marginally isolated (code=1) and 64 were interacting galaxies (code=2).

One of the improvements of the AMIGA project over the CIG sample was to revise in a computerised way the Karatchenteva's criteria using the digitised POSS. Verley (2006) have revised the

[1]This research has made use of the NASA/IPAC Extragalactic Database (NED) which is operated by the Jet Propulsion Laboratory, California Institute of Technology, under contract with the National Aeronautics and Space Administration.

[2]We acknowledge the usage of the HyperLeda database (http://leda.univ-lyon1.fr), Paturel et al. 2003a.

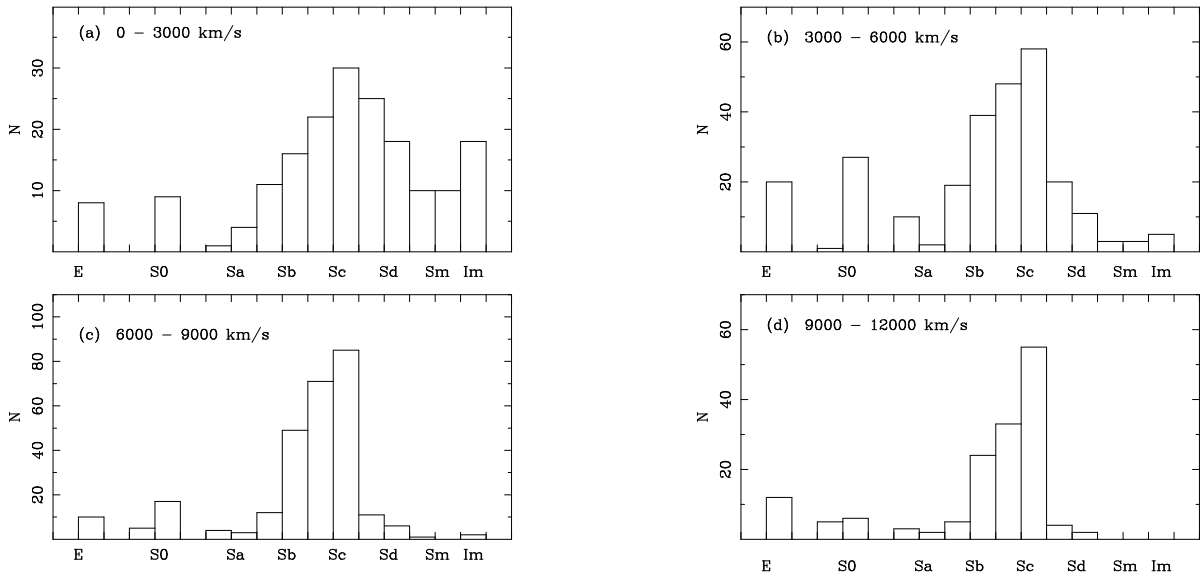


Figure 2.3: Type distribution of the CIG galaxies considering four recession velocity bins: 0 - 3000, 3000 - 6000, 6000 - 9000 and 9000 - 12000 km $s^{-1}$ (Sulentic et al. 2006).

Table 2.1: Main results of the morphological reclassification of the CIG sample (Sulentic et al. 2006).

| Type | $T$ | $N$ | $N/1018$ |
|---|---|---|---|
| E | −5 | 58 | 0.057 |
| E/S0 | −3 | 14 | 0.014 |
| S0 | −2 | 67 | 0.066 |
| S0/a | 0 | 19 | 0.019 |
| Sa | 1 | 13 | 0.013 |
| Sab | 2 | 52 | 0.051 |
| Sb | 3 | 159 | 0.156 |
| Sbc | 4 | 200 | 0.196 |
| Sc | 5 | 278 | 0.273 |
| Scd | 6 | 61 | 0.060 |
| Sd | 7 | 41 | 0.040 |
| Sdm | 8 | 15 | 0.015 |
| Sm | 9 | 15 | 0.015 |
| Im | 10 | 26 | 0.026 |
| E–S0 | | 139 | 0.137 |
| Sa–Sd | | 804 | 0.790 |
| Sb–Sc | | 637 | 0.626 |

POSSI fields to check the isolation of the galaxies using SExtractor (Bertin & Arnouts 1996) and a star/galaxy separation procedure (Odewahn 1995, LMORPHO). The number of POSSI fields ($55' \times 55'$, the maximum size that can be downloaded) to be considered for each galaxy depends on the recession velocity of the galaxy: 1 for v $>$ 4687 km s$^{-1}$, 2 $\times$ 2 for 2343 $<$ v $<$ 4687 km s$^{-1}$ and 3 $\times$ 3 for v $<$ 2343 km s$^{-1}$. Visual revision of the star/galaxy separation and cross-checking with POSSII images have been performed to check for any possible misclassification. None of the previously flagged galaxies in the CIG catalogue were excluded.

Those sources classified as galaxies in the corresponding fields were gathered in order to quantify the isolation degree of the CIG galaxy. To do so Verley (2006) has considered different isolation coefficients, including:

- **k-density estimator**: from the distance to the k-th companion (neither the central galaxy nor the k-th companion are taken into account), we can obtain the following parameter:

$$\rho_{\rm k} = \frac{\rm k-1}{\rm V(r_k)} \tag{2.3}$$

  with V(r$_{\rm k}$) = $4\pi r_{k^3}/3$, where r$_{\rm k}$ is the distance to the k-th nearest neighbour.

- **Projected density within 0.5 Mpc**: variation of the previous k-density estimation, but counting all the companions over a 0.5 Mpc physical surface around each CIG galaxy. Only galaxies satisfying Karachentseva's criterion in Eq. 2.2 are included, to avoid the inclusion of foreground and background galaxies which are not close to the primary galaxy.

- **Tidal forces within 0.5 Mpc**: the tidal force per unit mass produced by a companion, as explained in Dahari (1984), is proportional to:

$$\frac{M_i}{r_{ip}^3} \alpha \frac{(D_i D_P)^{1.5}}{S^3} = Q \tag{2.4}$$

  where M$_i$ is the mass of the companion, r$_{ip}$ is the distance from the primary galaxy to the companion and S the projected separation between the centres of the two galaxies. Q, defined by this equation, is a dimensionless estimation of the gravitational interaction strength.

The use of these parameters will allow us to study magnitudes such as the asymmetry of the HI profiles, SF, nuclear activity, etc. as a function of the degree of isolation.

CIG is complemented by catalogues of galaxy pairs (CPG, Catalogue of Paired Galaxies; Karachentsev 1972), triplets (KTG, Karachentsev catalogue of Triplet Galaxies, Karachentseva et al. 1979) and compact groups (Hickson catalogue of Compact Groups, HCG; Hickson 1982). All of these interacting comparison samples were visually compiled using an isolation criterion.

We can compare the isolation level of the CIG with galaxies in denser environments in order to calibrate our isolation estimators. Fig. 2.4 shows the tidal forces estimator versus the k-th local density parameter for the primary galaxies of each CIG, triplets and HCGs. We have also included galaxies in some Abell clusters (ACO, Abell 1958), although Abell did not consider any isolation criterion. The tidal force is clearly sensitive to separate CIG, KTG and HCG galaxies (in order of interaction degree), and together with the k-th local density estimation we can have a picture of the repartition of galaxies surrounding the primary galaxy. The selected ACO galaxies are the nearest and poorest ones and therefore the tidal force parameter is not representative. On the other side, these galaxies have the highest k-th local density estimation among all considered galaxies.

Redshifts for the $\sim$ 54000 companions were also compiled when available from a dozen of surveys and catalogues (NED, LEDA, SDSS, 2dF, CfA, UZC, etc.) in order to identify the foreground and background population of the CIG galaxies. Redshifts for 70% of the companions are missing, but for $\sim$ 80 galaxies the fields are at least 80% complete in redshift. This subsample served as a reference to

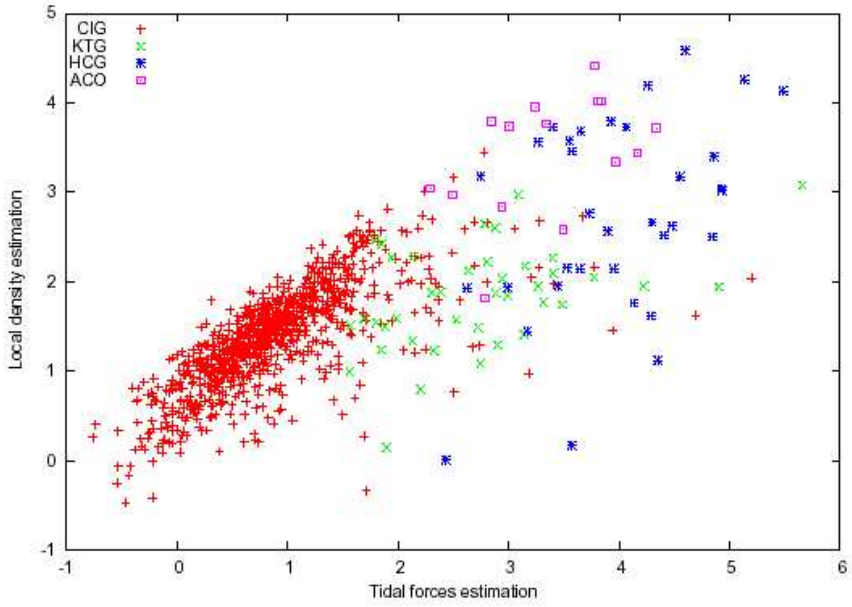


Figure 2.4: Tidal forces estimator vs the k-th local density parameter for the primary galaxies of each CIG, KTG, HCG and ACO (Verley 2006). For convenience, only galaxies with v $>$ 4687 km s$^{-1}$ were considered by Verley (2006) in CPG, HCG and ACO in order to inspect only one POSSI field.

check the validity of the study considering all projected galaxies. The final results for the classification of the isolation are the following: 28 can be considered as *very isolated* (Tidal forces TF $\sim$ 0), 333 as *isolated* (TF $\sim$ 1), 446 as *quite isolated* (Tidal forces $\sim$ 2), 117 as *poorly isolated* (TF $\sim$ 2.5) and 26 as *interacting* (TF $\gtrsim$ 3.5).

### 2.3.5 Optical luminosity and optical geometry

The optical luminosity is a tracer of the visible light and stellar content. The completeness and the optical luminosity function (OLF) of the CIG sample are studied in Verdes-Montenegro et al. (2005). The OLF is compared with that of other samples of isolated galaxies or galaxies in denser environments. The OLF of the CIG sample as a function of the morphology is studied in Sulentic et al. (2006).

In this section we discuss the calculations to obtain: a) the optical luminosities , b) the OLF , and c) the compiled parameters (and applied corrections) to describe the optical geometry of the galaxies (optical diameters, axis ratios, inclinations and position angles).

#### a) Corrected apparent blue magnitudes ($m_{B\ corr}$) and blue luminosities ($L_B$)

We have corrected the apparent magnitudes due to systematic errors in the CGCG catalogue, galactic dust extinction, internal extinction and K correction (see Verdes-Montenegro et al. 2005, § 4.2):

- **Systematic errors** in the CGCG catalogue were reported by Kron & Shane (1976), who showed that galaxies in Volume I of the CGCG had important systematic errors relative to the rest of volumes. We applied these corrections ($A_v$) to the CIG galaxies in Volume I (i.e. galaxies with $\delta < 15^\circ$ and 7h$<\alpha<$18h) and with $m_B$ up to 15.7 mag.

- **Galactic dust extinction** ($A_{g\ Sch}$) has been derived from IRAS/DIRBE measurements of diffuse IR emission (Schlegel et al. 1998).

Table 2.2: Optical magnitudes and luminosities of the CIG sample[1].

| CIG | $m_B$ mag | $m_{B-corr}$ mag | $L_B$ $L_\odot$ |
|---|---|---|---|
| 1 | 14.30 | 13.64 | 10.67 |
| 2 | 15.70 | 15.23 | 10.00 |
| 3 | 15.70 | 15.04 | – |
| 4 | 12.70 | 11.55 | 10.40 |
| 5 | 15.50 | 14.52 | 10.39 |
| 6 | 14.50 | 13.69 | 10.21 |
| 7 | 15.60 | 15.30 | 10.51 |
| 8 | 15.40 | 14.18 | 10.32 |
| 9 | 15.40 | 14.54 | 10.45 |
| . | .. | .. | .. |

[1] The full table is available in electronic form at http://www.iaa.csic.es/AMIGA.html.

- **Internal extinction** corrections ($A_i$) were calculated as a function of inclination and morphological type following RC3. Inclinations were estimated from the ratio of major to minor axis as given in LEDA. We used our revised morphologies (see § 2.3.3).
- **K corrections** (Pence 1976) were applied with a mean value of 0.05 mag, ranging from 0 to 0.3 mag depending on the morphological type.

Summarizing, the corrected $m_B$ was calculated as follows:

$$m_{B-corr} = m_B + A_v + A_g + A_i + A_K \tag{2.5}$$

See a full description of the different corrections and some examples in Appendix A. In Tab. 2.2 we list the CIG uncorrected and corrected magnitudes, as well as the **optical luminosities**, derived as:

$$log(L_B/L_\odot) = 12.192 + 2 \times log[D(Mpc)] - 0.4 \times m_{B-corr} \tag{2.6}$$

where $D = V_{3K}/H_0$ is the distance to the galaxy ($V_{3K}$ is the velocity after the 3K correction and we assume $H_0 = 75$ km s$^{-1}$ Mpc$^{-1}$) from Verdes-Montenegro et al. (2005).

### b) Optical luminosity function (OLF)

The optical luminosity function of our set of galaxies can be parametrised by means of a Schechter function model with the parameters M$^*$ and $\alpha$:

$$\Phi(M) = \Phi_* 10^{0.4(\alpha+1)(M^*-M)} exp(-10^{0.4(M-M^*)}) \tag{2.7}$$

Verdes-Montenegro et al. (2005) used N = 725 galaxies with known distances and magnitudes in the range 11-15 mag, based on the $< V/V_m >$ completeness estimator (see Fig. 2.11), once having excluded 9 galaxies with very high or low luminosity scattered in bins containing a low number of galaxies. The fit is shown in Fig. 2.5 and the parameters are detailed in Tab. 2.3 where M$^*$ is given in corrected Zwicky magnitudes (see § 2.3.5).

This derivation of the CIG OLF is consistent with other studies for low density environments. A comparison via the Schechter parameter formalisation shows that: 1) $M^*$ increases with galaxy surface density on the sky (excess of high luminosity galaxies in denser environments), and 2) $\alpha$ shows a weaker tendency to become more negative for denser environments.

Table 2.3: Optical luminosity function for the CIG sample ($V_r < 1500$ km s$^{-1}$ excluded).

| Sample | $\Phi$(Mpc$^{-3}$ mag$^{-1}$) | $\alpha$ | M* | Mag range for the fit |
|---|---|---|---|---|
| CIG N = 725 | 6.3(± 0.7) × $10^{-4}$ | -1.27 ± 0.06 | -20.31 ± 0.07 | -16.3 to -22.3 |
| CIG N = 666 | 7.5(± 0.6) × $10^{-4}$ | -0.82 ± 0.09 | -20.11 ± 0.07 | -16.3 to -22.3 |

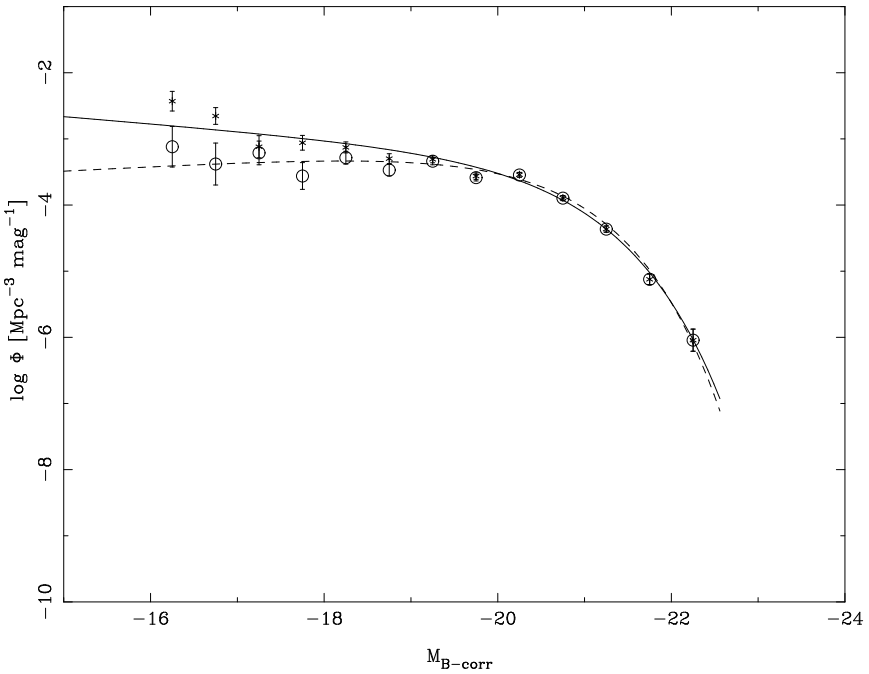


Figure 2.5: Optical luminosity function for CIG galaxies for which velocity information exists and with apparent magnitudes between 11 and 15 (Verdes-Montenegro et al. 2005, N = 725). The Schechter fit to this sample is plotted as a solid line. The dashed line corresponds to a fit to the same sample when galaxies with $V_r < 1500$ km s$^{-1}$ are removed.

Sulentic et al. (2006) discussed that early and late-type OLF's for the CIG sample are not similar, in spite of the claims by other authors. This effect is mainly due to the lack of bright ellipticals in the CIG sample, which are found in denser environments.

### c) Optical geometry

#### c.1) Optical diameter and axis ratio ($D_{25}$ and $R_{25}$)

Accurate values of the optical diameters are needed because: a) $M_{HI}$, $M_{H_2}$ and other magnitudes are often predicted as a function of the (linear) size of the galaxy, and inaccuracies in these parameters can lead to higher dispersions in these predictions, and b) we need to estimate the atomic and molecular gas extents of the galaxy based on the optical diameters. These extents are used to calculate a correction factor to the integrated density flux due to the beam attenuation of the radio-telescope (see Appendix D).

We have made use of the LEDA database in the compilation of the major axis $D_{25}$ (isophotal level of 25 mag/arcsec$^2$) and axis ratios $R_{25}$ ($R_{25} = D_{25}/d_{25}$, where $d_{25}$ is the minor axis, at an isophotal level of 25 mag/arcsec$^2$), as well as their errors (see Tab. 2.4). These quantities are expressed in the B-band according to the convention of the Second Reference Catalogue (de Vaucouleurs et al. 1976). Although the type of diameter calculated in different sources of the literature is not homogeneous (see

Appendix B where a comparison is done), many papers have studied a way to reduce the different diameters into one standard system, usually the isophotal level 25 mag/arcsec$^2$ (e.g. Paturel et al. 1991a; Paturel et al. 1997). We also compiled from LEDA the diameters in the $D_{25}$ system corrected by inclination and galactic extinction. The correction used for inclination and galactic extinction is (Bottinelli et al. 1995 for T > 1, see morphological codes in Tab. 2.1):

$$\log D_C = \log D_{25} - \mathrm{C}\ logR_{25} + A_{g\ Sch}\ K_d \tag{2.8}$$

where C = 0.3 for the E class (T ≤ -4), C = 0.15 for -3 ≤ T ≤ -1, C= 0.05 for T = 0, and C = 0.04 if T ≥ 1 (Bottinelli et al. 1995), $A_{g\ Sch}$ is the galactic extinction (Schlegel et al. 1998) and $K_d$ is given by Fouque & Paturel (1985) as $K_d$ = 0.094 for spiral galaxies (T ≥ 0) and $K_d$ = 0.081 - 0.016 × T for early type galaxies (T < 0).

See a full description of the obtention of the corrected and uncorrected angular diameters in Appendix B.

Table 2.4: Geometrical parameters of the CIG sample.

| CIG | log($D_{25}$) | $\sigma$ log($D_{25}$) | log($R_{25}$) | $\sigma$ log($R_{25}$) | log($D_C$)+1 | $D$ (Mpc) | $a$ (kpc) |
|---|---|---|---|---|---|---|---|
| 1 | 1.214 | 0.126 | 0.319 | 0.081 | 1.21778 | 92.2 | 44.38 |
| 2 | 0.868 | 0.068 | 0.142 | 0.039 | 0.885538 | 88.7 | 19.82 |
| 3 | 0.609 | 0.059 | 0.228 | 0.04 | 1.53314 | 26.1 | 25.91 |
| 4 | 1.534 | 0.03 | 0.609 | 0.061 | 0.851082 | 100.2 | 20.6 |
| 5 | 0.844 | 0.056 | 0.347 | 0.041 | 0.946752 | 55.8 | 14.35 |
| 6 | 0.922 | 0.094 | 0.34 | 0.075 | 0.836586 | 165.3 | 33.00 |
| 7 | 0.834 | 0.051 | 0.168 | 0.068 | 1.02548 | 79.8 | 24.61 |
| 8 | 0.998 | 0.106 | 0.455 | 0.059 | 0.957788 | 108.2 | 28.56 |
| 9 | 0.965 | 0.063 | 0.42 | 0.08 | 1.05906 | 57.5 | 19.16 |
| ... | ... | ... | ... | ... | ... | ... | ... |

### c.2) Linear (physical) diameter (a)

The linear diameter is calculated as follows:

$$a[kpc] = 10^3 \times D \tan(\frac{D_C[']}{60} \frac{\pi}{180} \frac{1}{1+z}) \tag{2.9}$$

where D is the distance calculated as D = $V_{3K}$/$H_0$ ($H_0$ = 75 km s$^{-1}$ Mpc$^{-1}$) and $D_C$ is the corrected face-on angular diameter calculated above.

The distribution of linear diameters (in units of kpc) is shown in Fig. 2.6 for the CIG galaxies with known z (N = 989). The mean value is around 20 kpc. Early type (T < 1) galaxies seem to be statistically smaller (red histogram) than spiral galaxies (T ≥ 1) in our sample. Only a few (≃ 10) early type galaxies are larger than 40 kpc. It also shows the histogram of linear diameters for the complete sample.

### c.3) Inclinations and position angles

The inclination ($i$) was determined from the value of $R_{25}$ in LEDA and our revised morphological type (Sulentic et al. 2006) with the following equation (Heidmann et al. 1972b):

$$sin^2(i) = \frac{1 - 10^{-2log(R_{25})}}{1 - 10^{-2log(R_0)}} \tag{2.10}$$

where log($R_0$) = 0.43 + 0.053 × T for T = -5 .. 7 and log($R_0$) = 0.38 for T > 7.

It seems that there are other ways of calculating the inclinations, but they are similar. For example in Solanes et al. (1996) spirals are considered like oblate spheroids of intrinsic axial ratio $q$ and $i$ is

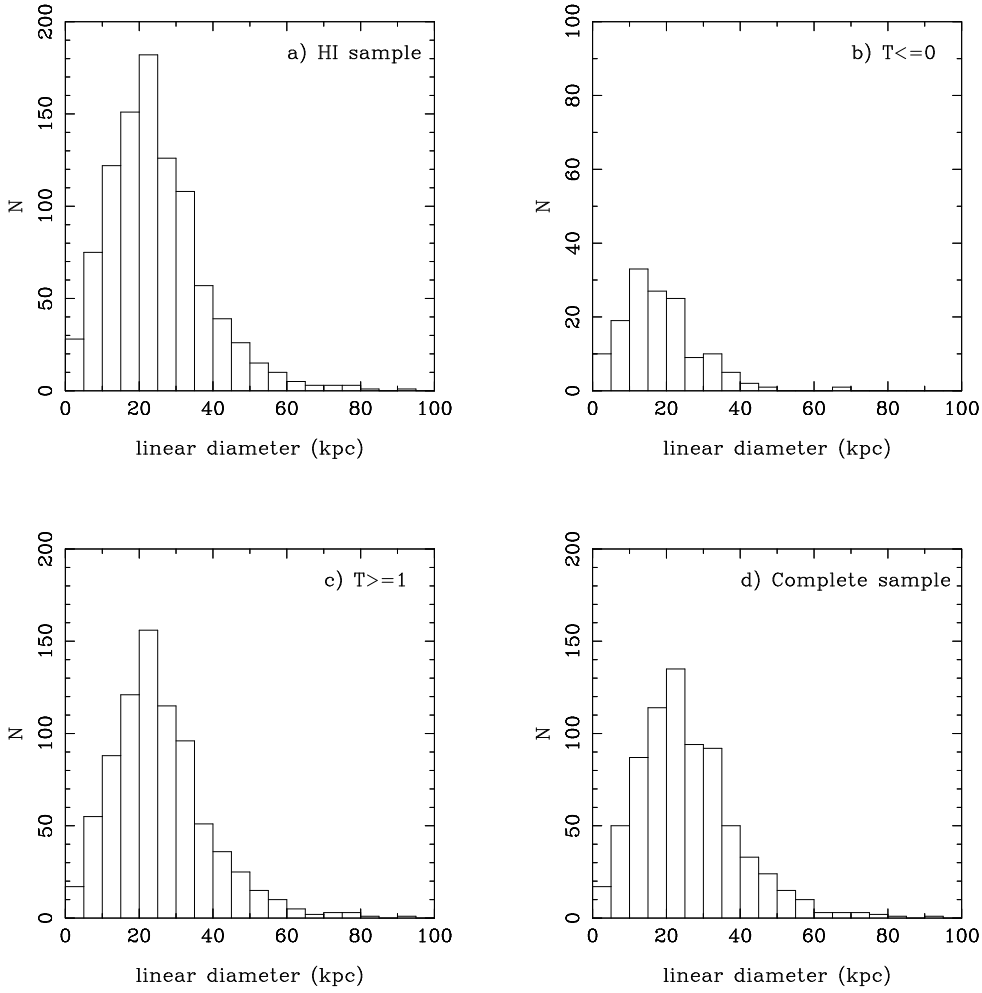


Figure 2.6: Histogram of linear diameters for the CIG sample: a) upper left, all galaxies in the sample observed in HI; b) upper right, early type galaxies (T $<$ 1); c) lower left, late type galaxies (T $\geq$ 1); d) lower right, the complete CIG sample. Only galaxies with known redshift are included.

calculated as:

$$cos^2(i) = \frac{(b/a)^2 - q^2}{1 - q^2} \tag{2.11}$$

where $a$ and $b$ are major and minor visual diameters, $q$ is taken to be $q = 0.32$ for Sa, $q = 0.23$ for Sab and $q = 0.18$ for Sb - Sc (Binney & de Vaucouleurs 1981). Whenever $b/a < q$, $i$ is set to 90°. Eq. 2.10 is more general than Eq. 2.11 since it includes other morphological types (this equivalence is straightforward using the relation $sin^2(i) + cos^2(i) = 1$).

The position angle (PA) was directly compiled from LEDA. It is calculated with respect to the 25 mag/arcsec$^2$ isophote in the B-band measured from North (PA = 0) to East between 0 and 180° (Paturel et al. 1989). Usually only galaxies with inclinations larger than 10° are included since the PA can not be accurately calculated. In Fig. 2.7 we see that the PA of the sample is approximately distributed in a homogeneous way.

A comparison of inclinations (and position angles) in LEDA versus those in NED for the CIG sample are shown in Fig. 2.8. Inclinations have been calculated using the diameters in both catalogues and with our revised morphologies (Sulentic et al. 2006). The large scatter is due to differences in $R_{25}$. In Fig. 2.9 we see the inclination as a function of $R_{25}$ and morphology, calculated as in Eq. 2.10, where the dependence on the morphology is included in the parameter $R_0$. As we can see, any change in the morphological classification can lead to strong differences in the inclination.

We show in Fig. 2.10 a comparison of the inclinations directly compiled from LEDA with respect to our inclinations calculated with the same equation but using our morphological types. We see that for a given $R_{25}$ differences between LEDA and our values are larger for higher inclinations. This is due to the fact that lines in Fig. 2.9 are less separated for smaller inclinations, but for inclinations larger than 50° a reclassification of the morphological type from early (or irregular) to late type or vice versa can result in a change of inclination of even 30°. For example, CIG 51 was classified as a Sbc galaxy and revised by us to be S0, changing the inclination from i = 69° to 90° with this reclassification. Additionally, there is a large uncertainty in the classification for highly inclined galaxies.

Table 2.5: Inclinations and position angles for the CIG sample.

| CIG | P.A. (°) | Inclination (°) |
|---|---|---|
| 1 | 47.3 | 64.3 |
| 2 | 94.3 | 44.7 |
| 3 | 165 | 62.5 |
| 4 | 47 | 84.8 |
| 5 | 137 | 69.8 |
| 6 | 155.2 | 66.8 |
| 7 | 19 | 49.1 |
| 8 | 74.5 | 72.1 |
| 9 | 68.5 | 72.6 |
| ... | ... | ... |

[1] Note that in Verdes-Montenegro et al. (2005) we used the inclinations compiled directly from LEDA.

### 2.3.6 Completeness of the sample.

Since the CIG sample is an optically selected sample, its completeness needs to be evaluated on the basis of the optical apparent magnitude (see § 2.3.5). We have evaluated the completeness of our sample following the $<V/V_m>$ test (Schmidt 1968), as explained in Verdes-Montenegro et al. (2005). For each object we calculate the volume V contained in a sphere whose radius is the distance to the

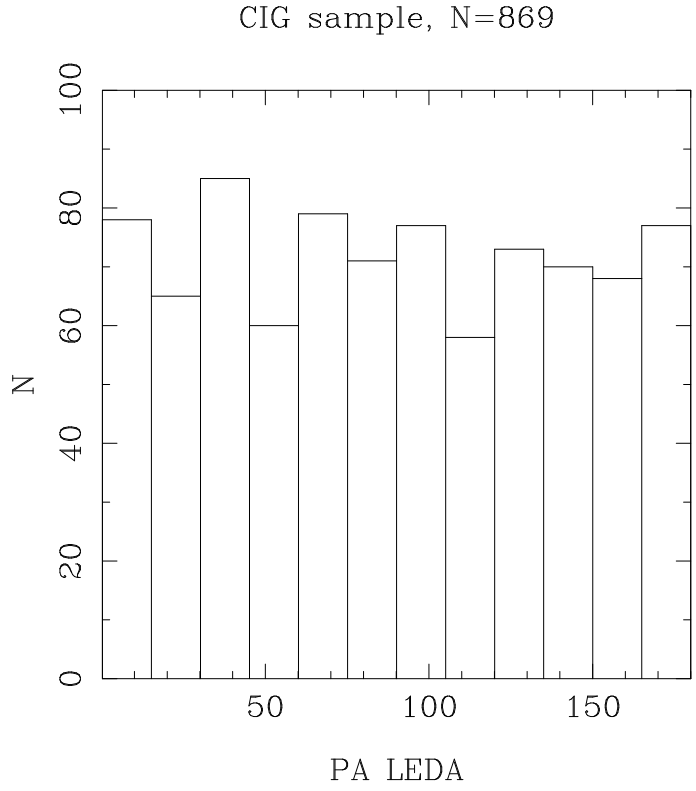


Figure 2.7: Histogram of position angles (LEDA) for the CIG sample.

object and the maximum volume $V_m$ contained in a sphere whose radius is the maximum distance at which the galaxy would still be visible given the limit magnitude of the CIG. Finally we calculate the average of the objects brighter than the limit magnitude. This has allowed us to select a complete subset of galaxies that will allow us to eliminate biases in our statistical studies.

We choose to neglect galaxies brighter than 11.0 mag because for these values the sample is incomplete due to their small number per magnitude bin. Our test suggests that the CIG is surprisingly complete (between 80-95%) brighter than 15.0 mag, but the sample becomes rapidly less complete at fainter limiting magnitudes. We therefore selected those galaxies with known distance and in the range of 11.0 to 15.0 mag (N = 746). This yields to an almost complete sample with $< V/V_m > =$ 0.41. The OLF has been calculated using these galaxies except for 10 galaxies with very low ($M_B >$ -16, N = 8 galaxies) or high ($M_B <$ -22.5, N = 2 galaxies) luminosity , since they are scattered in bins containing a low number of galaxies. For the rest of this work we will refer to these N = 736 galaxies as the 'complete CIG sample'.

## 2.4 Interstellar medium study

In order to study the properties of the different components of the ISM in isolated galaxies, we have observed or compiled multiwavelength information for the CIG sample: optical (H$\alpha$), infrared (FIR) and radio (continuum plus HI and CO lines) information. A description of the studies performed up to now for each one is explained next.

### 2.4.1 FIR luminosities

The far-infrared emission (FIR) is mainly due to the emission produced by gas and dust grains warmed by ultraviolet radiation from newly formed massive stars (M > 8 $M_\odot$). Most of the studies about FIR emission are skewed toward bright galaxies, which are usually much brighter than isolated ones.

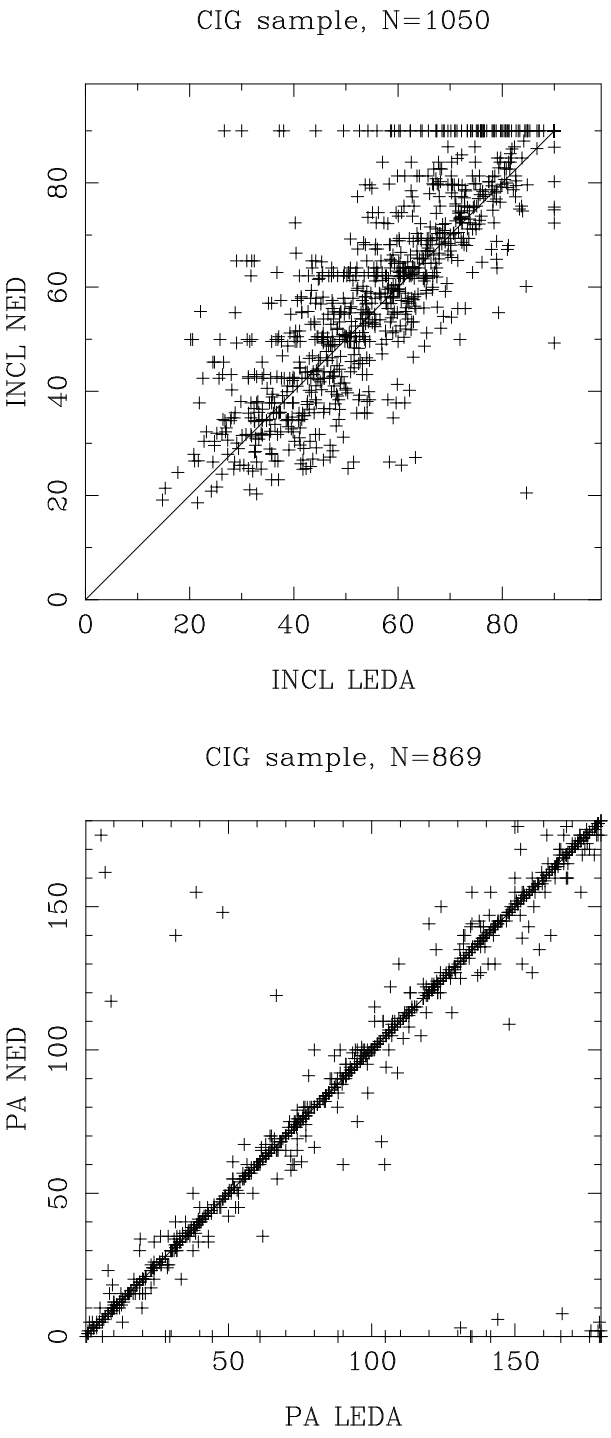


Figure 2.8: Comparison of inclinations (N = 1050) and position angles (N = 869) in LEDA versus NED for the CIG sample.

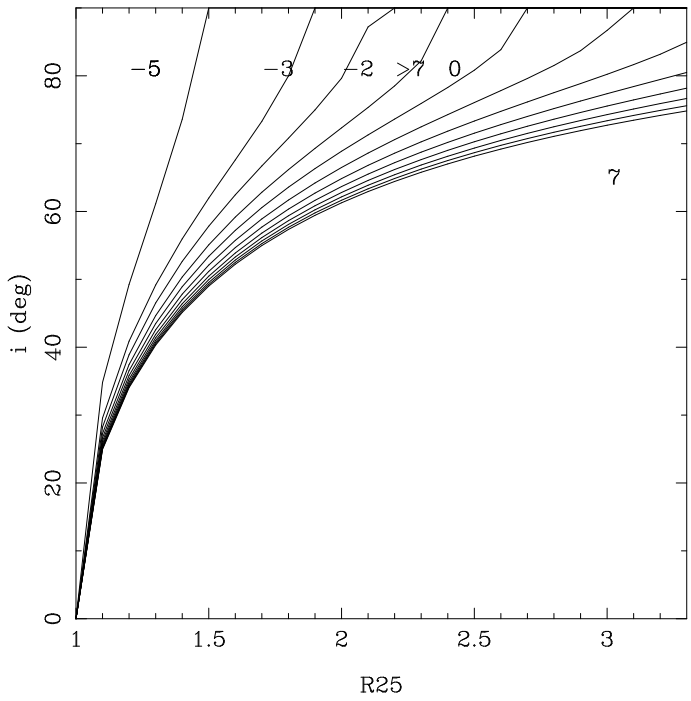


Figure 2.9: Inclination as a function of the axial ratio $R_{25}$ and morphological type (in the RC3 system).

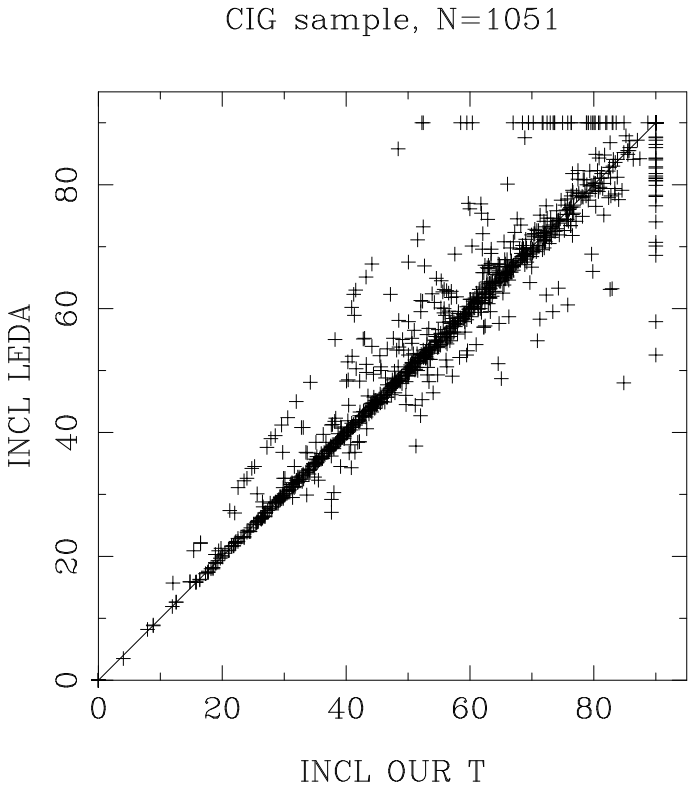


Figure 2.10: Comparison of inclinations in LEDA with respect to those calculated with the revised morphological types for the CIG sample. Note that outliers are due to a different estimation of the morphology: a reclassification of the morphological type from early (or irregular) to late type or vice versa can result in a change of inclination of even 30°.

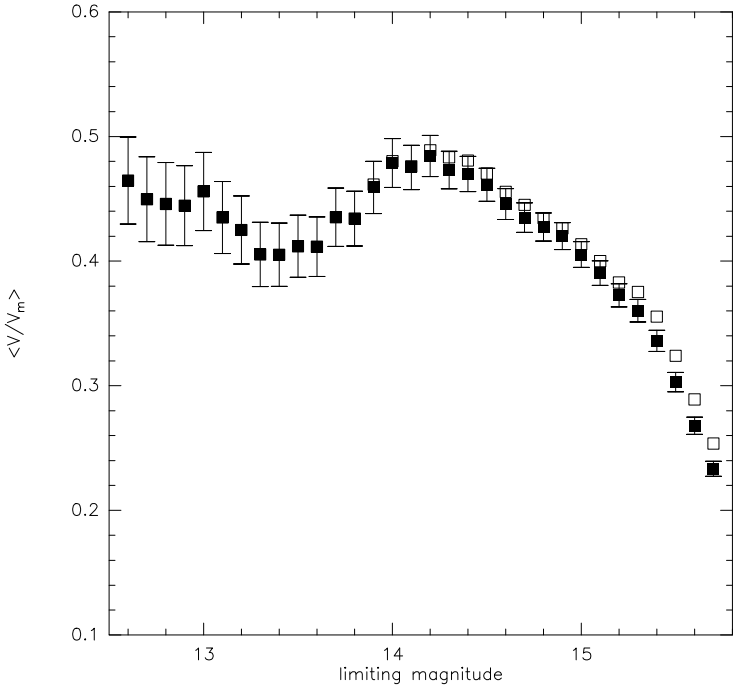


Figure 2.11: The $< V/V_m >$ test for the CIG sample excluding galaxies brighter than 11 mag (Verdes-Montenegro et al. 2005). The open squares indicate the whole sample ($N = 1031$), and the filled squares the subsample for which recession velocities are available ($N = 937$) and which will be used to construct the OLF. The error bars are the statistical errors in the mean $< V/V_m >$ and are given for the latter subsample.

Lisenfeld et al. (2006) have compiled and reprocessed 12, 25, 60 and 100 $\mu$m IRAS data (Sanders et al. 1989) for 1030 galaxies, using co-added ADDSCAN/SCANPI fluxes. It doubles the number of galaxies previously used in samples of isolated galaxies and with better detection rates and signal to noise ratios than former studies that used the IRAS Point Source Catalogue (PSC) and Faint Source Catalogue (FSC). Galaxies without FIR data (N = 20) are in the IRAS gap, region which was not covered by the satellite.

The FIR luminosity function (FIRLF) was calculated using the optical luminosity function described before and the fractional bivariate function between the FIR and optical luminosity. The complete CIG sample was used, N = 734, 509 of which are firm detections in the FIR. The resulting FIRLF is in agreement with previous studies. The M$^*$ and $\alpha$ are indicated in Tab. 2.6. An excess of luminous galaxies is found and the FIRLF is better described by a double power-law than by a Schechter function (see Fig. 2.12).

Furthermore, Lisenfeld et al. (2006) have studied in detail $L_{FIR}$ over $L_B$ and IRAS colors (e.g. $F_{60}/F_{100}$ as an indicator of dust temperature, $F_{25}/F_{60}$ as indicator of Seyfert activity). As expected, a good correlation is found between $L_{FIR}$ and $L_B$, but no relevant difference is found as a function of morphological type for late-type galaxies. For other samples of interacting galaxies the data are better fitted by linear regressions with steeper slopes. Early types have a lower $L_{FIR}/L_B$ and a higher $F_{60}/F_{100}$ than spirals, suggesting a hotter dust temperature possibly due to a larger concentration in their inner regions.

### 2.4.2 Radiocontinuum

Radiocontinuum emission is an useful tracer of current SFR and nuclear activity which is not affected by extinction. There exists a close correlation between radiocontinuum and FIR luminosities, although the nature of these two emissions are very different. Radiocontinuum emission is produced by thermal radiation (mainly due to supernovae) and synchrotron radiation (non-thermal, due to relativistic electrons accelerated by magnetic fields) whose contribution is important if the galaxies possess nuclear

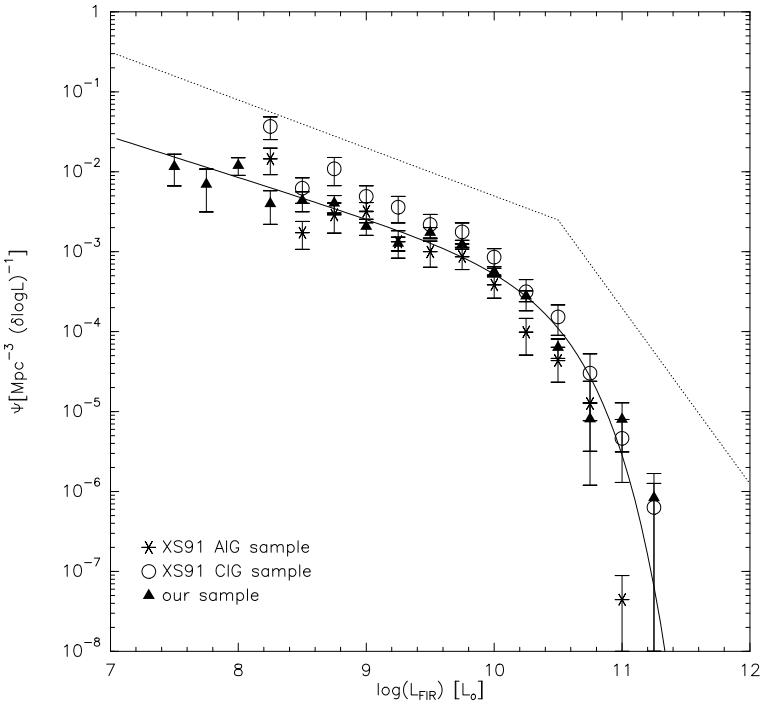


Figure 2.12: FIR luminosity function for the CIG sample (Lisenfeld et al. 2006), in comparison to that by Xu & Sulentic (1991, AIG and CIG)). The full line is a Schechter fit to our data.

Table 2.6: Parameters of the FIR luminosity function for the complete CIG sample that have $F_{60}$ and $F_{100}$ fluxes (N = 734).

| Sample | $\Phi$[Mpc$^{-3}$ mag$^{-1}$] | $\alpha$ | M* | log($L_{FIR}$[L$_\odot$]) Range of the fit |
|---|---|---|---|---|
| CIG (N = 734) | 6.1($\pm$ 1.7) $\times$ $10^{-3}$ | 2.1 $\pm$ 0.2 | 10 $\pm$ 0.17 | 7.4 to 11 |

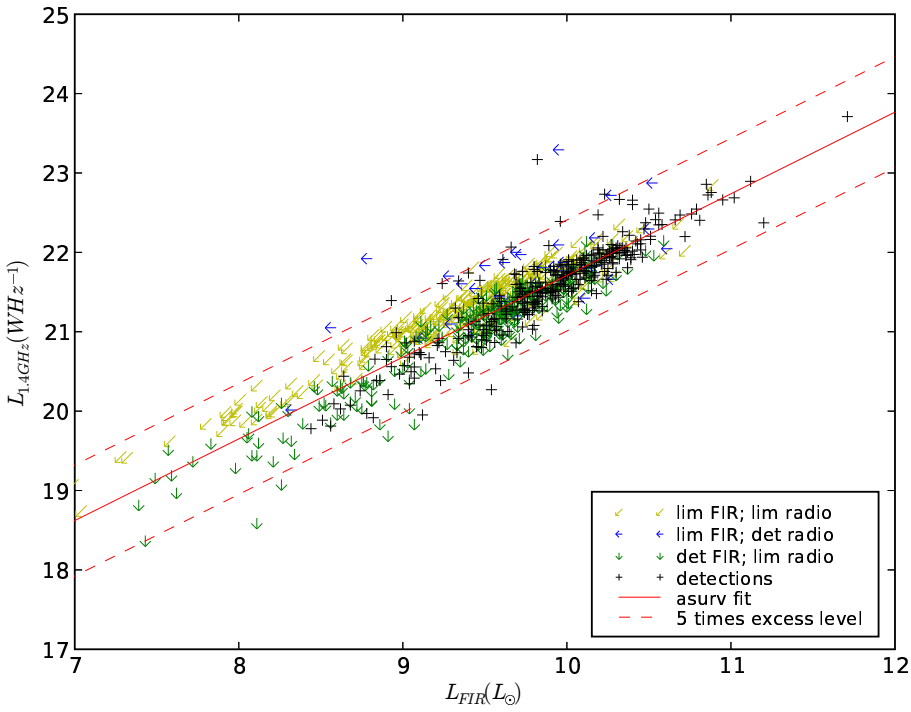


Figure 2.13: Radiocontinuum 1.4 GHz - FIR correlation for the CIG sample (Sabater et al. 2006).

activity. Candidates to host active galactic nuclei can then be identified by looking to the outliers of such correlation.

Leon et al. (2006) have compiled radiocontinuum information for the CIG sample from three different sources:

- WENSS: Westerbork Northern Sky Survey at 325 and 352 MHz ($\sim$ 90 cm),
- NVSS: NRAO VLA Sky Survey at 1.4 GHz (20cm), and
- GB6: Green Bank at 4.85 GHz (6cm).

The latter has not been used because of the low resolution and quality with respect to the others. These data have been reprocessed using SExtractor, obtaining in this way a higher detection rate. Leon et al. (2006) have also performed the radiocontinuum luminosity function analysis and the study of stellar formation.

Using several selection techniques (radiocontinuum-FIR correlation, q parameter, IRAS colors, etc.), Sabater et al. (2006) have identified CIG galaxies which are good candidates to host nuclear activity. In Fig. 2.13 we show the radiocontinuum-FIR luminosity correlation for the CIG sample. This correlation is surprisingly valid for a large range of galaxies (from spirals to dwarf ellipticals, from non active to starburst galaxies). The fact that these very different galaxies lie along the same correlation suggests that their radio continuum and FIR luminosities have a common origin, probably massive stars. UV photons from these stars are converted into IR radiation by dust grains, while the supernovae generate the cosmic rays responsible for the radio continuum radiation.

The obtained fit is the following:

$$\log L_{1.4GHz} = (1.03 \pm 0.03) \times \log L_{FIR} + (14.4 \pm 0.3) \tag{2.12}$$

From an additional search in the bibliography, 26 galaxies with confirmed nuclear activity are found. Only 1% of the CIG sample show a radiocontinuum excess, a very low rate when compared with galaxies in denser environments.

### 2.4.3 Atomic gas (HI)

The atomic gas is a fundamental ingredient of the ISM and is the most sensible tracer of interaction, due mainly to the fact that the extent of this component is usually much larger than any other component of a galaxy. HI spectra have been obtained for the CIG galaxies from a compilation in the bibliography and from our observations at four radio-telescopes: Arecibo, GBT, Effelsberg and Nançay. A total of 910 galaxies in the whole sample have HI data. The obtention, reduction and analysis of the HI data is explained in detail in Chapter 3 and in Chapter 4. In Chapter 5 we compare the lopsidedness properties obtained from the HI spectra in isolated galaxies with respect to the results found in the literature for galaxies in denser environments. A study of the origin of lopsidedness in isolated galaxies is presented in Chapter 6, where synthesis observations of some of the most asymmetric galaxies are summarised.

### 2.4.4 CO(1-0)

The J = 1-0 rotational transition of the CO molecule traces the molecular gas component, which is the raw material for SF. The search for CO data has been focused on a subsample containing the 204 CIG galaxies with velocities between 1500 and 5000 km $s^{-1}$ as we discuss in more detail in Chapter 9 Data have been obtained from a compilation in the bibliography and from our observations with two single-dish radio-telescopes: FCRAO 14m (N = 102 galaxies) and IRAM 30m (N = 103) and Nobeyama 45m (N = 9). The results of this study as well as a comparison of the properties of the molecular gas in galaxies located in high density regions are also discussed in Chapter **??**.

### 2.4.5 $H_\alpha$

$H_\alpha$ is a good tracer of recent SF in places where the extinction is not high. Verley (2006) has studied the properties of $H_\alpha$ for the CO subsample (containing 205 CIG spiral galaxies with velocities between 1500 and 5000 km $s^{-1}$). A total of 90% of the galaxies in the subsample have been observed at several 1-2 meter-class telescopes: OSN (Observatorio de Sierra Nevada - IAA), CAHA (Calar Alto Hispano Alemán - MPI,IAA) , EOCA (Estación de Observación de Calar Alto - OAN), JKT (Jakobus Kapteyn Telescope - ING) and SPM (San Pedro Mártir - UNAM). For a first study 45 of the largest and less inclined galaxies were selected to analyze their $H_\alpha$ morphology and to compare it with r-gunn filter images tracing the old stellar population. A numerical program developed by Dr. F. Combes was used to study the potential, density and torques. The main result is the inference of an evolutive sequence, from galaxies in the first stage of the bar (presenting $H_\alpha$ emission all over the bar) to galaxies where the star formation is gradually depopulated from the bar due to infall of material towards the centre (thus possessing a strong central peak in the $H_\alpha$ emission). The latter is the most frequent phase in this subsample (N = 45 galaxies). Numerical simulations trying to model the $H_\alpha$ distribution suggest that the SF law may differ from a simple Schmidt law. In a further work the $H_\alpha$ luminosity function will be derived using the data for the $\sim$ 200 galaxies.

# Part II

# Atomic gas

# Chapter 3

# HI data for the AMIGA sample

We present the atomic gas (HI) data for a large sample of isolated galaxies as part of the AMIGA project, which has been described in the previous chapter, and that includes HI data for 910 galaxies. The number of isolated galaxies in our HI study is much larger than any previous study of this kind, leading to substantial improvements in the statistics. Our database includes archival data as well as new observations from different single-dish radio-telescopes: Green Bank, Nancay, Arecibo and Effelsberg.

## 3.1 Introduction

As explained before, interactions play a key role in the formation and evolution of galaxies. HI is a fairly good probe to study this issue since: 1) it is one of the most sensible components of the ISM to interactions since it is usually more extended than any other component (typically twice the optical extent for spiral galaxies), and 2) it constitutes a significant component of the ISM, that will be the fuel for future star formation through the formation of molecular clouds. Therefore the study of the HI content of a given galaxy can give us clues about recent interactions with its environment (minor or major mergers, gas accretion, etc.). In order to perform statistical studies of irregularities in the HI content and possible asymmetries as a function of the environment, HI spectra obtained with single dish radio-telescopes is the best approach. From each HI profile the HI content can be accurately quantified without the bias that an interferometer could introduce due to its lack of sensitivity to extended structures. Additionally an asymmetry quantification can be calculated through several parameters, but the perturbations in the HI density distribution can not be distinguished from those in the velocity field. HI synthesis imaging is needed in order to have high spatial resolution of both the HI content distribution and velocity field.

In the early 1970s the first interferometers started to measure the 21-cm line with a considerable improvement in the resolution of the images. However, the integration time required by an aperture-synthesis telescope to reach the same S/N is usually longer than that for a "similar sized" single-dish antenna, and in addition the former has the inconvenient of flux losses due to insensitivity to large-scale smooth distribution of HI. The amount of available single-dish data is much larger than aperture-synthesis data: several thousands of galaxies have been observed in the 21-cm line with the help of single-dish telescopes. From a simple HI profile very accurate information can be obtained about both the HI content and the kinematics (systemic velocity and rotation velocity) of a given galaxy.

Interactions between galaxies can produce peculiar features such as tidal tails, or even the depletion of the HI in the galaxies. The HI deficiency is usually quantified by the difference between the observed HI mass and that expected for an isolated galaxy with the same morphological type and optical luminosity (or linear optical diameter) (see Haynes & Giovanelli 1984). Another key factor for the depletion of the neutral gas in cluster galaxies is ram pressure stripping due to the intracluster medium.

For example, due to this effect the optical and HI extent is seen to diminish in these high density regions, and the proportion of gas-poor spirals seems to increase continuously toward the cluster center (e.g. Solanes et al. 2001). HI deficiencies are also found in other high density environments, such as compact groups of galaxies (e.g. Verdes-Montenegro et al. 2001a).

Asymmetries in the HI distribution and/or in the velocity field are quite common. Previous works on small samples of isolated galaxies give a rate of asymmetric HI profiles of about 50% (Haynes et al. 1998; Matthews 1998, N = 104 and N = 30 respectively). Surprisingly, other samples of galaxies in denser environments show similar values of this rate (50 - 80%; Sulentic & Arp 1983; Richter & Sancisi 1994; Swaters et al. 2002a). More information about the quantification of the lopsidedness in HI profiles can be found in Chapter 5.

Although a large body of HI data for galaxies already exists, not many studies about the characterization of the HI in isolated galaxies have been performed so far. The main characterizations of strictly isolated galaxies were performed by Haynes & Giovanelli (1984) and Solanes et al. (1996) with the Arecibo telescope (AGC catalogue). In Haynes & Giovanelli (1984) a total of 324 of the galaxies in the CIG are considered (including galaxies with $v < 1500$ km s$^{-1}$) in the so-called "Arecibo isolated galaxy sample". In Solanes et al. (1996) the HIMF of field Sa to Sc spirals is determined (N = 532, lowest density environments of the Pisces-Perseus supercluster).

We have observed or compiled from the literature HI single-dish data for almost all the galaxies (N = 910) in the AMIGA sample (see Chapter 2 for details about the sample). These data are described in the present chapter, as well as the calculated parameters (HI content, systemic velocity, linewidth, asymmetry coefficients, etc). Our database contains around 3 times more galaxies than the sample in Haynes & Giovanelli (1984), allowing for a better quantification of the properties for individual subsamples (e.g. bins of morphological type). The outline of this Chapter is as follows. In § 3.2 we introduce the general properties of the HI emission in galaxies. In § 3.3 we show the characteristics of the considered HI sample (radial velocities, morphologies, optical luminosities and diameters). In § 3.4 we include a description of the observations that we performed and the search for HI data in the literature. The data reduction of the HI profiles is explained in § 3.5, as well as the derivation of useful parameters from the HI profiles (HI content and kinematics). In § 3.6 we present relevant notes to the individual profiles. In Chapter 4 we include correlations between HI content, morphology, blue luminosity and linear size, and we also study the HI content residuals for our sample. In Chapter 5 the asymmetry of the HI single-dish profiles is evaluated.

Finally, in Chapter 6 an especially interesting set of galaxies is studied: a subset of the most isolated galaxies showing significant asymmetries in their HI profiles. HI synthesis imaging of very isolated galaxies with a highly lopsided HI profile may clarify the origin of these asymmetries (companions, mergers, intrinsic- self-induced perturbation, HI cloud without optical counterpart, etc.).

## 3.2 Introduction to the HI properties

The HI can be detected by the hyperfine transition of hydrogen at $\lambda = 21$ cm. This transition was formally discovered by Van de Hulst (1945), and simultaneously detected by three groups in 1951: Harvard (Ewen & Purcell), Leiden (Müller & Oort) and Sydney (Christiansen & Hidman). The properties of HI regions are expressed in Tab. 3.1. The general properties of HI in galaxies are introduced in the following section.

### 3.2.1 General properties of HI in galaxies

HI typically accounts for one half of the cold phase of the interstellar gas in a galaxy and this fraction is seen to be type dependent (Combes et al. 1995). The HI extent is normally larger than any other component of the ISM, and therefore it is the best tracer to diagnose interactions in a recent past. The HI morphology and distribution of a given galaxy can change enourmously depeding on the event, from major mergers to the accretion of small HI clouds. Moreover, sometimes evidences that galaxies are interacting are only present in their HI distribution and kinematics (e.g. HI tidal tails).

Table 3.1: Properties of HI regions.

| | |
|---|---|
| Density | n $\simeq$ 50 - 150 (cm$^{-3}$) |
| Temperature | T $\simeq$ 80 (K) |
| Pressure | P $\simeq 3 \times 10^{-13}$ (dyn cm$^{-}$2) |

The HI extent and content of a galaxy depends on the environment (Haynes et al. 1984). Galaxies in high density environments are HI deficient and their disk extents are smaller. Since HI is the reservoir for the molecular gas (and therefore star formation), any perturbation or deployment in the HI can lead to a different evolution of the galaxy, producing changes in its morphology and decay/enhancement in its star formation, among other effects.

The HI tends to be located at large radii and late type spirals are on the average more gas rich than early type spirals (Roberts & Haynes 1994). As a consequence, a galaxy's Hubble type may be in part determined by its HI content and it may be also susceptible to environmental influences. This conjecture is supported by the morphology-density relation which states that late-type galaxies are rare in high density regions. Moreover, spirals in the Virgo cluster tend to be deficient in HI (Solanes et al. 2001), while Szomoru et al. (1996) find that galaxies in the Bootes void are unusually gas-rich.

### HI mass content ($M_{HI}$)

The total atomic hydrogen mass of a galaxy, $M_{HI}$, can be calculated from the integrated 21 cm line emission as:

$$M_{HI} = 2.36 \times 10^5 D^2 \int S_v dv \tag{3.1}$$

where D is the distance to the source and $\int S_v dv$ is the HI line flux in Jy km s$^{-1}$.

If the 21 cm line is not detected then an upper limit to $M_{HI}$ is usually calculated in the following way: we can assume that the emission is rectangular, with an amplitude three times the rms noise and a width equal to a constant value, typically taken to be 250 km s$^{-1}$.

The $M_{HI}$ is a parameter that is seen to vary at least 4 orders of magnitude. It is well known that early type galaxies - E and S0 - contain in proportion lower HI masses than spirals. While some E's and S0's have $M_{HI}$ similar to those of Sb - Sc spirals, other are several orders of magnitude poorer in HI. For this reason and because the HI within S0's is often located in an annulus exterior to the optical disk, van Driel and Woerden (1991) have suggested that the HI gas in this kind of galaxies has an external origin.

### Radial density profiles

From observations with the Westerbork Synthesis Radio Telescope of 50 spiral galaxies with no optical irregularities, Broeils & van Woerden (1994) find the following relation between the radius $R_{HI}$ (at which 1 M$_\odot$pc$^{-2}$ of HI is reached) and the optical $R_{25}$:

$$log\ R_{HI} = (0.9 \pm 0.1)\ log\ R_{25} + (0.26 \pm 0.07) \tag{3.2}$$

resulting in $R_{HI} \sim 2 \times R_{25}$, which is the value that we will consider in this study.

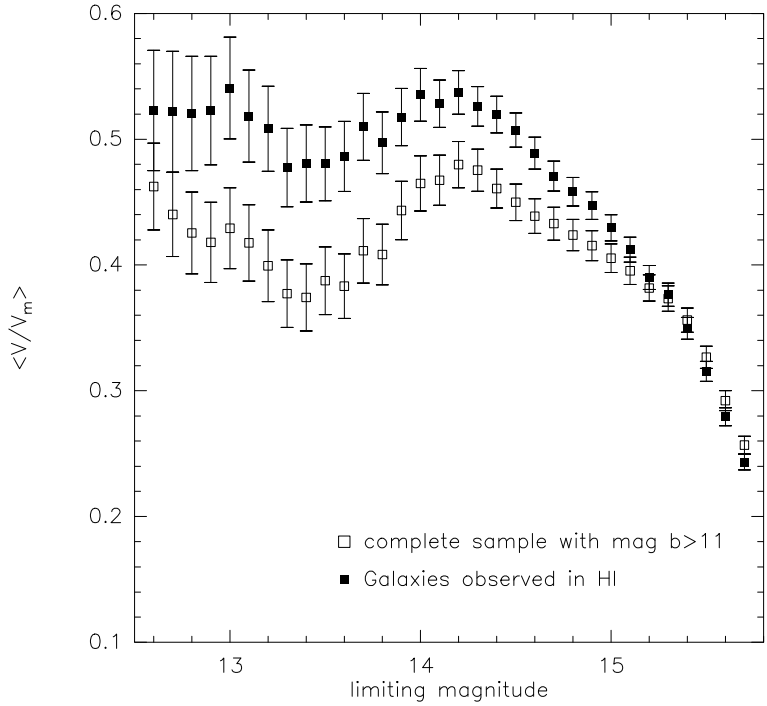


Figure 3.1: Comparison of the $< V/V_m >$ cumulative distribution for galaxies in the HI CIG sample (close square symbols), with respect to the whole CIG sample (open square symbols). The error bars are the statistical errors in the mean $< V/V_m >$ .

Table 3.2: Summary of considered samples.

| sample | N | N with known z |
|---|---|---|
| CIG sample | 1050 | 988 |
| Complete CIG sample | 736 | 736 |
| HI CIG sample | 910 | 837 |
| HI complete CIG sample | 662 | 662 |

## 3.3 The HI sample and the HI complete sample

In our HI study we consider all the CIG galaxies except those with v $<$ 1500 km s$^{-1}$. Galaxies without known redshift are included. A total of N = 910 galaxies have HI information in our database. We will refer to it as the "HI CIG sample". In Fig. 3.1 we show the $< V/V_m >$ test for the galaxies in the HI sample with known redshift and $m_{B\ corr} > 11$. We choose to neglect galaxies brighter than 11 mag because they are obviously incomplete due to their small number per magnitude bin. A total of N = 746 galaxies in the range 11 to 15 mag have known distances. We select this set of galaxies minus those galaxies with very high or low luminosity (absolute magnitude $M_B >$ -16 (8 galaxies) and $<$ -22.5 (2 galaxies), since they are scattered in bins containing a low number of galaxies. For comparison we have also plotted $< V/V_m >$ for the complete CIG sample. To avoid any possible bias coming from incompleteness of the sample, we can consider the galaxies in the HI sample between 11 and 15 mag (N = 662). We will refer to it as the "HI complete sample". The different samples considered in this work are summarized in Tab. 3.2.

### 3.3.1 Properties of the HI sample

We describe in this section the velocities, morphological types and optical luminosities of the HI sample.

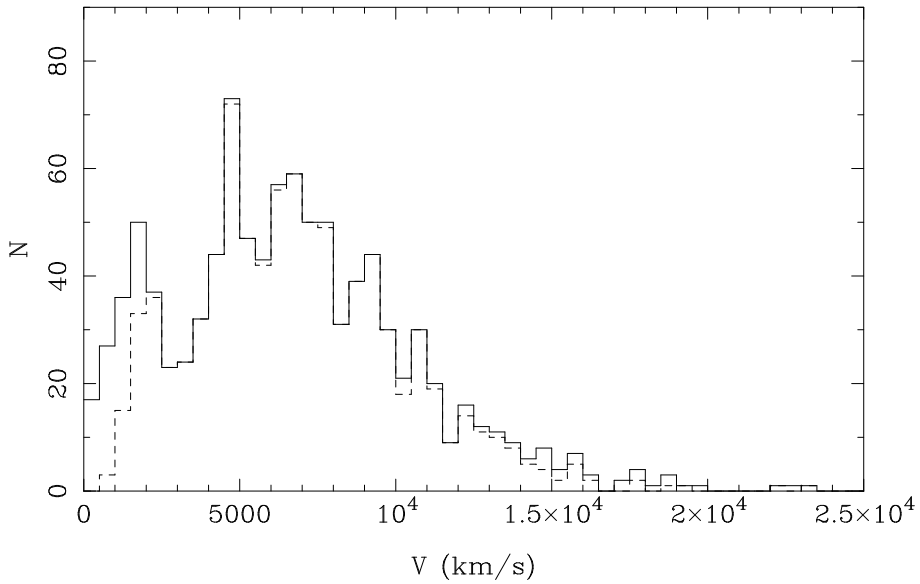


Figure 3.2: Histogram of the optical heliocentric velocities with HI data and redshift (dashed line) versus the N = 988 CIG galaxies with redshift data (solid line).

### Velocities

We have redshifts for 988 out of 1050 CIG galaxies. In Fig. 3.2 we compare the velocity distribution for all galaxies in the CIG sample with known redshift and those galaxies with HI data. The plotted curve is the expected velocity for a spatially homogeneous population of objects with the same apparent magnitude as those with HI data, as calculated by Verdes-Montenegro et al. (2005). Note that we have not observed in HI galaxies with v $<$ 1500 km s$^{-1}$, but we have compiled data for some galaxies with HI data in the literature below this limit.

### Morphologies

The CIG sample is large enough to permit discrimination on the basis of galaxy type. See Tab. 3.3 to note the improvement in number of our sample over Haynes & Giovanelli (1984, N = 324 CIG galaxies, HG84) sorted by morphological type. This is especially relevant for early type galaxies.

The accuracy in the morphological classification is extremely important for statistical studies as a function of the morphological type. A revision of the morphologies for the whole sample has been performed by Sulentic et al. (2006), as explained in Chapter 2. We can compare our new classification with respect to the morphologies used by HG84. The morphologies therein are based on a visual examination of the Palomar Sky Survey plates or, when available, on the classifications by Sandage and Tammann. It is stated that types are accurate, at least for statistical purposes by $\Delta$T = $\pm$ 1, and usually in agreement with respect to the UGC morphological classification.

In Fig. 3.3 we show the comparison between their values and ours. The classification for almost one third of the galaxies in HG84 coincide with our types ($\Delta$T = 0), but there is a large scatter between their values and ours of about $\Delta$T = $\pm$ 2. A systematic trend in the classification by HG84 with respect to our classification is seen, in the sense that HG84 types are larger (i.e. later). This is probably due to the fact that we are using POSSII, which have better resolution than POSSI, and this allowed us to better resolve the bulge component of the galaxies.

The morphological distribution for the whole sample observed in HI is presented in Fig.3.4.

### Optical properties

$L_B$ has been calculated from our revised distances and the corrected Zwicky magnitudes ($m_{B\ corr}$) (see § 2.3.5). The distribution of $L_B$ for the HI sample is presented in Fig. 3.5. See § 2.3.5 to have further

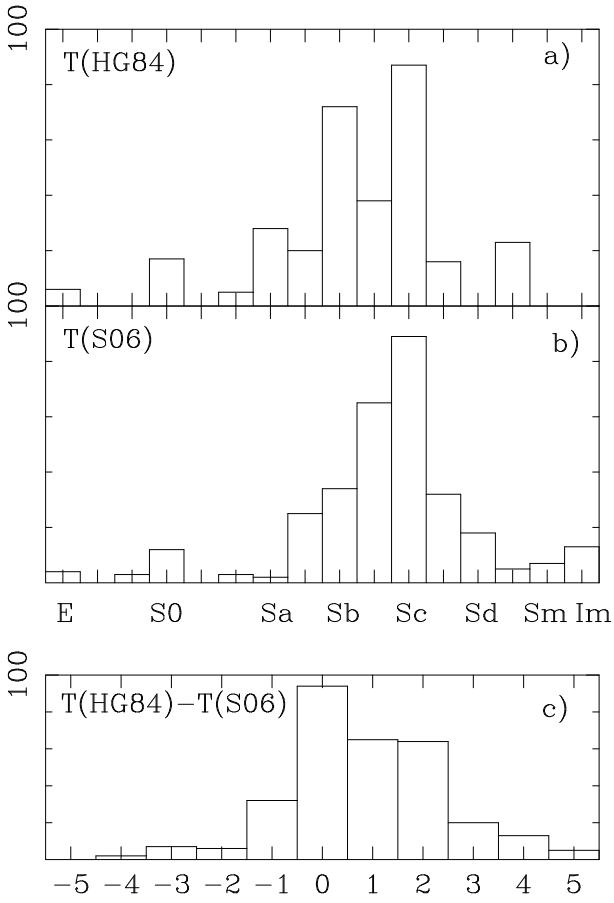


Figure 3.3: Morphological types for Haynes & Giovanelli (1984, called HG84 in the plot, N = 324) and Sulentic et al. (2006, S06) samples: a) Types in HG84 using POSSI converted to the RC3 morphological system, b) revised types using POSSII as in S06 and c) comparison of both classifications, HG84 minus S06.

Table 3.3: Comparison of AMIGA vs HG84 in terms of the morphological binning.

| Type | T | $N_{AMIGA}$ | $N_{HG84}$ |
|---|---|---|---|
| E, E/S0, S0, S0/a | -5, -3, -2, 0 | 140 | 14 |
| Sa, Sab | 1,2 | 59 | 37 |
| Sb | 3 | 149 | 71 |
| Sbc | 4 | 192 | 38 |
| Sc | 5 | 250 | 80 |
| Scd, Sd | 6,7 | 80 | 38 |
| Sdm,Sm ,Im,Pec | 8, 9, 10, 998 | 40 | 9 |
| All | | 910 | 287 |

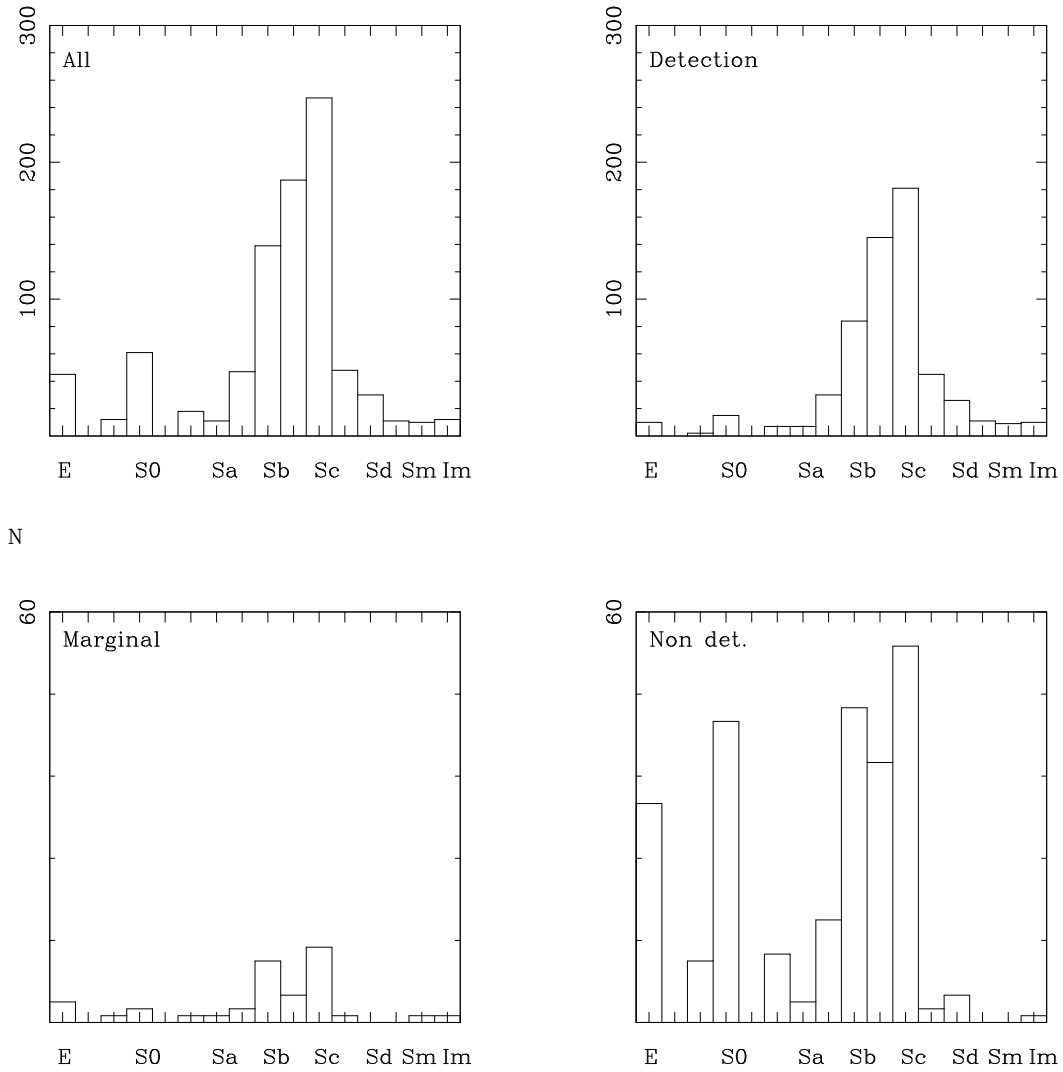


Figure 3.4: Morphological distribution following the RC3 codes for galaxies with HI data in the AMIGA sample (N = 910).

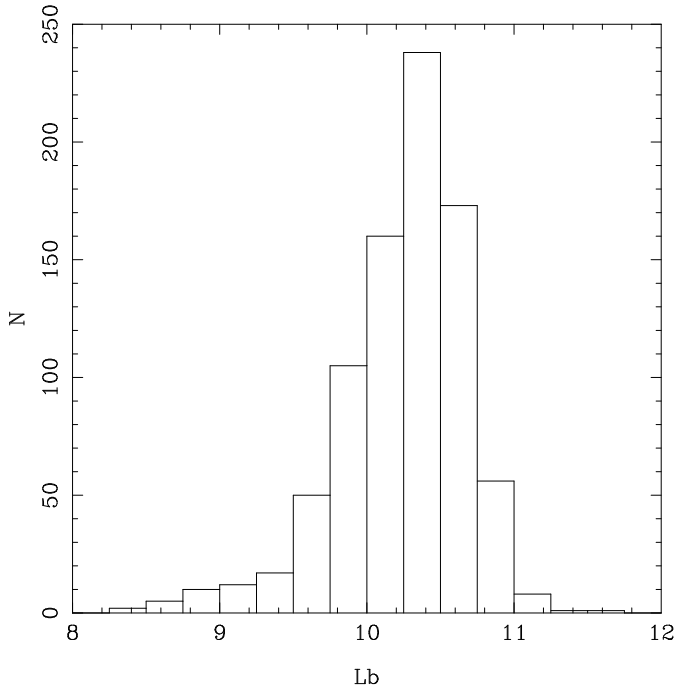


Figure 3.5: $L_B$ distribution for the CIG galaxies for which we have HI data (N = 910).

information about the optical diameter and axis ratio ($D_{25}$ and $R_{25}$), linear diameter, inclination and position angle.

## 3.4 HI data

We have gathered HI data for N = 910 galaxies, either compiled from the bibliography (N = 422) or from own observations at several radio-telescopes (N = 488, Effelsberg, Nançay, Arecibo and GBT).

### 3.4.1 Data from the bibliography

The information on the HI profiles is usually summarized in the literature as a set of characteristic quantities, like the integrated density flux, mean velocity, widths and asymmetry coefficients, but the HI profiles are not always included. We have compiled HI parameters directly from the bibliography, and digitized the HI profiles when available in order to be able to calculate all parameters in an homogeneus way for these data and ours. We find a number of drawbacks resulting from a direct compilation of HI parameters:

a) There are no standards in the presentation of HI data. All the characteristic parameters are not always presented, and if errors are included, they are not usually calculated in the same way. For example: a) widths are calculated at different levels (20%, 30% or 50 %) with respect to the maximum or the mean of the profile (if double peaked, some authors use the mean of both horns); b) Systemic velocities can be calculated as the first moment of the spectra, or as the mean point of these widths; c) the signal to noise ratio, S/N, varies if the mean or the maximum of the profile is chosen; d) quantities measuring the shape of the profile are expressed in many different ways: flux ratios of the two halves with respect to the mean (with different equations), differences between the characteristic velocitities (mean and median, for example) or even classifying qualitatively the spectra by visual inspection.

b) The same situation is found in the application of corrections to these quantities (e.g. HG84 or Theureau et al. 1998). This requires to combine measurements with a very different nature: resolution (from the spectrometers), smoothing (from the processing software), noise (from the

receivers), S/N and broadening (in the case of the width). There is no standard procedure to calculate the corrections of the different HI parameters using these corrections. In addition, as we explain below, the integrated fluxes are usually corrected by beam attenuation, pointing offsets and HI self-absorption. See for example Tab. 3.4 and 3.5 to check the differences in the application of corrections to the integrated density fluxes in several sources in literature. Widths need to be corrected by inclination of the galaxy and by a factor 1/(1+z) (although this is not relevant for galaxies in the nearby universe).

c) Different data reduction algorithms are used by different authors, resulting in a lack of homogeneization. For example, to calculate the HI profile width some authors make a fit to the wings of the HI profile to eliminate the trend of the noise while others measure directly on the profile. Another example is the correction for beam attenuation, which is dependent on the model considered for the HI surface brightness distribution.

Published HI profiles can be digitized, recovering in this way much of the information, although these digitized profiles can not substitute the original profiles since the process always implies some errors. At any rate, this is useful not only because we can have an estimation of those properties in a homogeneous way but also because we will have information about HI parameters that have not been calculated in some of the papers (e.g. the shape of the profile, that will allow us to detect the presence of an asymmetry that could trace any kind of interaction).

We have compiled HI data for 431 CIG galaxies from 50 articles which are listed in Tab. 3.4. These HI global profiles come from the following radio-telescopes: 305-m Arecibo (National Astronomy and Ionosphere Center, Puerto Rico), Nançay 200 × 30-m (Observatoire de Paris, France), Effelsberg 100-m (Max Planck Institut für Radioastronomie, Germany), 91-m and 42-m Green Bank (National Radio Astronomy Observatory, USA), 76-m Jodrell Bank (University of Manchester, United Kingdom) and 64-m Parkes (Australia Telescope National Facility). Information about these telescopes is summarized in Tab. 3.6. The antenna size as well as the half power beam width (HPBW) and gain (at zenith) are indicated in the table. As can be seen in this table, the Arecibo and Nançay radio-telescopes have two and three references respectively, since these instruments have been upgraded (Arecibo Gregorian in 1998 and Nançay-FORT in 2001). Information about the old receivers ("dual circular" and "flat") of the Arecibo telescope can be found in HG84. The current Gregorian optical system began its operation in 1997. As for the Nançay radio-telescope, the old hoghorn receiver was changed by a new receiver and focal system (Nançay-FORT). It permits to observe the four stokes parameters with a 8192 chanels autocorrelator that can be splitted into four different banks, with a considerable improvement in the gain.

In the compilation of the HI data we have used:

1) HI catalogues such as RC3 (de Vaucouleurs et al. 1991), Hyperleda (Paturel et al. 2003b) and Huchtmeier & Richter (Huchtmeier & Richter 1989), and

2) ongoing surveys such as AGC (Arecibo General Catalogue, compilation of several radio-telescopes, but especially Arecibo; Springob et al. 2005) or KLUN/KLUN+ (Nançay radio-telescope; Theureau et al. 1998, 2005), as well as HI blind surveys such as HIPASS (HI Parkes All Sky Survey, Parkes radio-telescope; Barnes et al. 2001).

We describe next in detail the data from each of these sources.

### 3.4.2 HI data from RC3, Hyperleda and Huchtmeier & Richter HI catalogues

HI data (N = 431) for 352 galaxies were obtained from a search in the literature, looking for the individual papers cited in the RC3, the Hyperleda catalogue and the HI Huchtmeier & Richter catalogue. A total of 50 articles have been used in the compilation, extracting all available HI parameters. We show in Tab. 3.4 the list of papers where most of the HI data have been found.

Table 3.4: List of papers from which we have compiled most of the HI data[1].

| Bibl. code (1) | (2) | Article (3) | Corr. code (4) | Tel. code (5) | N total (Sel.) (6) |
|---|---|---|---|---|---|
| 127 | Bi86 | Bicay & Giovanelli (1986) | 1,2,3 | 5 | 7 (4) |
| 123 | DS83 | Davis & Seaquist (1983) | 2 | 10 | 5 (0) |
| 147 | FT81 | Fisher & Tully (1981) | 2 | 8 | 4 (0) |
| 106 | GH93 | Giovanelli & Haynes (1993) | 1,2,3 | 8, 5 | 16 (0) |
| 140 | GH85 | Giovanelli & Haynes (1985) | 1,2,3 | 5 | 6 (0) |
| 141 | GH97 | Giovanelli et al. (1997) | 1,2 | 8, 5 | 6 (0) |
| 120 | He83 | Hewitt et al. (1983) | 2,4 | 9, 5 | 17 (6) |
| 150 | HG80 | Haynes & Giovanelli (1980) | - | 8 | 10 (2) |
| 110 | HG84 | Haynes & Giovanelli (1984) | 1,2,3,4 | 8, 5, 6 | 178 (65) |
| 111 | HG88 | Haynes et al. (1988) | 1,2,3 | 8 | 17 (2) |
| 103 | HG91 | Haynes & Giovanelli (1991) | 1,2,3 | 8 | 17 (1) |
| 137 | HG99 | Haynes et al. (1999) | 1,2 | 10,8 | 27 (0) |
| 136 | HH98 | Haynes et al. (1998) | 2 | 10 | 2 (0) |
| 143 | Le85 | Lewis et al. (1985) | 2 | 5 | 2 (1) |
| 138 | Le87 | Lewis (1987) | 2 | 5 | 9 (5) |
| 126 | Ma94 | Magri (1994) | 2,3 | 5 | 4 (2) |
| 130 | RH87 | Richter & Huchtmeier (1987) | - | 2,8 | 3 (2) |
| 115 | Sc92 | Schneider et al. (1992) | 1 | 8 | 7 (1) |
| 121 | Sm00 | Smoker et al. (2000) | 1 | 11 | 1 (0) |
| 122 | St88 | Staveley-Smith & Davies (1988) | 2 | 8 | 2 (1) |
| 123 | St87 | Staveley-Smith & Davies (1987) | 2 | 8 | - (2) |
| 108 | Th98 | Theureau et al. (1998) | 2 | 4 | 17 (6) |
| 142 | TC88 | Tifft & Cocke (1988) | 2 | 8 | 16 (8) |
| 124 | VD95 | van Driel et al. (1995) | - | 5 | 11 (4) |
| ... | ... | ... | ... | ... | ... |
| Total | | | | | 431 (115) |

(1) and (2) Bibl. code: bibliographic code number in the AMIGA database and abbreviation name code

(3) Article: full name reference

(4) Corr. code: correction code according to Tab. 3.5

(5) Tel. code: radio-telescope code according to Tab. 3.6

(6) N. compiled (Sel.): number of compiled HI data and in parenthesis the total number finally selected after comparison with our own observations and/or HI data from other catalogues.

Due to the dependence of the integrated HI integrated density flux (S) on the ratio of the HI extent to the beam size of the radio-telescope, published uncorrected fluxes have been also compiled. This effect can be easily seen in galaxies with a large HI extent observed at different radio-telescopes. For these galaxies, in most cases the larger the radio-telescope beam size is, the larger the S found. Since this may be due in part to the inclusion in the beam of a close HI rich source, we searched for companions in the neighbourhood of the galaxies using the revision made by Verley (2006).

In addition to this we have compiled other related informations about the HI profiles, such as comments given by the authors, visual inspection of the HI profile lopsidedness, baseline problems or possible interferences. All this information allowed us to better understand any disagreement among the different observations.

Once all this information was gathered, we selected for each galaxy the best HI data and available profile. The final compilation from the literature is presented in Tab. 3.10.

### Presentation of HI data compiled from the literature

The compilation of the HI data is presented in Tab. 3.10 using the following notation:

1) CIG: Entry number in the Catalogue of Isolated Galaxies.

2) S/N: signal (maximum of the profile) to noise ($\sigma$) ratio.

3) $\sigma$: rms noise per channel in mJy.

4) $S$: flux density integrated over the observed signal in Jy km s$^{-1}$.

5) $S_c$: corrected S in Jy km s$^{-1}$. Tab. 3.4 shows the corrections that have been employed in the papers used for the HI data compilation, as well as the radio-telescopes used and the corrections to S.

6) $V$: heliocentric radial velocity at a given level with respect to the maximum of the HI profile.

7) $\sigma_V$: error of the mean velocity in km s$^{-1}$.

8)-10) $W_i$: width at a level of i = 20%, 30% and 50% in km s$^{-1}$ of the maximum of the peak. In most cases we find them corrected for redshift broadening in their respective references.

11) $\sigma_W$: error of the widths in km s$^{-1}$.

12) $W_c$: correction to the line width at a given level with respect to the maximum of the peak.

13) $Tel$: code of the radio-telescope used for the observation, as in Tab. 3.6.

14) $Art$: code of the article from where the selected data have been retrieved, following Tab. 3.4.

15) $S_p$: S calculated for the observation of the profile in $Art_p$ (see column 17).

16) $Tel_p$: radio-telescope used for the observation in $Art_p$ (see column 17).

17) $Art_p$: code of the article from where the selected profile has been retrieved. In most cases Art and $Art_p$ coincide. Sometimes no spectrum was shown in the selected paper and hence the profile was selected from another available one.

Table 3.5: Main corrections to the integrated flux ($S$) used in the bibliography.

| Correction code | Type of correction |
|---|---|
| 1 | Pointing offsets |
| 2 | Beam attenuation, source extent/beam |
| 3 | Internal HI self-absorption |
| 4 | Mapping (different pointings) |

Table 3.6: Radio-telescopes used in our observations (Arecibo, Nançay, Effelsberg and GBT) and in the HI data compiled from the archives.

| Tel. code | Radio-telescope | Diameter (m) | $\theta_{HPBW}$ 21cm ($'$) | Gain (K Jy$^{-1}$) |
|---|---|---|---|---|
| 1 | Arecibo "Gregorian" | 305 | 3.5 | 11.0 |
| 2 | Effelsberg | 100 | 9.3 | 1.5 |
| 3 | GBT | 100 × 110 | 9 | 2 |
| 4 | Nançay "optimized focal" | 200 × 35 | 4 × 22 | 1.6 |
| 5 | Arecibo "dual circular" | 305 | 3.3 | 8.0 |
| 6 | Arecibo "flat" | 305 | 3.9 | 6.0 |
| 7 | Nançay "hoghorn" | 200 × 35 | 4 × 22 | 1.1 |
| 8 | Green Bank 91m | 91 | 11 | 1.1 |
| 9 | Jodrell Bank 76m | 76 | 12 | 0.8 |
| 10 | Green Bank 43m | 43 | 22 | 0.3 |
| 11 | Parkes HIPASS | 64 | 14 | 0.6 |

Table 3.7: Archival HI data[1].

| CIG (1) | S/N (2) | $\sigma$ (3) | $S$ (4) | $S_c$ (5) | V (6) | $\sigma_V$ (7) | $W_{20}$ (8) | $W_{30}$ (9) | $W_{50}$ (10) | $\sigma_W$ (11) | $W_c$ (12) | Tel (13) | Art (14) | $S_p$ (15) | $Tel_p$ (16) | $Art_p$ (17) |
|---|---|---|---|---|---|---|---|---|---|---|---|---|---|---|---|---|
| 2 | 2.2 | - | 2.84 | 3.30 | 6984 | - | 249 | - | - | - | 429 | 4 | HG84 | - | - | HG84 |
| 4 | 0.6 | 5.4 | 13.2 | 14.3 | 2301 | - | 444 | - | - | - | - | 9 | TC88 | - | - | TC88 |
| 11 | 4.0 | 15.9 | 11.32 | 15.23 | 3956 | - | - | - | 291 | 4.6 | 279 | 4 | HG99 | - | - | - |
| 18 | 1.2 | - | 2.94 | 3.60 | 7208 | - | 274 | - | - | - | 315 | 4 | HG84 | - | - | HG84 |
| 29 | - | - | 4.71 | - | 4148 | - | - | - | - | - | 200 | 4 | Ca99 | - | - | Ca99 |
| 30 | 2.5 | 11.8 | 4.15 | 4.33 | 4586 | - | 228 | 218 | 208 | - | - | 4 | Le87 | - | - | Le87 |
| 31 | 5.3 | 6.3 | 5.26 | 5.38 | 5610 | - | 277 | - | 255 | - | 286 | 9 | HG88 | - | - | HG88 |
| 33 | 3.0 | - | 9.16 | 12.43 | 4174 | - | 300 | - | - | - | 379 | 4 | HG84 | - | - | HG84 |
| 34 | 1.2 | - | 2.68 | 3.20 | 4956 | - | 250 | - | - | - | 272 | 4 | HG84 | - | - | HG84 |
| 37 | 1.1 | 6.0 | 1.25 | 1.57 | 6765 | - | 335 | 287 | - | - | 352 | 4 | GH85 | - | - | GH85 |
| | ... | ... | ... | ... | ... | ... | ... | ... | ... | ... | ... | ... | ... | ... | ... | ... |

[1] The symbol $''-''$ indicates that no data were available. The radio-telescopes codes can be found in Tab. 3.6 and the bibliographic codes in Tab. 3.4. The whole list can be downloaded from http://www.iaa.es/AMIGA.html.

Table 3.8: Used surveys and number of selected galaxies[1].

| Bibliography code | Reference | N total (Selected) |
|---|---|---|
| HG | Haynes (private comm.) | 273 (269) |
| KLUN | Theareau et al., KLUN/KLUN+ project | 42 (14) |
| HIP | HI Parkes All-Sky Survey | 120 (24) |
| Total | | 435 (307) |

[1]HI profile files were gathered from these surveys. Selection was performed from the criteria given in § 3.5.4.

### 3.4.3 Compilation from ongoing HI surveys

In this section the surveys from which we have obtained HI profile files are explained in more detail. The number of spectra gathered and those finally selected are shown in Tab. 3.8.

#### Arecibo General Catalogue

The Arecibo General Catalogue (AGC) is a database maintained by R. Giovanelli and M. P. Haynes. It contains a compilation of HI data (and also optical data), mainly from Arecibo. Most of the data come from the works by: Haynes & Giovanelli (1980, 1984); Haynes et al. (1988); Haynes & Giovanelli (1991); Haynes et al. (1999) and Giovanelli & Haynes (1993, 1985); Giovanelli et al. (1997); Hewitt et al. (1983). A revision of this archive is presented in Springob et al. (2005)[2]. In particular the work by HG84 includes 324 members of the CIG (120 of them were previously selected in the archival compilation of HI data).

However, only N = 257 CIG galaxies with HI data in Springob et al. (2005) are detected, 3 are marginal detections and 13 non-detected. M. Haynes kindly provided us the HI profile files for these detected and marginally-detected galaxies. The rest of HI spectra for the CIG galaxies previously observed by R. Giovanelli and M. P. Haynes have been lost.

#### KLUN/KLUN+

Another important source of data has been the Kinematics of the Local Universe catalogue (KLUN/KLUN+, Theureau et al.). The data were mainly taken at the Nançay radio-telescope, and include profiles and HI parameters of four main publications, two before the 2000 refurbishment of the radio-telescope (Theureau et al. 1998; Paturel et al. 2003b) and one using the new FORT receiver or the Arecibo telescope (Theureau et al. 2005), accounting in total to 4000 observed galaxies in the nearby universe. In January 2001, they obtained the status of key-project for the general Tully-Fisher survey (KLUN+) and since then they have used an average of about 20% of the total telescope time to observe around 8000 galaxies. The first set of HI measurements has been published in Theureau et al. (2005).

A total of 42 CIG galaxies have been found in this survey. HI digitized profiles for these galaxies were kindly provided by G. Theureau.

#### HIPASS

HIPASS is a 21-cm HI survey of the southern sky undertaken with a multibeam receiver in the Parkes telescope (Staveley-Smith et al. 1996; Barnes et al. 2001). The HI profiles were downloaded from its webpage[3]. The overlapping of HIPASS data release with our HI subsample amounts in total to N = 120 galaxies, although most of the profiles were not satisfactory due to bad signal to noise ratio or instabilities in the baselines.

[2]We have made use of the tables available in http://egg.astro.cornell.edu/hiarchive/hiarchive.html
[3]http://www.atnf.csiro.au/research/multibeam/release/

### 3.4.4 Observations

#### Description of the observations

We have splitted the CIG galaxies for which no data were found in the bibliography to be observed at several radio-telescopes (Effelsberg, Nançay, Arecibo and GBT), based on the sensitivity of the telescopes and the distance, declination, size and morphology of the galaxies. A general summary of all the runs at each telescope is shown in Tab. 3.9, as well as the technical details. The radio-telescope, dates of observation and some technical information (velocity resolution, bandwitdh, configuration of the banks, system noise and sensitivity achieved after 30 min considering the radiometer equation) are indicated in this table.

HI observations were performed in total power mode, substracting an empty field from the target field (ON-OFF observations). The two channels in all considered HEMT-receivers were used to observe both polarizations. At the Nançay radio-telescope up to two linear plus two circular polarizations could be recorded simultaneously. The two/four channels were added after baseline substraction, doubling the integration time, under the assumption that the HI emission line is randomly polarized.

A total of 488 galaxies have been observed, and 154 of them were not detected. Tab. 3.10 shows the number of observed galaxies and the detection rate achieved in each antenna. A more detailed description of the observations is presented in the following subsections.

#### Effelsberg

Observations for 186 galaxies have been performed at the Effelsberg radio-telescope, from July 2002 to March 2004. Most of the observed galaxies have redshifts lower than 10000 km s$^{-1}$ in the declination range below 1 or above 37 degrees (i.e. outside the range accesible to the Arecibo telescope). We have performed 10 min ON-OFF observations, with a typical total observing time of 1 hour per galaxy. Because of baseline problems and radio frequency interferences we splitted the 1024 channel autocorrelator into 4 bands operated at the same frequency (bandwidth 6.25 MHz) with 256 channels each band, covering a radial velocity interval of about 1200 km s$^{-1}$. Using this bandwidth the baselines were flat even during daytime. We had typically 10 km s$^{-1}$ (48 kHz) channel spacing and a velocity resolution of 20 km s$^{-1}$ after Hanning smoothing. With less than one hour per source we were able to detect a few times $10^9$ M$_\odot$ of HI at a distance of 30 Mpc with a line width of 250 km s$^{-1}$ at a $3\sigma$ level. A more recent autocorrelator has been also used, the AK90 in a 4 banks with 2048 channels configuration, but we achieved more stability in the baselines with the AK1024 autocorrelator so we use this preferentially when available. The system noise was around 30 K.

#### Arecibo

A total of 34 galaxies have been observed at this radio-telescope with its new Gregorian optics. We have selected the more distant of the CIGs to take advantage of the high sensitivity of the Arecibo telescope. We used the L-wide receiver combined with the autocorrelator, obtaining a bandwidth of 1400 or 5550 km s$^{-1}$ (high or low resolution). We had total integration times of about 30 min for each galaxy. With this procedure we had upper limits for the HI content ranging between $1.5 \times 10^9$ and $7.5 \times 10^9 M_\odot$ assuming a width of 200 km s$^{-1}$ and a v $>$ 9000 km s$^{-1}$, considering a noise contribution of the noise of about 30 K at the 21-cm line.

#### Nançay

Up to now we have obtained data for 277 galaxies with the recently refurbished Nançay Radiotelescope, during a total of 600 hours. Sixty of them had severe problems (bad baseline or very strong interferences in the spectra) and we have not consider them. A total of 72 galaxies were detected and 28 are marginal detections. The observations were performed with the new 21-cm receiver in the total power mode, comparing ON-source and OFF-source observations every 4 minutes. This new receiver, whose new focal system gain is more than twice the previous one, permits to perform observations

Table 3.9: Summary of our HI observations[1].

| Tel. | Observation date | Resolution (km s$^{-1}$) | Bandwidth (km s$^{-1}$) | Banks × channels | Sens./30 min (Jy) |
|---|---|---|---|---|---|
| Arecibo | Oct 2002 | 0.67/2.66 | 1400/5550 | 2x2048 | 0.0012/0.0006 |
| Nançay | Jan 2002-June 2005 | 2.57 | 10550/2600 | 2x4096/4x2048 | 0.012 |
| Effelsberg | Jul 2002-March 2004 | 5.24 | 1200 | 4x256 | 0.005 |
| GBT | 2002-2003 | 1.20/2.5 | 1200/ 2500 | 2x1024 | 0.003 |

[1] Note that since T and Gain vary with zenith angle, the sensitivity in 30 min can vary as well.

Table 3.10: Number of galaxies observed and the detection rate at each radio-telescope.

| Source | Number of galaxies | detection rate |
|---|---|---|
| 100m Effelsberg | 186 | 67% |
| 305m Arecibo | 34 | 70% |
| 200mx35m Nançay | 217 | 30% |
| 100m GBT | 51 | 94% |
| Total | 488 | |

with up to four stokes parameters. The 8192 chanels autocorrelator can be splitted into two or four different banks. The procedure employed for the observations is the following: the autocorrelator was splitted into 1) four different banks of about 2500 km s$^{-1}$ (12.5 MHz) bandwidth and each centered at the systemic velocity for galaxies with known redshift, and 2) two banks (two polarizations) operated at the same frequency (using a bandwidth of 50 MHz) covering a radial velocity interval of about 10500 km s$^{-1}$ for galaxies with unknown redshift. In the latter mode the bandwidth was centered at 7000 km s$^{-1}$ in order to maximize the probability of detecting the galaxies, since we would expect that galaxies with v $<$ 2000 km s$^{-1}$ would have been already detected. This way we had a channel spacing of 2.6 km s$^{-1}$ (12.2 kHz) which was smoothed to a velocity resolution of 10 and 20 km s$^{-1}$ using Hanning smoothing or averaging several individual channels. A total of 10 galaxies with no previously reported velocity have been detected by means of the latter autocorrrelator mode. The minimal system temperature at 21-cm (at $\delta = 15^{o}$) is about 35 K in all polarisations.

We usually had minor baseline problems while using both bandwidths (12.5 and 50 MHz), but interferences at 8000 (only in a few cycles if seen at all), 9400, 11500, 12600 and 14600 km s$^{-1}$ were almost always present. In the last run (April to June 2005, 200 hours) we had high order baseline features, both at 12.5 and 50 MHz. The origin of this effect is still unknown. A new blanker is currently being tested which will allow us to observe in the range where these interferences take place and where probably many of the recession velocities of our galaxies are.

**Green Bank Telescope**

During the commissioning phase of the Green Bank Telescope (GBT) in the fall and winter of 2001 and 2002, 51 CIG galaxies have been observed. ON-OFF spectral line measurements were done at systemic velocities v $<$ 10000 km s$^{-1}$, using integration times between 10 and 60 minutes and typical bandwidths of 5 or 10 MHz, depending on the expected signal strength and line profile width. All observations used the FFT spectrometer, which has 1024 channels on each of the two linear receiver polarizations. The system temperature is slightly under 20 K at high elevations. Some minor interferences were present in the spectra every couple of MHz due to the servo electronics at the telescope focus area, that were easily eliminated.

## 3.5 Data reduction

The pre-processing of the raw data was done with the standard software provided by each radio-telescope (e.g. NAPS at Nançay, Toolbox of the MPIfR-Bonn at Effelsberg, etc.). This includes the elimination of bad integrations, first substraction of the baseline, average of all integrations for each acquisition phase, performation of the phase arithmetics (for instance ON-OFF/OFF) for each cycle and calculation of the flux density scale calibration and finally the average of the cycles. Since the output containing the calibrated scans had a different format depending on the telescope, they were converted to FITS format, in order to reduce them in a homogeneized way. For that reason we have built a software written in IDL, to perform the final reduction. Among other capabilities, this software includes baseline substraction, oscillatory functions extraction via FFT, elimination of RFIs, addition of different scans and calculation of standard and derived parameters. These parameters include: 1) Integrated flux density, 2) kinematics (e.g. velocities and widths), 3) offset pointings and beam attenuation, 4) several asymmetry coefficients and 5) $M_{HI}$.

In some cases radio frequency interferences (RFIs) in the 21-cm band were found. They can produce substantial changes in the calculated parameters, such as the integrated flux density, and therefore they had to be interpolated. Low level RFIs due mainly to communication services and radars occasionally were present at the Nançay, Effelsberg and Arecibo radio-telescopes producing spikes in the observed profiles. The GBT is inside a radio quiet zone but the servo electronics at the telescope focus area was a source of RFI that produced narrow features in the spectra every couple of MHz (this occured during the commisioning phase of the radio-telescope). In most cases all these interference defects were edited out without loss of information. If any interference spikes were located within the flux integral velocity range, they were removed by interpolation before the profile was measured. The subtraction of baselines are performed by fitting the lowest order Chebishev polynomials reproducing the shape of the ground line.

Several resolutions have been achieved for the different observations, due mainly to the fact that the bandwidth and therefore the number of channels could be different from one observation to another (see information about the resolution of our raw data in Tab. 3.9). If needed, final profiles have been smoothed using a boxcar function in order to improve the signal to noise ratio (except for the digitized spectra since in general they had been already smoothed). This yields to a decrease in the resolution of the profiles. The achieved noise in the HI profiles is shown sorted by radio-telescope in Fig. 3.6. The histogram in Fig. 3.7 show the final resolution of the profiles after smoothing, except for those galaxies for which we only had the digitized profiles (see § 3.5.2). Nearly 75 % have a final resolution better than 10 km s$^{-1}$.

Integrated flux density is calculated as the area under the HI profile. Widths are calculated at a certain height level (25%, 30% and 50%) with respect to the maximum of the smoothed profile. The algorithm seeks for the crossing point between a given height level and the HI profile. For low S/N ratios accurate measurements are not expected at low levels. In addition, the smoothing of the data (boxcar) could result in a systematic decrease of the width (see Springob et al. 2005). Corrections to the calculated physical quantities are addressed in Appendix D. After reduction, all these results have been collected in a database that will be publicly accessible via http://www.iaa.es/AMIGA.

We have performed comparisons of the parameters obtained with our software with respect to other reduction softwares in order to explore any possible bias. A total of 185 galaxies have been reduced with the standard Effelsberg "toolbox" program (those galaxies observed at Effelsberg) (see comparison in Fig. 3.12). Observations performed at the GBT have been reduced with another reduction package developed by R. Fisher. No significant deviations are found when comparing with the results obtained using our reduction package.

### 3.5.1 Correction to the integrated flux: pointing errors and beam attenuation

In this section we address the problem of a bad pointing, beam attenuation, and their implications in the calculation of the HI parameters.

An inappropriate pointing of the radio-telescope can be due to:

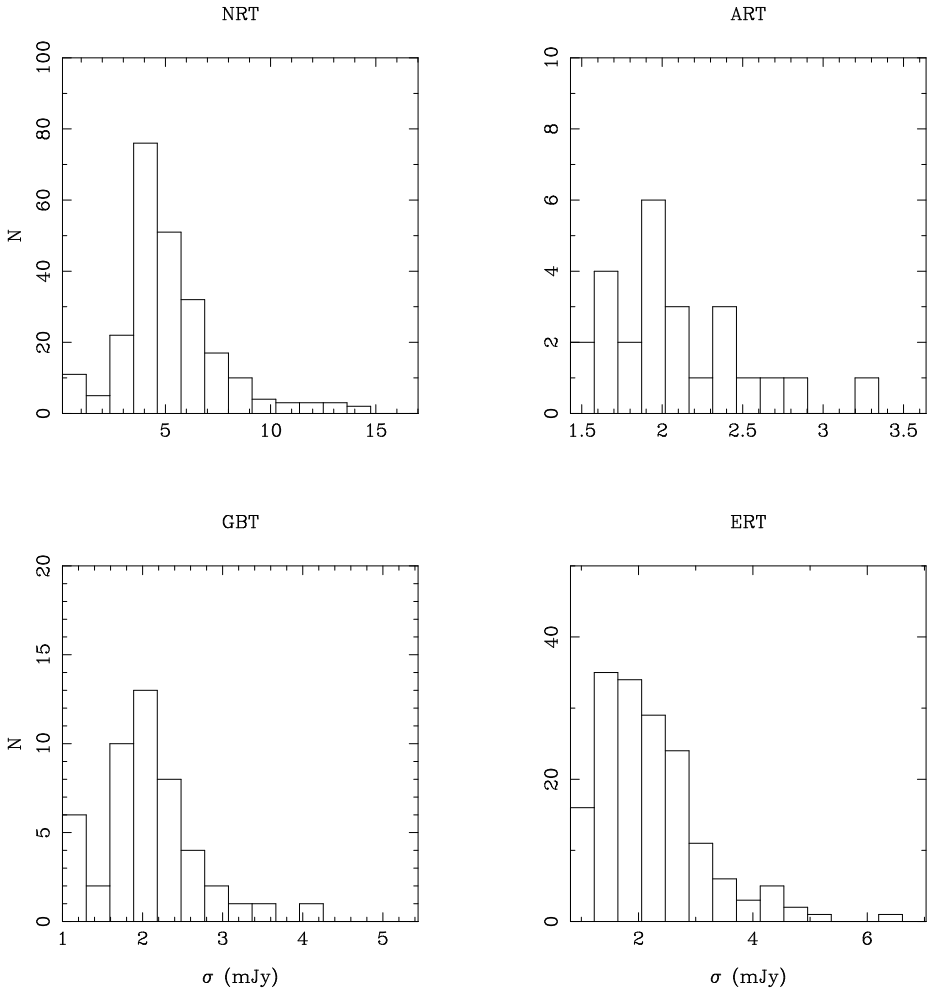


Figure 3.6: Histogram showing the final noise of the HI profiles after smoothing (NRT = Nancay, ERT = Effelsberg, GBT = Green Bank and ART = Arecibo).

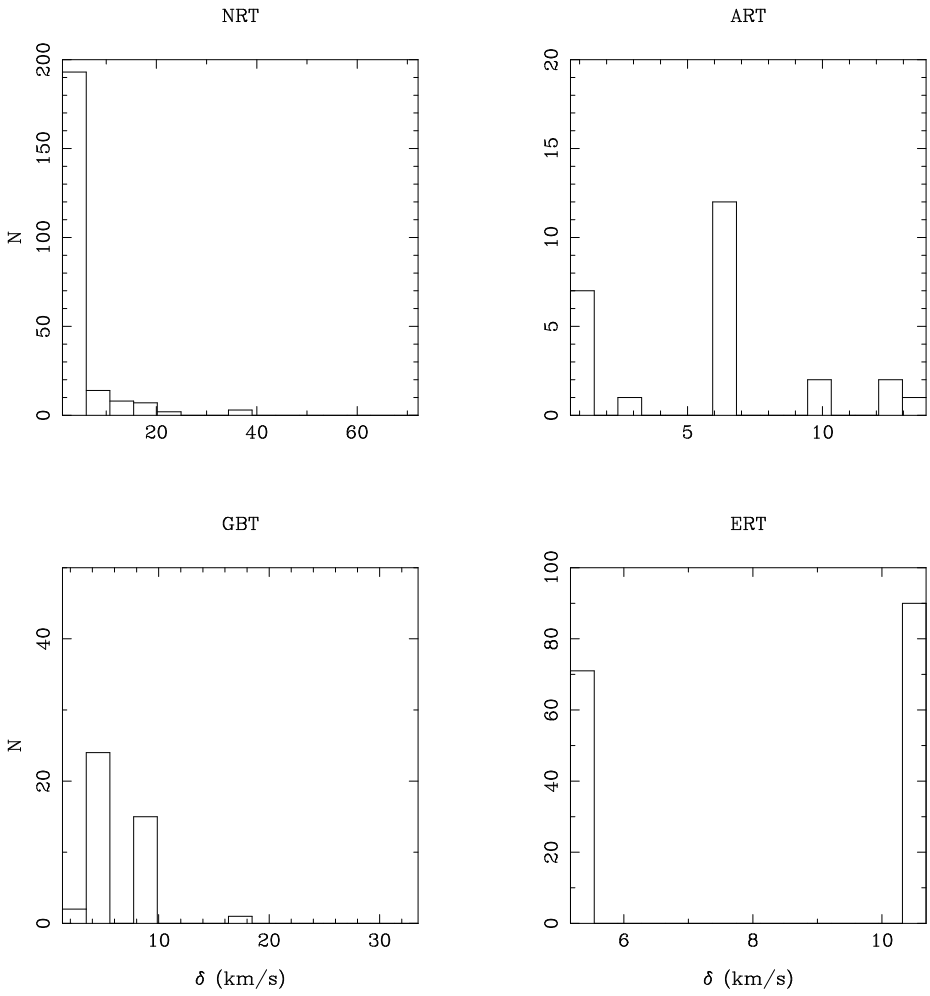


Figure 3.7: As in Fig. 3.6 but for the achieved resolution after smoothing.

1) Uncertainties in the source position, since HI and optical do not need to be centered at the same location.

2) The intrinsic radio-telescope technical pointing accuracy as well as errors in the pointing calibration. For example, the design pointing accuracy for the Effelsberg radio-telescope is around 5″, 5″for Arecibo, 15″for Green Bank 91m, etc. However, deviations from the theoretical value occurs due to other effects. For example, Springob et al. (2005) consider that the real pointing accuracy of the Arecibo radio-telescope is around 15″ both in RA and Dec. HG84 consider that flux losses at the Arecibo radio-telescope due to this effect is random and of the order of 5%.

The loss of flux is especially relevant for sources whose HI extent is much larger than the radio-telescope beam. In addition to the flux loss, this effect will also result in changes in the systemic velocity and widths as well as differences in the profile shape. As Tifft & Huchtmeier (1990) claim, a 2′ offset with a 9′ beam telescope and a galaxy size comparable to the beam extent have an effect of approximately $\Delta V \sim 2.5$ km s$^{-1}$, although the effect on the width is almost negligible. This will depend of course on the considered height level. On the other hand, the asymmetry coefficients are very dependent on a good pointing (e.g. the definition by Tifft & Cocke 1988, see Chapter 5). Tifft & Huchtmeier (1990) report a study to compare the obtained HI data from Green Bank 91m and Effelsberg (both have a similar beam size, around 9′), in order to find the consistency of the data taken from different telescope systems. Comparisons of asymmetry coefficients for those profiles with S/N > 10 lead to differences of about 0.04 to 0.1 from one telescope to the other, although the signs of the asymmetry parameter correlate. Hewitt et al. (1983) also studied flux losses in maps performed with the Arecibo telescope with respect to the GB91.

We analitically calculate a correction factor to assess the problem of pointing offsets and beam attenuation. In Fig. 3.8 we show this correction factor for the Arecibo telescope (3.4′) as a function of the diameter of the source and the pointing offset. Note that for larger galaxy to beam size ratios an important amount of flux is lost even if there is no pointing offset. See Appendix D for details.

In Fig. 3.11 and 3.12 we show the offsets of the radio-telescope position with respect to the revision of the positions obtained by Leon & Verdes-Montenegro (2003). The beam size of each radio-telescope is also shown for comparison. For the Arecibo radio-telescope any offset is very important since its beam size is quite small. In general the effect is not very relevant, except for some exceptions. For example, there are offsets in RA in some galaxies observed at the Effelsberg radio-telescope (offsets of $\sim 2'$: CIG 209, 212, 327 and 901; or even larger offsets: 708 and 868). New observations were needed for these galaxies since the estimated flux was highly uncertain. The upper right and middle right plots in Fig. 3.11 (Arecibo and Effelsberg radio-telescopes respectively) show a high level of scatter. In the former this is because most of the HI data come from the compilation from the literature or from the Haynes & Giovanelli catalogue, which does not include the revision in positions. In the latter plot, this is due to the fact that most of the observations at the Effelsberg radio-telescope were performed by us before the results of Leon & Verdes-Montenegro (2003) were available.

### 3.5.2 Digitizations

When the original HI spectra were not available we proceeded to scan the published HI profiles. We benefit from the digitization product since we can calculate the parameters with the same reduction program, homogenizing in this way the HI parameters for the whole sample.

The spectra were included in $\sim 80\%$ of the cases, and then we proceeded to digitize them using *Dexter*[1]. A total of 285 profiles were scanned and digitized. Units were unified and formats were converted to our reduction package. Finally, our reduction procedure was applied to the digitized profiles.

In order to evaluate the goodness of our digitization we compare the parameters calculated by us and those compiled from the bibliography. Fig. 3.13 shows the linear regression and residuals between

[1] *Dexter* is a tool to digitize plots from scanned pages included in the NASA-ADS abstract service (http://dexter.sourceforge.net) by Demleitner et al. 2001

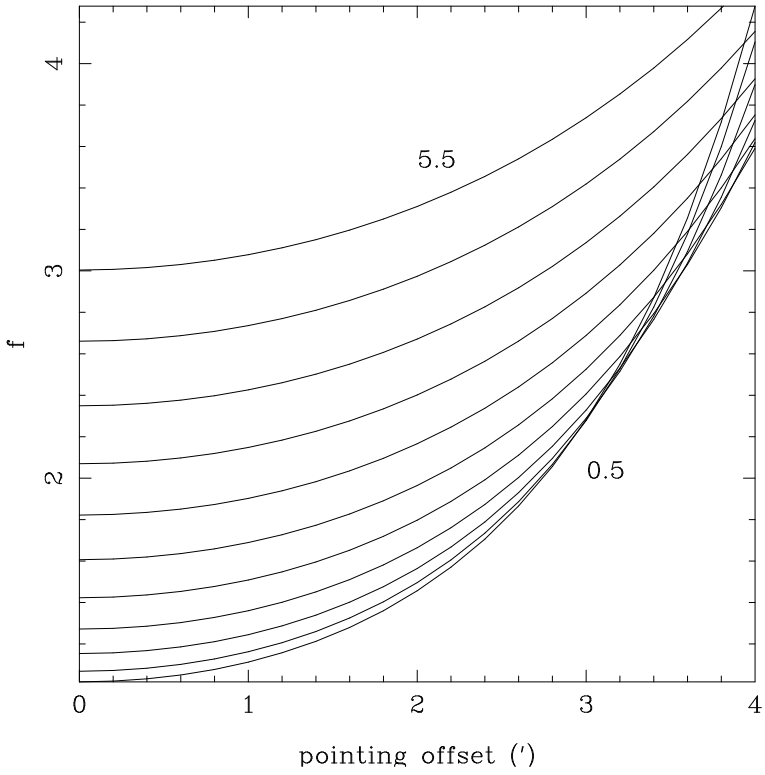


Figure 3.8: Plot showing the correction factor due to pointing offsets and beam attenuation. Each line corresponds to a different optical size of the source, from 0.5 to 5.5′(interval=0.5).

several representative parameters and those measured using the digitized profiles and our reduction package. In most of the cases the agreement is satisfactory:

- S (uncorrected HI integrated flux density): 268 out of the 285 scanned profiles had S available, 165 out of the 268 ($\sim$ 60%) have a difference lower than 10% while 213 out of the 268 ($\sim$ 80%) have a difference lower than 20%. Differences larger than 20% are mainly marginal detections or profiles with bad baselines.
- V (mean velocity at 20%): 264 out of 274 ($\sim$ 96%) with velocity information available in its reference have a difference lower than 2%.
- W (width at 20%): 222 out of 246 ($\sim$ 90%) have a difference lower than 5%.

Therefore this seems to be a fairly good method to recover relevant information through digitizations. We can derive with this method we can derive not only the parameters listed in the bibliography but also to calculate some other derived parameters, such as widths at different levels, asymmetry coefficients, etc., completing in this way our database for a large number of galaxies.

### 3.5.3 Presentation of the HI parameters and their corrections

The main parameters that we have calculated are:

- integrated flux density and HI mass,
- offset pointings and beam attenuation factors,
- kinematics: widths are calculated at given levels (25%, 30% and 50%) with respect to the maximum of the smoothed profile. The algorithm calculates the two points of the spectra that

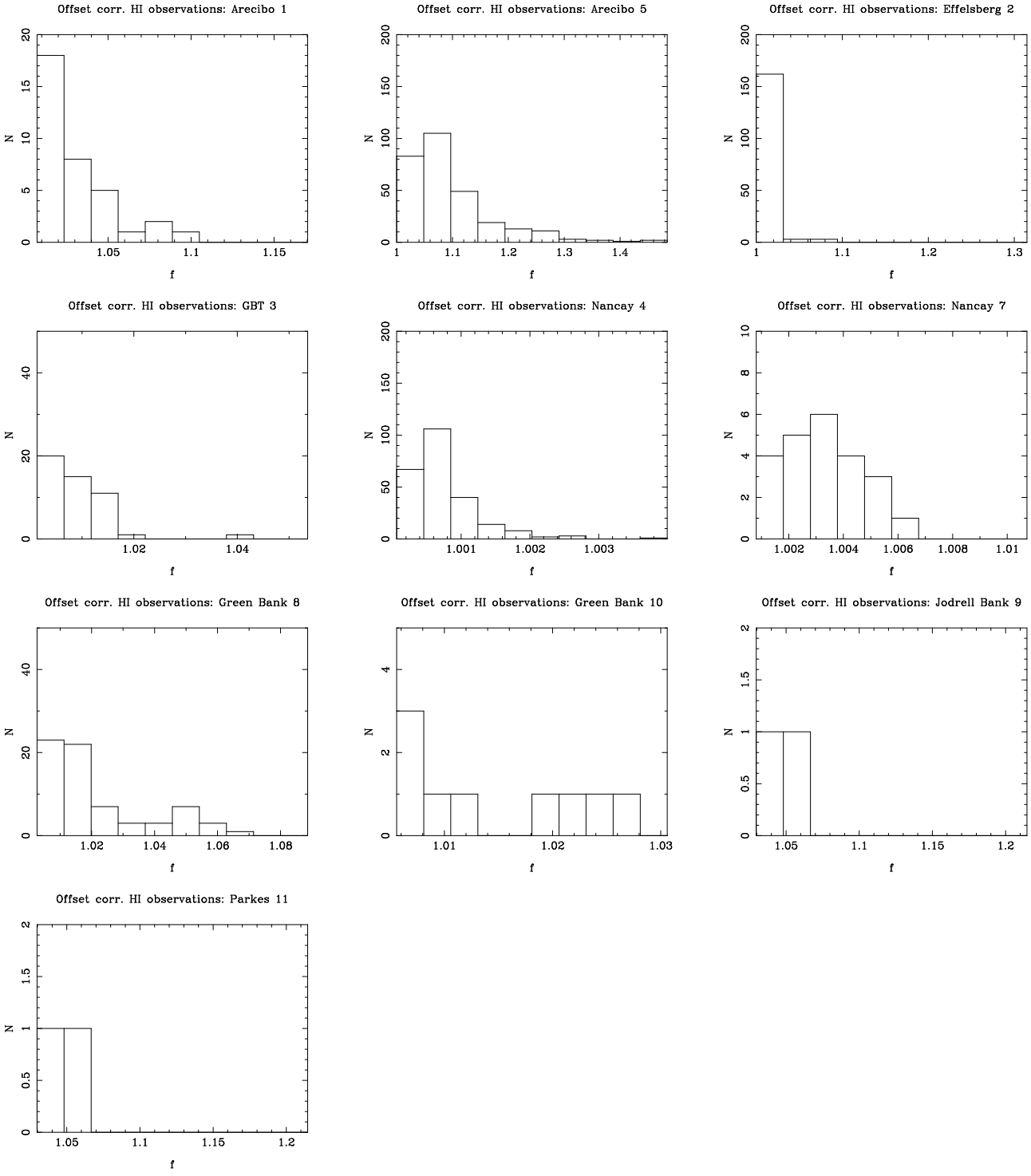


Figure 3.9: Distributions of the corrections to the integrated flux due to offset and beam attenuation, sorted by telescope. Only selected data are included.

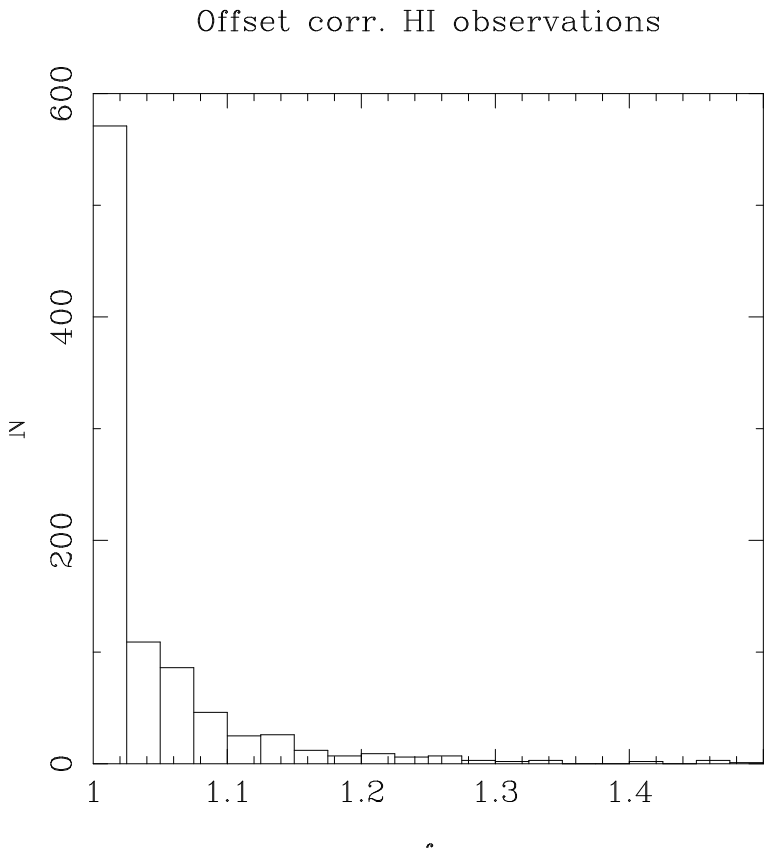


Figure 3.10: Same as Fig. 3.9 but merging all data from different telescopes. Again only selected data are included.

crosses the line at a given level, beginning from the outer regions of the spectra and going towards the HI profile. For low S/N ratios we do not expect accurate measurements of the widths, especially at low levels. Additionally the smoothing of the data (boxcar) results in a systematic decrease of the width. Improvements in the algorithms will be done in the future to get rid of this effects (e.g. considering fits to the wings of the profiles in order to calculate the widths and mean velocities). The final systemic velocities obtained from the spectra are the midpoints at this level. Mean and median velocities of the profile are calculated as well.

- asymmetry coefficients calculations.

We also study the limiting precision for the integrated flux, systemic velocity and width, when we consider several antennas, as a function of the S/N ratio of the profile.

The obtained parameters are presented in Tab. 3.14, using the following format:

1) CIG: Entry number in the Catalogue of Isolated Galaxies.

2) det: is the detection code: 0 = detected, 1= non-detected and 2 = marginal detection.

3) Tel: code for the radio-telescope, as in Tab. 3.6.

4) S/N: signal to noise ratio (with respect to the maximum of the profile).

5) S $\pm$ $\sigma_S$: integrated flux density over the observed signal and its error, in Jy km s$^{-1}$. If non-detected then an upper limit for the HI mass content is calculated, assuming a typical line width of 250 km s$^{-1}$ and a signal equal to 3$\sigma$, except when the redshift is not known. The error was

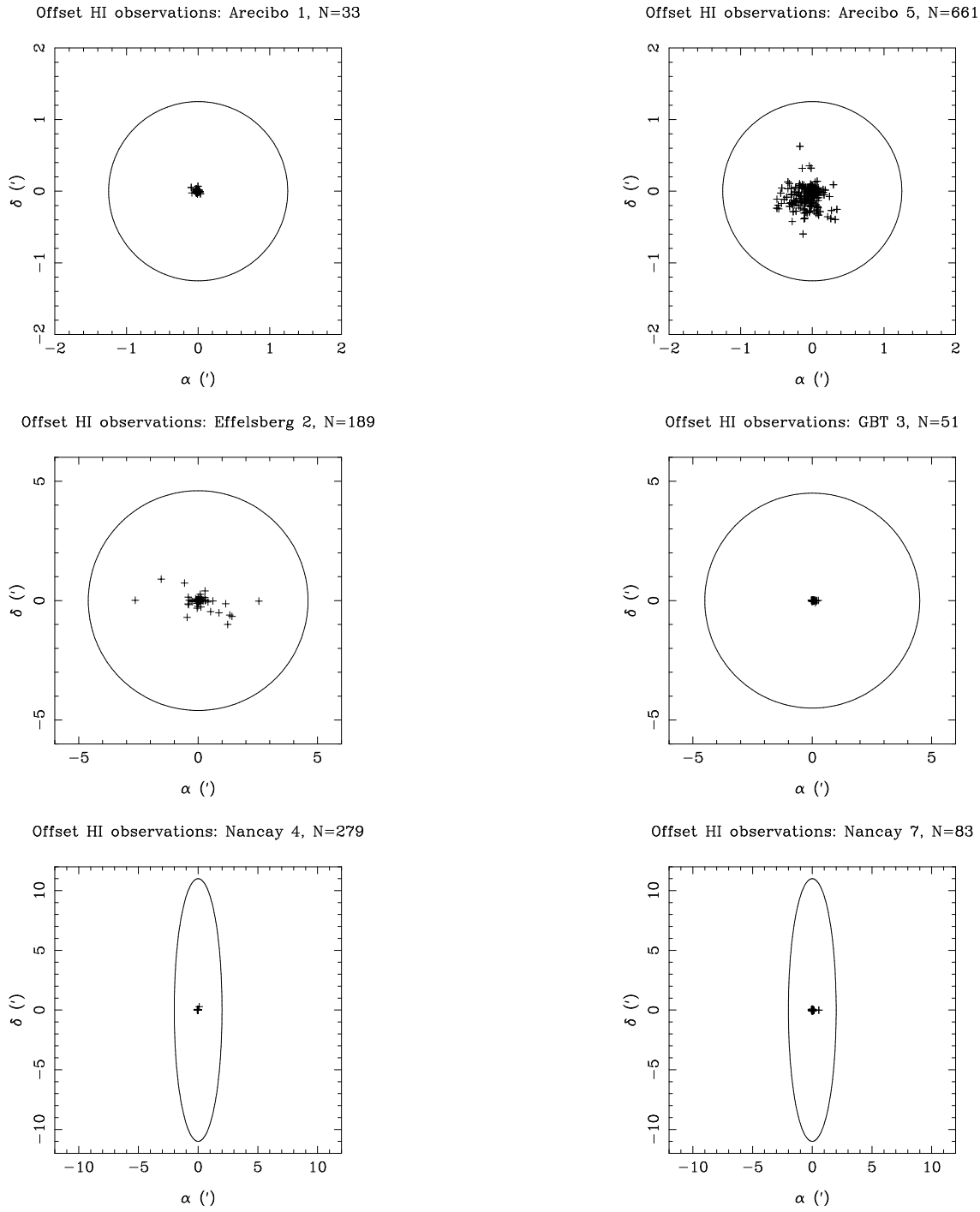


Figure 3.11: Pointing of the HI observations at Arecibo, Effelsberg, GBT and Nançay versus the revised positions by Leon & Verdes-Montenegro (2003). The ellipse represents the beam of each radio-telescope.

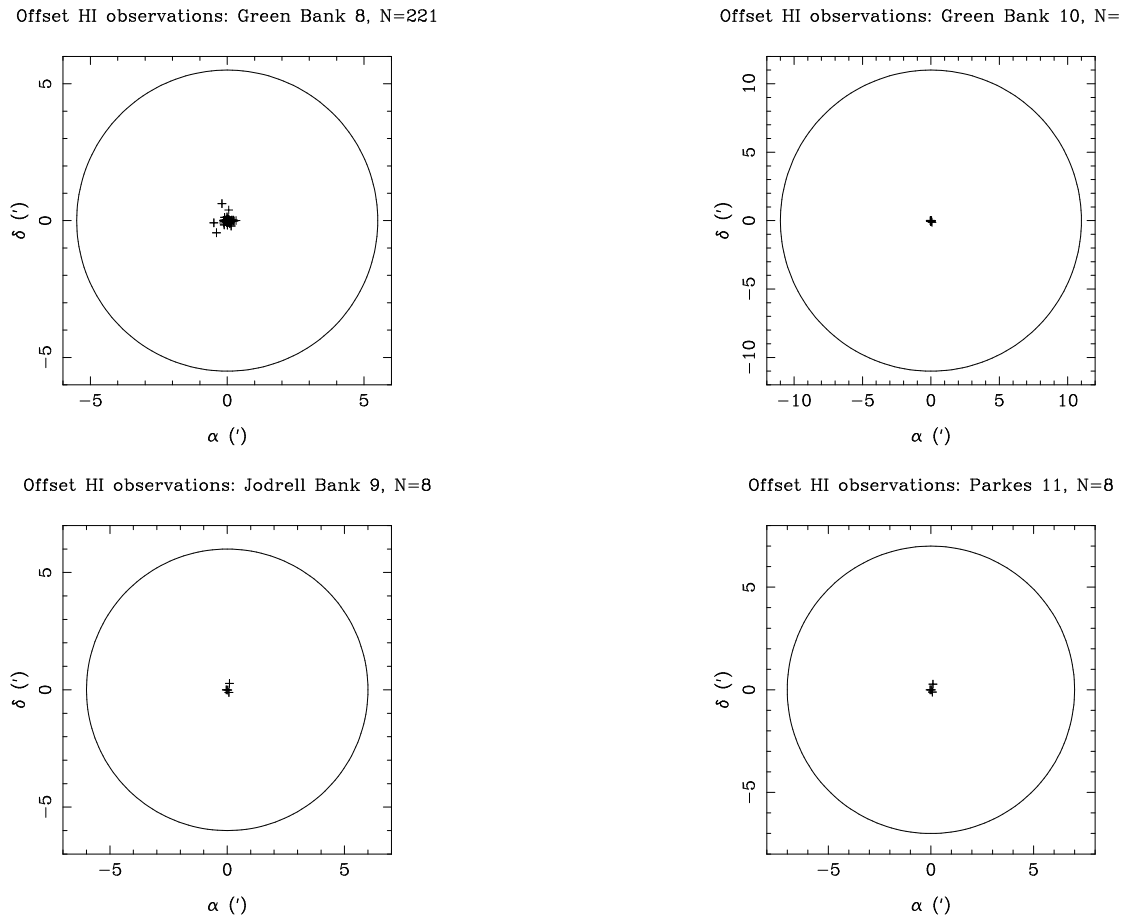


Figure 3.12: Same as Fig. 3.11, but for Green Bank 91m, Jodrell Bank and Parkes.

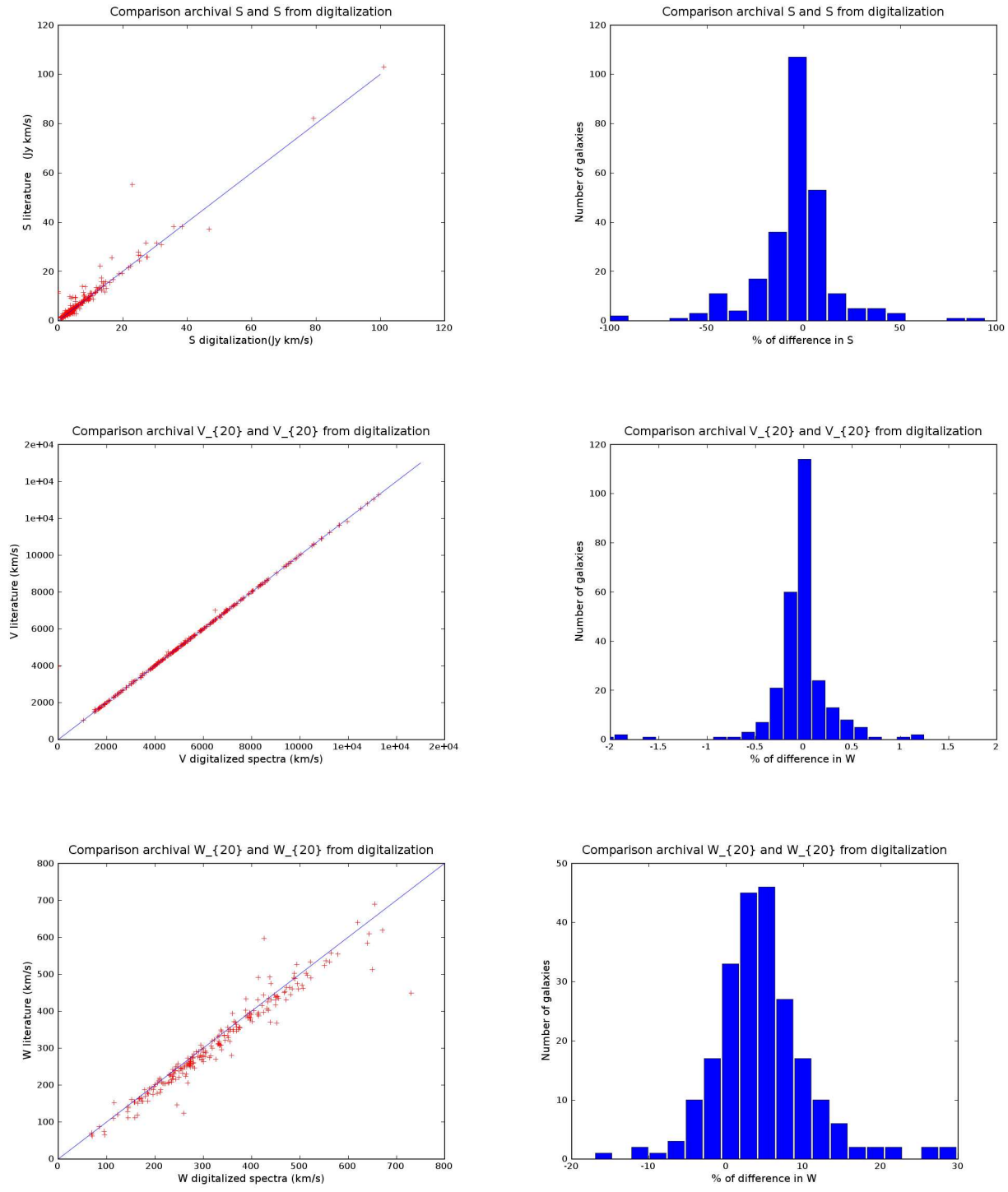


Figure 3.13: Linear regression and residuals showing differences between our measured integrated fluxes, velocities and widths from the digitized spectra and the original ones from the literature.

calculated as in Fouqué et al. (1990):

$$\sigma_S = \frac{5[(\delta Sh)]^{\frac{1}{2}}}{S/N} \tag{3.3}$$

where h is the maximum global heigth of the profile.

6) $S_c \pm \sigma_{S_C}$: S corrected by beam filling and offsets and its error, in Jy km s$^{-1}$, as explained in Appendix D. To calculate this correction we have used our revised morphologies and optical diameters from LEDA. Only 3% of the observations needed corrections larger than 30% of S. We do not consider random pointing errors in the calculations of the corrections. Internal HI auto-absorption corrections (see Appendix B in HG84) are usually small, unless the inclination of the galaxy is high (2 %, 6%, 19% respectively at 60°, 75° and 85°, Heidmann et al. 1972b). The calculation of this type of correction suffers of much uncertainty due to the dependence on the morphological type and the modeling of the gas distribution, and therefore it has not been taken into account in this work.

7) V $\pm \sigma_V$: heliocentric radial velocity at 20% level with respect to the maximum of the profile. Its error was calculated following Fouqué et al. (1990):

$$\sigma_V = \frac{4[(\delta\ (W_{20} - W_{50})/2]^{\frac{1}{2}}}{S/N} \tag{3.4}$$

where $(W_{20} - W_{50})/2$ is calculated to see the slope of the profile.

8) $V_C \pm \sigma_{V_C}$: same as column 7) but corrected following Fouqué et al. (1990).

9) and 11) $W_i \pm \sigma_{W_i}$: width at a $i = 20\%$ and 50% level with respect to the maximum of the peak, in km s$^{-1}$. The error of the widths are calculated according to Fouqué et al. (1990):

$$\sigma_{W_{20}} = 3\sigma_V, \sigma_{W_{50}} = 2\sigma_V \tag{3.5}$$

10) and 12) $W_{C,i} \pm \sigma_{W_{C,i}}$: the correction of the line width at a given level with respect to the maximum of the peak, taking into account the resolution effect, internal velocity dispersion and inclination, as explained in Appendix D.

### 3.5.4 Selection of HI data for a given galaxy

The calculated HI parameters (integrated flux, asymmetry coefficients, etc.) can depend on the used radio-telescope (e.g. Tifft & Huchtmeier 1990, where they compare HI data obtained from spectra observed both in the GB 91m and the Effelsberg telescope, both with a similar beam size). In our study we consider different telescopes with different characteristics (e.g. the beam size). We need to minimize any possible bias that can result from this fact. We want to obtain homogeneized data for the whole sample of isolated galaxies. For this reason we have left overlapping subsamples in the observations between telescopes, in order to check for any error coming from technical problems like bad calibration of the spectra for a given radio-telescope, etc. In our tests we consider that data coming from one telescope in different dates do not change considerably, except in the cases where a given radio-telescope has been upgraded, like in the case of Arecibo with the new Gregorian Optical system and Nançay with the FORT upgrade. After these changes were performed, we have considered that the observations were performed with a different telescope.

According to the software used to reduce the data, we have two kind of data. First, the HI data that have been obtained with our reduction package:

1) HI data from our own observations (NRT, ART, ERT).

Table 3.11: Linear fits of several HI parameters (integrated flux, mean velocity and width at 20% level) calculated with our software (from both our observations or the digitized profiles) versus those directly compiled from HG84 (see Fig. 3.14).

| HI parameter | Slope | Intercept | $\rho$ | N |
|---|---|---|---|---|
| S | 1.02 ± 0.01 | -0.020 ± 0.006 | 0.99 | 240 |
| V | 1.000 ± 0.001 | 19 ± 4 | 0.99 | 240 |
| W | 0.94 ± 0.03 | 23 ± 8 | 0.92 | 240 |

Table 3.12: Linear fits of several HI parameters (integrated flux, mean velocity and width at 20% level) calculated with our software from our observations at Effelsberg versus those calculated with TOOLBOX (see Fig. 3.15).

| HI parameter | Slope | Intercept | $\rho$ | N |
|---|---|---|---|---|
| S | 0.98 ± 0.05 | -0.01 ± 0.02 | 0.91 | 80 |
| V | 0.999 ± 0.002 | 15 ± 14 | 0.99 | 80 |
| W | 0.99 ± 0.05 | 12 ± 12 | 0.93 | 80 |

2) HI data from spectra given by HG, GBT, KLUN and HIPASS.

3) HI data from digitizations of profiles in the bibliography.

and second, the data that were obtained from other reduction packages:

4) HI data obtained directly from each reference.

5) HI data obtained directly from HG (ANALYZ-GALPAC), ERT (TOOLBOX), GBT, KLUN, HIPASS, etc.

In the next subsection we test the results obtained with our software with respect to those calculated with other packages, in the same way as in § 3.5.2 where we tested 3) vs 4), but considering this time only a given reduction program (in particular, ANALYZ-GALPAC for Arecibo and TOOLBOX for Effelsberg). In a second step we compare different values for a given galaxy to check consistency between radio-telescopes.

**a) Comparison of HI parameters obtained with our software and with other reduction packages (5 vs 1 and 5 vs 2)**

Fig. 3.14 and Tab. 3.11 show the consistency between the HI parameters calculated with our reduction package and those calculated by Haynes & Giovanelli with ANALYZ-GALPAC. Integrated density fluxes, mean velocities and widths at a 20% level are in reasonable agreement. The same is seen in Fig. 3.15 and Tab. 3.12 for the reduction package used in the Effelsberg radio-telescope (TOOLBOX).

**b) Comparison of HI parameters obtained from our own software with respect to the compiled values (1, 2 and 3 vs 4)**

Fig. 3.16 and Tab. 3.13 show the consistency between the HI parameters calculated with our reduction package with respect to those directly compiled from the bibliography. Offsets are mainly due to the use of digitized profiles, which do not have the same quality as the original ones. Some other differences can arise from the use of different reduction packages.

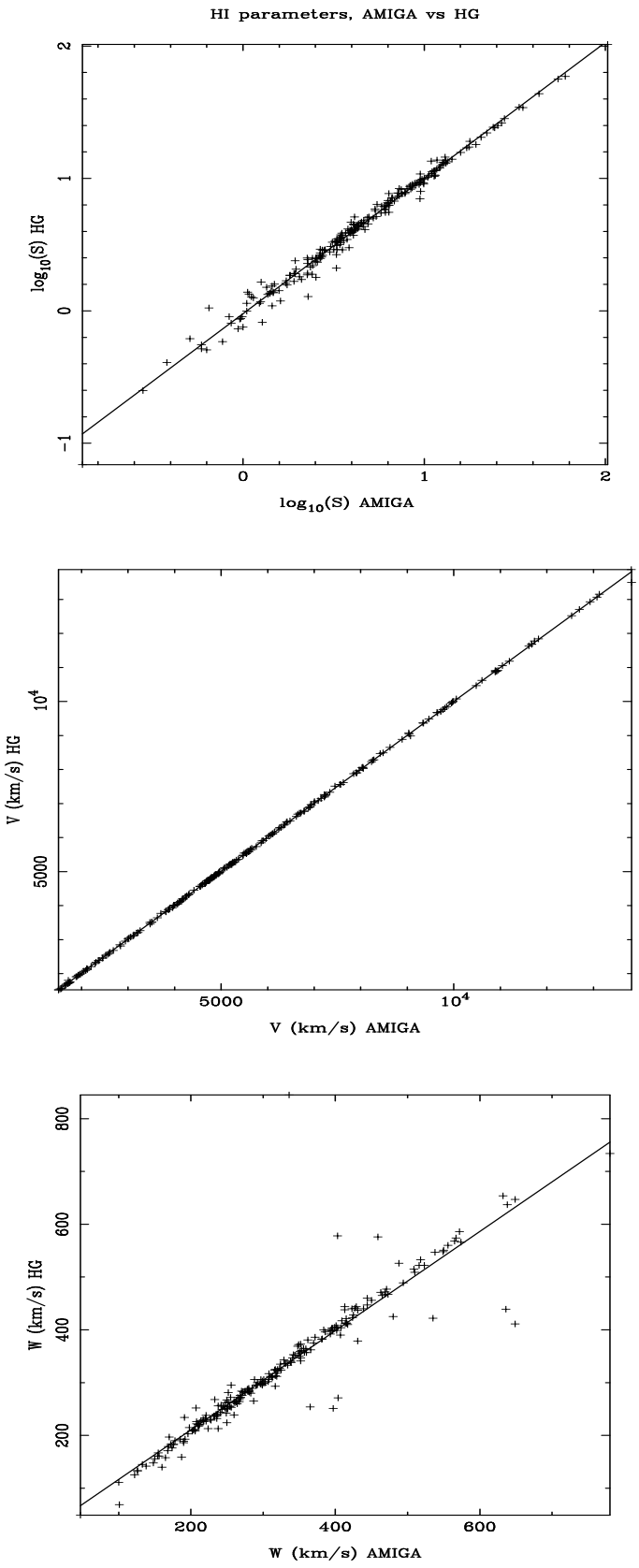


Figure 3.14: HI parameters (integrated density flux, mean velocity and width at a 20% level) from either our observations or the digitized profiles calculated with our software versus those directly compiled from HG84 (N = 240).

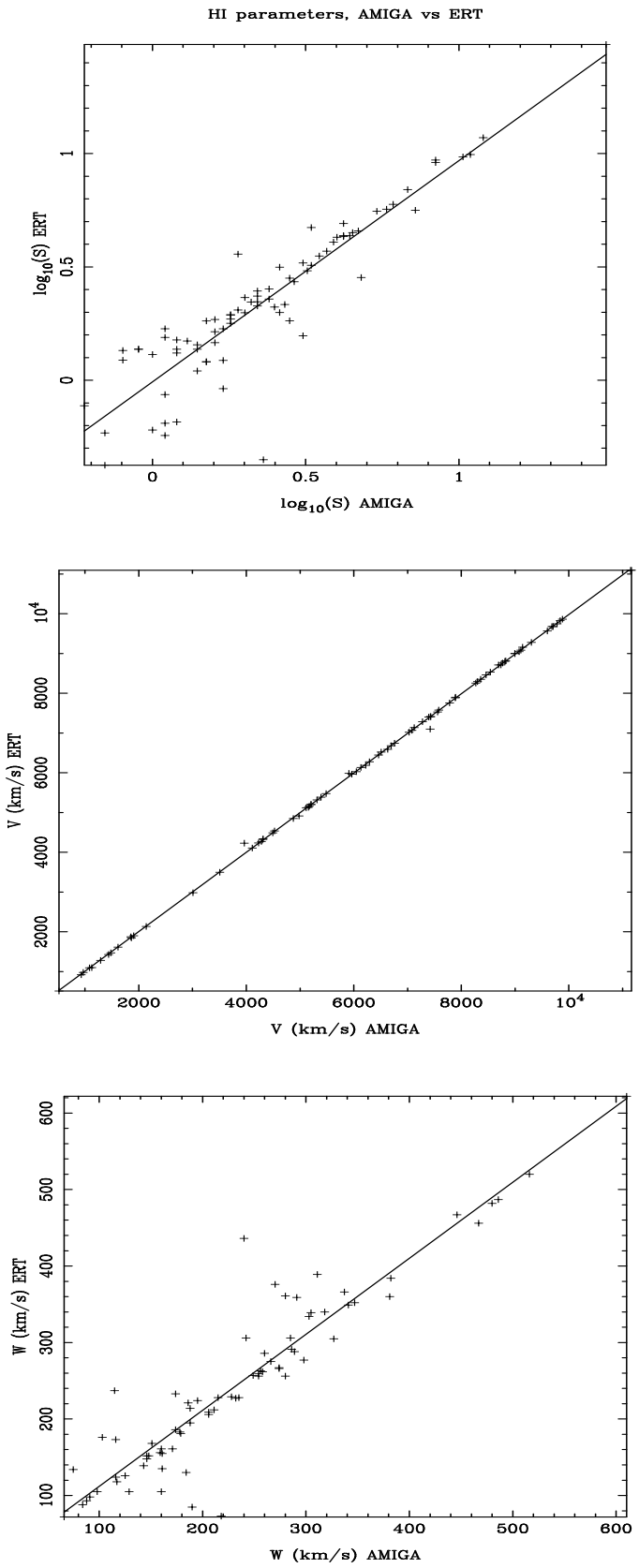


Figure 3.15: HI parameters (integrated density flux, mean velocity and width at a 20% level) from our observations at the Effelsberg radio-telescope calculated with our software versus those calculated with TOOLBOX (N = 80).

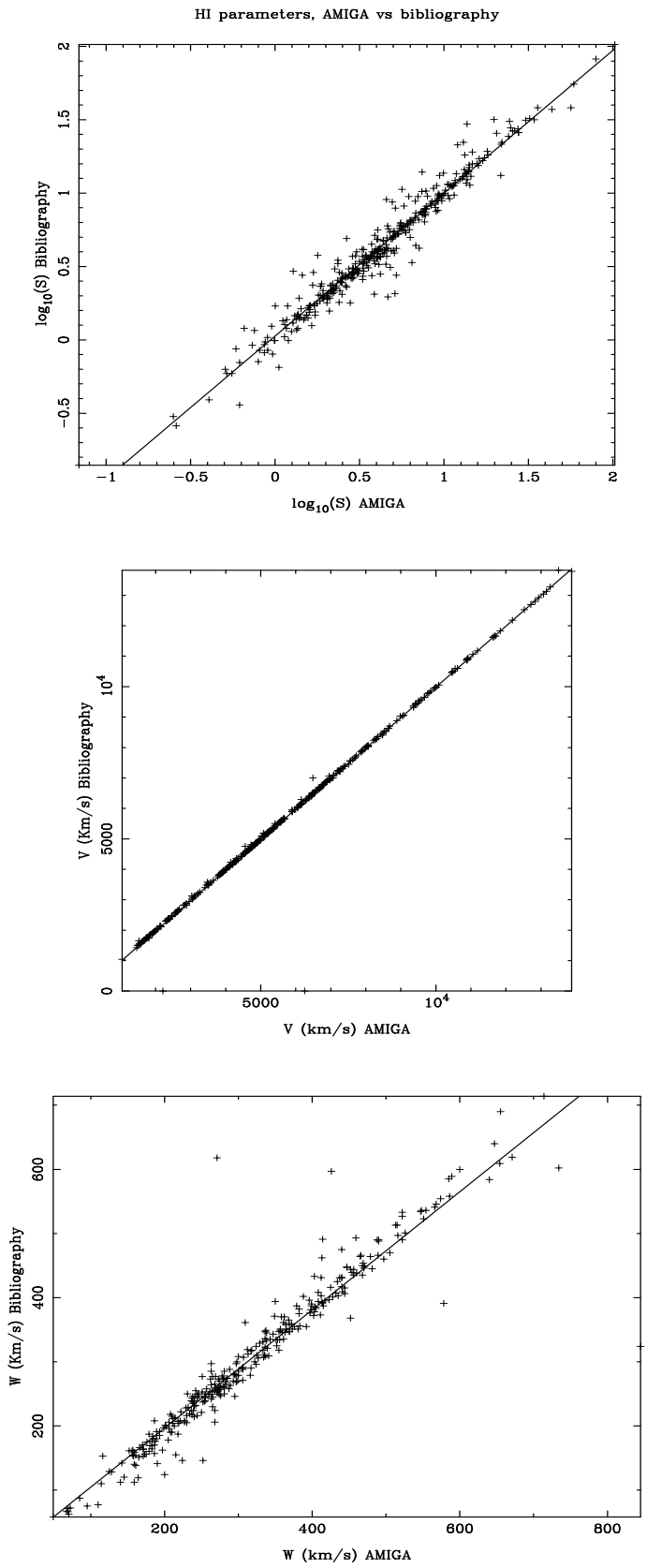


Figure 3.16: HI parameters (integrated flux, mean velocity and width at a 20% level) from our observations or digitized profiles calculated with our software versus those directly compiled from the bibliography (N = 430).

Table 3.13: Linear fit of HI parameters calculated with our software versus those compiled from the bibliography (see Fig. 3.16).

| HI parameter | Slope | Intercept | $\rho$ | N |
|---|---|---|---|---|
| S | 0.97 ± 0.01 | 0.03 ± 0.01 | 0.97 | 378 |
| V | 1.00 ± 0.006 | -31 ± 40 | 0.99 | 379 |
| W | 0.92 ± 0.02 | 13 ± 6 | 0.94 | 328 |

**c) Final selection of HI data**

In this section we describe the selection of the HI data for those galaxies that had more than one observation available (either from our observations or compiled from the literature). The criteria are the following:

- The beam to HI extent ratio: this criterion was taken into account in order to avoid flux losses. If we had different observations from different radio-telescopes for a given galaxy, we chose one observation performed with a beam size larger than the assumed HI extent. Of course, the ratio can not be too large because other sources would be included in the beam. Parameters to note this effect are the total integrated flux and/or the resulting asymmetries in the profile,

- Quality of the profile: profiles with higher S/N ratios were prefered,

- Any possible problem with the spectra, like interferences in the middle of the profile, bad baseline substraction, etc. The comments by the authors of the inspected papers were checked.

Once the selection was performed, we only had one selected entry for a given galaxy in our database. From now on, we will only refer to the previously selected HI data attending to these criteria.

In Tab. 3.14 we present the final HI parameters for the selected HI observation of each galaxy, as well as their derived parameters. The columns are explained in § 3.5.3. In Tab. 3.15 we show a summary of the procedence of the final selected HI data, in total N = 910 galaxies. In Appendix **??** we show the HI profiles for the detected galaxies after reduction of the data.

Table 3.14: List of the selected HI data[1].

| CIG (1) | det (2) | Tel (3) | $S/N$ (4) | S $\pm\sigma_S$ (5) | $S_c \pm \sigma_{S_c}$ (6) | $V \pm \sigma_V$ (7) | $V_c \pm \sigma_{V_c}$ (8) | $W_{20} \pm \sigma_{W_{20}}$ (9) | $W_{c20} \pm \sigma_{W_c 20}$ (10) | $W_{50} \pm \sigma_{W_{50}}$ (11) | $W_{c50} \pm \sigma_{W_{c50}}$ (12) |
|---|---|---|---|---|---|---|---|---|---|---|---|
| 1 | 0 | 5 | 9.4 | 5.8 ±0.1 | 20.7 ±0.1 | 7264.2 ±0.5 | 7265.7 ±0.5 | 484 ±1 | 468 ±1 | 485 ±1 | 490 ±1 |
| 2 | 0 | 4 | 14.2 | 3.1 ±0.1 | 3.2 ±0.1 | 6975.0 ±2.2 | 6983.5 ±2.2 | 274 ±6 | 241 ±4 | 320 ±6 | 304 ±4 |
| 3 | 1 | 5 | 0.0 | 0.0 ±0.0 | 0.0 ±0.0 | 0.0 ±0.0 | 0.0 ±0.0 | 0 ±0 | 0 ±0 | 0 ±0 | 0 ±0 |
| 4 | 0 | 9 | 25.9 | 14.9 ±0.5 | 15.5 ±0.7 | 2301.5 ±2.2 | 2304.5 ±2.2 | 425 ±6 | 393 ±4 | 372 ±6 | 366 ±4 |
| 8 | 0 | 4 | 12.0 | 4.8 ±0.6 | 5.1 ±0.3 | 6336.5 ±2.6 | 6344.5 ±2.6 | 274 ±7 | 241 ±5 | 237 ±7 | 224 ±5 |
| 9 | 0 | 4 | 13.7 | 4.4 ±0.3 | 4.5 ±0.5 | 8477.1 ±6.8 | 8469.7 ±6.8 | 376 ±21 | 339 ±13 | 329 ±21 | 324 ±13 |
| 10 | 0 | 7 | 9.1 | 2.2 ±0.1 | 2.2 ±0.3 | 4996.0 ±4.6 | 4996.0 ±4.6 | 272 ±14 | 251 ±9 | 253 ±14 | 256 ±9 |
| 12 | 0 | 4 | 10.0 | 5.0 ±0.1 | 5.3 ±0.4 | 5481.0 ±4.5 | 5483.8 ±4.5 | 334 ±13 | 301 ±8 | 286 ±13 | 276 ±8 |
| 14 | 0 | 7 | 6.9 | 0.9 ±0.1 | 0.9 ±0.1 | 5237.0 ±8.6 | 5247.4 ±8.6 | 409 ±26 | 367 ±17 | 451 ±26 | 429 ±17 |
| | ... | | | | | | ... | | | | ... |

[1] This table is explained in 3.5.3. The radio-telescopes codes can be found in Tab. 3.6. The whole list can be downloaded from http://www.iaa.es/AMIGA.html.

Table 3.15: Summary of the procedence of the selected HI data.

| Source | Number of galaxies |
|---|---|
| Our observations | 488 |
| HG, HIP or KLUN (digitized) | 307 |
| Literature | 115 |
| Total | 910 |

### 3.5.5 Detection rate

Fig. 3.4 shows the morphological distribution of galaxies with HI data. We also plot histograms for HI detected galaxies, upper limits and marginal detections. The detection rate is as follows: 66 % are firm detections, 4 % marginal detections and 30 % upper limits. The detection rate as a function of the morphology is presented in Tab. 3.16. As expected, the detection rate is higher for late type galaxies (from Sa to Sm, 70 % to 100% respectively) than for early types ($\sim$ 25 %). No trend is found as a function of inclination.

## 3.6 Individual HI profiles

The HI profiles can be directly inspected in Appendix **??**. Next we list notes to some galaxies whose HI profiles are specially interesting. The shape of the HI profiles are shown in § 5.

### 3.6.1 Peculiar profiles

CIG 63: We have two observations for this galaxy: at NRT and ERT. The HI profile seems to be the one of a face-on galaxy in both observations, but this galaxy is edge-on ($80^o$). The morphological classification in NED is Sc. It has been classified in Sulentic et al. (2006) as an interacting galaxy with a companion or HII galaxy.
CIG 915: Galaxy with three horns in its HI profile, seen both with high and low resolution at Arecibo.

### 3.6.2 New redshifts

New redshifts for 10 galaxies have been obtained: CIG 307, 364, 526, 647, 658, 659, 718, 720, 725, 728. In Tab.3.17 we show the new redshifts.

### 3.6.3 Problems with interferences or bad baseline

The following galaxies (N = 13) have interferences that may alter the shape of the HI profile (in parenthesis the telescope of the observation according to the codes given in Tab. 3.6): CIG 18 (5), 22 (5), 169 (2), 173 (3), 194 (3), 218 (3), 230 (3), 231 (3), 243 (2), 277 (2), 374 (2), 625 (5), 684 (2), 891 (2) and 966 (1).

The following galaxies (N = 47) have spectra with bad baselines (i.e. ripples) and/or uncertain parameters: 3 (4), 16 (4), 35 (4), 36 (8), 46 (4), 48 (4), 110 (4), 118 (4), 182 (3), 228 (4), 256 (4), 301 (11), 304 (4), 305 (2), 316 (2), 320 (4), 346 (3), 364 (11), 366 (2), 482 (2), 520 (4), 522 (4), 526 (3), 535 (4), 556 (2), 572 (4), 583 (4), 592 (4), 594 (4), 596 (4), 617 (4), 632 (4), 640 (4), 666 (7), 667 (4), 673 (4), 679 (4), 705 (4), 707 (11), 715 (11), 742 (4), 749 (4), 752 (4), 795 (2), 999 (2) and 1029 (1). Most of the galaxies with bad baseline come from NRT and are non-detected.

### 3.6.4 Profiles with HI absorption

There are several galaxies candidates to have a HI profile in absorption: CIG 99, 124 and 946.

Table 3.16: Detection rate as a function of the morphology.

| Type | T | N | detected | non-detected | marginal | Det. rate (%) |
|---|---|---|---|---|---|---|
| E | -5 | 46 | 11 | 31 | 4 | 22 |
| E/S0 | -3 | 13 | 2 | 10 | 1 | 15 |
| S0 | -2 | 63 | 16 | 45 | 2 | 25 |
| S0/a | 0 | 18 | 7 | 10 | 1 | 39 |
| Sa | 1 | 11 | 9 | 3 | 0 | 75 |
| Sab | 2 | 48 | 32 | 13 | 3 | 67 |
| Sb | 3 | 149 | 92 | 49 | 9 | 61 |
| Sbc | 4 | 192 | 148 | 41 | 4 | 77 |
| Sc | 5 | 250 | 184 | 59 | 11 | 72 |
| Scd | 6 | 50 | 47 | 2 | 1 | 94 |
| Sd | 7 | 30 | 27 | 4 | 0 | 87 |
| Sdm | 8 | 10 | 10 | 0 | 0 | 100 |
| Sm | 9 | 12 | 12 | 0 | 0 | 100 |
| Im | 10 | 12 | 10 | 1 | 1 | 83 |
| Pec | 998 | 6 | 3 | 2 | 1 | 50 |
| | All | 910 | 602 | 270 | 38 | 66 |

Table 3.17: New redshifts obtained from our observations at GBT and Nançay.

| CIG | Velocity (km $s^{-1}$) |
|---|---|
| 307 | 11802 |
| 364 | 6615 |
| 526 | 11625 |
| 647 | 15481 |
| 658 | 10684 |
| 659 | 8854 |
| 718 | 10312 |
| 720 | 7286 |
| 725 | 12930 |
| 728 | 2110 |

### 3.6.5 HI-rich early type galaxies

A number of early type galaxies (Sulentic et al. 2006) have been detected in HI and will be studied further in Chapter 4:

- Elliptical galaxies: CIG 4, 136, 164, 393, 582, 824, 870, 877, 895, 981, 1025 and 1029.
- Elliptical - lenticular galaxies: CIG 128, 264 and 811.
- Lenticular galaxies: CIG 83, 125, 134, 141, 161, 295, 332, 338, 352, 467, 481, 483, 501, 918, 1015 and 1032.

# Chapter 4

# HI content characterisation

In this chapter we derive the HI content ($M_{HI}$) for the members of our HI sample of isolated galaxies (N = 910). We present simple relationships to derive the expected $M_{HI}$ of a given galaxy as a function of its morphology and optical parameters such as the luminosity ($L_B$) or the linear diameter ($a$), and compare with those found by HG84.These fits that can be used in order to compare with the HI content in galaxies in denser environments.

## 4.1 $M_{HI}$ calculation

$M_{HI}$, expressed in $M_\odot$, was calculated using Eq. 3.1 in § 3.2.1. $D$ is the distance in Mpc obtained from Verdes-Montenegro et al. (2005) and $S_c$ is the corrected integrated flux calculated as explained in Chapter 3. Upper limits of $S_c$ are also considered for non-detected galaxies. In Tab. 4.1 we list $M_{HI}$ for the galaxies in the HI sample (note that we will refer to the HI sample as those galaxies with HI observations and with known redshift, see § 3.3), and in Fig. 4.1 we represent its distribution (marginal detections and upper limits are included).

The distribution of the ratio between the HI content and the optical luminosity, $M_{HI}/L_B$, is presented in Fig. 4.2. This distribution peaks at $M_{HI}/L_B \simeq 0.2$ - 0.3 for HI detected galaxies. We also show the distribution of the upper limits.

## 4.2 $M_{HI}$ as a function of $L_B$, size and morphology

We study in this section the correlations between $M_{HI}$ and some optical properties of the galaxy, in particular the optical luminosity ($L_B$), size ($a$) and morphological type. These correlations are seen to be tight enough to permit a rough prediction of $M_{HI}$ by using its optical information (e.g. HG84, N = 324).

To do so we consider linear regression fits using a standard ordinary least square (OLS) distance minimisation, as well as the bisector correlation (see Appendix E for more information). In both cases we use survival analysis in order to take into account censoring, using as regression procedure the Schmitt's two-dimensional Kaplan-Meier estimator. Therefore, we not only use the detections, but also all the information which is contained in the upper limits. In total we consider N = 910 data points (N = 602 detected galaxies plus N = 38 marginal detections). The increase in number of the sample (we double the number of detected galaxies with respect to HG84) will allow us to better sample the less populated bins when sorting by morphological type (see 3.3.1).

In particular we use the TWOKM subroutine developed in ASURV v1.1 (Isobe et al. 1992), that uses the Schmitt's method (1988). A bootstrapping procedure provides error analysis for this method. The dataset can have mixed censoring, but this need to be distributed in a random way for each variable (that means, the probability that the measurement is censored can not depend on the value of the censored variable). This is true for our sample for two reasons: 1) the censored variable is

Table 4.1: List of $M_{HI}$ for the CIG galaxies[1].

| CIG | $M_{HI}$ ($10^9$ $M_\odot$) | Det. |
|---|---|---|
| 1 | 11.60 | 0 |
| 2 | 5.92 | 0 |
| 3 | - | 1 |
| 4 | 3.52 | 0 |
| 5 | 1.50 | 0 |
| 6 | 2.04 | 0 |
| 7 | 8.06 | 0 |
| 8 | 6.40 | 0 |
| 9 | 1.44 | 0 |
| ... | ... | ... |

[1] Detection codes are: 0 = detected, 1= non-detected and 2 = marginal detection. "−" indicates that it is a galaxy with unknown redshift. The full table can be downloaded from http://www.iaa.es/AMIGA.html.

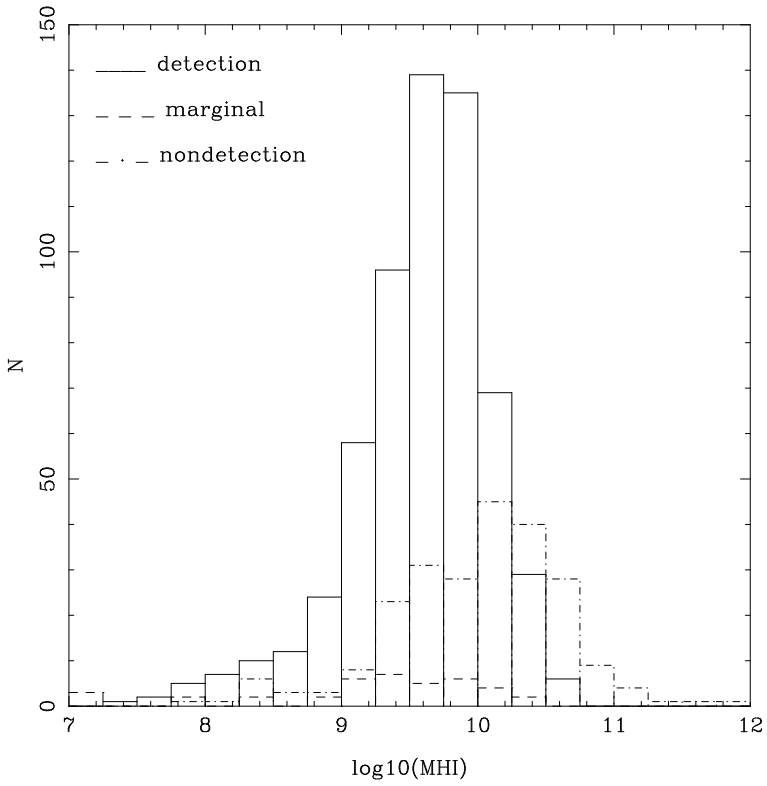


Figure 4.1: Distribution of $M_{HI}$ for the galaxies in the HI sample.

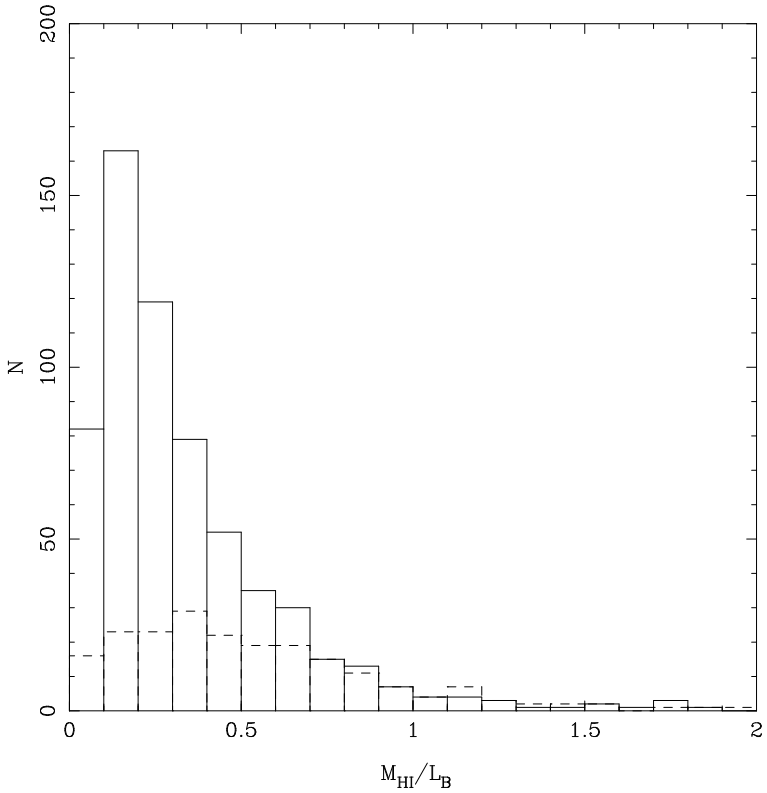


Figure 4.2: Distribution of $M_{HI}/L_B$ for detected (or marginal detections) galaxies (solid line histogram) and distribution of upper limits for non-detected galaxies (dashed line).

not correlated with the variable by which the sample was initially identified (HI observations of an optically selected sample of galaxies) and 2) brighter objects are not always the most luminous, since we need to take into account the distance of each object.

We discuss in the following sections the Ordinary Least Squares (OLS) regression fits of $M_{HI}$ as a function of $L_B$ and $a$, in bins of morphological type.

### 4.2.1 $M_{HI}$ - $L_B$

In Fig. 4.3(a) we show a comparison between the linear regression given by HG84 and our fit, for their sample but using our revised measurements for both $M_{HI}$ and $L_B$. In order to compare their fit to their data with the fit to our revised values we have transformed their coefficients to the $H_0 = 75$ value used in this work. The residuals of the linear fit to our data points is represented in Fig. 4.3(b).

In Fig. 4.4 we show $M_{HI}$ - $L_B$ as a function of the telescope (only Arecibo, Effelsberg, GBT, Nancay and Green Bank 91m, which corresponds to the majority of our data). No clear trend is seen as a function of the used radio-telescope.

The OLS($M_{HI}$ - $L_B$) for the HI sample (N = 837) and HI complete sample (N = 662) are represented in Fig. 4.5(a) and 4.5(b). In Tab. 4.2 we show the coefficients for the linear regressions considering: 1) only detections, 2) survival analysis and 3) the bisector fit.

The OLS($M_{HI}$ - $L_B$) are also represented as a function of morphology for the HI sample and HI complete sample in Fig. 4.6 and 4.7, respectively. See Tab. 4.3 and 4.4 for detailed information about the fits. We have consider the same bins in morphology used in HG84 in order to compare with them. The fits given by HG84 are also shown in the plots.

### 4.2.2 $M_{HI}$ - $a^2$

In Fig. 4.8 we show $M_{HI}$ - $a^2$ as a function of the telescope. We see that there is no visible trend, as for $L_B$. As for $M_{HI}$ - $L_B$, we present the OLS($M_{HI}$ $-$ $a^2$) for the HI sample and HI complete sample

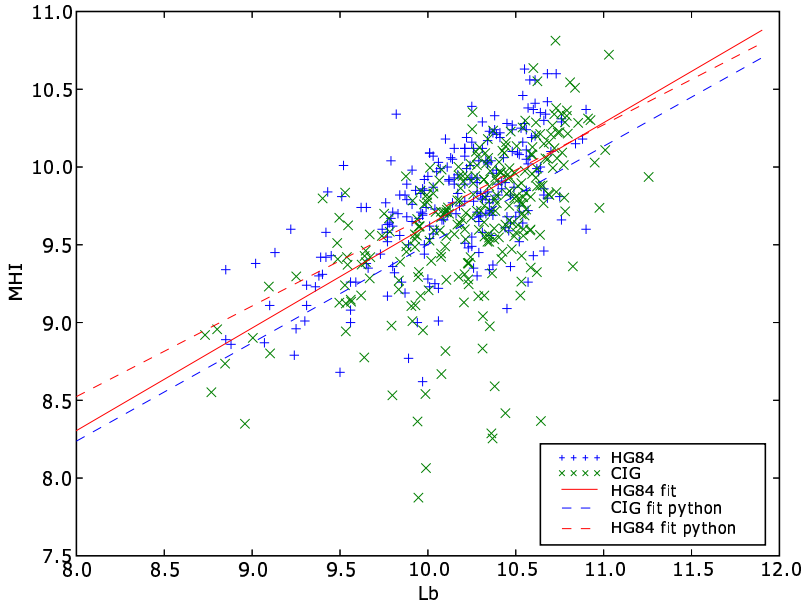


(a) $M_{HI}$ -$L_B$ HG84 vs AMIGA linear regressions.

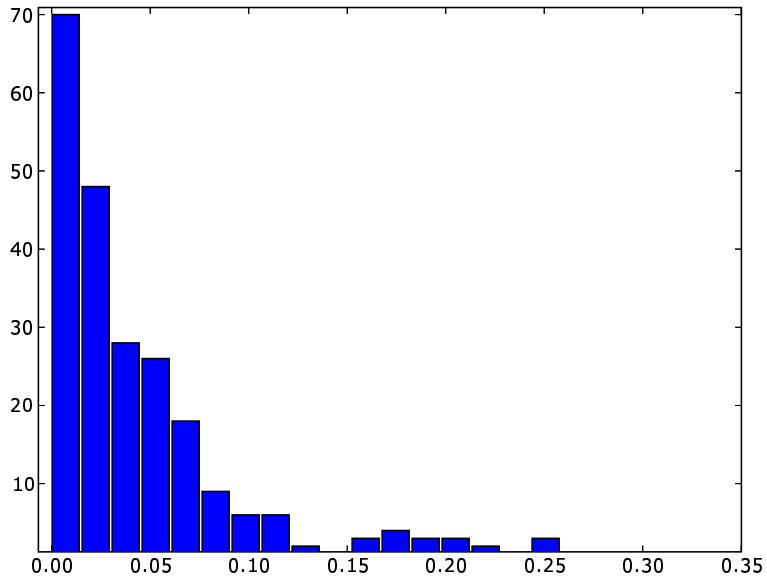

(b) Distribution of residuals (squared).

Figure 4.3: (a) $M_{HI}$ -$L_B$ comparison between our HI sample and the values given in HG84 (only detections are considered, N = 240). Blue crosses correspond to the dataset obtained by HG84, and green $x$ signs to our data points. Lines: 1) red line: fit given by HG84, 2) blue dashed line: fit to our revised HI data. (b) Distribution of residuals (squared) with respect to our linear regression.

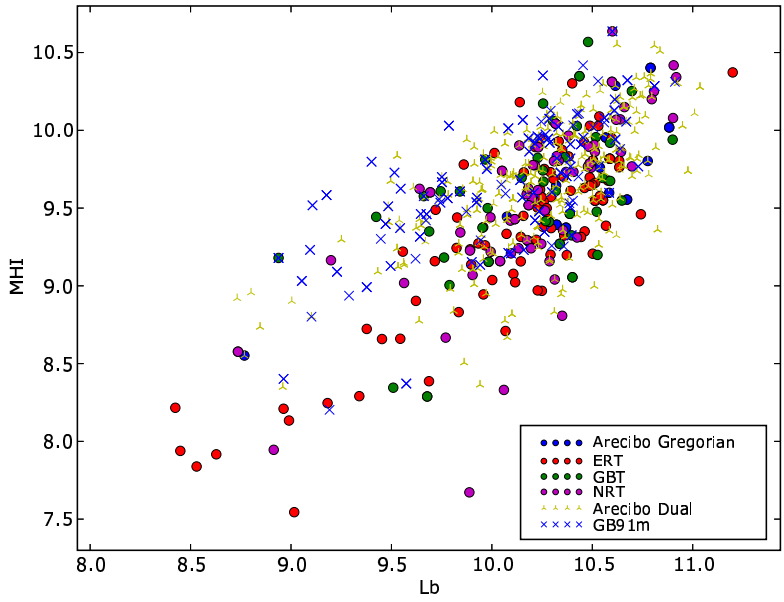


Figure 4.4: $M_{HI}$ - $L_B$, showing the procedence of the HI data.

Table 4.2: Correlations OLS($M_{HI}$ - $L_B$), with and without survival analysis, and bisector fit.

| Correlation | Intercept ($\pm$ $\sigma$) | Slope ($\pm$ $\sigma$) | N |
|---|---|---|---|
| **HI sample** | | | |
| $M_{HI}$ - $L_B$ (AMIGA fit, survival) | 1.9 $\pm$ 0.4 | 0.74 $\pm$ 0.03 | 837 |
| $M_{HI}$ - $L_B$ (AMIGA fit, only det) | 2.2 $\pm$ 0.4 | 0.73 $\pm$ 0.03 | 602 |
| $M_{HI}$ - $L_B$ (AMIGA fit, bisector, survival) | -2.5 | 1.18 | 837 |
| **HI complete sample** | | | |
| $M_{HI}$ - $L_B$ (AMIGA fit, survival) | 1.7 $\pm$ 0.5 | 0.76 $\pm$ 0.05 | 662 |
| $M_{HI}$ - $L_B$ (AMIGA fit, only det) | 2.1 $\pm$ 0.4 | 0.74 $\pm$ 0.04 | 494 |
| $M_{HI}$ - $L_B$ (AMIGA fit, bisector, survival) | -3.2 | 1.24 | 662 |
| **HG84** | | | |
| $M_{HI}$ - $L_B$ | 3.0 | 0.66 | 287 |

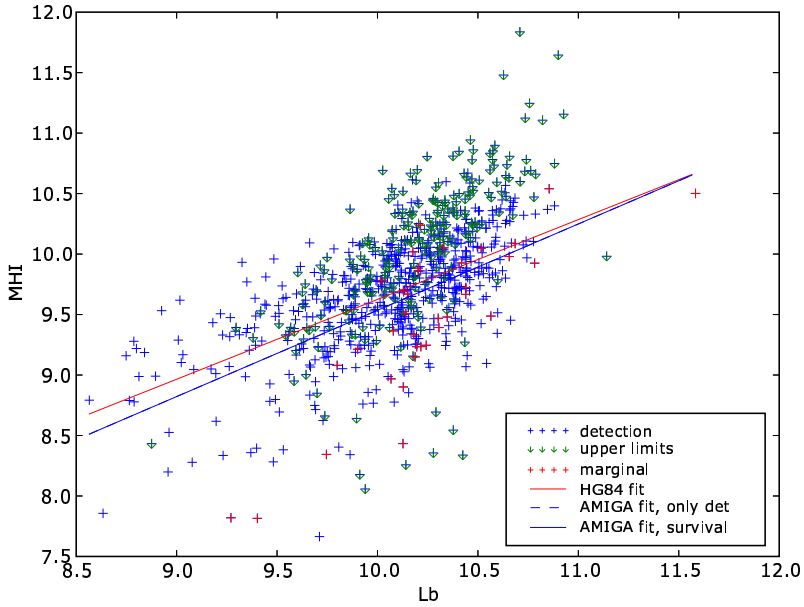


(a) OLS($M_{HI}$ - $L_B$) for the HI sample.

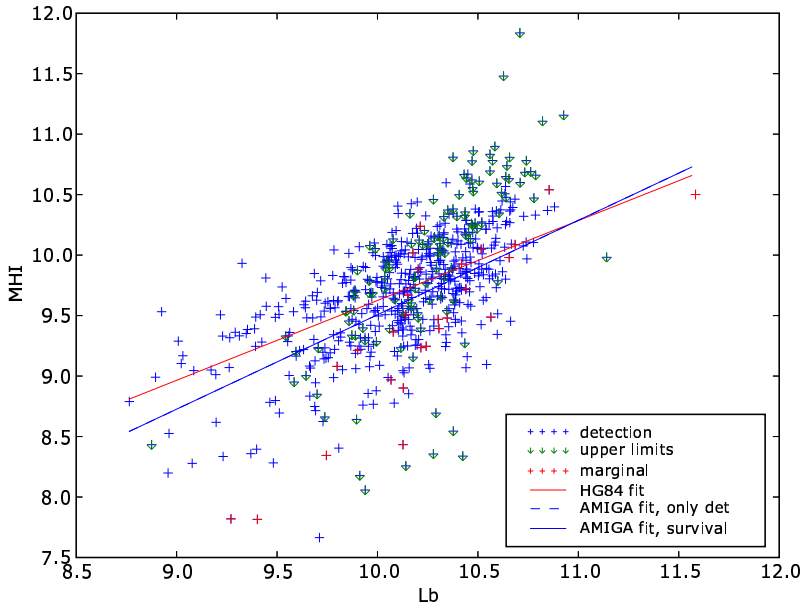


(b) OLS($M_{HI}$ - $L_B$) for the HI complete sample.

Figure 4.5: Fits OLS($M_{HI}$ - $L_B$) for the HI sample (N = 837) and HI complete subsample (N = 662). Blue crosses are detections, green arrows are upper limits and red crosses are marginal detections. Red line is the HG84 fit, blue dashed-line is the AMIGA fit considering only detections and blue line is the AMIGA fit using survival analysis.

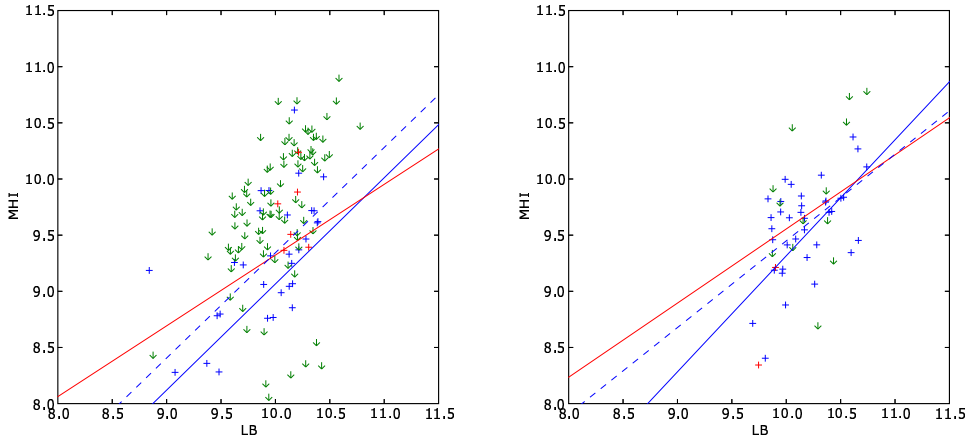


(a) T = (-5,-3,-2,0)




(b) T = (1,2)

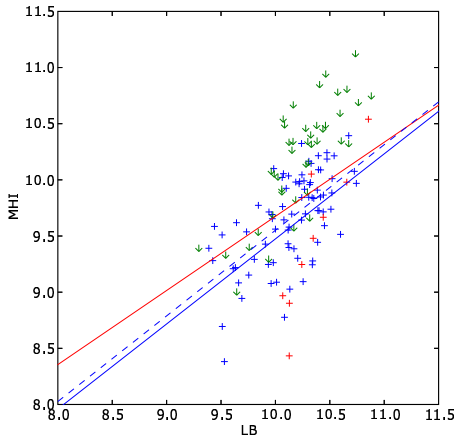


(c) T = 3

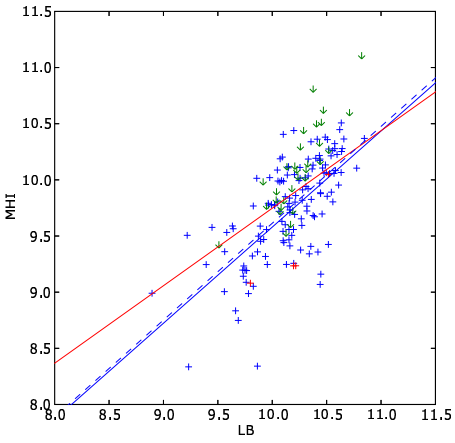


(d) T = 4

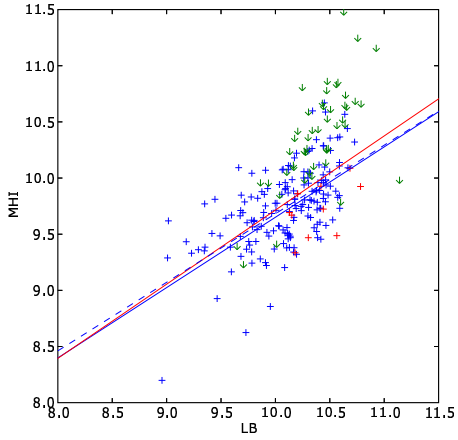


(e) T = 5

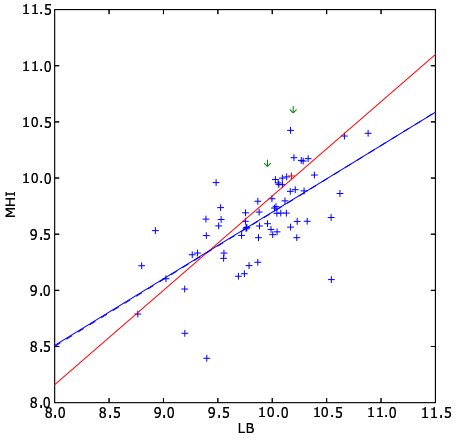


(f) T = (6,7)

Figure 4.6: OLS($M_{HI}$ - $L_B$) as a function of morphology for the HI sample (N = 873). Red line is the HG84 fit, blue dashed line is the AMIGA fit considering only detections and blue line is the AMIGA fit using survival analysis. T > 8 bin has not been included in this figure, but the coefficients of the fit are detailed in Tab. 4.3.

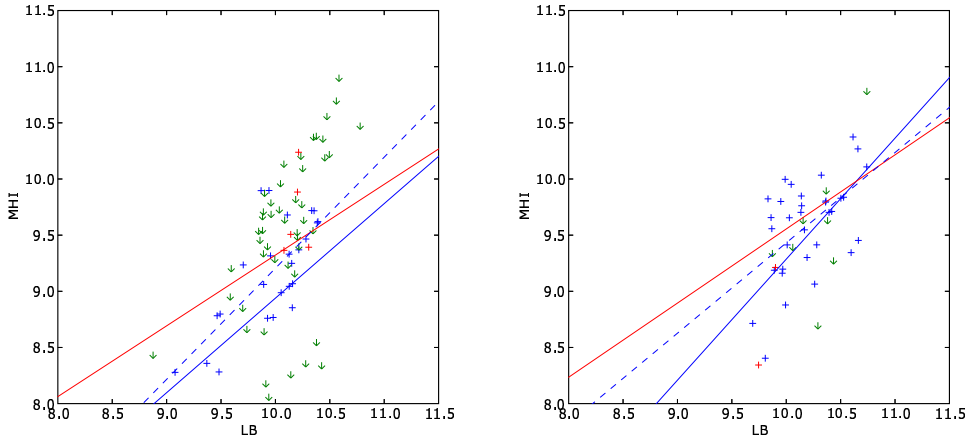


(a) T = (-5,-3,-2,0)

(b) T = (1,2)

(c) T = 3

(d) T = 4

(e) T = 5

(f) T = (6,7)

Figure 4.7: The same as in Fig. 4.6 but for the HI complete sample (N = 662).

Table 4.3: OLS($M_{HI}$ - $L_B$) and bisector fit as a function of the morphology for the HI sample (N = 873).

| Types | Correlation | Intercept ($\pm \sigma$) | Slope ($\pm \sigma$) | N |
|---|---|---|---|---|
| -5, -3, -2, 0 | AMIGA fit, survival | 0 ± 3 | 0.91 ± 0.25 | 130 |
| | AMIGA fit, only det | 1 ± 2 | 0.85 ± 0.19 | 32 |
| | HG84 fit | 3.02 | 0.63 ± | 14 |
| | AMIGA fit, bisector | -7.6 | 1.69 ± | 130 |
| 1, 2 | AMIGA fit, survival | -1 ± 2 | 1.04 ± 0.22 | 53 |
| | AMIGA fit, only det | 1 ± 2 | 0.76 ± 0.23 | 37 |
| | HG84 fit | 2.95 | 0.66 | 37 |
| | AMIGA fit, bisector | -7.1 | 1.61 | 53 |
| 3 | AMIGA fit, survival | 1.0 ± 0.9 | 0.82 ± 0.09 | 132 |
| | AMIGA fit, only det | 1.7 ± 1.1 | 0.76 ± 0.11 | 81 |
| | HG84 fit | 3.07 | 0.66 | 71 |
| | AMIGA fit, bisector | -3.9 | 1.32 | 132 |
| 4 | AMIGA fit, survival | 0.6 ± 0.8 | 0.87 ± 0.08 | 172 |
| | AMIGA fit, only det | 0.8 ± 0.8 | 0.86 ± 0.08 | 137 |
| | HG84 fit | 2.85 | 0.69 | 38 |
| | AMIGA fit, bisector | -3.3 | 1.27 | 172 |
| 5 | AMIGA fit, survival | 3.5 ± 0.7 | 0.59 ± 0.07 | 234 |
| | AMIGA fit, only det | 3.4 ± 0.8 | 0.60 ± 0.08 | 175 |
| | HG84 fit | 3.11 | 0.66 | 80 |
| | AMIGA fit, bisector | -1.3 | 1.08 | 234 |
| 6, 7 | AMIGA fit, survival | 3.7 ± 0.9 | 0.58 ± 0.09 | 69 |
| | AMIGA fit, only det | 3.5 ± 1.1 | 0.59 ± 0.11 | 66 |
| | HG84 fit | 1.44 | 0.84 | 38 |
| | AMIGA fit, bisector | 0.3 | 0.91 | 69 |
| 8, 9, 10, 998 | AMIGA fit, survival | 3.5 ± 0.6 | 0.59 ± 0.06 | 51 |
| | AMIGA fit, only det | 2.8 ± 0.6 | 0.67 ± 0.06 | 45 |
| | HG84 fit | 5.13 | 0.45 | 9 |
| | AMIGA fit, bisector | 1.8 | 0.77 | 51 |

Table 4.4: OLS($M_{HI}$ - $L_B$) and bisector fit as a function of the morphology for the HI complete sample (N=662).

| Types | Correlation | Intercept ($\pm \sigma$) | Slope ($\pm \sigma$) | N |
|---|---|---|---|---|
| -5, -3, -2, 0 | AMIGA fit, survival | -1.3 ± 3 | 1.01 ± 0.26 | 80 |
| | AMIGA fit, only det | -1.0 ± 1.4 | 1.00 ± 0.14 | 27 |
| | HG84 fit | 3.0 | 0.63 | 14 |
| | AMIGA fit, bisector | -8.5 | 1.75 | 80 |
| 1, 2 | AMIGA fit, survival | -2 ± 2 | 1.06 ± 0.21 | 47 |
| | AMIGA fit, only det | 1 ± 3 | 0.78 ± 0.25 | 36 |
| | HG84 fit | 2.95 | 0.66 | 37 |
| | AMIGA fit, bisector | -7.4 | 1.63 | 44 |
| 3 | AMIGA fit, survival | 1.4 ± 1.2 | 0.78 ± 0.11 | 110 |
| | AMIGA fit, only det | 2.0 ± 1.0 | 0.74 ± 0.10 | 83 |
| | HG84 fit | 3.07 | 0.66 | 71 |
| | AMIGA fit, bisector | -3.9 | 1.32 | 110 |
| 4 | AMIGA fit, survival | 1.2 ± 0.8 | 0.82 ± 0.07 | 151 |
| | AMIGA fit, only det | 1.4 ± 0.9 | 0.81 ± 0.09 | 124 |
| | HG84 fit | 2.84 | 0.69 | 38 |
| | AMIGA fit, bisector | -2.8 | 1.22 | 146 |
| 5 | AMIGA fit, survival | 2.8 ± 0.8 | 0.67 ± 0.08 | 177 |
| | AMIGA fit, only det | 2.7 ± 1.0 | 0.68 ± 0.09 | 140 |
| | HG84 fit | 3.11 | 0.66 | 80 |
| | AMIGA fit, bisector | -2.1 | 1.15 | 173 |
| 6, 7 | AMIGA fit, survival | 2.6 ± 1.2 | 0.69 ± 0.12 | 64 |
| | AMIGA fit, only det | 2.7 ± 1.1 | 0.68 ± 0.11 | 62 |
| | HG84 fit | 1.4 | 0.84 | 38 |
| | AMIGA fit, bisector | -0.4 | 0.99 | 58 |
| 8, 9, 10, 998 | AMIGA fit, survival | 3.4 ± 0.9 | 0.60 ± 0.09 | 30 |
| | AMIGA fit, only det | 2.9 ± 1.3 | 0.65 ± 0.13 | 27 |
| | HG84 fit | 5.12 | 0.45 | 9 |
| | AMIGA fit, bisector | 1.44 | 0.80 | 30 |

Table 4.5: Correlation OLS($M_{HI}$ - $a^2$), with and without survival analysis.

| Correlation | Intercept ($\pm$ $\sigma$) | Slope ($\pm$ $\sigma$) | N |
|---|---|---|---|
| **HI sample** | | | |
| $M_{HI}$ - a$^2$ (AMIGA fit, survival) | 7.34 $\pm$ 0.08 | 0.81 $\pm$ 0.03 | 837 |
| $M_{HI}$ - a$^2$ (AMIGA fit, only det) | 7.41 $\pm$ 0.07 | 0.80 $\pm$ 0.03 | 602 |
| $M_{HI}$ - a$^2$ (AMIGA fit, bisector, survival) | 6.55 | 1.10 | 837 |
| **HI complete sample** | | | |
| $M_{HI}$ - a$^2$ (AMIGA fit, survival) | 7.35 $\pm$ 0.1 | 0.80 $\pm$ 0.03 | 662 |
| $M_{HI}$ - a$^2$ (AMIGA fit, only det) | 7.42 $\pm$ 0.08 | 0.79 $\pm$ 0.03 | 494 |
| $M_{HI}$ - a$^2$ (AMIGA fit, bisector, survival) | 6.42 | 1.14 | 662 |
| **HG84** | | | |
| $M_{HI}$-a$^2$ | 7.12 | 0.88 | 287 |

in Fig. 4.9(a) and 4.9(b) (see Tab. 4.5). In Fig. 4.6 and 4.7 we show the OLS($M_{HI}$ - a$^2$) as a function of morphology for the HI sample and HI complete sample, respectively. The coefficients of the linear regressions sorting by morphology are detailed in Tab. 4.6 and 4.7 for the HI sample and HI complete sample.

## 4.3 $M_{HI}$ residuals

In order to study deficiencies in the HI as a function of the environment, Chamaraux et al. (1980) and HG84 defined the measure of HI content as the difference between the observed $M_{HI}$ of a given galaxy and the expected $M_{HI}$ as it were isolated. To predict the $M_{HI}$ of a given galaxy they consider the $L_B$ or $a^2$ information and use the $M_{HI}$ - $L_B$ or $M_{HI}$ - $a^2$ correlations for a reference sample of isolated objects. Then, the HI deficiency of a given galaxy can be calculated as follows:

$$Def = log(M_{HI\ pred}) - log(M_{HI\ obs}) \tag{4.1}$$

where $M_{HI\ obs}$ and $M_{HI\ pred}$ are the observed and predicted HI contents, respectively.

We can use this definition in order to characterize the typical standard deviation of the $M_{HI}$ residuals distribution for a well-defined sample of isolated galaxies. These residuals could be originated by errors in the calculation of distances, $M_{HI}$, $L_B$, morphological types, etc. Part of the contribution may be due to intrinsic scatter of both variables too.

For the HI complete sample the standard deviation of error is 0.33 with an average close to 0. In Fig. 4.12 we show the distribution of the residuals ($Def$) for the detected galaxies in the HI sample, taking into account the OLS(M$_{HI}$ - $L_B$) fits for the HI complete sample. In Tab. 4.8 we detail the residuals ($Def$) for our HI sample.

The distribution of $M_{HI}$ residuals for this sample of isolated galaxies can be compared later with samples of galaxies in denser environments in order to see whether they are out of this reference of normalcy. If so, then the galaxies in these denser environments would be classified as HI deficient.

## 4.4 Results and conclusions

The results of this Chapter can be summarised as follows. First we have calculated the $M_{HI}$ for our two samples (HI sample and HI complete sample) and obtained correlations between $M_{HI}$, $L_B$ and

Table 4.6: OLS($M_{HI}$ - $a^2$) and bisector fit as a function of the morphology for the HI sample (N = 837).

| Types | Correlation | Intercept ($\pm \sigma$) | ($\pm \sigma$) | N |
|---|---|---|---|---|
| -5, -3, -2, 0 | AMIGA fit, survival | 8.0 ± 0.3 | 0.63 ± 0.12 | 130 |
| | AMIGA fit, only det | 7.4 ± 0.2 | 0.77 ± 0.10 | 35 |
| | HG84 fit | 6.9 | 0.89 | 14 |
| | AMIGA fit, bisector | 6.4 | 1.3 | 130 |
| 1, 2 | AMIGA fit, survival | 7.4 ± 0.8 | 0.8 ± 0.3 | 53 |
| | AMIGA fit, only det | 7.0 ± 0.6 | 0.9 ± 0.2 | 39 |
| | HG84 fit | 7.2 | 0.82 | 37 |
| | AMIGA fit, bisector | 5.8 | 1.4 | 53 |
| 3 | AMIGA fit, survival | 8.1 ± 0.3 | 0.61 ± 0.09 | 138 |
| | AMIGA fit, only det | 7.8 ± 0.3 | 0.67 ± 0.09 | 91 |
| | HG84 fit | 7.3 | 0.83 | 71 |
| | AMIGA fit, bisector | 6.6 | 1.1 | 138 |
| 4 | AMIGA fit, survival | 7.6 ± 0.2 | 0.78 ± 0.07 | 173 |
| | AMIGA fit, only det | 7.45 ± 0.17 | 0.80 ± 0.06 | 141 |
| | HG84 fit | 7.3 | 0.85 | 38 |
| | AMIGA fit, bisector | 6.63 | 1.1 | 173 |
| 5 | AMIGA fit, survival | 7.4 ± 0.2 | 0.85 ± 0.08 | 232 |
| | AMIGA fit, only det | 7.4 ± 0.2 | 0.84 ± 0.07 | 176 |
| | HG84 fit | 6.9 | 0.95 | 80 |
| | AMIGA fit, bisector | 6.18 | 1.3 | 232 |
| 6, 7 | AMIGA fit, survival | 7.6 ± 0.3 | 0.74 ± 0.10 | 74 |
| | AMIGA fit, only det | 7.4 ± 0.2 | 0.80 ± 0.08 | 72 |
| | HG84 fit | 7.0 | 0.94 | 38 |
| | AMIGA fit, bisector | 6.9 | 1.0 | 74 |
| 8, 9, 10, 998 | AMIGA fit, survival | 7.5 ± 0.2 | 0.78 ± 0.09 | 37 |
| | AMIGA fit, only det | 7.3 ± .14 | 0.86 ± 0.06 | 34 |
| | HG84 fit | 7.8 | 0.66 | 9 |
| | AMIGA fit, bisector | 7.3 | 0.86 | 37 |

Table 4.7: Same as Tab. 4.6 but for the HI complete sample (N = 662).

| Types | Correlation | Intercept ($\pm \sigma$) | Slope ($\pm \sigma$) | N |
|---|---|---|---|---|
| -5, -3, -2, 0 | AMIGA fit, survival | 7.8 ± 0.3 | 0.59 ± 0.13 | 80 |
| | AMIGA fit, only det | 7.4 ± 0.4 | 0.71 ± 0.15 | 27 |
| | HG84 fit | 6.9 | 0.89 | 14 |
| | AMIGA fit, bisector | 6.2 | 1.23 | 80 |
| 1, 2 | AMIGA fit, survival | 7.2 ± 0.9 | 0.8 ± 0.3 | 47 |
| | AMIGA fit, only det | 7.0 ± 0.5 | 0.90 ± 0.18 | 36 |
| | HG84 fit | 7.2 | 0.82 | 37 |
| | AMIGA fit, bisector | 5.8 | 1.35 | 47 |
| 3 | AMIGA fit, survival | 8.1 ± 0.3 | 0.58 ± 0.09 | 110 |
| | AMIGA fit, only det | 7.8 ± 0.2 | 0.65 ± 0.09 | 83 |
| | HG84 fit | 7.3 | 0.83 | 71 |
| | AMIGA fit, bisector | 6.8 | 1.0 | 110 |
| 4 | AMIGA fit, survival | 7.5 ± 0.2 | 0.81 ± 0.08 | 151 |
| | AMIGA fit, only det | 7.40 ± 0.16 | 0.81 ± 0.05 | 126 |
| | HG84 fit | 7.3 | 0.85 | 38 |
| | AMIGA fit, bisector | 6.50 | 1.14 | 151 |
| 5 | AMIGA fit, survival | 7.4 ± 0.2 | 0.86 ± 0.08 | 177 |
| | AMIGA fit, only det | 7.3 ± 0.3 | 0.85 ± 0.09 | 139 |
| | HG84 fit | 6.9 | 0.95 | 80 |
| | AMIGA fit, bisector | 6.25 | 1.26 | 177 |
| 6, 7 | AMIGA fit, survival | 7.5 ± 0.3 | 0.76 ± 0.10 | 64 |
| | AMIGA fit, only det | 7.3 ± 0.2 | 0.83 ± 0.08 | 62 |
| | HG84 fit | 7.0 | 0.94 | 38 |
| | AMIGA fit, bisector | 6.9 | 1.01 | 64 |
| 8, 9, 10, 998 | AMIGA fit, survival | 7.56 ± 0.18 | 0.78± 0.07 | 23 |
| | AMIGA fit, only det | 7.64 ± 0.18 | 0.73± 0.07 | 21 |
| | HG84 fit | 7.8 | 0.66 | 9 |
| | AMIGA fit, bisector | 7.3 | 0.88 | 23 |

Table 4.8: List of observed and predicted $M_{HI}$ for the HI sample [1].

| CIG | $\log(M_{HI\ obs})$ | $\log(M_{HI\ pred})$ | Def |
|---|---|---|---|
| 1 | 10.06 | 9.82 | -0.24 |
| 4 | 9.54 | 9.66 | 0.11 |
| 5 | 9.17 | 9.73 | 0.55 |
| 6 | 9.31 | 9.43 | 0.12 |
| 8 | 9.80 | 9.78 | -0.02 |
| 9 | 10.15 | 9.68 | -0.47 |
| 10 | 9.24 | 9.31 | 0.07 |
| 11 | 9.89 | 9.37 | -0.52 |
| 12 | 9.55 | 9.35 | -0.20 |
| ... | | | ... |

[1] The full table can be downloaded from http://www.iaa.es/AMIGA.html.

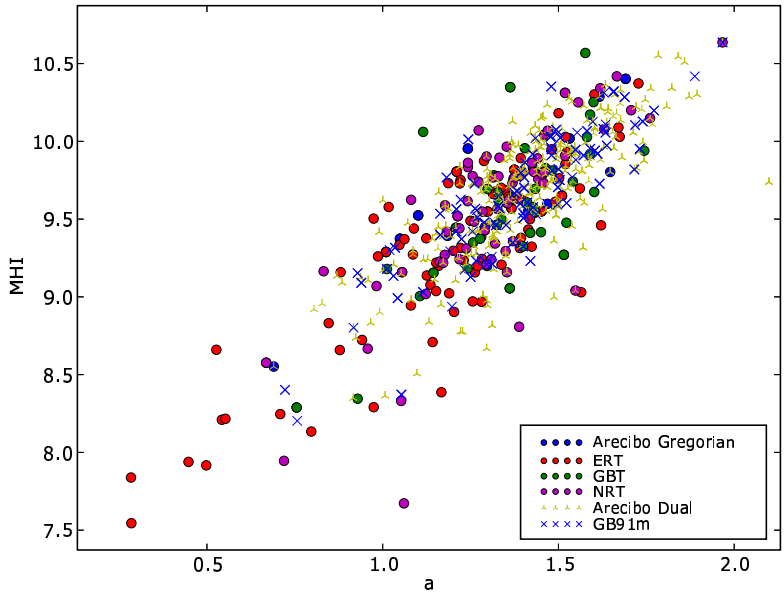


Figure 4.8: Fit $M_{HI}$ - $a^2$, showing the procedence of the HI data.

$a^2$, as a function of the morphology. It is remarkable to note that:

- We find a number of improvements with respect to the HG84 fits. Our fits obviously consider a larger number of points and in a larger range in $L_B$ and $M_{HI}$ than HG84 ones and then the fits are more significant from a statistical point of view. In addition we have revised $M_{HI}$, $L_B$, $a^2$ and our morphologies in order to be as accurate as possible. The agreement between the fits in HG84 and ours for both the HI sample and the HI complete sample are reasonably good.

- There is a slight difference between the HG84 $M_{HI}$ - $L_B$ fits and ours, in the sense that our fits are below the HG84 ones. This is true in general not only when we consider the HI sample or the HI complete sample as a whole, but also when we sort by morphological types. This is mainly due to our smaller corrections to $S$ with respect to HG84.

- It is apparent that $M_{HI}$ - $L_B$ presents a larger dispersion than $M_{HI}$ - $a^2$.

- When sorting by morphological type, $M_{HI}$ - $L_B$ fits in HG84 and ours show some differences whereas $M_{HI}$ - $a^2$ ones are almost identical, even considering survival analysis.From Tab. 4.3 and 4.4 we can see that the slope systematically decreases for later types. This dependence on the morphology is not seen in the HG84 fits.

- The fits for early type galaxies (T = -5,-3,-2,0) are not accurate ($M_{HI}$ vs $L_B$ or $a^2$) since this bin is not very populated (early type galaxies are difficult to detect in HI). However, the fits seem more accurate than before since we have better sampled this morphological bin with respect to HG84.

- The linear regression fits for both the HI sample and the HI complete sample show the same trends, but the latter is recommended since it is more complete and therefore possible biases are minimized.

We have also calculated the $M_{HI}$ residuals for the galaxies in the HI sample, using the fits $M_{HI}$ vs $L_B$ for the HI complete sample. We have obtained a value of 0.33 for the standard deviation of the error, which is similar to the value given by HG84.

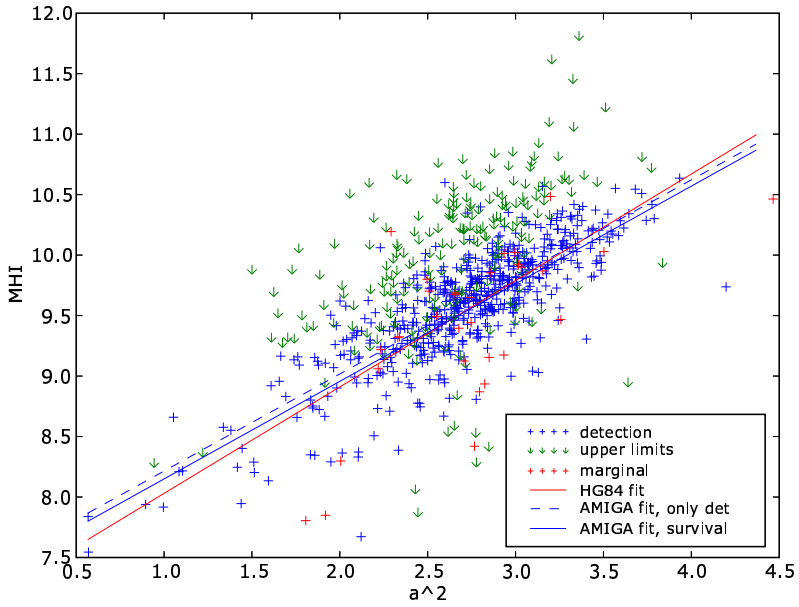


(a) OLS($M_{HI}$ - $a^2$) for the HI sample.

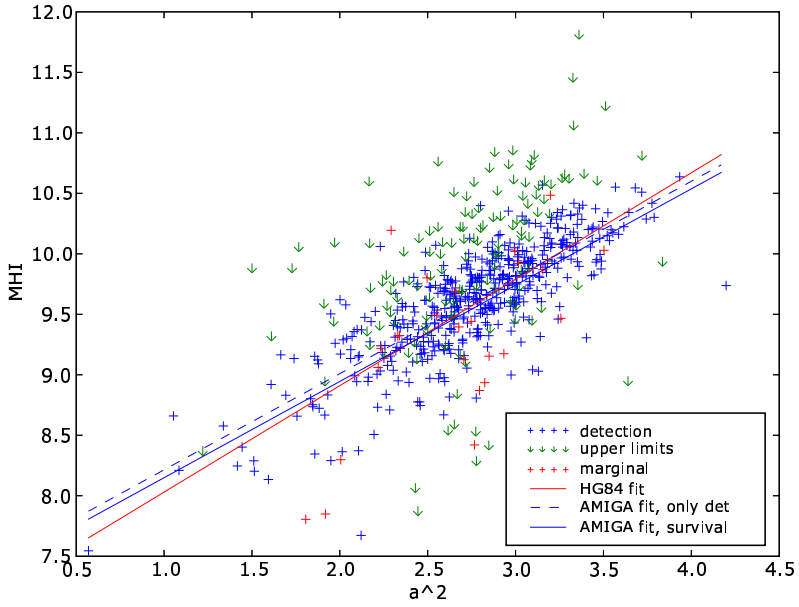


(b) OLS($M_{HI}$ - $a^2$ ) for the HI complete sample.

Figure 4.9: Fits OLS($M_{HI}$ - a$^2$) for the HI sample (N = 873) and HI complete subsample (N = 662). Blue crosses are detections, green arrows are upper limits and red crosses are marginal detections. Red line is the HG84 fit, blue dashed line is the AMIGA fit considering only detections and blue line is the AMIGA fit using survival analysis.

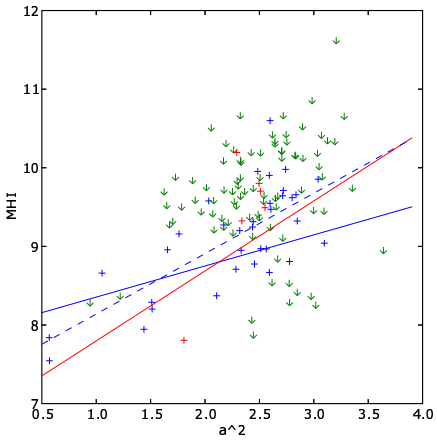


(a) T = (-5,-3,-2,0)

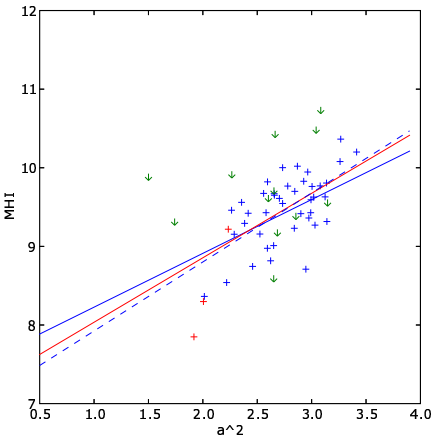


(b) T = (1,2)

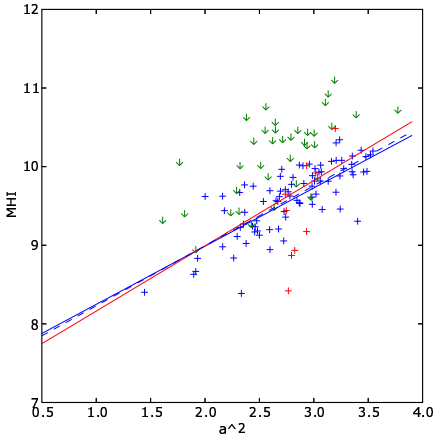


(c) T = 3

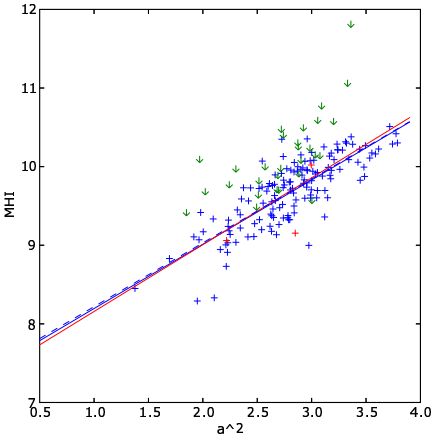


(d) T = 4

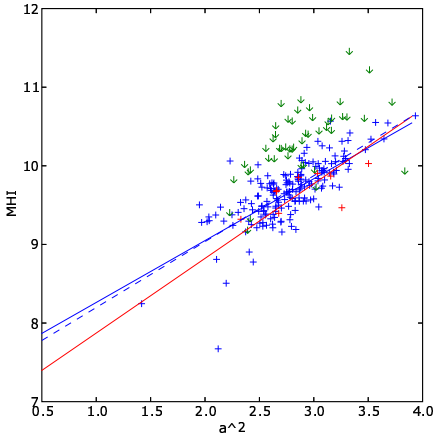


(e) T = 5

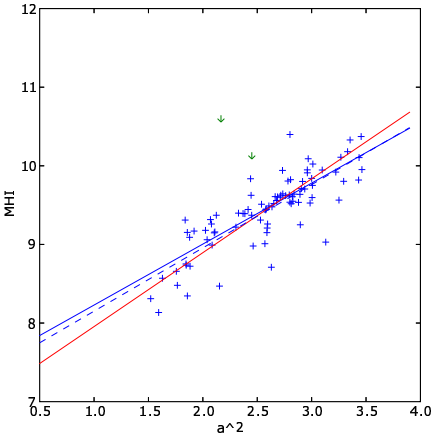


(f) T = (6,7)

Figure 4.10: $M_{HI}$ - $a^2$ for the HI sample (N = 873) as a function of morphology. Red line is the HG84 fit, blue dashed-line is the AMIGA fit considering only detections and blue line is the AMIGA fit using survival analysis. T > 8 bin have not been included in this figure, but the coefficients are detailed in Tab. 4.6.

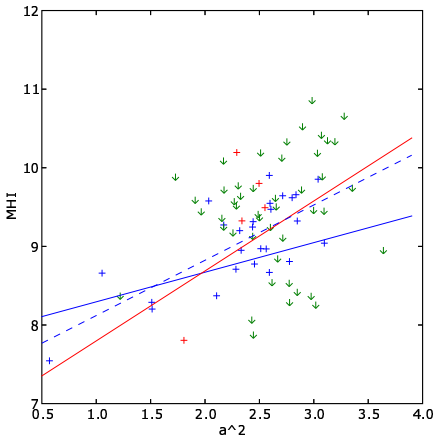


(a) T = (-5,-3,-2,0)

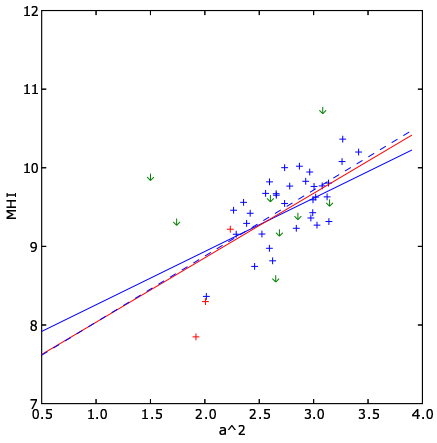


(b) T = (1,2)

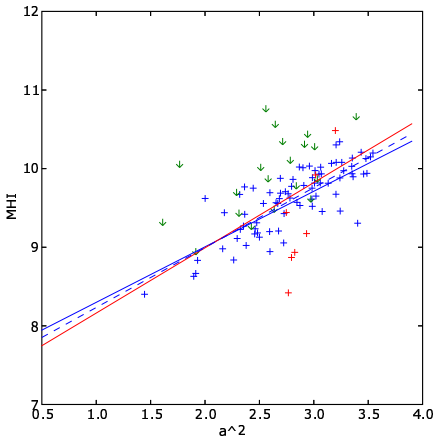


(c) T = 3

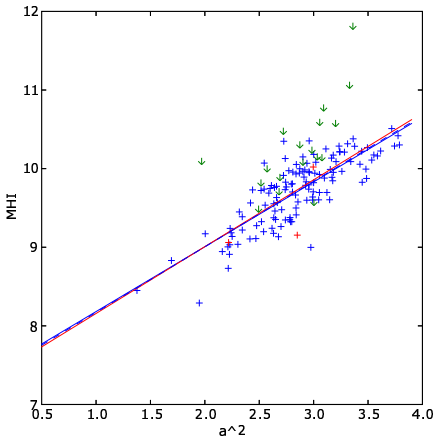


(d) T = 4

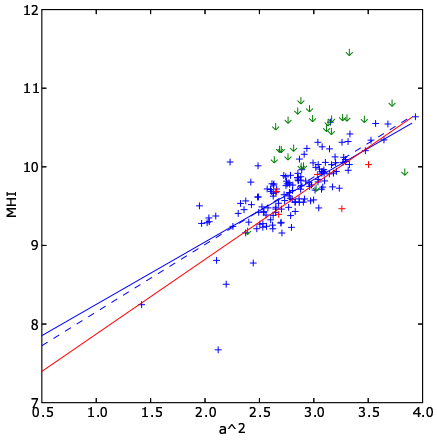


(e) T = 5

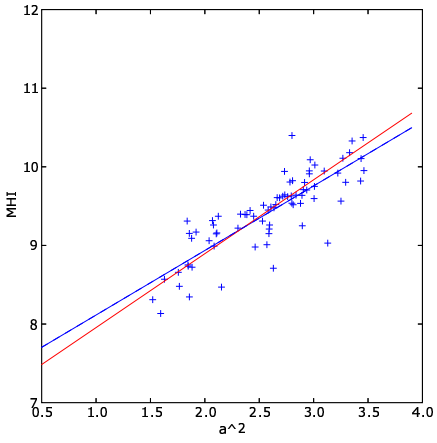


(f) T = (6,7)

Figure 4.11: The same as in Fig. 4.10 but for the HI complete sample (N = 662).

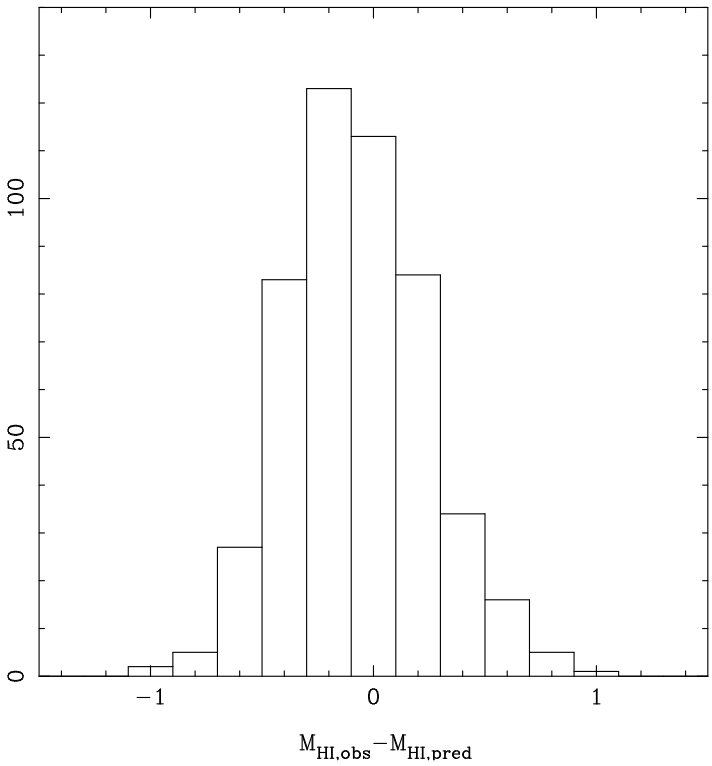


Figure 4.12: $M_{HI}$ residuals for the HI sample.

# Chapter 5

# Lopsidedness in the HI profiles of isolated galaxies

In this Chapter we study the rate of lopsided HI profiles in our sample of isolated galaxies. In order to do so we have inspected all of our HI profiles for all the galaxies and selected 338 of them which presented no problems due to baseline irregularities or interferences and with good S/N ratio. In order to clean this sample for beam attenuation and pointing offsets we use the factor $f$ calculated in Chapter 3. With this factor we derive the expected flux ratio asymmetry coefficient, which is compared to the observed one. Considering those profiles whose flux ratio asymmetry coefficient is not likely to be artificial, we study the percentage rate of asymmetric profiles with respect to other studies found in the literature for galaxies in different environments. We find that the percentage rate of symmetric profiles in our sample is the highest, with 80% of the HI profiles flux ratios lower than 15%. Other samples including galaxies in denser environments find about 50% with the same criterion. Possible origins of the lopsided HI profiles in galaxies of our sample are discussed.

## 5.1 Introduction

The HI is the most extended component of the ISM and therefore the most sensible to interactions. HI profiles can be a very useful tool to study the lopsidedness of gaseous disks, since they contain information about both the HI kinematics and distribution. Using these data, lopsidedness in the HI is found to be very frequent, but up to date there is no general accepted answer about its origin and what is the typical time for the galaxy to become symmetric afterwards.

Asymmetries in the stellar component, traced by optical or near infrared images, are not necessarily correlated with lopsidedness in the HI distribution or velocity field (Kornreich et al. 2000; Wilcots & Prescott 2004). Several studies over the last decade state that the asymmetry in the HI component is not highly dependent on the environment: those works based on small samples of isolated galaxies (N = 104 Haynes et al. 1998; N = 30 Matthews et al. 1998) suggest that 50% of them have asymmetric profiles, whereas other samples of galaxies in different environments (e.g. Swaters et al. 2002a; Richter & Sancisi 1994; Sulentic & Arp 1983) give rates of 50 to 75 % of asymmetric profiles. However, the high percentage rate of lopsided profiles can be a result of the use of galaxies in the field, which lacks of a restrictive isolation criteria. Whether the asymmetries in really isolated galaxies are due to irregularities in the HI velocity field or HI distribution has not been studied in detail up to date either. Moreover, it seems that there is no statistical difference between the degree of asymmetry in the profiles of those galaxies with companions as compared with those galaxies without (e.g. Wilcots & Prescott 2004). On the other hand, it seems that the origin of the lopsidedness may be linked to the morphology of a galaxy, in the sense that asymmetries in late-type galaxies are more frequent (Bournaud et al. 2005, studying NIR images).

The study of a well-defined sample of isolated galaxies is especially relevant since major interactions are minimized over secular evolution, but samples of galaxies in low density regions studied up to date

are not large enough and their isolation does not usually follow any precise criteria. Thus, the origin of the high percentage of lopsidedness found in really isolated galaxies is still an open question. A well-defined sample of isolated galaxies is still needed in order to characterise the degree of symmetry in their HI.

Our sample of isolated galaxies provides a suitable approach in order to shed light over this issue since Karachentseva's criteria assure us that no major interaction has occured approximately in the last 1-2 Gyr. This period of time would be enough for the lopsidedness in the HI to weaken in the absence of interaction (e.g. simulations by Bournaud et al. 2005). In this chapter we present a study of the symmetry of the AMIGA HI profiles with a special emphasis in those with the best S/N ratio, in order to try to understand: 1) the frequency of lopsideness as a function of environmental density, 2) the dependence of asymmetries in the profiles with the morphological type (including bars), and finally 3) the origin of lopsidedness in isolated galaxies.

## 5.2 Introduction to lopsidedness in HI profiles

In many cases a lopsidedness in a given profile can be explained by pointing offsets or inclusion of unidentified companions located within the telescope beam. If this is not the case, then the shape of the global HI profile is only due to the HI distribution and velocity field, although it cannot uniquely determine them. The shape is primarily determined by the kinematics within the galaxy and only secondarily by the HI distribution (Haynes et al. 1998), as we will see in the next chapter for the sample observed at the VLA.

The possible origin of these asymmetries in the HI are usually explained in the literature by the following mechanisms (or combinations of them):

1) **Sustained long-lived lopsidedness due to non-circular motions**: if the lopsided pattern is associated to elliptical orbits, the survival time of the asymmetries increases to typically one or two rotation periods, or 1-2 Gyr (Baldwin et al. 1980). However, from a theoretical point of view these asymmetries are not long-lived enough to produce such a high percentage of lopsided profiles seen in galaxies.

2) **Halo - disk misalignment**: Levine & Sparke (1998) and Noordermeer, Sparke & Levine (2001) have produced models of a rotating disk not centered in a dominant axisymmetric halo and that yields to an off-centered disk over a long period of time. The asymmetry is more pronounced for counter-rotating disks with respect to the halo.

3) **Minor mergers**: based on N-body simulations, Walker et al. (1996) and Zaritsky & Rix (1997) proposed that minor mergers could produce lopsided distributions. However, Zaritsky & Rix (1997) and Rix & Zaritsky (1995) found that very few of the lopsided galaxies in their sample had obvious companions. This kind of asymmetries would have a quite short-life too, of $\sim$ 1 Gyr, and a large accretion rate of 0.07 - 0.25 $Gyr^{-1}$ for a companion of 10% the mass of the main galaxy. Pisano et al. (2002) and Wilcots & Prescott (2004) do not find a strong correlation between lopsidedness and the presence of companions.

4) **Cosmological gas accretion**: accretion of large gas clouds have been reported, for example, by Haynes, Giovanelli & Buskhead (1978), and Schlman, Bregman & Roberts (1994). Bournaud et al. (2005) and Combes (2006) suggest that cosmological gas may be accreted with intermittence, and this could be in part responsible for the high percentage of lopsidedness. Additionally they claim that cosmological gas accretion in galaxies is needed in order to maintain: a) the star formation rate (SFR): in principle galaxies would run out of atomic gas, but SFR is seen to be constant over the Hubble time (e.g. Kenicutt et al. 1983), and b) bars: it is a gravitational instability driving gas toward the center which seems to be self-destroyed when a large amount of gas is concentrated, and therefore a constant rate of gas accretion is needed in order to replenish the spiral disks.

4) **Distant tidal encounters**: Strong kinematic peculiarities can be generated by means of gravitational perturbations. However, although the resulting disk reproduces many of the kinematical features observed in HI synthesis maps, the effects are relatively short-lived, lasting only on the order of a dynamical timescale (e.g. Kornreich et al. 2002).

## 5.3 Quantifying lopsidedness: visual inspection and asymmetry coefficients

In this section we present two ways of quantifying lopsidedness: first with several criteria by visual inspection and second by numerical calculation of several lopsidedness parameters.

### 5.3.1 Visual inspection

Richter & Sancisi 1994 studied the possible lopsidedness of a given profile in a qualitative way by visual inspection. The criteria that they followed are the following: a) significant peak flux differences between the receding and approaching horns ($> 8\ \sigma$, or $> 20$ %) b) total flux differences between the approaching and receding halves of the HI profile with respect to the mean ($> 55 : 45$ %), and c) width differences ($> 50$ km s$^{-1}$).

This kind of classification is visually estimated and therefore it can be somewhat subjective. For this reason we have also quantified several asymmetry parameters that are presented below. A comparison between both visual and numerical criteria for our sample is performed in § **??**.

However, in order to make quantitative studies (e.g. Tifft & Huchtmeier 1990) a measurement that represents the asymmetry of the profile is required.

### 5.3.2 Numerical lopsidedness parameters

The main set of measurements found in the literature are the following:

1) **Integrated flux density ratios**: It is usually calculated as a ratio of the areas under the profile at velocities lower and higher than a characteristic velocity, $v_m$ (or $v_{med}$):

$$A_{l/h} = \frac{A_l}{A_h} = \frac{\int_{v_l}^{v_m} S_v dv}{\int_{v_m}^{v_h} S_v dv}$$

A characteristic lopsidedness measurement (Haynes et al. 1998, Kornreich et al. 2001) is:

$$A_{flux\ ratio} = \begin{cases} A_{l/h} & \text{, if } \mathrm{A}_{l/h} > 1, \\ 1/A_{l/h} & \text{, otherwise.} \end{cases}$$

Other alternative quantity is defined as (Matthews et al. 1998):

$$A = \frac{A_l - A_h}{A_l + A_h}$$

2) **Velocity differences**: Comparisons between different measurements of the velocity are considered: $\mathrm{v}_m$, the mean velocity of the profile at a certain level (usually 20%); $\mathrm{v}_{med}$, the median velocity of the distribution; and $\mathrm{v}_{wt}$, the flux density-weighted mean velocity. $\mathrm{v}_{med}$ and $\mathrm{v}_{wt}$ are less sensitive to extreme scores than $\mathrm{v}_m$ and this makes them a better measure than the mean for highly skewed distributions. The mean is higher than the median in positively skewed distributions and lower than the median in negatively skewed distributions.

The following asymmetry index are defined in Tifft & Cocke (1988):

$$A^v = \begin{cases} A^v_{l/h} & \text{, if } \mathrm{v}_{med} < \mathrm{v}_m, \\ -1/A^v_{l/h} & \text{, otherwise.} \end{cases}$$

where $A^v_{l/h}$ is:

$$A^v_{l/h} = -\frac{(v_{med} - v_l)}{(v_h - v_{med})}$$

where $\mathrm{v}_l$ and $\mathrm{v}_h$ are the low and high velocity limit of the profile. Widths differences are also considered. For example, in Zasov & Sulentic (1994) they quantify the asymmetry of the profile using the difference between $\mathrm{W}_{20}$ and $\mathrm{W}_{50}$:

$$\Delta W = W_{20} - W_{50}$$

3) **Height asymmetry index**: ratio of the peak flux of the weakest to the peak flux of the strongest profile horn (Matthews et al. 1998):

$$P = \frac{P_{low}}{P_{high}}$$

In order to quantify the HI lopsidedness rate in our sample of isolated galaxies we use two approaches: visual inspection and the $\mathrm{A}_{flux\ ratio}$. We also choose the $\mathrm{A}_{flux\ ratio}$ asymmetry coefficient because it is the most used quantity in the literature. Using this coefficient will allow us to compare with other samples of galaxies.

## 5.4 Relationship between $\mathbf{A}_{flux\ ratio}$ and flux loss (f)

We can use the quantification of the flux loss due to bad pointing and/or beam attenuation performed in Chapter 3, $f$, in order to flag those HI profiles that are likely to have an artificial lopsidedness in the profile. We assume that the flux loss is only located in one side of the profile. We call the integrated density flux loss $\mathrm{S}_{loss}$ and the integrated density flux to the left side and right side $\mathrm{S}_{l,real}$ and $\mathrm{S}_{h,real}$. We assume that the loss is located in the leften side, and then $\mathrm{S}_{l,real}$=$\mathrm{S}_{l,obs}$+$\mathrm{S}_{loss}$, $\mathrm{S}_{h,real}$=$\mathrm{S}_{h,obs}$, $\mathrm{S}_{real}$=$\mathrm{S}_{h,real}$+$\mathrm{S}_{l,real}$). The flux loss coefficient can be written as:

$$f = \frac{S_{real}}{S_{obs}} = \frac{S_{real}}{S_{real} - S_{loss}} = \frac{S_{real}}{S_{real} - S_{loss}} = \frac{1}{1 - 1/2 \times S_{loss}/S_{l,real}}$$

The maximum flux ratio asymmetry coefficient can be expressed as:

$$A^{expected}_{flux\ ratio} = \frac{S_{h,real}}{S_{l,real} - S_{loss}} = \frac{1}{1 - S_{loss}/S_{l,real}}$$

and then $f$ can be written as a function of $\mathrm{A}_{flux\ ratio}$:

$$f = \frac{2A^{expected}_{flux\ ratio}}{A^{expected}_{flux\ ratio} + 1}$$

or:

$$A^{expected}_{flux\ ratio} = \frac{1}{2/f - 1}$$

This equation is used later in order to minimise the effect of beam attenuation and/or bad pointing.

## 5.5 Statistical analysis of lopsidedness for the AMIGA sample

### 5.5.1 Visual inspection of the lopsidedness

We have visually revised the shape of the HI profiles that did not showed any confusion by noise and do not have peculiar features such as baseline problems, interferences, bad S/N ratio, etc. We classified the profiles in symmetric, slightly asymmetric, and asymmetric, according to the same classification criteria used by Richter & Sancisi (1996).

In total we have classified the HI profiles for N = 337 galaxies: 95 very symmetric (28%), 138 slightly asymmetric (41%) and 104 asymmetric (31%). We see from this inspection that two thirds of the profiles are symmetric or nearly symmetric (70 %). They are detailed as follows:

- very symmetric (N = 95) : CIG 8, 10, 23, 30, 49, 50, 53, 59, 60, 63, 66, 67, 90, 94, 102, 103, 107, 131, 135, 137, 138, 143, 148, 149, 151, 154, 159, 165, 183, 188, 192, 200, 208, 213, 224, 231, 232, 238, 240, 242, 250, 260, 266, 280, 299, 325, 335, 339, 340, 367, 376, 390, 397, 409, 427, 439, 454, 463, 474, 527, 564, 568, 598, 601, 604, 613, 616, 653, 655, 668, 695, 723, 728, 736, 741, 772, 808, 828, 838, 866, 870, 890, 906, 909, 910, 914, 916, 919, 951, 953, 970, 972, 974, 1021, 1048.

- slightly asymmetric (N = 138): CIG 9, 12, 18, 28, 31, 32, 38, 39, 42, 54, 58, 62, 64, 77, 119, 125, 126, 132, 133, 139, 146, 147, 155, 166, 167, 168, 170, 171, 172, 176, 178, 181, 194, 201, 204, 217, 218, 222, 227, 230, 236, 247, 267, 268, 279, 281, 286, 288, 290, 312, 319, 326, 336, 338, 344, 366, 382, 407, 433, 494, 497, 505, 507, 532, 538, 545, 562, 566, 579, 600, 603, 611, 612, 622, 626, 630, 633, 634, 643, 645, 651, 661, 672, 680, 689, 700, 702, 706, 711, 712, 739, 750, 757, 767, 773, 778, 785, 800, 810, 817, 818, 840, 848, 852, 854, 858, 859, 875, 876, 880, 892, 895, 902, 904, 913, 915, 917, 921, 925, 927, 928, 941, 960, 963, 969, 979, 980, 983, 990, 1004, 1012, 1018, 1023, 1028, 1029, 1036, 1039, 1046.

- asymmetric (N = 104): CIG 4, 11, 29, 33, 34, 40, 41, 69, 71, 75, 80, 82, 84, 85, 86, 88, 91, 95, 96, 115, 122, 123, 130, 134, 144, 152, 164, 169, 182, 191, 198, 199, 234, 246, 291, 293, 296, 298, 317, 333, 361, 362, 416, 421, 423, 457, 484, 502, 509, 511, 512, 551, 555, 561, 569, 573, 575, 581, 615, 625, 631, 638, 652, 654, 660, 692, 694, 716, 724, 743, 744, 756, 793, 805, 812, 830, 844, 847, 861, 879, 881, 884, 884, 897, 897, 901, 912, 931, 932, 933, 934, 937, 938, 959, 976, 982, 1005, 1015, 1019, 1025, 1027, 1038, 1047, 1051.

Note that along this chapter we will consider this sample of galaxies for the characterisation of the HI profile lopsidedness. In order to illustrate the visual classification we show some examples of symmetric and asymmetric HI profiles in Fig. 5.1.

## 5.6 Quantifying lopsidedness

In Tab. 5.1 we show the different calculated asymmetry parameters ($A_{flux\ ratio}$, $A_{skewness}$ and $A_{v_m - v_{med}}$) as well as the used radio-telescope (Tel.), S/N ratio and the evaluation of the visual classification (Visual class., S = symmetric, SA = slightly asymmetric and A = asymmetric). We also show the calculated $A^{expected}_{flux\ ratio}$ coefficient, as explained in § 5.4.

### 5.6.1 Are asymmetric profiles due to beam attenuation or bad pointing?

In Fig. 5.2(a) we show the $A^{expected}_{flux\ ratio}$ versus $A_{flux\ ratio}$ for all the visually selected HI profiles. Except two cases, all the HI profiles have $A_{flux\ ratio} > A^{expected}_{flux\ ratio}$ , but we clearly see that we are including cases where $A^{expected}_{flux\ ratio}$ is large. Moreover, there is some concentration of the data points close to the line $A_{flux\ ratio} = A^{expected}_{flux\ ratio}$, which may indicate that the real value of $A_{flux\ ratio}$ is being affected.

In order to avoid this bias, we have chosen HI profiles with $A^{expected}_{flux\ ratio} < 1.05$. When this consideration is taken into account we see that the number of symmetric profiles increases, as is shown in

Table 5.1: Lopsidedness coefficients, f and $A_{flux\ ratio}^{expected}$ for the HI profiles of the galaxies in the AMIGA sample[1].

| CIG | Tel. | S/N | $A_{flux\ ratio}$ | f | $A_{flux\ ratio}^{expected}$ | Visual class. |
|---|---|---|---|---|---|---|
| 4 | 10 | 18.2 | 1.10 | 1.01 | 1.02 | A |
| 8 | 5 | 25.6 | 1.04 | 1.04 | 1.08 | S |
| 9 | 5 | 23.4 | 1.03 | 1.04 | 1.08 | SA |
| 11 | 7 | 18.9 | 1.47 | 1.00 | 1.01 | A |
| 12 | 5 | 19.1 | 1.06 | 1.02 | 1.04 | SA |
| 23 | 5 | 15.7 | 1.03 | 1.05 | 1.03 | S |
| | ... | | | ... | | ... |

[1]The full list can be downloaded from http://www.iaa.es/AMIGA.html.

Tab. 5.2 and Fig. 5.2(b). We see that for all the visually selected HI profiles (black histogram) 74% of the galaxies have $A_{flux\ ratio} < 1.15$ whereas if we restrict to those points with $A_{flux\ ratio}^{expected}$ to 1.05 (red

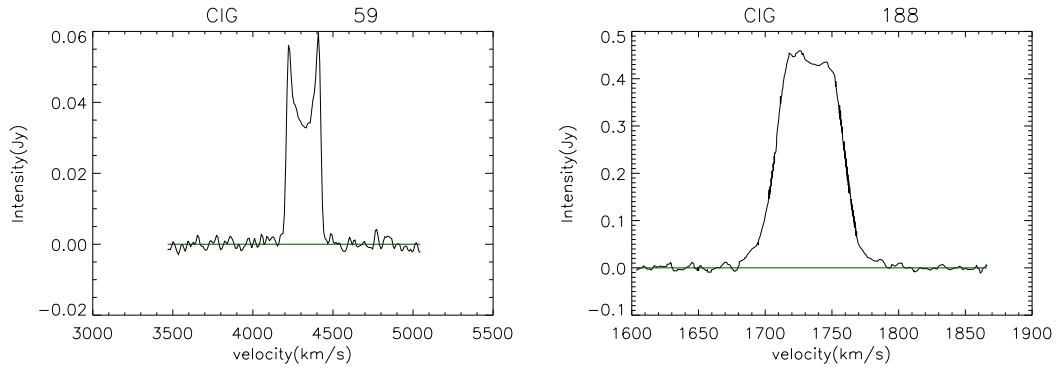


(a) CIG 59; $A_{flux\ ratio} = 1.04$

(b) CIG 188; $A_{flux\ ratio} = 1.03$

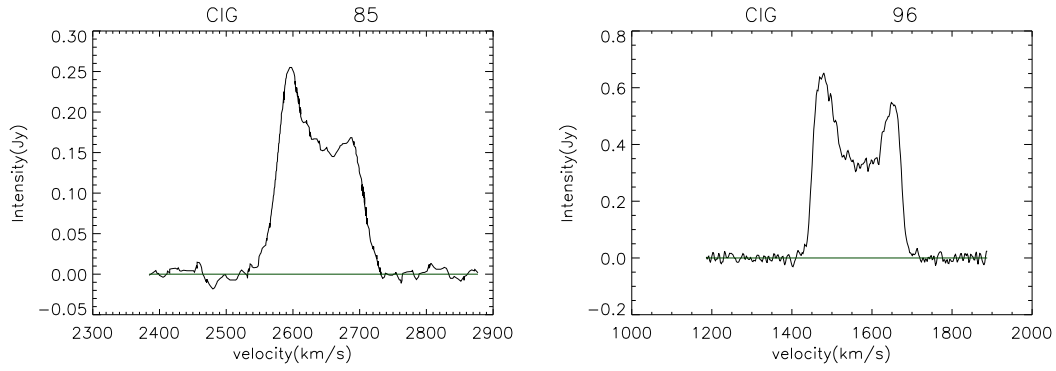


(c) CIG0085; $A_{flux\ ratio} = 1.20$

(d) CIG0096; $A_{flux\ ratio} = 1.23$

Figure 5.1: Examples of two symmetric HI profiles ($A_{flux\ ratio} < 1.15$) and two asymmetric ones ($A_{flux\ ratio} > 1.15$).

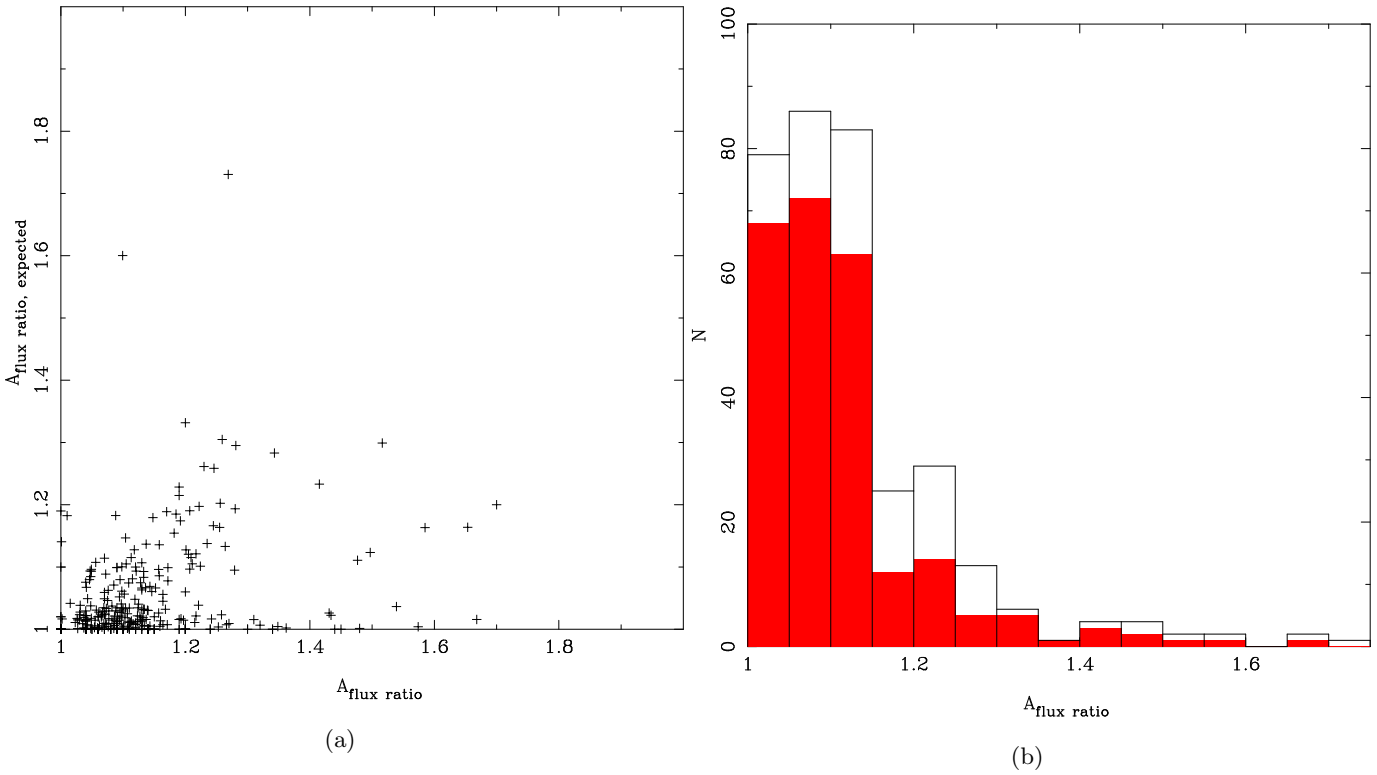


(a) (b)

Figure 5.2: (a) $A^{expected}_{flux\ ratio}$ against $A_{flux\ ratio}$ for the visually selected HI profiles. (b) Distribution of $A_{flux\ ratio}$ for all the galaxies in the visually selected galaxies (black histogram), and those with $A_{flux\ ratio} < 1.05$ (red filled histogram).

Table 5.2: Lopsidedness rate in visually selected HI profiles.

| Sample | N | $A_{flux\ ratio} < 1.15$ | $A_{flux\ ratio} > 1.15$ |
|---|---|---|---|
| All vis. selected profiles | 337 | 220 (65 %) | 117 (35%) |
| $A^{expected}_{flux\ ratio} < 1.05$ | 248 | 197 (79 %) | 51 (21%) |

histogram) the rate increases to 82%. From now on we will consider this sample in order to minimize biases that may arise from beam attenuation and/or bad pointing.

### 5.6.2 Characterization of HI lopsidedness

We consider the N = 248 HI profiles with $A^{expected}_{flux\ ratio} < 1.05$ in order to quantify the mean asymmetry coefficients and compare it with the visual classification performed before. Beam attenuation and offsets in the pointing are minimized by using this sample.

In Fig 5.3 we represent the symmetric, slightly asymmetric and asymmetric sample (N = 83, 106 and 61 respectively). In Tab. 5.3 we show the statistical parameters of these samples. As expected, we see that the distribution of $A_{flux\ ratio}$ for symmetric profiles has a mean equal to 1.06, with values always lower than 1.15. The distribution of slightly asymmetric profiles is very close to that of symmetric profiles, but with a mean of about 1.10. The dispersion is larger for asymmetric profiles, and is mainly distributed from 1.1 to 1.7.

Due to the errors in our measurements (noise, bad estimation of the mean velocity, etc. $\simeq 0.05$), together with the $A^{expected}_{flux\ ratio} < 1.05$ that we have taken into account due to pointing errors or beam attenuation, it is reasonable to consider a limit of 1.15 between symmetric and asymmetric HI profiles.

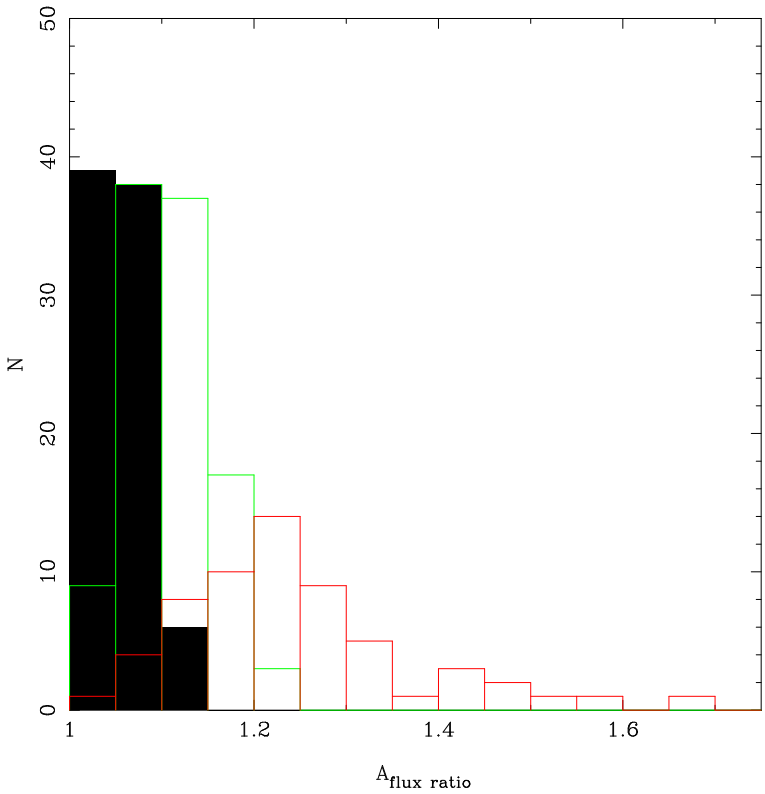


Figure 5.3: $A_{flux\ ratio}$ for the visually selected HI profiles: symmetric (black), slightly asymmetric (green) and asymmetric (red).

Table 5.3: Mean, median and standard deviation of the parameters for the N = 248 HI profiles with $A^{expected}_{flux\ ratio} < 1.05$.

| Subsample | N | Mean | Median | $\sigma$ |
|---|---|---|---|---|
| Symmetric | 83 | 1.06 | 1.06 | 0.03 |
| Slightly asymmetric | 106 | 1.10 | 1.09 | 0.05 |
| Asymmetric | 61 | 1.23 | 1.20 | 0.20 |

### 5.6.3 Comparison with the literature

In this section we discuss our results in comparison with different studies from the bibliography, and summarise in Tab. 5.5. Different limits between symmetric and asymmetric profiles are taken along the different sources in the literature. In order to consider the same limit we use 1.15 as the value to distinguish between a symmetric and an asymmetric profile. This is reasonable due to the errors in our measurements, but still statistically significant. We consider the following references in the literature for comparison: Tifft & Huchtmeier (1990), Richter & Sancisi (1994), Matthews et al. (1998), Haynes et al. (1998) and Bournaud et al. (2005). In Tab. 5.5 we show the total number of profiles considered in each reference, as well as those classified as symmetric or asymmetric and the percentage of profiles without significant asymmetry.

Richter & Sancisi (1994) classified the HI profiles for a sample of 1371 galaxies using the criteria described in § 5.3. The data were compiled from different surveys in the literature: Tifft & Huchtmeier (1990), Giovanelli & Haynes (1985), Giovanelli et al. (1986), Haynes et al. (1988), Haynes & Giovanelli (1991), Richter & McMaster (1994) and Huchtmeier & Richter (private communication) and Broeils (1992). No isolation criteria are used to define the sample, but they describe it as being about a half nearby field galaxies and other half found in general in superclusters fields. They also consider that the two steep edges present in all selected profiles are characteristic of isolated spiral galaxies, and reject other possible peculiar profiles. Their rate of asymmetric galaxies is 54%, whereas we find a higher detection rate equal to 66%, using the same visual inspection method. This is a natural result since our sample has a definition of isolation, while field galaxies do not exclude possible one-on-one interactions.

Matthews et al. (1998) studies a sample of 30 late-type spirals which exhibit regular optical structures and centralised light concentrations. Their galaxies lie between 2°-6° from the center of the Fornax cluster, and the rest are field galaxies, but no strict isolation criteria is considered. Matthews et al. (1998) also used their definition of lopsidedness coefficient, as indicated in § 5.3. Although in Matthews et al. (1998) it was stated that 77% of their H I profiles showed at least some degree of asymmetry, after translating it to our system and limit we see that their rate is 53 % galaxies with $A_{flux\ ratio} < 1.15$, which is similar to other samples of interacting samples. However, due to the small number of galaxies, it is hard to obtain meaningful statistics.

Haynes et al. (1998) consider 104 galaxies that meet a 0.5° (78 with a 1°) isolation criterion, using to do so all the objects catalogued in the AGC database. Note that the AGC is complete in redshift up to $m_B$ 15.4 and/or diameter greater than 1′. When using their values we find a 74 % symmetry rate, similar rate to ours, but note that their percentage may be overestimated since they consider $v_{med}$ instead of $v_m$.

Bournaud et al. (2005) study 76 galaxies, which may be in general interacting ones. They consider a symmetry parameter defined as E1=10 × (1-$A_{flux\ ratio}$). Once transformed their values to $A_{flux\ ratio}$ we obtain a percentage of symmetric profiles of about 44 %, using our limit between asymmetric and symmetric profiles. This is the sample with more asymmetric profiles in comparison with the rest of samples in the literature.

We show in Fig. 5.4 the distributions of $A_{flux\ ratio}$ for the galaxies in Matthews et al. (1998), Haynes et al. (1998) and Bournaud et al. (2005) and for comparison our $A^{flux\ ratio}$ distribution for HI profiles with $A^{expected}_{flux\ ratio} < 1.05$ (N = 248). Both Haynes et al. (1998) and our sample seem to have a strong decrease in number of galaxies located in $A_{flux\ ratio} = 1.15$, but this is less pronounced in the galaxies considered by Bournaud et al. (2005).

## 5.7 Lopsidedness as a function of morphology

Matthews et al. (1998) find that the strongest asymmetries occur in the Sdm galaxies of their sample of Magellanic-type spirals. An increase in the H I asymmetry frequency in Sdm spirals may be expected if Magellanic-type spirals are formed as the result of past tidal perturbations, as suggested by Odewahn (1994; see also Pisano et al. 1998). Bournaud et al. (2005) also find a correlation between disk

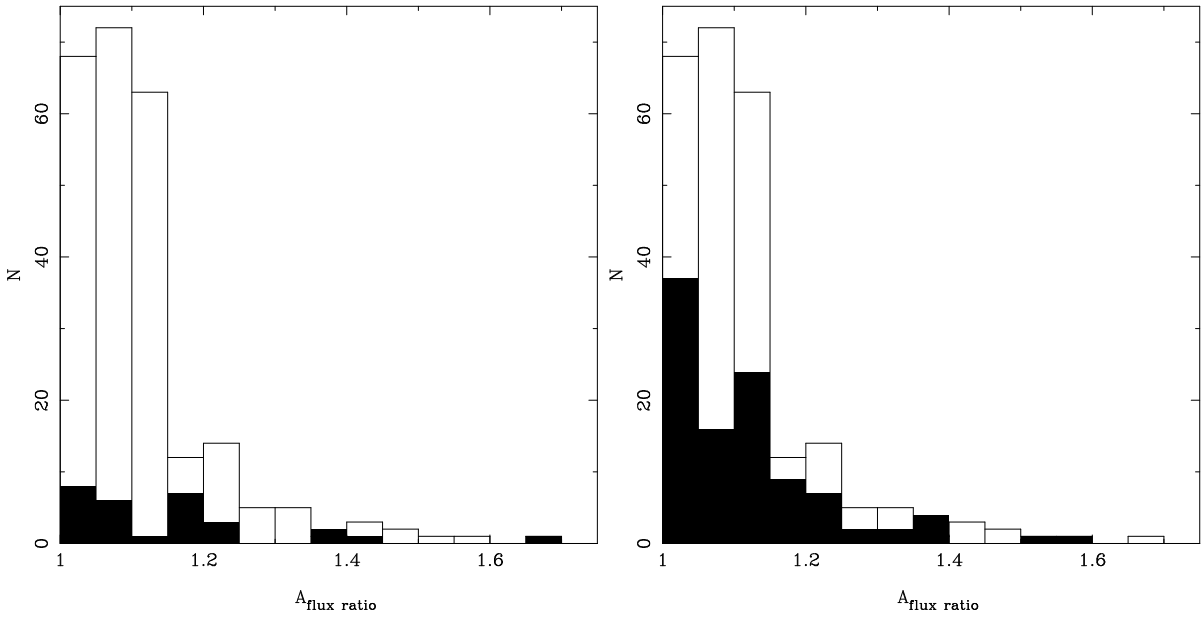


(a) (b)

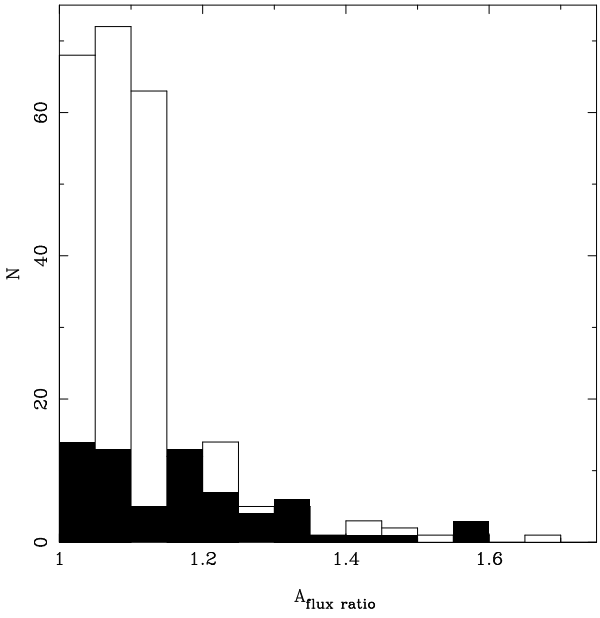


(c)

Figure 5.4: Comparison of $A_{flux\ ratio}$ between our sample (S/N > 10) and: a) Matthews et al. (1998, N = 30), b) Haynes et al. (1998, N=104) and c) Bournaud et al. (2005, N=76).

Table 5.4: $A_{flux\ ratio}$ for the visually selected profiles of the HI sample in AMIGA, and comparison with other samples in the literature

| Sample | N | $A_{flux\ ratio} < 1.15$ | $A_{flux\ ratio} > 1.15$ | Symmetry rate |
|---|---|---|---|---|
| All vis. selected profiles | 337 | 220 | 117 | 65 % |
| All vis., $A^{expected}_{flux\ ratio} < 1.05$ | 248 | 197 | 51 | 79 % |
| Haynes et al. (1998) | 104 | 77 | 27 | 74 % |
| Matthews et al. (1998) | 30 | 16 | 14 | 53 % |
| Bournaud et al. (2005) | 76 | 32 | 38 | 44 % |

lopsidedness and Hubble type, in the sense that it is stronger for late type galaxies.

In this section we search a possible link between lopsidedness in the HI profiles and the morphology of the galaxy. In Fig. 5.5 we show the distributions of $A_{flux\ ratio}$ as a function of Hubble type (T $\leq$ 0: E to S0a; T = 1, 2, 3: Sa to Sb;T = 4, 5: Sbc-Sc ; and T = Scd, Sd, Sdm. We see that spiral galaxies have the higher rate of asymmetric profiles, with almost 30 % of asymmetric profiles. The rate for early type galaxies is not statistically meaningful and no conclusion can be extracted from them. As Matthews et al. (1998), we also find a weak trend of late type spirals being more symmetric, on the contrary than the result found by Matthews et al. (1998) and Bournaud et al. (2005).

Table 5.5: $A_{flux\ ratio}$ for the selected profiles of the HI sample in AMIGA, and comparison with other samples in the literature

| Sample | N | $A_{flux\ ratio} < 1.15$ | Symmetry rate |
|---|---|---|---|
| T $\leq$ 0 | 13 | 11 | 85 % |
| T = 1, 2, 3 | 48 | 33 | 69 % |
| T = 4, 5 | 131 | 89 | 68 % |
| T $\geq$ 6 | 55 | 42 | 76 % |

## 5.8 Conclusions

We have selected by visual inspection the best quality HI profiles, in the same way Richter & Sancisi (1996) did. We classify the profiles attending to three classes: symmetric, slightly asymmetric and asymmetric, with the following percentages: X%, % and %. We find a lower lopsidedness rate with respect to the 1371 galaxies studied by Richter & Sancisi (1994, 66% to 50% approximately).

We apply the most used asymmetry coefficient in the literature to the HI profiles in our sample, $A_{flux\ ratio}$. We have studied the $A_{flux\ ratio}$ distribution for each class: quantitatively symmetric and slightly asymmetric $A_{flux\ ratio}$ distributions are similar, being the mean of the latter a bit larger than the former. The $A_{flux\ ratio}$ distribution for the asymmetric profiles has a larger dispersion in addition to the expected larger mean. We have decided to consider only two groups in the rest of the study, since symmetric and slightly asymmetric distributions are not very different one with respect to the other, and errors in the flux ratio coefficient is expected to be $\pm$ 0.1. We have considered as quantitative limit between the symmetric and the asymmetric group the value of 1.15 (15 % more integrated density flux in one of the horns with respect to the other).

We have shown that using $A^{expected}_{flux\ ratio}$ is especially useful in order to clean for possible observations which are affected either by telescope pointing errors or beam attenuation. When $A^{expected}_{flux\ ratio} < 1.05$ is taken into account we increase the detection rate from 66 % to 79 %.

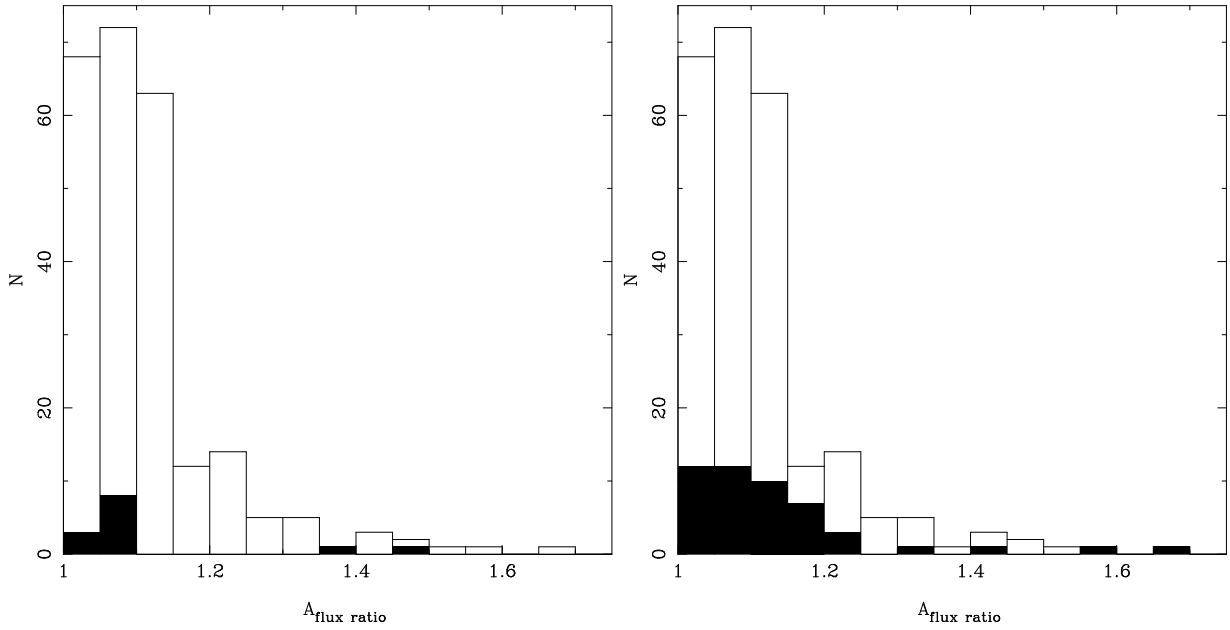


(a) T $\leq$ 0

(b) T = 1, 2, 3

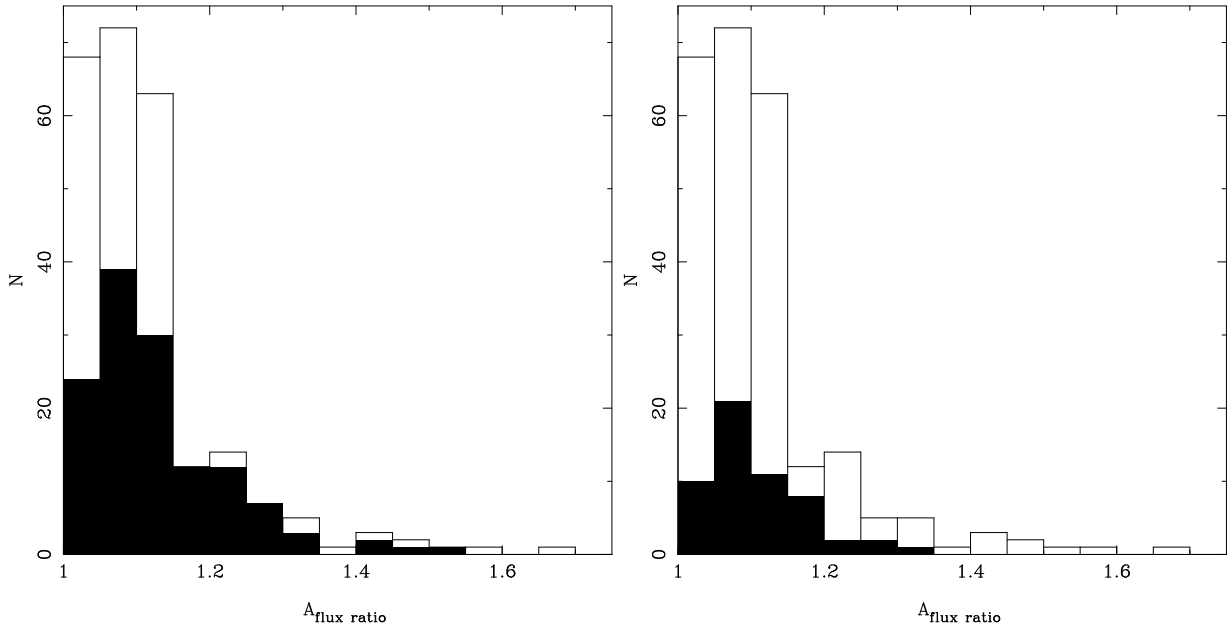


(c) T = 4, 5

(d) T $\geq$ 6

Figure 5.5: $A_{flux\ ratio}$ distribution as a function of morphology

We have considered other studies in the literature with quantitative studies about HI profiles lopsidedness. Using our same criteria we find a percentage of X for the isolated galaxies in Haynes et al. (1998), and a lower rate for other samples of galaxies which are in principle interacting (e.g. Bournaud et al. 2005). Our global symmetry rate is larger than any other found in the literature. This may be a result of the strict isolation criteria of our sample.

Now we discuss the possible origin of the remaining lopsided HI profiles in our sample of isolated galaxies. We minimize the option of past tidal interactions because we consider a strict isolation criteria and we do not see similarly sized companions around. The contribution of confusion with companions does not seem to be important either. Moreover, looking at the individual profiles we see that in most of the asymmetric profiles one horn is higher than the other (as is the case of CIG 96 whose HI synthesis imaging is studied in detail in Chapter 7).

Bournaud et al (2005) suggest that gas accretion is needed in order to explain the high rate of asymmetric profiles in isolated galaxies and the fact that lopsidedness in the disk increases with Hubble type. We do find a smaller rate of asymmetric profiles for isolated galaxies than other samples (which in principle includes galaxies in denser environments), and probably the rate could be higher if we reduce more any artificial contribution to the shape of the profiles (beam attenuation, pointing offsets, baseline substraction, etc.)

As for the trend of lopsidedness with morphology, we see no relevant increase in the lopsidedness with Hubble type. Then at least for our sample the percentage of asymmetric profiles could be explained by minor merger scenarios, and gas accretion is not needed.

If we assume that there is no important telescope pointing errors in other samples, then we can extract a conclusion from the fact that we see a trend with environmental density. Since denser environments have larger lopsidedness rates then it seems reasonable to think that it is likely that much of the seen asymmetries in other samples of galaxies are mainly due to tidal interactions or minor mergers which have perturbed the HI disk of the main galaxy, whereas in our case tidal interactions is minimized and we would see only the contribution of minor mergers.

A final revision of these results will be joined to those made in Chapter 6, where we will study VLA synthesis images for a subsample of a dozen of the isolated galaxies with asymmetric and symmetric HI profiles.

# Chapter 6

# Lopsidedness: VLA HI subsample

The origin of lopsidedness in isolated galaxies is not well understood yet. Some of the open questions are the following: are they always induced by the presence of companions? What is the influence of recent captures, and how long does it take for a parent galaxy to again become axisymmetric afterwards? Could some originate from internal, as yet not well studied, long-lived dynamical instabilities (e.g. Baldwin et al. 1980)?. In order to study the origin of asymmetries in the atomic gas of well isolated spiral galaxies, we have made use of the large statistical HI study of isolated galaxies performed in former chapters to select a well defined sample of isolated galaxies with lopsided HI profiles and with a minimized probability of contamination by companions. We have observed a total of 12 isolated galaxies (referred in this chapter as the VLA HI subsample) at the VLA in D-array configuration in order to discriminate whether the lopsidedness is in the HI density distribution, the velocity field or is due to confusion with a HI-rich companion. The sample comprises 8 galaxies with lopsided HI profiles and 4 with symmetric profiles for comparison. In this chapter we present the observations as well as the HI distribution, velocity fields and channel maps. The main aim is to introduce and describe the HI synthesis images, and the detailed analysis for each galaxy is left for later, as we have done for the first of these galaxies, CIG 96, in Chapter 7.

## 6.1 Introduction

In Chapter 2 we have presented the single-dish 21-cm line spectra for a total of 910 isolated galaxies. When more than one HI profile was available for a given galaxy, we selected the HI data that minimized the probability of confusion with close companions or undesired pointing offsets of the radio-telescope. In Chapter 3 we have shown that 50% of these galaxies show asymmetric HI profiles, consistent with the results from previous works on smaller samples of isolated galaxies (104 galaxies in Haynes et al. 1998; 30 galaxies in Matthews 1998). Surprisingly, other samples of galaxies in denser environments show only slightly larger values of this rate (50 - 80%, e.g. Swaters et al. 2002b, Richter & Sancisi 1994, Sulentic & Arp 1983). HI synthesis imaging of very isolated galaxies with a highly lopsided HI profile may clarify the origin of these asymmetries. Not only can HI-rich companions be identified, but the presence of tidal features can be revealed, which would trace a past interaction. Up to now few HI synthesis studies of samples of isolated galaxies are found. Two approaches are usually done (see Table 6.1): 1) attending to different morphological types (e.g. Jore 1997 for Sa types) or 2) attending to the environment (e.g. Cayatte et al. 1990, 1994 for the Virgo cluster).

Jore (1997) investigated the dynamics of gas and stars in a sample of 20 nearby, morphologically normal isolated Sa galaxies. For nine gas-rich objects, H I synthesis maps were obtained with the Very Large Array (see Kornreich et al. 2001). These galaxies exhibit kinematical peculiarities ranging from warps to extended counter-rotating disks and are possibly the remnants of minor mergers. Swaters et al. (2002b) find that about half of the late-type dwarf galaxies in their sample have asymmetric global profiles, a third has a lopsided H I distribution, and about half shows signs of kinematical lopsidedness. Wilcots & Prescott (2004) studies the HI of 13 barred Magellanic spirals, 4

of which have companions detected in HI. However, in general terms the lopsidedness of these systems does not depend strictly on the existence of companions and they suggest that it can be a long-lived phenomenon which is not related to the environment.

In clusters with hostile intra-cluster medium many galaxies show HI deficiencies (as shown in Chapter 4), and HI disks in the central regions of the cluster appear shrunken and/or asymmetric (**?**). Cayatte et al. (1990) studied 25 galaxies in an evolved cluster such as Virgo and find that many of them present strong asymmetries and deficiency in their atomic gas which is combined with signs of enhanced star formation. A more recent study by Chung (2005) of 41 galaxies in the Virgo cluster reveals strong lopsidedness and truncated HI disks in many of these galaxies as well, both in the centre and in the outer region. Some of them show extended HI tails, almost all pointing away from the cluster centre. Verheijen (2001) presented the results of a 21-cm line survey of spiral galaxies in the Ursa Major cluster with the WSRT (Westerbork Synthesis Radio Telescope). The Ursa Major cluster does not have any ellipticals and only a few lenticulars, there is no central core and no X-ray emitting intra-cluster gas. These facts suggest that these galaxies may be similar to those in the field. A similar situation is found in Hydra cluster (McMahon, 1993): both systems do not show a significant HI deficiency. Verheijen stated that at least half of their galaxies show lopsided HI distribution and/or kinematics. Other extreme environments are Hickson Compact Groups, which have been already introduced in the former chapter. About 20 HCGs have been studied up to now using interferometry. It is usual to see highly HI-deficient galaxies and irregularities in the HI distribution and velocity fields of their members (Verdes-Montenegro et al. 2001a).

In order to isolate the dependence of the lopsidedness on the environmental density of the galaxy HI, it is necessary to select a well-defined set of the most isolated galaxies in the nearby universe. But to our knowledge, there is only one HI synthesis imaging survey focused on isolated galaxies: Pisano et al. (2002), who searched for HI clouds remnants of the galaxy formation process around 41 galaxies in low density regions, using the VLA in its D-configuration. Their sample was selected not to have *known* companion galaxies with redshifts reported by Tully & Fisher (1988) within 6 Mpc. However, galaxies that did not have redshift in this catalog may be actually closeby. This is clearly seen in some of their HI maps, and therefore many of the galaxies that they present are clearly interacting galaxies. Only four CIG galaxies are included in their sample. A direct comparison of the isolation parameters between most of Pisano's "isolated" galaxies and our sample show that our local density estimation (Verley 2006) has lower values, minimizing the possibility of a recent interaction with similarly sized galaxies. They find 13 HI-rich companions around 41 galaxies in an average volume of 0.77 $Mpc^3$ around each galaxy. From a visual inspection, 17 of their galaxies are nearly symmetric in both their HI distribution and velocity field, whereas 4 present a slight asymmetry and 20 are lopsided. As seen in previous works, they state that the presence of companions does not seem to be connected to lopsidedness: 3 symmetric galaxies and 2 lopsided have companions. That means that the situation for lopsidedness in this set of galaxies is very similar to galaxies in denser environments. Of course one-on-one encounters (major or minor) and the IGM affects to the symmetry of the galaxy, but other possibilities are necessary to explain the similar rate of lopsidedness in all kind of environments. Bournaud et al. (2005) show that gas accretion is the most reasonable solution to explain the high rate of lopsided profiles.

We intend to use our sample of isolated galaxies in order to shed light to this issue, as we describe in the following sections. The immediate objectives of our study are the following:

1. to study whether the asymmetry in the HI profiles is produced by confusion with HI-rich companions which are too optically faint to be detected on the optical plates (POSS I),

2. to look for the presence of tidal extended structures which may imply interaction with another galaxy,

3. to check whether the lopsided distribution or non circular motions may have been produced by a past accretion (major or minor merger), using the analysis of the gas distribution and kinematics.

Table 6.1: HI synthesis imaging studies in the literature.

| Reference | N | Telescope | Comments |
|---|---|---|---|
| **Samples attending morphology** | | | |
| Wilcots & Prescott (2004) | 13 | VLA | barred Magellanic Spirals |
| Swaters et al. (2002b) | 73 | WSRT | late-type dwarf galaxies |
| Jore (1997); Kornreich et al. (2001) | 9 | VLA D | Sa optically normal |
| Broeils & van Woerden (1994) | 50,12[1] | WSRT | spiral galaxies, extended HI |
| Rhee & van Albada (1996) | 60 | WSRT | late type spiral galaxies |
| **Samples in dense environments** | | | |
| Warmels (1988) | 12 | WSRT | low galaxy density, Virgo cluster |
| Cayatte et al. (1990, 1994) | 25 | VLA D/C | Virgo cluster center |
| Chung (2005) | 50 | VLA | Virgo cluster |
| Bravo-Alfaro et al. (1997) | 11 | WSRT | A 262 cluster |
| Bravo-Alfaro et al. (2000, 2001) | 19 | VLA | Coma cluster |
| Dickey (1997) | 61 | VLA | Hercules cluster |
| van Gorkom et al. (2003) | - | VLA C | A2670, A496, A85, A754, A2192 |
| McMahon (1993) | | | Hydra cluster |
| Verheijen (1997) | 49 | WSRT | Ursa Major cluster galaxies |
| Verdes-Montenegro et al. (2001b) and references therein [2] | 16 groups | VLA | Hickson Compact Groups |
| **Samples of isolated galaxies** | | | |
| Pisano et al. (2002) | 41 | VLA D | |

In § 6.2 we detail the selection criteria for the considered subsample and in § 6.3 we show the isolation properties of this subsample. The HI synthesis images are presented in § 6.4 and finally we present the results and conclusion in § 6.5 and § 6.6 respectively.

## 6.2 Selection of the VLA HI subsample

We have selected from our database a well-defined sample of the most isolated galaxies showing significant asymmetries in their HI profiles, and mapped them with the VLA[1] in the 21-cm HI line in order to look for signs of external interaction by analysing in detail the HI distribution and its kinematics.

The main drivers in the selection of the used sample are isolation using (as explained in Chapter 1) and lopsidedness of the HI spectra (as explained in Chapter 5). We have quantified the lopsidedness using the flux ratio parameter (parameter $A_{flux\ ratio}$ in Chapter 5).

The galaxies were selected by the following criteria:

1. v > 1500 km/s, because for smaller velocities the area in which we had to search for potential companions of the nearby CIG would be spread over a too large region on the sky,

2. HI spectra with S/N > 10, in order to have reasonably good quality spectra,

[1] in order to select galaxies with extended HI, 50 galaxies were observed in a short observation with the WSRT to obtain one-dimensional information about the kinematics and spatial distribution of the neutral hydrogen (HI) along the major axis of each galaxy. Then 12 galaxies were observed in longer integrations for synthesis imaging.

[2] HCG 40, 49, 54, 95 and 96 are presented in Verdes-Montenegro et al. (2001b). HCG 18 in Williams & van Gorkom (1988). HCG 31, 44 and 79 in Williams et al. (1991). HCG 23 and 26 in Williams & van Gorkom (1995). Five other spiral dominated groups have also been reported in Williams et al. (1999) and Verdes-Montenegro et al. (2000,?). HCG 92 (Stephan's Quintet) was studied at WSRT by Shostak et al. (1984).

[1] The National Radio Astronomy Observatory is a facility of the National Science Fundation Operated under cooperative agreement by Associated Universities, Inc.

Table 6.2: Parameters of the target galaxies.

| CIG | $D_{25}$ (′) | cz (km/s) | $W_{20}$ (km/s) | HI peak (mJy) | $A_{flux\ ratio}$ |
|---|---|---|---|---|---|
| Asymmetric single-dish profiles | | | | | |
| 96 | 4.7 | 1555 | 238 | 65 | 1.12 |
| 123 | 1.9 | 5903 | 278 | 80 | 1.20 |
| 134 | 1.2 | 5199 | 277 | 35 | 1.06 |
| 421 | 1.3 | 6647 | 206 | 70 | 1.16 |
| 551 | 3.0 | 2300 | 258 | 100 | 1.18 |
| 660 | 1.3 | 2136 | 144 | 76 | 1.14 |
| 744 | 2.1 | 2596 | 238 | 75 | 1.07 |
| 812 | 2.8 | 3118 | 431 | 21 | 1.06 |
| Symmetric single-dish profiles | | | | | |
| 240 | 1.5 | 4685 | 420 | 15 | 1.02 |
| 463 | 2.5 | 2207 | 240 | 85 | 1.02 |
| 616 | 2.6 | 6132 | 490 | 28 | 1.01 |
| 736 | 4.7 | 1568 | 370 | 14 | 1.03 |

3. galaxy size to beam ratio larger than 0.5 in order to assure that we are not missing emission and/or suffering of pointing problems as seen in Chapter 5,

4. flux ratio coefficient $A_{flux\ ratio} > 1.10$ for asymmetric profiles (see Chapter 5), and $A_{flux\ ratio} \sim 1$ for symmetric profiles.

From this selection we have chosen 12 galaxies to perform HI observations with the VLA:

- 8 galaxies displaying the most extreme asymmetries in their HI profiles: CIG 96, 123, 134, 421, 551, 660, 744 and 812.

- 4 galaxies showing no sign of asymmetry, to be used as a control sample: 240, 463, 616 and 736.

The most compact configuration (D) of the VLA was selected in order to be as sensitive as possible to diffuse HI-rich companions. A follow-up in a more expanded configuration of five of these galaxies have been performed to have more details about the HI distribution lopsidedness and/or irregularities in the velocity field and will be left for a further study.

Detailed information about these 12 galaxies is presented in Tab. 6.2. It contains the following information: CIG number, optical major axis diameter at a 25 mag arcsec$^2$ blue isophote level, systemic velocity as obtained from the single-dish HI profile, width at a 20% level with respect to the maximum of the profile, maximum of the profile, and flux ratio asymmetry coefficient.

The HI profiles are shown in the corresponding figures for each galaxy at the end of this chapter, except for CIG 240 (symmetric profile), 421 (asymmetric) and 616 (symmetric) whose VLA observations are strongly affected by solar interferences and for which we show their single-dish profiles in Fig. 6.1.

## 6.3 Isolation properties of the VLA subsample

In this section we discuss the isolation properties of each CIG galaxy in the VLA subsample reported by Verley (2006). Verley (2006) have looked for their velocities in different catalogs to check whether these sources are just projected or are real companions.

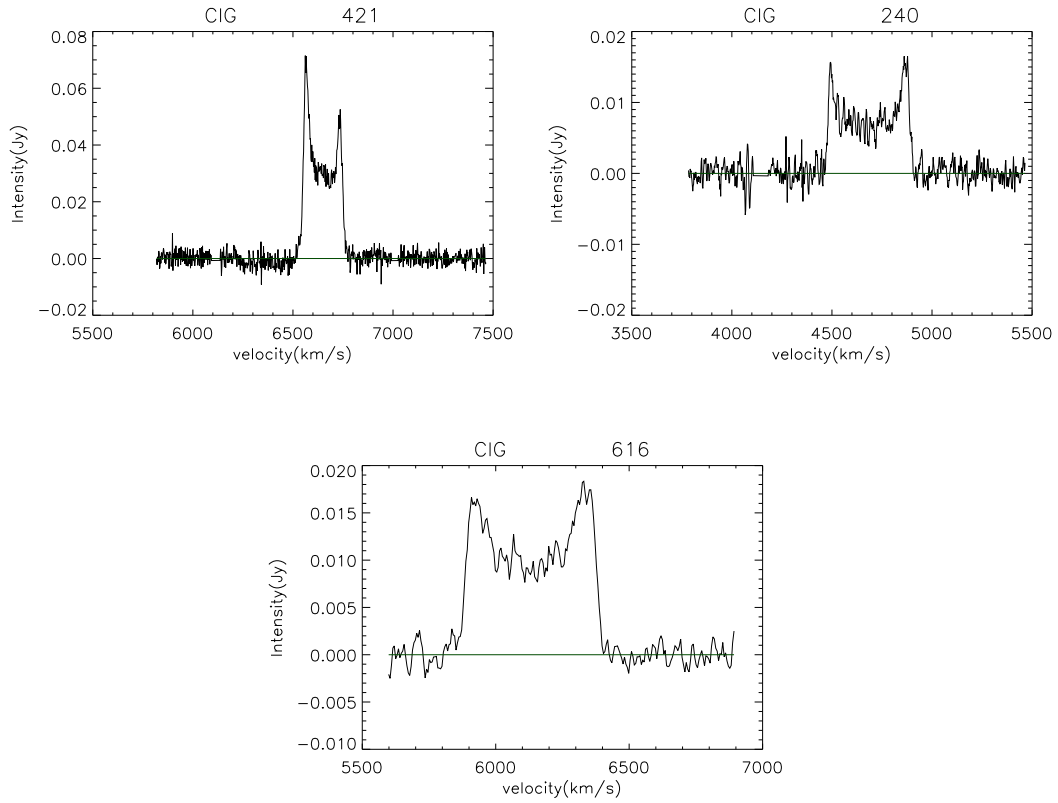


Figure 6.1: Profiles for the galaxies with strong solar interferences in the VLA observations.

In Tab. 6.3 we present the projected galaxies that are included in the primary beam of our VLA observations (HPBW of the VLA primary beam is $\sim 30'$). The position, magnitude, distance to the main galaxy, diameter and velocity (when available in the literature) of these sources are included. Many of these sources have velocities very different ($\Delta V > 10000$) to that of the main galaxy and therefore they are not real companions. For example this is the case of CIG 463, 551 and 744. In general we expect this to occur in the rest of galaxies since these companion galaxies are small and are likely located in the background.

We show in Fig. 6.2 the environment on the VLA primary beam extent for the galaxies for which we have found HI-rich companions (see §6.4): CIG 96, 421 and 812. The HI-rich companions are identified in Tab. 6.3 as 137 for CIG 96 and 10 for CIG 812. The HI-rich companion for CIG 412 does not seem to have optical counterpart. The CIG galaxies are located in the center of the images in Fig. 6.2, whereas the HI-rich companions are shown as green crosses and all the catalogued sources as red squares.

## 6.4 HI synthesis imaging of the VLA HI subsample

In this section we explain the procedure followed to perform the HI imaging of the 12 isolated galaxies in our subsample, and to discuss the features of the HI. It is divided into four parts: a) first we explain the strategy to perform the observations, b) the calibration and imaging of the HI data, c) the presentation of the channel maps, HI distribution and velocity fields (moment 0 and 1) as well as the comparison of single-dish and VLA profiles, and d) a brief study of the relationship between HI extent, $M_{HI}$ and the optical extent.

Table 6.3: Projected companion galaxies in the primary beam of the VLA ($\sim 30'$).

| Id. | $\alpha$ (2000) (deg) | $\delta$ (2000) (deg) | magnitude | distance ($'$) | $D_{25}$ ($''$) | V (km s$^{-1}$) |
|---|---|---|---|---|---|---|
| CIG 96: $D_{25} = 4.7'$, V = 1555 km s$^{-1}$ | | | | | | |
| 133 | 34.1093 | 5.78792 | 17.268 | 19.4 | 22.5 | - |
| 134 | 33.5825 | 5.82099 | 15.896 | 20.1 | 35.2 | - |
| 136 | 33.8432 | 5.85152 | 16.872 | 9.1 | 24.5 | - |
| 137 | 34.1107 | 5.93479 | 16.171 | 15.1 | 34.1 | - |
| 139 | 33.6952 | 6.31193 | 15.895 | 21.1 | 39.5 | - |
| 140 | 33.7047 | 6.31521 | 16.848 | 21.0 | 24.6 | - |
| 141 | 33.654 | 6.16987 | 17.028 | 16.1 | 26 | - |
| 144 | 33.6054 | 6.06277 | 17.324 | 15.9 | 19.4 | - |
| CIG 123: $D_{25} = 1.9'$, V = 5903 km s$^{-1}$ | | | | | | |
| 0 | 48.3989 | 4.40009 | 17.284 | 21.4 | 18.7 | - |
| 4 | 48.069 | 4.54599 | 15.29 | 12.9 | 23.7 | - |
| 5 | 48.2581 | 4.58166 | 16.418 | 7.9 | 23.5 | - |
| CIG 134: $D_{25} = 1.2$ , V = 5199 | | | | | | |
| 25 | 57.9921 | -1.40028 | 16.906 | 7.5 | 17.5 | - |
| 26 | 57.9495 | -1.41706 | 17.398 | 8.4 | 17 | - |
| CIG 240: $D_{25} = 1.5'$, V= 4685 km s$^{-1}$ | | | | | | |
| 1 | 124.778 | 68.5588 | 16.434 | 8.4 | 20.8 | - |
| 9 | 125.395 | 68.6465 | 17.565 | 6.1 | 14.9 | - |
| 10 | 124.516 | 69.0059 | 17.131 | 27.8 | 15.4 | - |
| 11 | 126.142 | 68.8979 | 17.151 | 28.0 | 15.1 | - |
| 12 | 125.693 | 68.3323 | 16.727 | 20.1 | 17.6 | - |
| 13 | 126.002 | 68.2961 | 17.593 | 26.2 | 16.5 | - |
| 14 | 125.448 | 68.2224 | 16.358 | 23.6 | 23.3 | - |
| 15 | 125.166 | 68.2296 | 16.776 | 22.2 | 17.6 | - |
| 16 | 125.655 | 68.2117 | 16.764 | 25.9 | 21.8 | 17221 |
| 17 | 125.718 | 68.2033 | 15.96 | 26.9 | 24.9 | - |
| 18 | 125.744 | 68.2009 | 17.4 | 27.3 | 11.8 | - |
| 19 | 125.782 | 68.1924 | 17.278 | 28.2 | 14.4 | - |
| CIG 421: $D_{25} = 1.3'$, V = 6647 km s$^{-1}$ | | | | | | |
| 64 | 157.593 | 72.0226 | 18.081 | 7.4 | 10.9 | - |
| 66 | 158.013 | 72.027 | 17.552 | 7.0 | 10.6 | - |
| 67 | 157.822 | 72.0353 | 17.003 | 5.4 | 21 | - |
| 68 | 158.054 | 72.0345 | 17.459 | 7.1 | 11.4 | - |
| 70 | 157.88 | 72.0534 | 18.232 | 4.5 | 10.1 | - |
| 77 | 157.62 | 72.096 | 17.542 | 3.9 | 14.1 | - |
| 79 | 157.452 | 72.115 | 17.922 | 6.6 | 11.3 | - |
| 130 | 157.794 | 72.2494 | 16.063 | 7.3 | 11.6 | - |
| 142 | 157.826 | 72.214 | 17.061 | 5.2 | 18.7 | - |
| 146 | 157.823 | 72.1833 | 17.321 | 3.3 | 19 | - |
| 151 | 157.814 | 72.163 | 16.58 | 2.1 | 10.2 | - |

Table 6.3: Continued.

| Id. | $\alpha$ (2000) (deg) | $\delta$ (2000) (deg) | magnitude | distance ($'$) | $D_{25}$ ($''$) | V (km s$^{-1}$) |
|---|---|---|---|---|---|---|
| CIG 463: $D_{25} = 2.5'$, V = 2207 km s$^{-1}$ | | | | | | |
| 91 | 166.578 | 51.138 | 16.991 | 6.8 | 20 | 31478 |
| 101 | 166.822 | 51.0745 | 17.431 | 8.5 | 19 | 35009 |
| 106 | 166.908 | 51.1164 | 17.446 | 8.5 | 16.9 | 34795 |
| CIG 551: $D_{25} = 3.0'$, V = 2300 km s$^{-1}$ | | | | | | |
| 45 | 191.191 | 64.6258 | 16.341 | 8.7 | 31 | 30683 |
| 46 | 191.251 | 64.6015 | 16.561 | 6.7 | 30.6 | 12652 |
| 48 | 191.33 | 64.5432 | 16.929 | 4.7 | 24.4 | 31283 |
| 49 | 191.34 | 64.5796 | 16.905 | 4.2 | 25.1 | 30444 |
| CIG 616: $D_{25} = 2.6'$, V= 6132 km s$^{-1}$ | | | | | | |
| 19 | 213.137 | 38.2601 | 16.285 | 8.7 | 18.7 | - |
| CIG 660: $D_{25} = 1.3'$, V = 2136 km s$^{-1}$ | | | | | | |
| 60 | 225.694 | 77.5102 | 16.962 | 8.5 | 15.3 | - |
| CIG 736: $D_{25} = 4.7'$, V = 1568 km s$^{-1}$ | | | | | | |
| 122 | 245.227 | -2.50932 | 16.04 | 19.1 | 22.5 | - |
| 123 | 245.726 | -2.47771 | 15.873 | 20.0 | 19.4 | - |
| 124 | 245.752 | -2.40256 | 16.212 | 19.3 | 23.8 | - |
| 125 | 245.745 | -2.30626 | 16.643 | 17.5 | 21.6 | - |
| 134 | 245.259 | -2.07624 | 16.414 | 17.0 | 21.7 | - |
| CIG 744: $D_{25} = 2.1'$, V = 2596 km s$^{-1}$ | | | | | | |
| 108 | 247.817 | 43.1786 | 17.431 | 10.3 | 12.7 | 41932 |
| 110 | 247.904 | 43.3849 | 15.976 | 5.7 | 25.6 | 9486 |
| CIG 812: $D_{25} = 2.8$, V = 3118 km s$^{-1}$ | | | | | | |
| 10 | 263.061 | 16.5948 | 15.509 | 13.0 | 27 | - |
| 12 | 263.095 | 16.3252 | 16.25 | 6.1 | 23.1 | - |
| 13 | 263.098 | 16.6662 | 16.837 | 16.3 | 15.9 | - |
| 14 | 263.147 | 16.2438 | 16.619 | 9.5 | 23.4 | - |
| 15 | 263.163 | 16.4887 | 16.125 | 5.1 | 19.8 | - |
| 19 | 263.208 | 16.3968 | 16.785 | 2.4 | 19.2 | - |

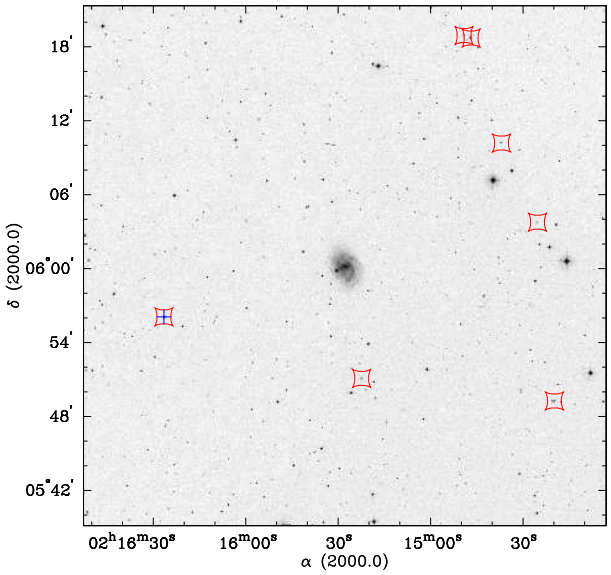


(a) CIG 96

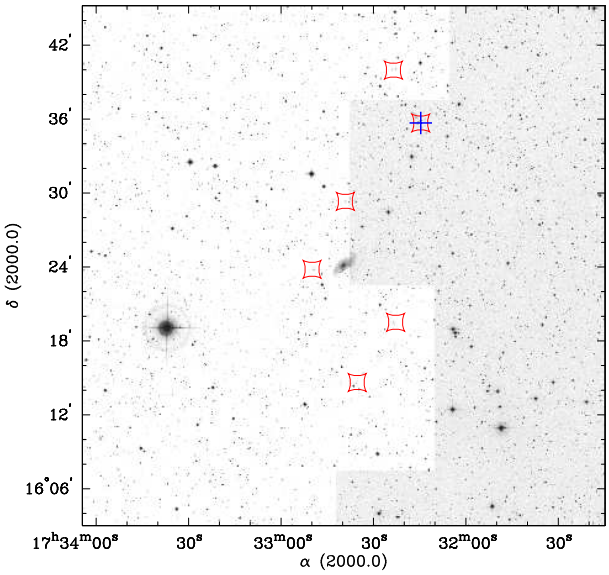


(b) CIG 812

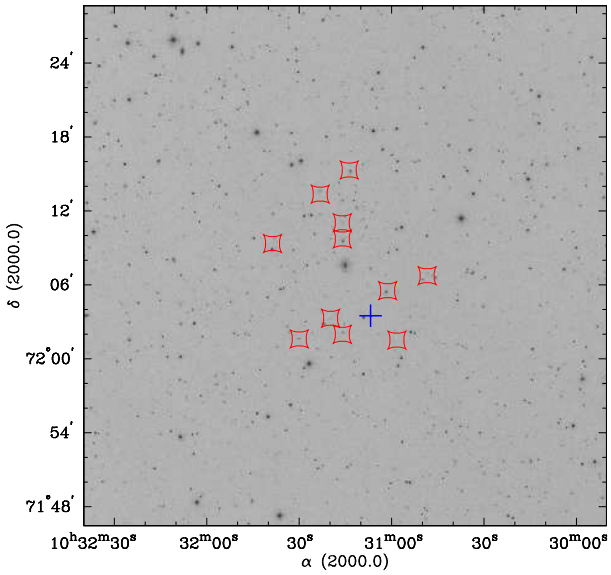


(c) CIG 421

Figure 6.2: Catalogued companion candidates (red squares) for CIG 96, 421 and 812 (galaxies with detected HI-rich companions). Crosses represent sources detected in HI with our VLA observations. Images are from POSSII (CIG 96 and 812) and POSSI (CIG 421).

### 6.4.1 Observations

Observations for 12 of our isolated galaxies were conducted at the VLA in the D configuration in the summer 2004 during a total of 40 hours. Typical optical sizes of the galaxies are between 1 and $5'$ (see Tab. 6.2). The HI disk size is typically about twice the optical diameter (see Chapter 1), so these HI disks were well resolved by the $45''$ beam, and each galaxy was imaged with the VLA using a single pointing. Observing in the 2IF mode we get a total bandwidth of 3.125 MHz with a frequency resolution of 48.8 kHz after Hanning smoothing. All galaxies were imaged using the same spectral configuration in order to achieve a uniform sensitivity and velocity coverage for the sample. The noise in each 48.8 kHz channel after 3.5 hr integration was typically about 0.54 mJy/beam (with 26 antennas). This corresponds to a $5\sigma$ HI column density detection limit of $1.6 \times 10^{19}$ cm$^{-2}$ averaged over the $\theta \sim 45''$(13 kpc at a mean distance of 60 Mpc) beam. The peak line measured with a typical $9'$ beam ranges between 50 and 100 mJy (see Tab. 6.2 and HI profiles in the plots for each galaxy, Fig. **??** to **??** in the end of this chapter).

All of these galaxies were detected and mapped with excellent S/N, except four galaxies due to interferences: CIG 134, 240, 421 and 616. The data cubes of CIG 421 and 616 were strongly corrupted by solar interferences. This produced large scale diagonal stripes which we were unable to remove. We do not present the final composition of images (Fig. 6.3) for these galaxies but we discuss qualitatively their properties (e.g. CIG 421 has a companion). We will maintain CIG 134 and 240 but note that the HI distribution and velocity fields might not be accurate.

### 6.4.2 Reduction

We have calibrated the HI observations using the standard VLA procedure in AIPS. TVFLG was used for the flagging of bad visibilities. We performed phase, amplitude, and bandpass calibration using the AIPS tasks CALIB, CLCAL and BPASS. The average of the line-free channels (continuum) has been subtracted from all the individual channels using UVLIN. Finally the resulting data were cleaned and imaged using IMAGR. Since interferometric measurements of the integrated density flux can be underestimated due to the missing short baselines, we have put special attention to a comparison of the VLA HI profiles with that obtained using single-dish radio-telescopes.

### 6.4.3 Presentation of the VLA synthesis images

The final plots for the 10 galaxies are presented at the end of this chapter (Fig. 6.8 to 6.8), including relevant data products such as the HI distribution, velocity field, HI profiles and the channel maps. The plots for the different galaxies are presented in ascending order of RA. The presentation of the HI data for each galaxy is summarised in Fig. 6.3. Page 1 includes a table containing the following information: Part 1) Source number in CIG, morphological type according to the RC3 system, RA and Dec (2000), and the sizes of the considered optical fields. Part 2) Observing parameters: integration time, central velocity, spatial resolution, channels, spectral resolution, total number of channels of the data cube, beam size, beam size with smoothing (factor $\sqrt{2}$, only used in the channel maps) and position angle. Part 3) Results from the HI data, divided into three parts: a) Channel map: considered field size, channels and velocity region where the source is detected, noise per channel and contour levels[1]. The contours are drawn according to the rms noise. b) comparison of VLA HI profile and single-dish profiles (reference is included), including HI flux, central velocity, HI profile width at a 20% level and $M_{HI}$. c) Moment 0 and moment 1 information, including the considered field size, the HI map contour levels (in two units, mJy/beam km s$^{-1}$ and atoms cm$^{-2}$) and velocity contours. Finally we include some comments (about the existence of HI-rich companion in the primary beam, problem in the observations, etc.). In the second half of Page 1 we show optical images, HI distribution (grey scale, darker regions corresponding to higher column densities; and contours), velocity field(contours) and HI profiles. The beam size is plotted in the upper leften region of the plots. Finally, in the Page 2 we present the channel maps. In the upper left we show the beam and in the righten side the velocity for each channel.

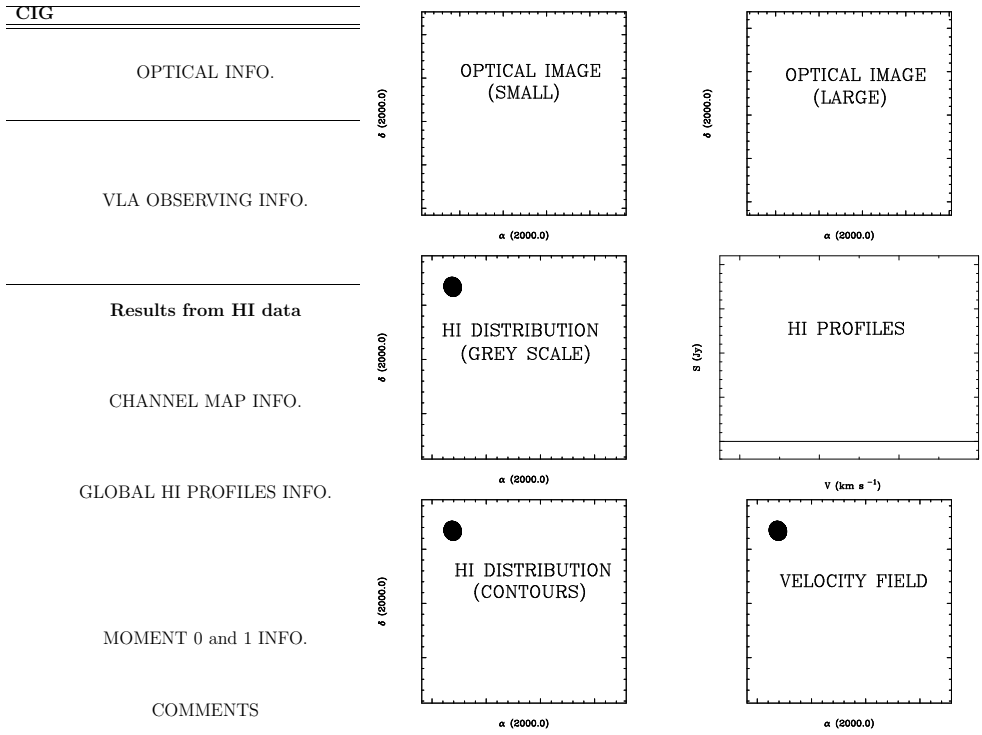


(a) Page 1

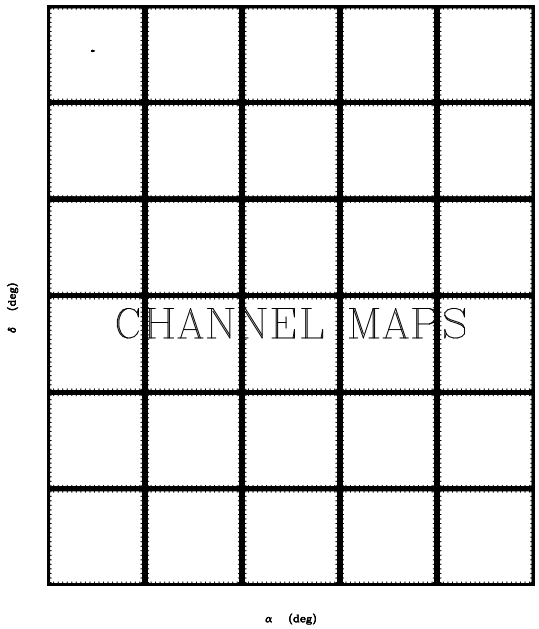


(b) Page 2

Figure 6.3: Scheme followed in the presentation of the VLA synthesis images and relevant information.

Table 6.4: Main characteristics of the observations performed by us at the VLA.

| CIG | channels | noise (mJy/beam) | beam ($''$) | $\Delta M_{HI}$ $10^6$ M$\odot$ | comments |
|---|---|---|---|---|---|
| Asymmetric single-dish prof. | | | | | |
| 96 | 20-46 | 0.66 | 49.8 × 46.0 | 0.5 | |
| 123 | 19-48 | 0.77 | 84.6 × 52.5 | 11.0 | |
| 134 | 17-47 | 0.80 | 68.1 × 52.5 | 9.0 | some RFI |
| 421 | 22-46 | 0.90-1.20 | 70.2 × 53.3 | 18.0 | corrupted by RFI |
| 551 | 19-45 | 0.49 | 60.6 × 54.6 | 1.3 | |
| 660 | 24-40 | 0.90 | 60.5 × 47.4 | 2.0 | |
| 744 | 18-46 | 0.53 | 61.2 × 55.7 | 1.6 | |
| 812 | 10-56 | 0.58 | 65.1 × 58.0 | 2.4 | |
| Symmetric single-dish prof. | | | | | |
| 240 | 10-54 | 0.80 | 62.1 × 54.4 | 8.0 | corrupted by RFI |
| 463 | 19-45 | 0.85 | 58.0 × 52.2 | 2.1 | |
| 616 | 6-57 | 0.90-1.20 | 56.1 × 54.3 | 13.4 | corrupted by RFI |
| 736 | 18-45 | 0.46 | 61.5 × 45.5 | 0.5 | |

In Tab. 6.4 we show the main parameters of the observations: channels where the galaxy is detected, achieved noise per beam, beam size (without smoothing), 1-sigma sensitivity per beam in M$_\odot$ and information about problems with the observations. The survey is typically sensitive up to $10^6$ - $10^7$ M$_\odot$ per beam.

### 6.4.4 Notes to individual galaxies

In this section we present some notes describing the HI data for the galaxies in the VLA subsample (without RFI problems). Note that this does not intend to be a full analysis of the observations, but just to make a general description of the HI data attending to the HI distribution, velocity field and channel maps. A further detailed analysis of each galaxy will be performed in the future, as we have done for CIG 96 (see Chapter 7).

Note that in some cases the resolution is not high enough to permit discrimination of any possible irregularity but for five of these galaxies new observations performed at the VLA in its C configuration will allow us to do so in the future.

#### Symmetric single-dish HI profiles

1. **CIG 463:** It is a Scd galaxy with a quite irregular central region (seems like two nuclei or central region is off-centered) and with bright HII regions which appear to form a ring. It probably has a relevant amount of dust in the center since the HI is well centered. We would need images in two bands, B and I, or a NIR image, in order to confirm that this is the case. Surprisingly the single-dish HI profile is weaker than the VLA one. The HI extent of this galaxy is 5.5 $'$and the

[1]To calculate the level of the contours in atoms $cm^{-2}$ from the value of mJy beam$^{-1}$ km s$^{-1}$ :

$$N(HI)[cm^{-2}] = 1.823 \times 10^{18} \int T(v)dv \quad (6.1)$$

assuming a low optical depth of the HI. For the VLA in its D configuration at 1.4 GHz the conversion factor from mJy to K is 3.3:

$$N(HI)[cm^{-2}] = 1.8224 \times 3.3 \times 10^{18} \int S_v[mJybeam^{-1}]dv \quad (6.2)$$

HPBW beam size of GBT is 8.5 ′. Therefore we would not expect such a flux loss in the GBT observation, unless there is some problem in its calibration. There were some interferences in the VLA observations, but we were able to eliminate them by flagging bad visibilities. The resulting HI distribution and velocity field are very symmetric. We see a hint of warp in the velocity field located in the approaching side, where an extension of the HI is seen towards the South-West, at velocities from about 2108.8 to 2129.7 km s$^{-1}$ (see channel maps). In the primary beam we do not find any companion around the galaxy which could be the responsible for this warp, both attending to the optical revision or in our HI observation. Higher angular resolution images are needed in order to understand this possible irregularity.

2. **CIG 736:** It is a very nice example of spiral galaxy, classified as Sbc. It is very symmetric both in the optical and in HI. The HII regions are located regularly along the spiral arms (Ryder & Dopita 1993). Looking at the HI distribution and channel maps we see that some extensions are probably present, both in the receding and approaching sides. This could be just an effect of the spiral arms. A depression in the central region of the galaxy seems to be present as well, just where the radio-continuum is strong (Condon 1987). The comparison of HI profiles suggest that we are losing some HI emission in the VLA observation, but the shape remains very symmetric. No HI companions are found in the VLA primary beam, and the optical companions are likely to be far away from the galaxy or very small in comparison with the main galaxy.

**Asymmetric single-dish HI profiles**

1. **CIG 96:** CIG 96 is a barred galaxy with two arms which are slightly asymmetric one with respect to the other. The HI is extremely asymmetric, as can be seen from a first inspection in the moment 0 distribution. It is relevant to note that we have found a HI-rich companion (see Fig. 6.2), but this is probably too small to have caused such a damage. The properties and modelling of the atomic gas of this galaxy are the subjects of Chapter 7.

2. **CIG 123:** This galaxy is a SBbc galaxy with two arms emerging from a ring-like structure. It is quite asymmetric in the optical: one of the arms (NE) is very pronounced while the other (SW) is more diffuse. Interferences were present in the HI data but we flagged most of them and reduced their effect. The VLA HI profile seems to be more symmetric than the single-dish one. Probably there was a problem with the single-dish observation and it would have been reasonable to classify this galaxy as one having a symmetric HI profile. The outer regions of the HI seems to be more extended in the approaching side, and the two maximum in the HI distribution may be related to the two spiral arms. The velocity field is slightly asymmetric. No companions are found in HI, and only three optical ones are catalogued by Verley (2006).

3. **CIG 134:** It has been classified by Sulentic et al. (2006) as S0, and as Sb in NED. The morphological classification is difficult given the low angular resolution of the optical images available. It seems that this galaxy presents shells in the optical. We also find weak interferences in the HI data, but we mostly could edit the data. The HI profile is well reproduced in comparison with the HI single-dish profile. The velocity field is asymmetric and the HI distribution is more extended in the receding side. No companions are detected up to the sensitivity of the VLA observation, and only two are catalogued in the optical and likely to be just projected.

4. **CIG 551:** It is a Sbc galaxy (Sulentic et al. 2006) seen edge-on with two arms. The arm of the approaching side seems more diffuse in the optical than the other (see SDSS image for example), but this could be explained by extinction since it corresponds to the receding arm. Both the HI distribution and the velocity field are very symmetric, and no companion galaxy is found neither in the HI nor in the optical (all the close companions have velocities much larger than the main galaxy). This was a galaxy selected due to the asymmetry in its HI profile (GBT) but the VLA profile turned to be symmetric.

5. **CIG 660:** It is a barred galaxy classified as Scd - Sd and presents two arms. It is very diffuse and asymmetric in the optical. The VLA HI profile reproduces well the one from GBT. Although it seems that we lose some flux in the receding side of the galaxy, this is due to the baseline of the VLA profile. The HI distribution (mom 0) is quite symmetric but the velocity field is not, and this causes the lopsidedness. No gas-rich companions are seen close to this galaxy.

6. **CIG 744:** This is a Sc galaxy, irregular and asymmetric in the optical with one arm being much brighter than the other (see POSSII image for example). Again the HI profile is not as lopsided as the single-dish observation told us. Probably a pointing problem caused this asymmetry in the single-dish profile, although this is not expected because of the optical to HI extent ratio for this galaxy. The HI distribution is very symmetric but the velocity field shows a strong irregularity in the approaching side.

7. **CIG 812:** This galaxy is classified as Sbc, with two arms and is asymmetric in the optical. The VLA HI profile and the single-dish agrees reasonably well. We see irregularities in both the HI distribution and velocity field. It is remarkable the extension to the West in channels 3174.6 to 3216.6. The velocity field is nearly symmetric up to the more external regions, where the approaching side's rotation curve is flatter. It presents a companion at v=3074 at $\alpha$=17:32:14.76, $\delta$=16.34.50.9 (see Fig. 6.2), but as in the former cases (CIG 96 and 421) the companion has of the order of $M_{HI} \sim 10^6$ (it is indicated below the HI profiles in the composition of images for this galaxy).

### 6.4.5 $R_{HI}$ as a function of the optical extent and $M_{HI}$

We briefly study the relation between the HI to optical extent ($R_{HI}$ vs $D_{25}$) and $M_{HI}$ vs $R_{HI}$. The latter is seen to be very tight (e.g. Verheijen, 2002). In fact, the correlation between $M_{HI}$ and the linear optical diameter is seen to be more spread than using $R_{HI}$. This is shown in Fig. 6.4(a) and Fig. 6.4(b). The data set is detailed in Tab. 6.5: distance, linear optical size, angular HI diameter (at a 1 M$\odot$ pc$^-$2 level), physical HI radius and HI mass. $R_{HI}$ vs $M_{HI}$ is quite tight for our VLA subsample, in agreement with Verheijen (2002). Our fit is $\log(M_{HI})= (0.92 \pm 0.07) \times \log({R_{HI}}^2) + (6.9 \pm 2.0)$, whereas in Verheijen (2002) is: $\log(M_{HI})= 0.94 \times \log({R_{HI}}^2) + 6.7$. The scatter is large when we represent the optical linear size versus the HI extent, as can be seen in Fig. 6.4(b). The fit is $\log(a)=(0.7 \pm 0.2)\times \log(R_{HI}) + (0.3 \pm 0.3)$ . These values are in agreement with the coefficients in Broeils & van Woerden (1994, see Chapter 2).

## 6.5 Results

In this section we summarise the properties of the HI for this set of isolated galaxies. None of these galaxies are clear interacting systems and their HI distribution and velocity field are very symmetric when compared with galaxies in denser environments, even if we consider some of the galaxies with the most lopsided HI profiles. The exception is CIG 96, which shows an important lopsided HI distribution and kinematics. This is without any doubt the most asymmetric galaxy in our subsample and will be studied in more detail in the following chapter.

The summary of the properties of these galaxies is presented in Tab. 6.6. We find that the presence of HI-rich companions does not seem to be the cause for the found asymmetries. Our data did not show evidences of pronounced tidal features, although short tails might still be unresolved by the beam. With this in mind we will answer the following questions:

1. Are there HI-rich companions around isolated galaxies with lopsidedness in their HI profiles? There are no objects with comparable sizes and masses in the surroundings of these galaxies. Moreover, only a few small companions are found in the optical but most of these objects are expected to be located in the background (this is the case of CIG 551, 744 or 463, for example)

[1] 1 M$\odot$/pc$^{-2}$=1.2 $\times$ $10^{20}$ cm$^{-2}$

Table 6.5: HI, optical sizes and $M_{HI}$ for the galaxies in the VLA subsample.

| CIG | $Dist_{75}$ (Mpc) | a (kpc) | $D_{HI}$ ($'$) | $R_{HI}$ (kpc) | $M_{HI}$ ($10^9$ $M_\odot$) |
|---|---|---|---|---|---|
| Asymmetric single-dish prof. | | | | | |
| 96 | 17.3 | 48.0 | 16.4 | 41.2 | 7.53 |
| 123 | 76.2 | 23.4 | 6.7 | 73.9 | 24.21 |
| 134 | 67.9 | 21.4 | 3.9 | 38.3 | 4.16 |
| 551 | 32.1 | 33.3 | 5.5 | 25.8 | 4.74 |
| 660 | 28.5 | 21.3 | 4.5 | 18.5 | 1.51 |
| 744 | 34.8 | 30.1 | 5.2 | 26.5 | 4.28 |
| 812 | 41.0 | 25.1 | 9 | 53.7 | 14.55 |
| Symmetric single-dish prof. | | | | | |
| 463 | 32.0 | 10.2 | 5.5 | 25.4 | 4.05 |
| 736 | 22.0 | 27.1 | 8.2 | 26.4 | 3.9 |

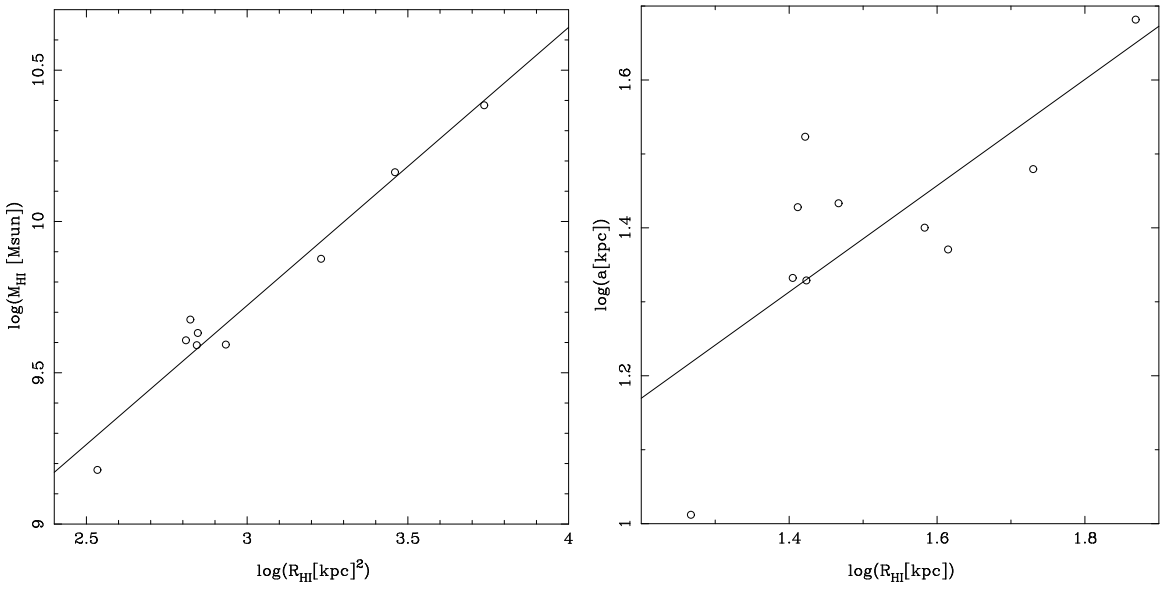


(a) (b)

Figure 6.4: $R_{HI}$ vs $M_{HI}$ and linear optical diameter for our VLA subsample.

Table 6.6: Summary of the HI properties of the sample, ordered (roughly) by disturbance in the HI.

| CIG | Optical asym. | HI profile asym. | HI-rich companion | Lopsided HI distr. | HI kin. |
|---|---|---|---|---|---|
| 96 | ? | Y | Y | Y | Y |
| 812 | Y | Y | Y | Y | ? |
| 134 | Y (shells) | ? | | ? | Y |
| 660 | ? | Y | | | Y |
| 744 | Y | Y | | | Y |
| 463 | Y | | | Y | ? |
| 736 | | | | | ? |
| 123 | | | | ? | ? |
| 551 | | | | | |

because they are too small. Only in three cases we have found HI-rich companions, that is CIG 96, 421 (although the plots are not included due to interferences) and 812, but have masses of around 100 times lower than the galaxies and we do not see any clear signature of interaction with them (e.g. tidal tails).

2. Is the lopsidedness in the HI connected to optical disturbances?: Although our criteria to decide whether a galaxy is optically disturbed is rather subjective, we see that there is some kind of correspondence between optical asymmetry and lopsided H I distributions. This is in disagreement with other studies which claim that no connection is seen between asymmetries in the optical or in the HI (e.g. Wilcots & Prescott 2004).

3. Is the lopsidedness in the HI profile due to asymmetries in the HI distribution or in the velocity field?: The asymmetries in the HI profiles are intrinsic to the galaxies and are not a result of projection with gas rich companions. It seems that HI kinematics disturbances are the rule more than the exception, even if the HI distribution and the HI profile looks like symmetric. There are no galaxies with lopsided HI distributions and without irregularities in the moment 1 distribution. Therefore the lopsidedness in the HI profiles have (almost) always the contribution of the velocity field. We have not found tidal tails in the asymmetric objects, except one small extension in CIG 463 (with hints both in the distribution and the velocity field). Whatever the reason for the lopsidedness is, we visually see that in many cases that the rotation curves for the different sides of the galaxies are not symmetric (CIG 96, 812, 463, 660, 736 and 744), especially in the external regions of the galaxies.

4. The $R_{HI}$ - $M_{HI}$ relationship is very tight, as reported previously for other samples of galaxies, as that for the galaxies in the Ursa Major Cluster studied by Verheijen (2002). Our fit is in agreement with them.

## 6.6 Discussion and conclusions

We have selected a sample of galaxies with minimized probability of contamination by comparable sized companions in order to investigate the origin of asymmetries in galaxies without external stimuli. We have mapped a number of galaxies found in the HI survey of isolated galaxies described above, concentrating on the most extreme cases of galaxies showing significant asymmetries in their HI profiles, while being in the low density end of our sample of isolated galaxies.

We see that most of the asymmetric profiles can be explained by irregularities in the velocity field, and only in some cases the HI distribution is also perturbed. The galaxies included in Pisano et al.

(2002) presents in general more irregular HI distributions than in our sample. This is probably due to our better isolation selection.

In order to assess the problem of why the rate of lopsidedness in the HI profiles is so large in samples of isolated galaxies, we can propose the following explanations:

1. The perturbation is more long-lived than previously thought. This can be due because of: a) the winding out by differential precession is quite long in the outer parts of galaxies (Baldwin et al. 1980), b) weakly damped modes (Weinberg 1994), c) amplification of density waves (Shu et al. 1990; Syer & Tremaine 1996), or d) the disk is distorted in a lopsided halo (Levine & Sparke 1998; Noordermeer et al. 2001).

2. The perturbation could be forced by tidal interactions (e.g. Kornreich et al. 2002), minor mergers (Zaritsky & Rix 1997) or accretion of external gas along cosmological filaments (Bournaud et al. 2005). These perturbations could be short-lived and depend on the number of interactions that suffer the galaxy (minor mergers or gas accretion may be more likely then because a galaxy can suffer a higher number of possible interactions). Walker et al. (1996) have done N-body simulations of galaxies perturbed by minor mergers, and the asymmetries can live for 1 Gyr. However it seems that there is no correlation between the existence of companions and the lopsidedness (Wilcots & Prescott 2004).

Since we can not test 1) with our data we will focus on 2) and assume from now on that the environment plays the key role in this problem. The galaxies in our subsample lack of comparable sized companions, but spiral galaxies are usually thought to be surrounded by small satellites. Moreover, around this set of galaxies, a reduced number of small companions are seen in the optical, although they are probably located in the background (as in the case of CIG 551). In fact, although the HI flux limit is typically $5 \times 10^6$ M$\odot$ (so we would detect Magellanic mass galaxies), we only see three HI-rich companions. At any rate, these satellites are probably not massive enough to have produced these asymmetries. If gas accretion (or high velocity clouds) is the solution to this (Bournaud & Combes 2005), the $M_{HI}$ of the HI clouds would be lower than our detection limit.

In addition, no tidal tails or any other signature of major interaction is present, and in most cases the HI is more or less settled (except CIG 96). In our subsample, if a galaxy presents irregularities in the HI distribution then its velocity field also suffers of some kind of irregularity, but the opposite is not always true. Then the event that produced the asymmetry still remains visible in the velocity field for a longer time than for the HI distribution, and this is what maintains the lopsidedness in the HI profiles. This is probably the reason of why we see such a high percentage of asymmetric profiles in our sample of isolated galaxies. Verheijen (2002) also stated that the majority of their galaxies with lopsided HI profiles showed kinematical asymmetries, even in systems that were non-interacting and with regular HI distributions.

From a visual inspection we see that the rotation curve of the galaxies seems to decline faster in the end of one side with respect to the other. This is the case for example of CIG 96, 123, 736, 744 and 812. The asymmetries in their velocity fields could have been caused by a common origin. We are probably seeing the result of a capture of a satellite just completed, and the HI still shows in many cases hints of irregularities in the velocity fields (and sometimes in the HI distribution), especially in the outer regions of the HI disk. The differences in shape of their velocity field asymmetries may be due to different degrees in the strength of the perturbations, or maybe we see similar objects in different stages of relaxation after the same kind of perturbation (by minor mergers or accretion of gas). If this scenario applies, It is probably a combination of these two the most reasonable answer.

## 6.7 Future work

A number of works are planned in the near future, that we describe as follows:

1. We will calibrate and analyze new observations of five of these galaxies (among them is CIG 96) from the VLA in its C configuration for a detailed higher spatial resolution study.

2. For the galaxies whose asymmetries are intrinsic we will determine, using the GIPSY software, the mean rotation curve based on the velocity field model and the 3-D spatial distribution best fitting the data. This will allow us to decide if the asymmetry is due to a disk warping, non-circular motions, etc. This analysis has already been achieved for one of the galaxies in the sample, CIG 96, which is presented in the Chapter 7.

## 6.8 Final VLA synthesis images

In this section we present the final VLA synthesis images, in order of ascending RA.

| **Source: CIG 96** | | |
|---|---|---|
| Morphology | | SBc |
| $\alpha$(2000) | (hh:mm:ss) | 02:15:27.6 |
| $\delta$(2000) | (dd:mm:ss) | 06:00:09.0 |
| Optical field sizes | ($'\times\ '$) | 5.6 × 5.6, 25.4 × 25.4 |
| Observing time | (hours) | 4 |
| Central velocity | (km s$^{-1}$) | 1572 |
| Spatial resolution | ($''$) | 15 |
| Number of channels | | 64 |
| Velocity resolution | (km s$^{-1}$) | 10.4 |
| Beam size | ($\alpha \times \delta$, $''\times\ ''$) | 49.8 × 46.0 |
| Conv. beam size | ($\alpha \times \delta$, $''$) | 70.4 × 65.3 |
| PA (N to E) | ($^o$) | -6 |
| **HI data parameters** | | |
| **Channel maps** | | |
| Field size, channels | ($'$) | 17.0 × 17.0, 22 - 46 |
| Velocities | (km s$^{-1}$) | 1436.7 - 1686.6 |
| rms noise channel | (mJy/beam) | 0.66 |
| Contours | (mJy/beam) | 3, 10, 21, 42, 56, 70, 84, 98, 112 |
| **Global HI profile** | | |
| | | VLA — GB43m (HG98) |
| HI flux | (Jy km s$^{-1}$) | 103 — 102.8 |
| Heliocentric velocity | (km s$^{-1}$) | 1557 — 1562 |
| HI profile width 20% | (km s$^{-1}$) | 238 — 239 |
| $M_{HI}$ | ($10^9$ $M_\odot$) | 7.24 — 7.53 |
| **HI maps** | | |
| Field size | ($'\times\ '$) | 5.6 × 5.6 |
| HI map contours | (mJy/beam km s$^{-1}$) | 1, 100, 250, 750, 1000, 1250, 1500, 1750, 2000, 2250, 2500 |
| | ($10^{20}$ cm$^{-2}$) | 0.1, 6, 15, 45, 60, 75, 90, 105, 120, 135, 150 |
| Velocity contours | ($v_{max}$ - $v_{min}$, $\delta$v) (km s$^{-1}$) | 1465 - 1675, 15 |
| **Comments** | | |
| Companion $\alpha$=02:16:26.90, | $\delta$=05:56:24.0, v=1605 | (1572-1655), $M_{HI}\simeq 10^6$ $M_\odot$ |

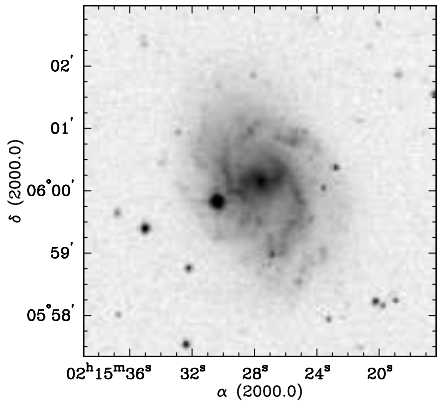


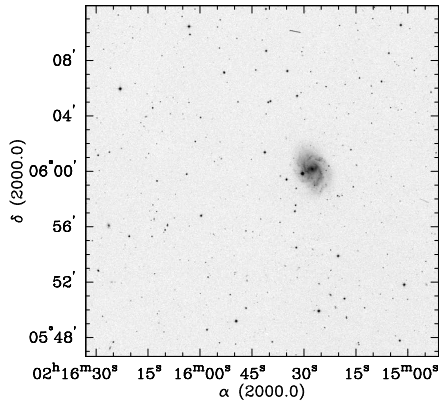


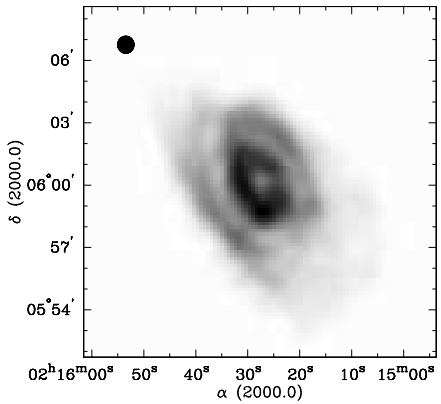


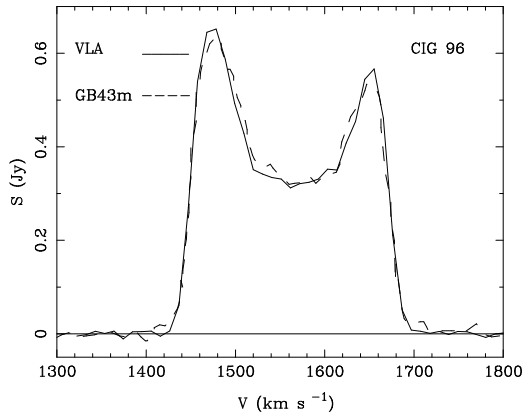


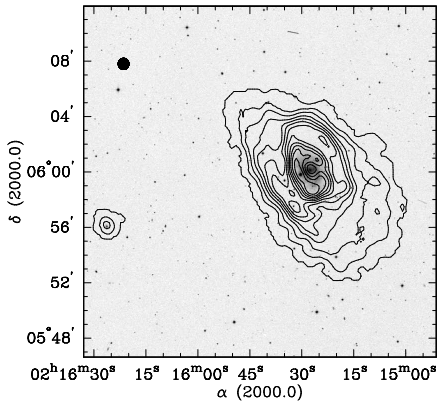


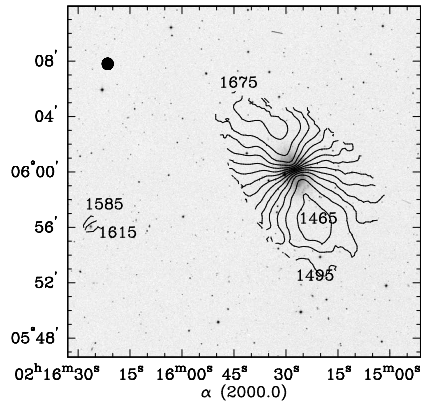

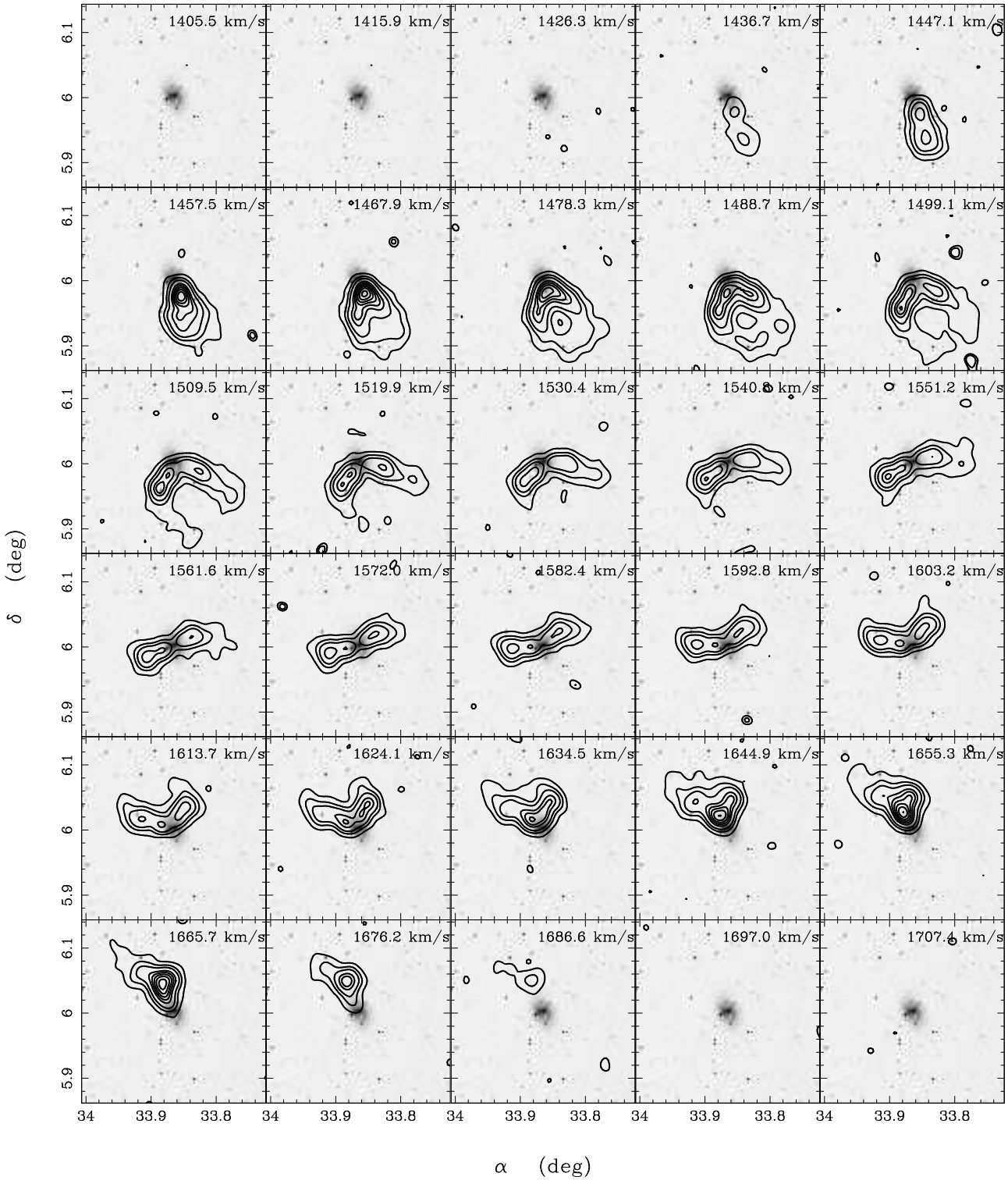


Figure 6.5: **CIG 96**

**Source: CIG 123**

| | | |
|---|---|---|
| Morphology | | SBbc |
| $\alpha$(2000) | (hh:mm:ss) | 03:12:51.30 |
| $\delta$(2000) | (dd:mm:ss) | 04:42:26.0 |
| Optical field sizes | ($'\times\ '$) | 2.8 × 2.8 , 17.0 × 17.0 |
| Observing time | (hours) | 3.0 |
| Central velocity | (km s$^{-1}$) | 5903 |
| Spatial resolution | ($''$) | 15 |
| Number of channels | | 64 |
| Velocity resolution | (km s$^{-1}$) | 10.6 |
| Beam size | ($\alpha \times \delta$, $''\times\ ''$) | 84.6 × 52.5 |
| Conv. beam size | ($\alpha \times \delta$, $''\times\ ''$) | 119.5 × 74.2 |
| PA (N to E) | ($^\circ$) | -48.7 |

**HI data parameters**

**Channel map**

| | | |
|---|---|---|
| Field size, channels | ($\alpha \times \delta$, $'\times\ '$) | 17.0 × 17.0, 19 - 48 |
| Velocities | (km s$^{-1}$) | 5758.2 - 6058.3 |
| rms noise channel | (mJy/beam) | 0.77 |
| Contours | (mJy/beam) | 3, 9, 20, 30, 40 |

**Global HI profile**

| | | VLA — GB91m (HG84) |
|---|---|---|
| HI flux | (Jy km s$^{-1}$) | 17.7 — 17.40 |
| Heliocentric velocity | (km s$^{-1}$) | 5906 — 5903 |
| HI profile width 20% | (km s$^{-1}$) | 279 — 278 |
| $M_{HI}$ | ($10^9$ $M_\odot$) | 24.21 — 23.93 |

**HI maps**

| | | |
|---|---|---|
| Field size | ($'\times\ '$) | 11.4 × 11.4 |
| HI map contours | (mJy/beam km s$^{-1}$) | 1, 100, 250, 500, 750, 1000, 1250, 1500, 1750, 2000, 2250, 2500 |
| | ($10^{20}$ cm$^{-2}$) | 0.1, 6, 15, 30, 45, 60, 75, 90, 105, 120, 135, 150 |
| Velocity contours | ($v_{max}$ - $v_{min}$, $\delta$v) (km s$^{-1}$) | 5795 - 6005, 15 |

**Comments**

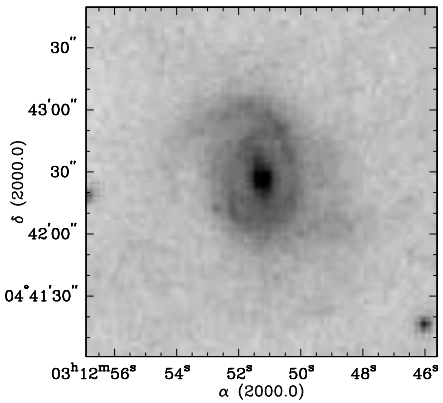


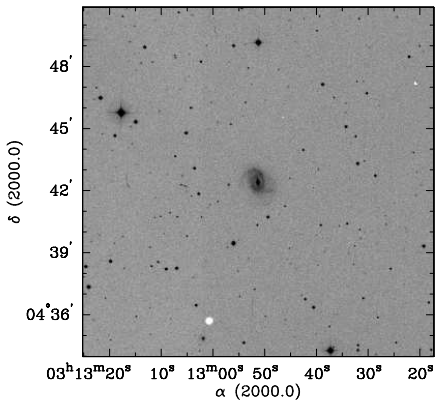


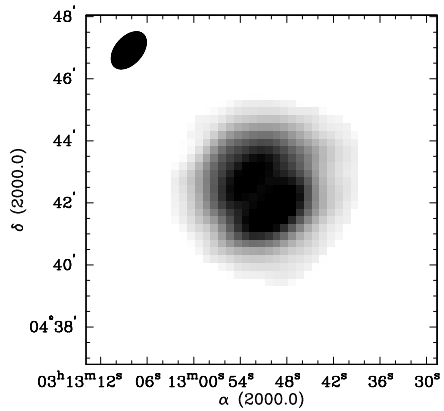


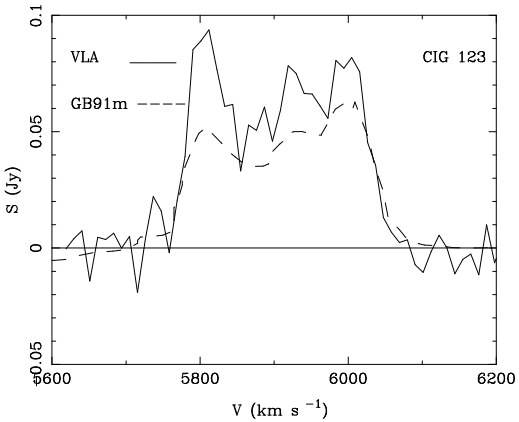


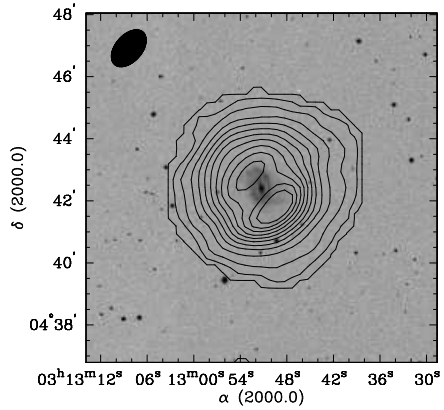


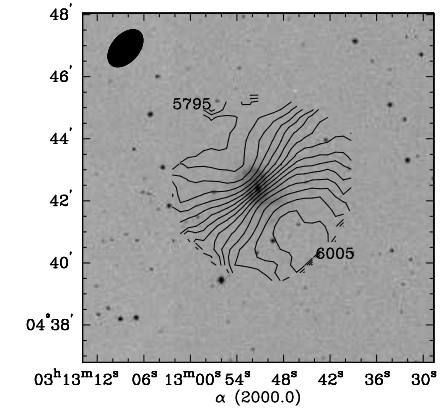

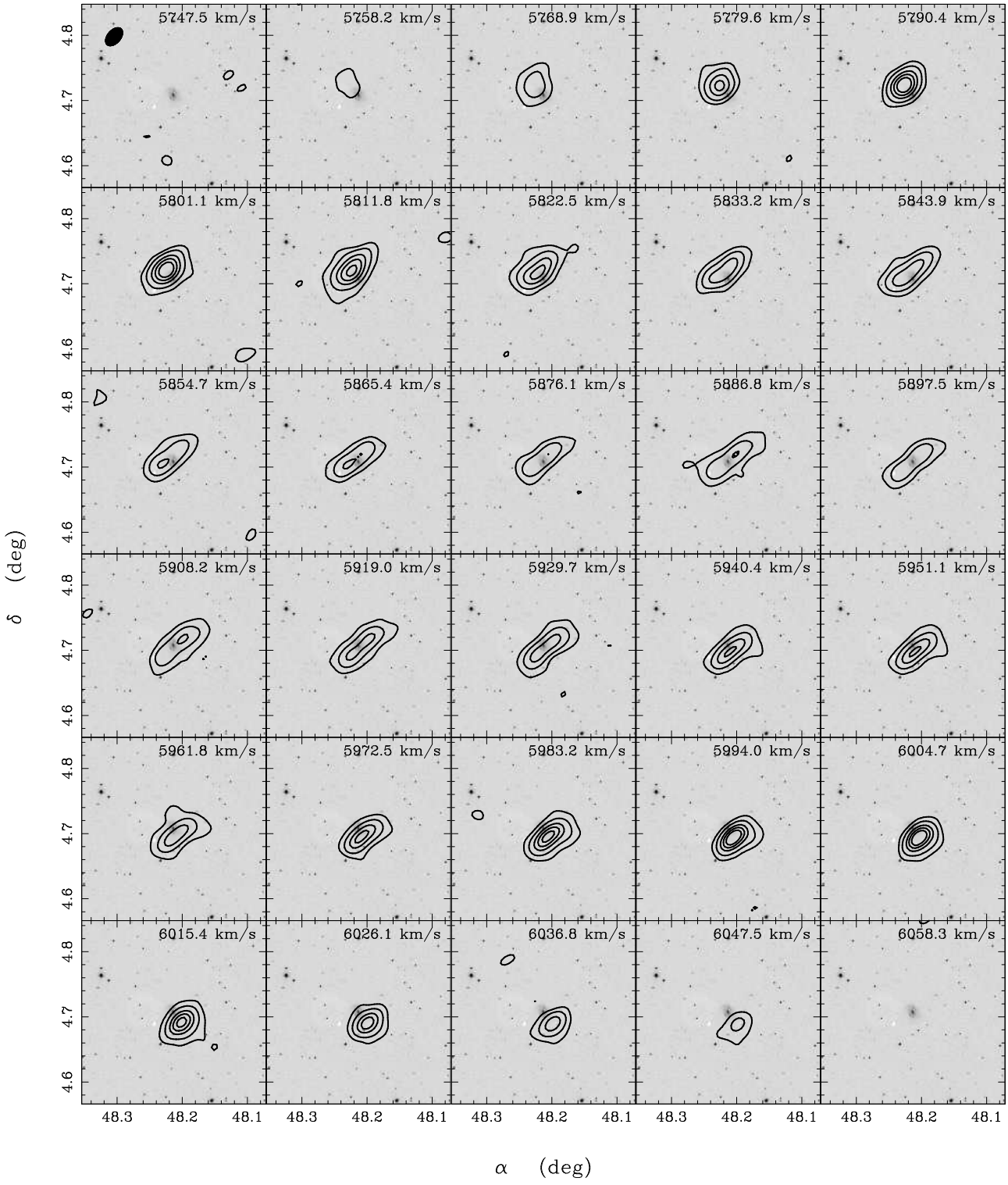


Figure 6.6: **CIG 123**

**Source: CIG 134**

| | | |
|---|---|---|
| Morphology | | Sb |
| $\alpha$(2000) | (hh:mm:ss) | 03:52:14.04 |
| $\delta$(2000) | (dd:mm:ss) | -01:30:28.6 |
| Optical field sizes | ($'\times\ '$) | 2.8 × 2.8, 17.0 × 17.0 |
| Observing time | (hours) | 3.0 |
| Central velocity | (km s$^{-1}$) | 5199 |
| Spatial resolution | ($''$) | 15 |
| Number of channels | | 64 |
| Velocity resolution | (km s$^{-1}$) | 10.6 |
| Beam size | ($\alpha \times \delta$, $''\times\ ''$) | 68.1 × 52.5 |
| Conv. beam size | ($\alpha \times \delta$, $''\times\ ''$) | 96.3 × 74.2 |
| PA (N to E) | ($^\circ$) | 25 |

**HI data parameters**

**Channel maps**

| | | |
|---|---|---|
| Field size, channels | ($\alpha \times \delta$, $'\times\ '$) | 11.4 × 11.4, 17 - 47 |
| Velocities | (km s$^{-1}$) | 5067.7 - 5355.7 |
| rms noise channel | (mJy/beam) | |
| Contours | (mJy/beam) | 0.2, 0.7, 1.4, 2.1, 2.8, 5.6 |

**Global HI profile**

| | | VLA — ERT |
|---|---|---|
| HI flux | (Jy km s$^{-1}$) | 3.72 — 3.79 |
| Heliocentric velocity | (km s$^{-1}$) | 5212 — 5200 |
| HI profile width 20% | (km s$^{-1}$) | 280 — 288 |
| $M_{HI}$ | ($10^9$ $M_\odot$) | 4.04 — 4.16 |

**HI maps**

| | | |
|---|---|---|
| Field size | ($'\times\ '$) | 5.6 × 5.6 |
| HI map contours | (mJy/beam km s$^{-1}$) | 1, 4, 14, 36, 71, 107, 143, 179 |
| | ($10^{18}$ cm$^{-2}$) | 0.6, 24, 84, 216, 427, 643, 860, 1076 |
| Velocity contours | ($v_{max}$ - $v_{min}$, $\delta$v) (km s$^{-1}$) | 5080 - 5320, 30 |

**Comments**

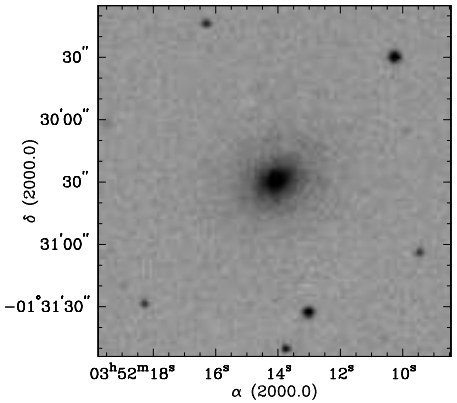


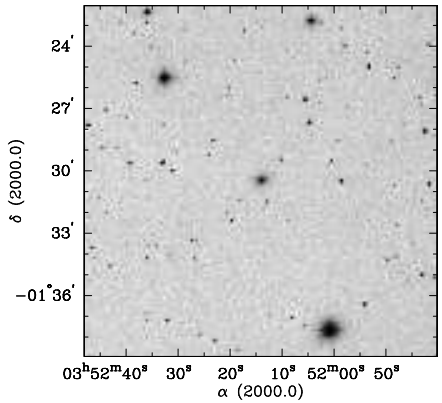


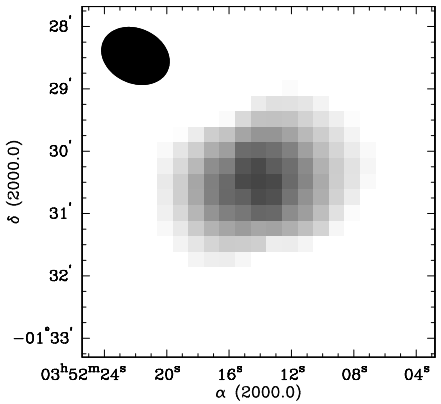


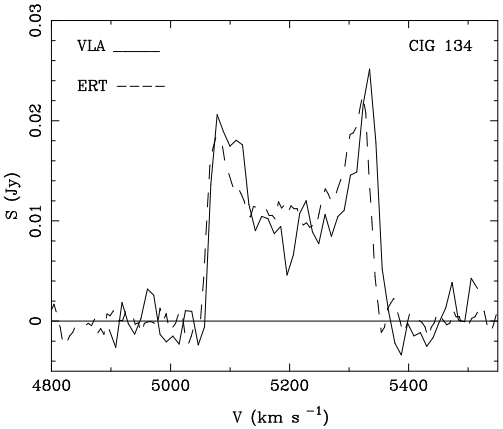


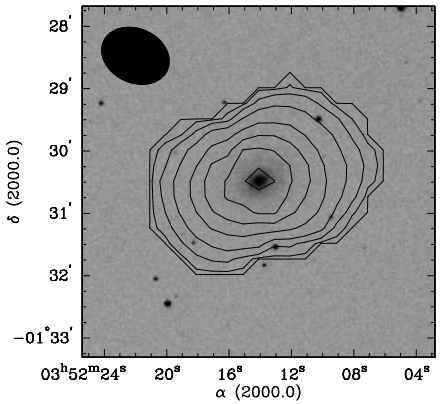


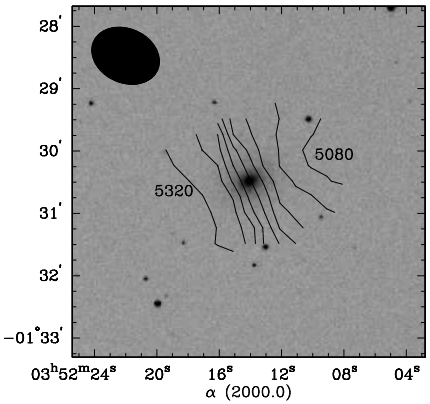

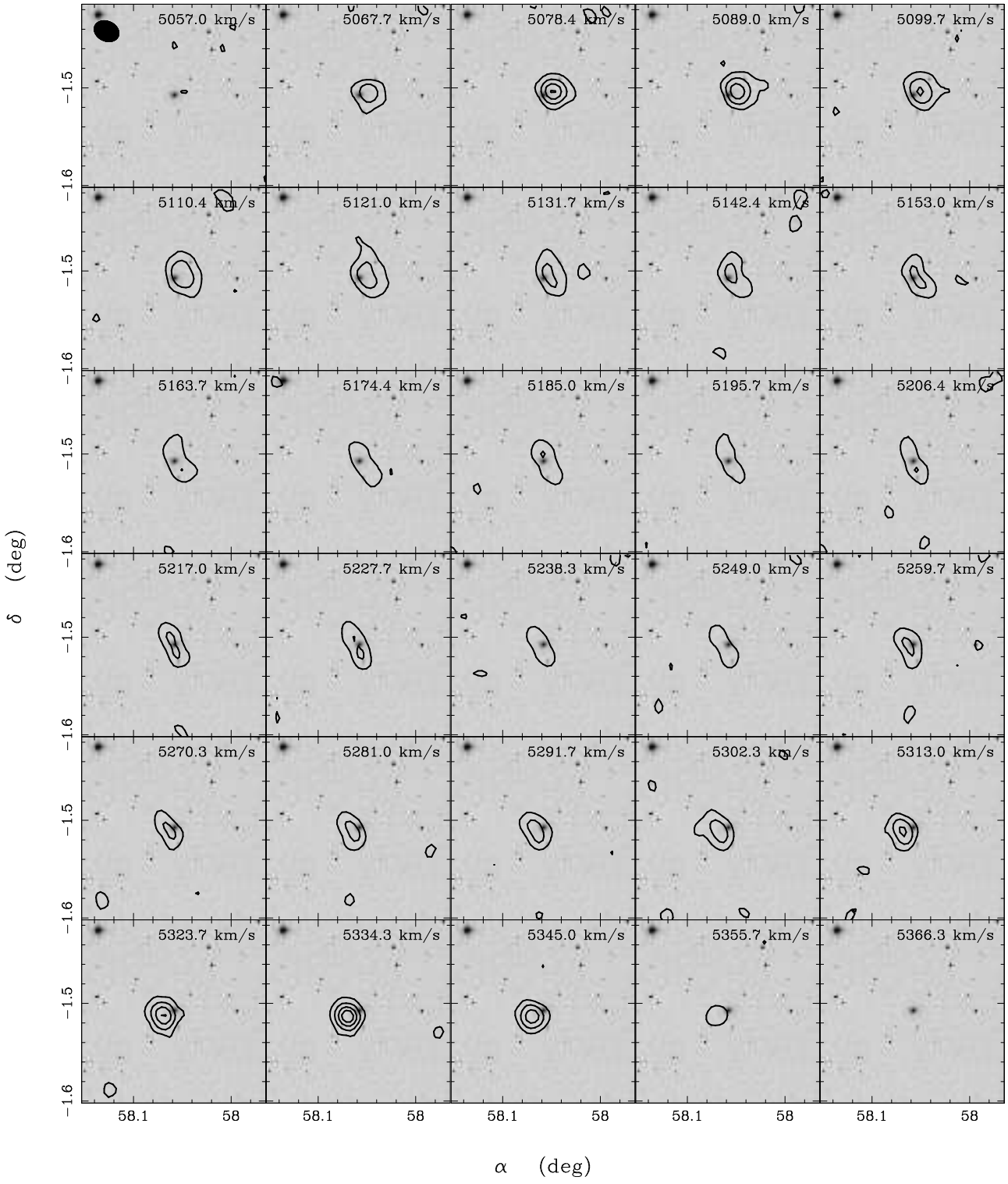


Figure 6.7: **CIG 134**

| **Source: CIG 463** | | |
|---|---|---|
| Morphology | | Scd |
| $\alpha$(2000) | (hh:mm:ss) | 11:06:54.65 |
| $\delta$(2000) | (dd:mm:ss) | 51:12:12.1 |
| Optical field sizes | ($'\times\ '$) | 2.8 × 2.8, 14.0 × 14.0 |
| Observing time | (hours) | 3 |
| Central velocity | (km s$^{-1}$) | |
| Spatial resolution | ($''$) | 15 |
| Number of channels | | 64 |
| Velocity resolution | (km s$^{-1}$) | 10.5 |
| Beam size | ($\alpha \times \delta$, $''\times\ ''$) | 58.0 × 52.2 |
| Conv. beam size | ($\alpha \times \delta$, $''\times\ ''$) | 82.1 × 73.9 |
| PA (N to E) | ($^o$) | 81 |
| **HI data parameters** | | |
| **Channel maps** | | |
| Field size, channels | ($\alpha \times \delta$, $'\times\ '$) | 8.4 × 8.4, 19 - 45 |
| Velocities | (km s$^{-1}$) | 2087.9 - 2328.4 |
| rms noise channel | (mJy/beam) | 0.85 |
| Contours | (mJy/beam) | 4, 7, 14, 21, 42, 56 |
| **Global HI profile** | | |
| | | VLA — GBT |
| HI flux | (Jy km s$^{-1}$) | 22.15 — 16.15 |
| Heliocentric velocity | (km s$^{-1}$) | 2208 — 2206 |
| HI profile width 20% | (km s$^{-1}$) | 240 — 240 |
| $M_{HI}$ | ($10^9$ $M_\odot$) | 5.34 — 4.05 |
| **HI maps** | | |
| Field size | ($'\times\ '$) | 8.4 × 8.4 |
| HI map contours | (mJy/beam km s$^{-1}$) | 100, 250, 500, 750, 1250, 1750, 2250, 2750, 3250, 3750 |
| | ($10^{20}$ cm$^{-2}$) | 6, 15, 30, 45, 75, 105, 135, 165, 196, 226 |
| Velocity contours | ($v_{max}$ - $v_{min}$, $\delta$v) (km s$^{-1}$) | 2120 - 2285, 15 |
| **Comments** | | |

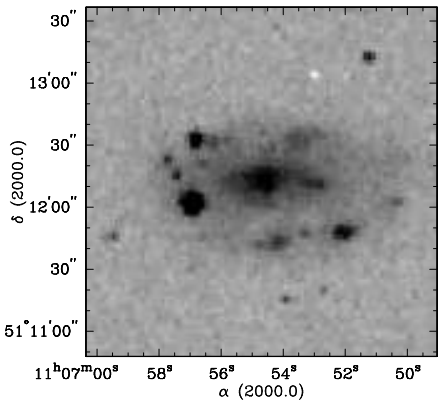


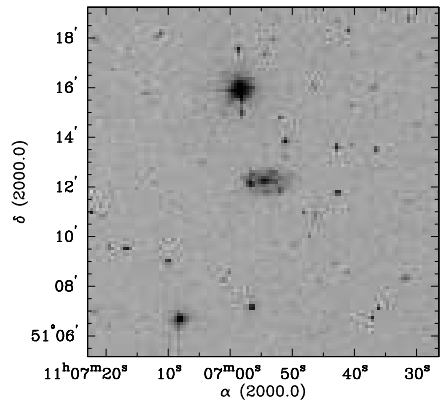


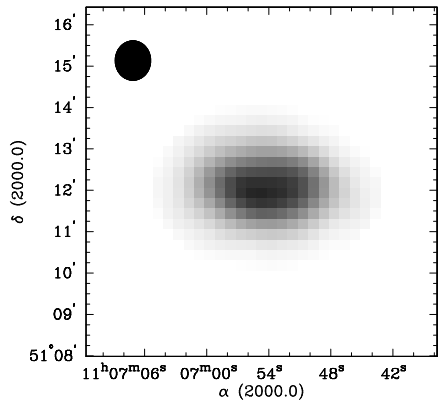


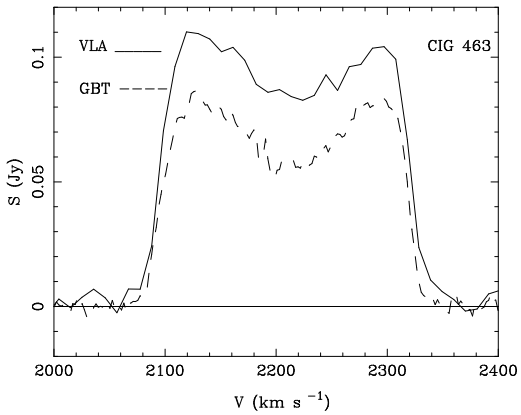


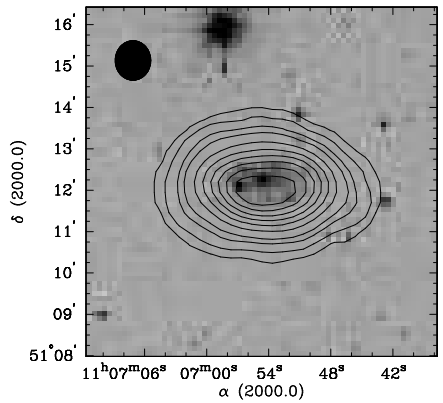


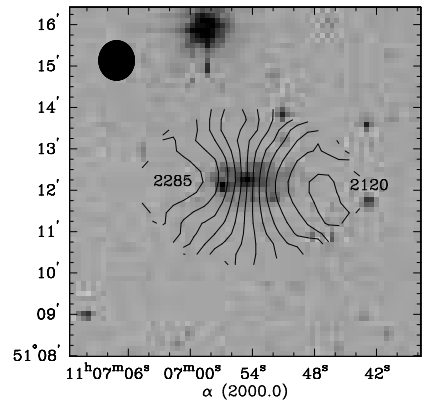

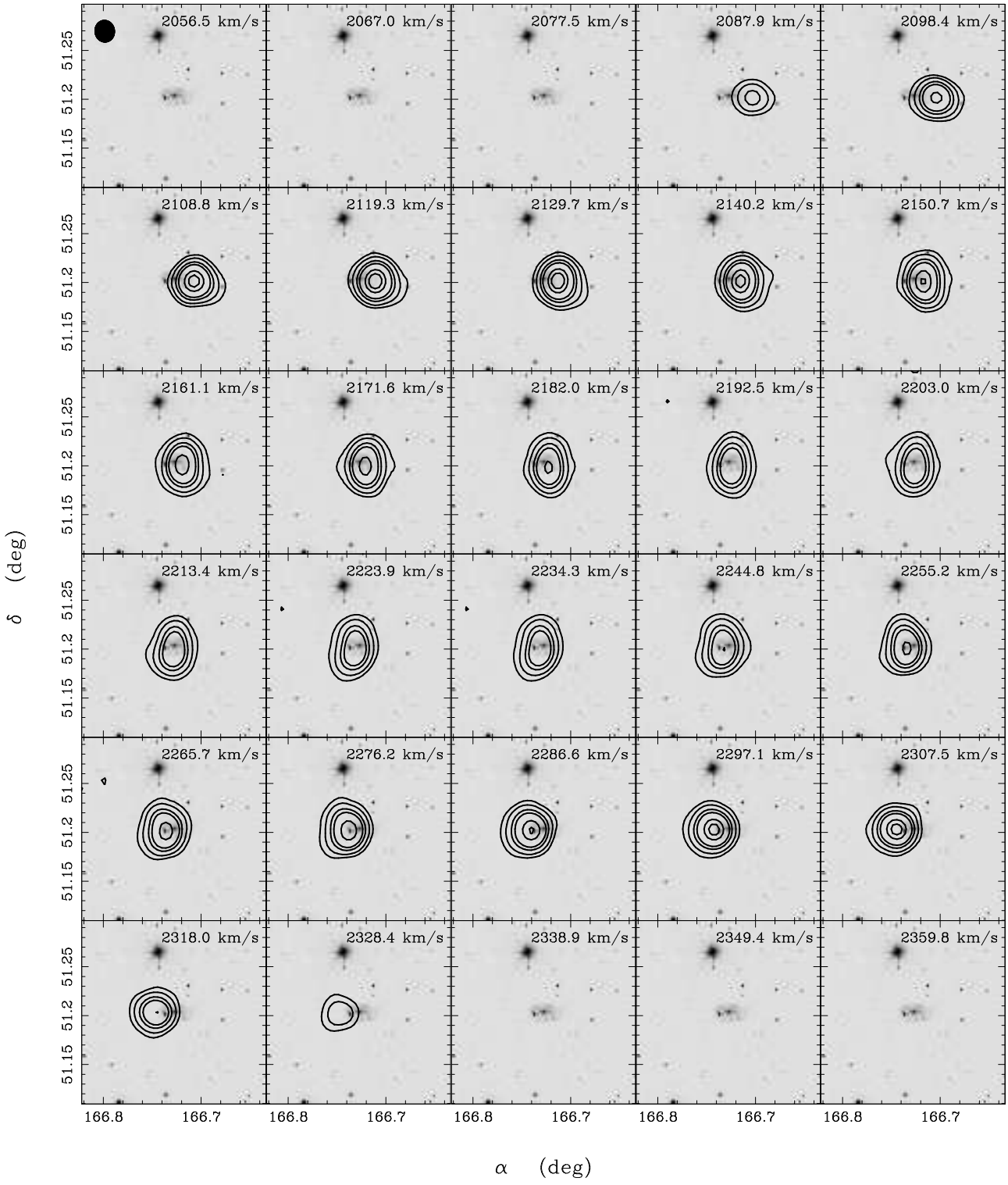


Figure 6.8: **CIG 463**

**Source: CIG 551**

| | | |
|---|---|---|
| Morphology | | Sbc |
| $\alpha$(2000) | (hh:mm:ss) | 12:46:0.73 |
| $\delta$(2000) | (dd:mm:ss) | 64:34:11.8 |
| Optical field sizes | ($'\times\ '$) | 2.8 × 2.8, 14.0 × 14.0 |
| Observing time | (hours) | 3.5 |
| Central velocity | (km s$^-$1) | |
| Spatial resolution | ($''$) | 15 |
| Number of channels | | 64 |
| Velocity resolution | (km s$^-$1) | 10.6 |
| Beam size | ($\alpha \times \delta$, $''\times\ ''$) | 60.6 × 54.6 |
| Conv. beam size | ($\alpha \times \delta$, $''\times\ ''$) | 85.7 × 77.1 |
| PA (N to E) | ($^\circ$) | 67 |

**HI data parameters**

| | | |
|---|---|---|
| **Channel maps** | | |
| Field size, channels | ($\alpha \times \delta$, $'\times\ '$) | 8.4 × 8.4, 19 - 45 |
| Velocities | (km s$^-$1) | 2174.4 - 2425.5 |
| rms noise channel | (mJy/beam) | 0.49 |
| Contours | (mJy/beam) | 3, 7, 15, 30, 40, 50, 60 |
| **Global HI profile** | | |
| | | VLA — GBT |
| HI flux | (Jy km s$^-$1) | 19.55 — 14.75 |
| Heliocentric velocity | (km s$^-$1) | 2303 — 2300 |
| HI profile width 20% | (km s$^-$1) | 253 — 242 |
| $M_{HI}$ | ($10^9$ $M_\odot$) | 4.74 — 3.77 |
| **HI maps** | | |
| Field size | ($'\times\ '$) | 8.4 × 8.4 |
| HI map contours | (mJy/beam km s$^-$1) | 10, 250, 750, 1250, 1750, 2250, 2750, 3750, 4750 |
| | ($10^{20}$ cm$^{-2}$) | 1, 15, 45, 75, 105, 135, 165, 225, 285 |
| Velocity contours | ($v_{max}$ - $v_{min}$, $\delta$v) (km s$^-$1) | 2210 - 2390, 15 |
| **Comments** | symmetric VLA profile | |

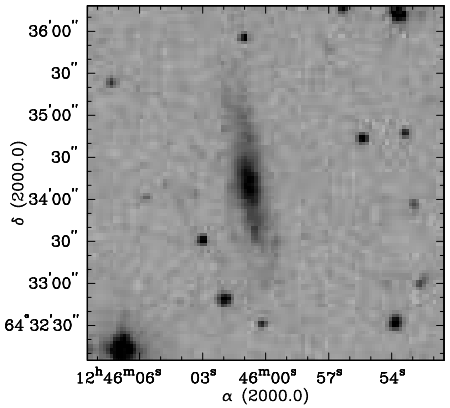


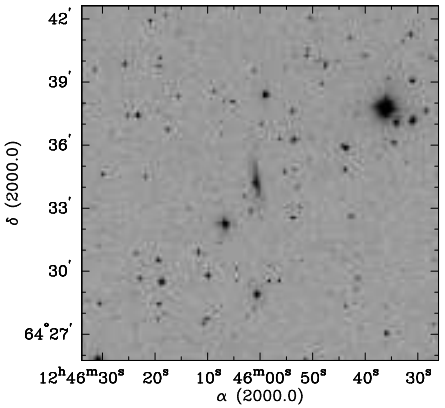


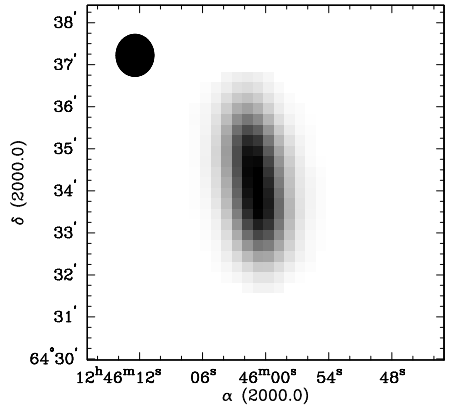


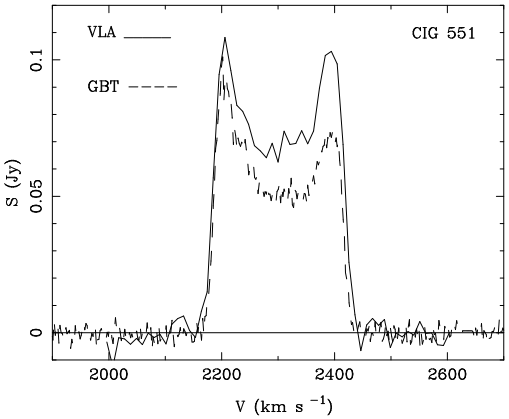


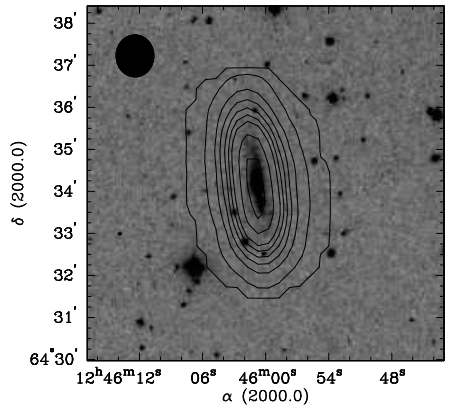


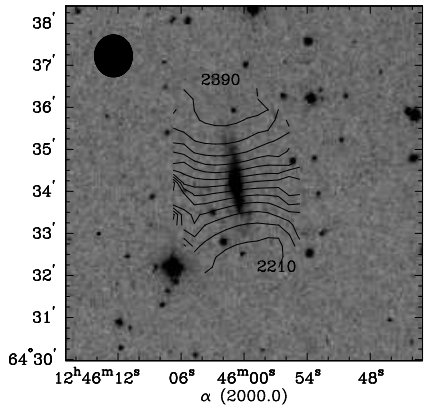

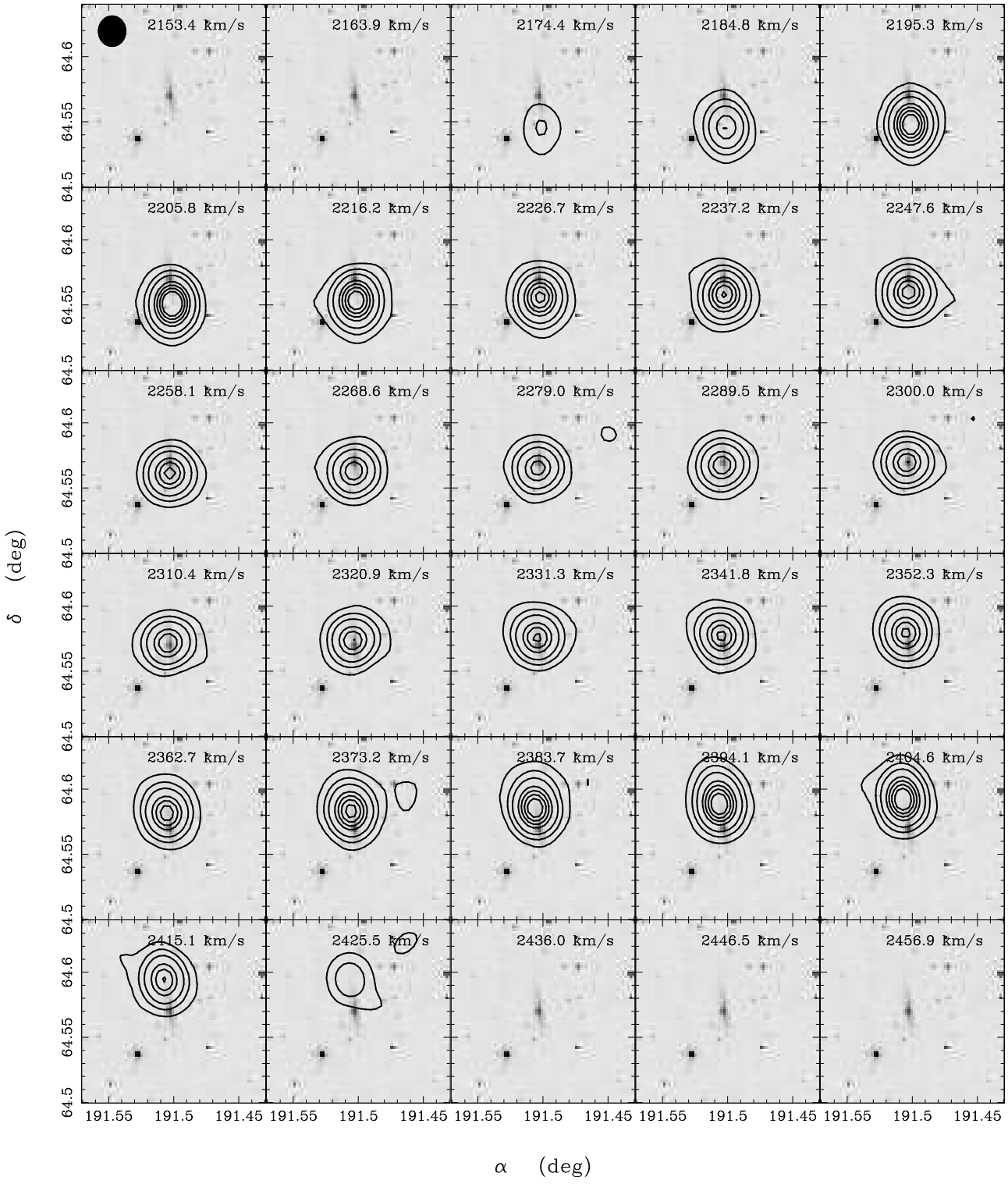


Figure 6.9: **CIG 551**

**Source: CIG 660**

| | | |
|---|---|---|
| Morphology | | SBcd |
| $\alpha$(2000) | (hh:mm:ss) | 15:04:02.32 |
| $\delta$(2000) | (dd:mm:ss) | 77:38:05.5 |
| Optical field sizes | ($'\times\ '$) | 2.8 × 2.8, 17.0 × 17.0 |
| Observing time | (hours) | 3.5 |
| Central velocity | (km s$^{-1}$) | 2136 |
| Spatial resolution | ($''$) | 15 |
| Number of channels | | 64 |
| Velocity resolution | (km s$^{-1}$) | 10.6 |
| Beam size | ($\alpha \times \delta$, $''\times\ ''$) | 60.5 × 47.4 |
| Conv. beam size | ($\alpha \times \delta$, $''\times\ ''$) | 85.5 × 67.0 |
| PA (N to E) | ($^\circ$) | |

**HI data parameters**

**Channel maps**

| | | |
|---|---|---|
| Field size, channels | ($\alpha \times \delta$, $'\times\ '$) | 8.4 × 8.4 , 24 - 40 |
| Velocities | (km s$^{-1}$) | 2062.8 - 2219.6 |
| rms noise channel | (mJy/beam) | 1.0 |
| Contours | (mJy/beam) | 3, 9, 18, 27, 36, 48 |

**Global HI profile**

| | | VLA — GBT |
|---|---|---|
| HI flux | (Jy km s$^{-1}$) | 7.60 — 7.78 |
| Heliocentric velocity | (km s$^{-1}$) | 2141 — 2136 |
| HI profile width 20% | (km s$^{-1}$) | 150 — 148 |
| $M_{HI}$ | ($10^9$ $M_\odot$) | 1.45 — 1.51 |

**HI maps**

| | | |
|---|---|---|
| Field size | ($'\times\ '$) | 8.4 × 8.4 |
| HI map contours | (mJy/beam km s$^{-1}$) | 1, 250, 750, 1250, 1750, 2250, 2750 |
| | ($10^{18}$ cm$^{-2}$) | 6, 1503, 4511, 7519, 10527, 13535, 16543 |
| Velocity contours | ($v_{max}$ - $v_{min}$, $\delta$v) (km s$^{-1}$) | 2090 - 2195, 15 |

**Comments**

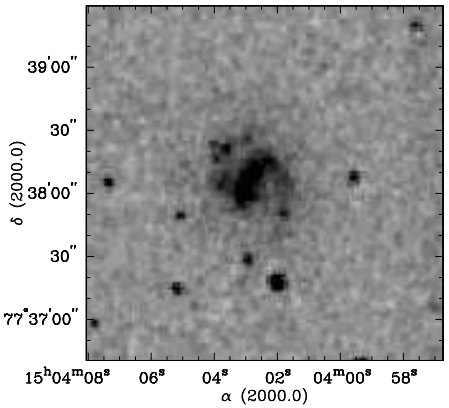


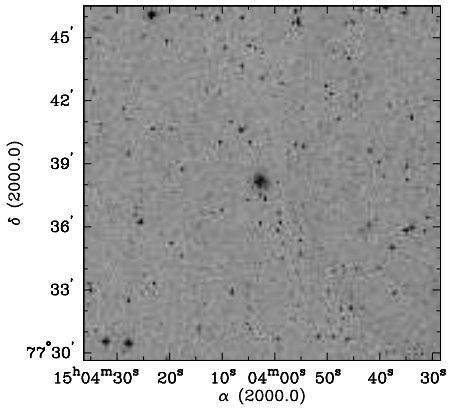


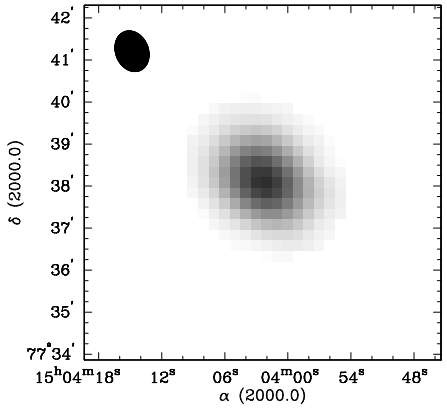


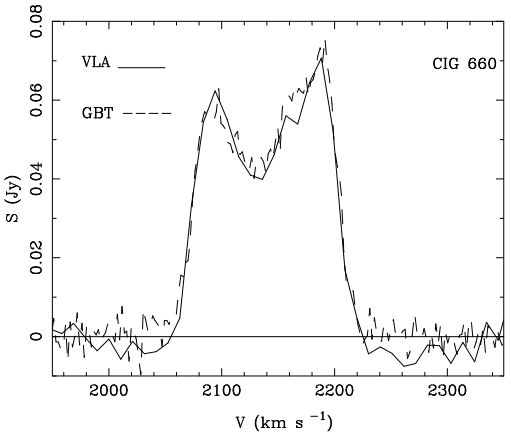


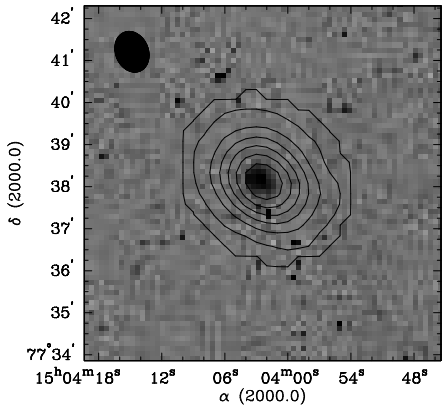


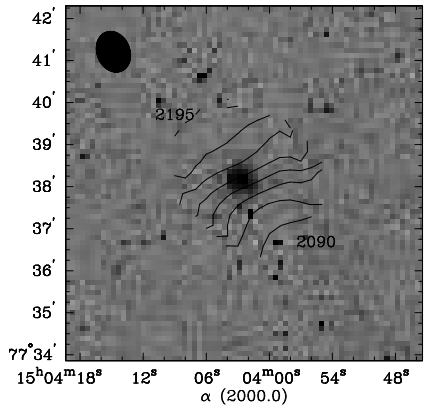

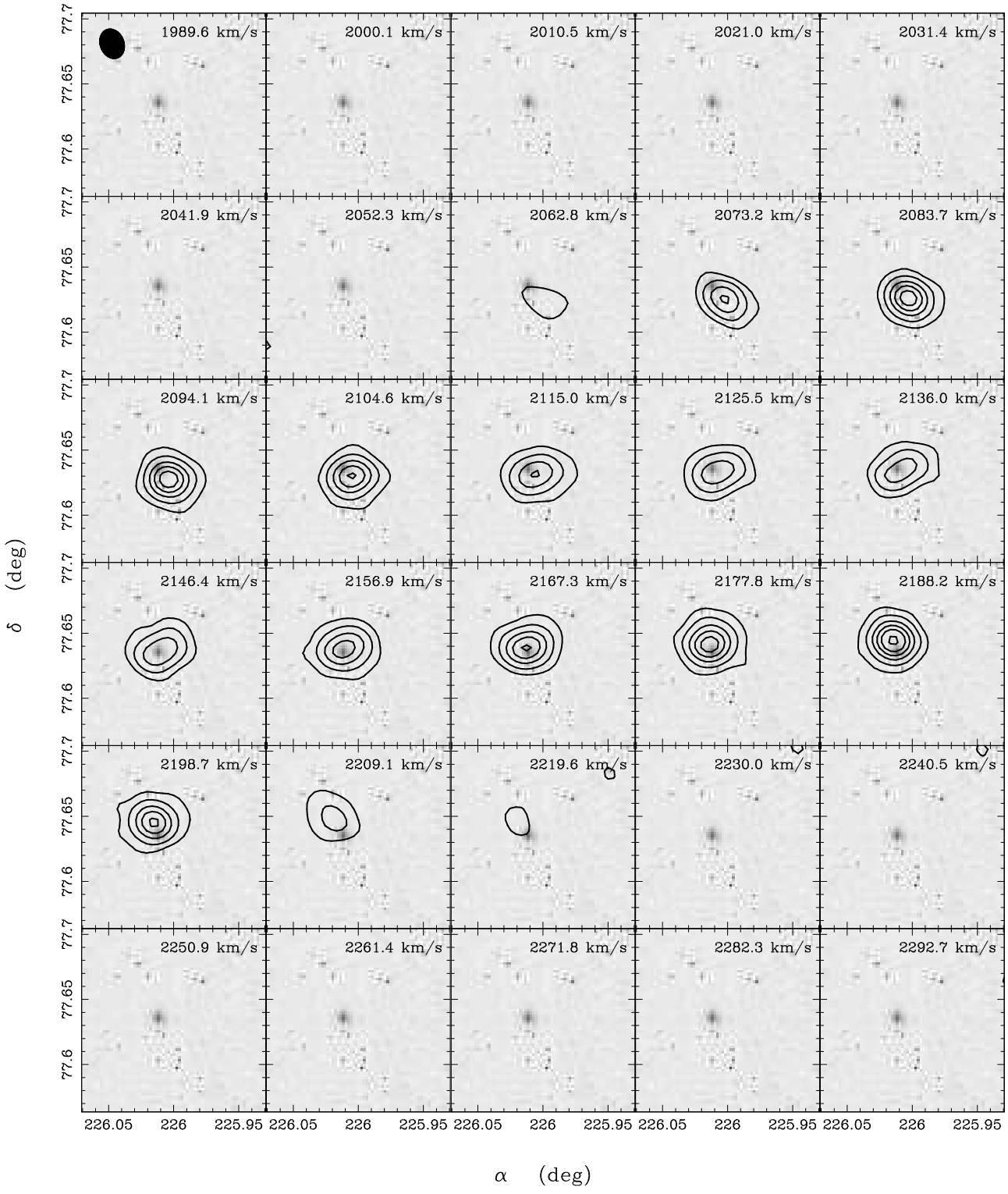


Figure 6.10: **CIG 660**

**Source: CIG 736**

| | | |
|---|---|---|
| Morphology | | Sbc |
| $\alpha$(2000) | (hh:mm:ss) | 16:21:48.62 |
| $\delta$(2000) | (dd:mm:ss) | -02:17:02.9 |
| Optical field sizes | ($'\times\ '$) | 4.2 × 4.2, 25.4 × 25.4 |
| Observing time | (hours) | 4 |
| Central velocity | (km s$^{-1}$) | 1568 |
| Spatial resolution | ($''$) | 15 |
| Number of channels | | 64 |
| Velocity resolution | (km s$^{-1}$) | 10.6 |
| Beam size | ($\alpha \times \delta$, $''\times\ ''$) | 61.5 × 45.5 |
| Conv. beam size | ($\alpha \times \delta$, $''\times\ ''$) | 87.0 × 64.3 |
| PA (N to E) | ($^\circ$) | -43 |

**HI data parameters**

**Channel maps**

| | | |
|---|---|---|
| Field size, channels | ($\alpha \times \delta$, $'\times\ '$) | 5.7 × 5.7, 18 - 45 |
| Velocities | (km s$^{-1}$) | 1385.2 - 1760.2 |
| rms noise channel | (mJy/beam) | 0.46 |
| Contours | (mJy/beam) | 3, 7, 15, 30, 40, 50, 70 |

**Global HI profile**

| | | VLA — GB43m (HG) |
|---|---|---|
| HI flux | (Jy km s$^{-1}$) | 30.31 — 34.29 |
| Heliocentric velocity | (km s$^{-1}$) | 1565 — 1573 |
| HI profile width 20% | (km s$^{-1}$) | 359 — 362 |
| $M_{HI}$ | ($10^9$ $M_\odot$) | 3.456 — 3.9 |

**HI maps**

| | | |
|---|---|---|
| Field size | ($'\times\ '$) | 11.4 × 11.4 |
| HI map contours | (mJy/beam km s$^{-1}$) | 5, 100, 750, 1750, 2750, 3750, 4750 |
| | ($10^{20}$ cm$^{-2}$) | 0.3, 6, 45, 105, 165, 226, 286 |
| Velocity contours | ($v_{max}$ - $v_{min}$, $\delta$v) (km s$^{-1}$) | 1410 - 1710, 30 |

**Comments**

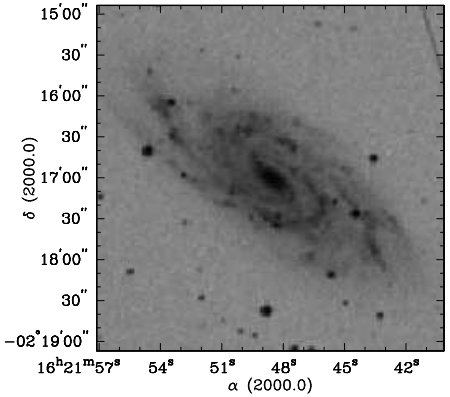


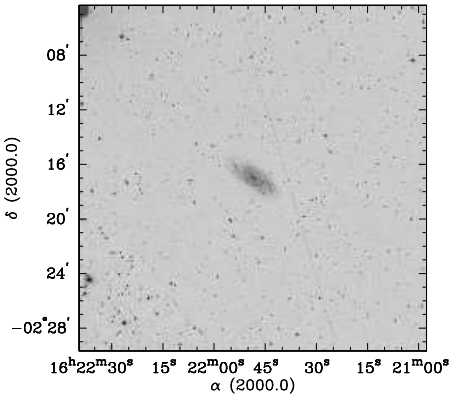


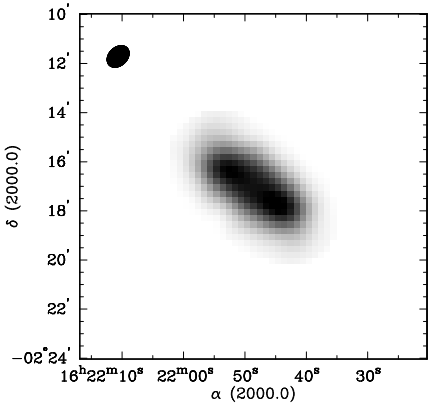


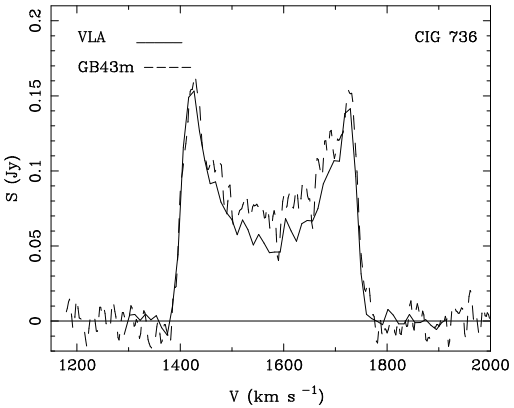


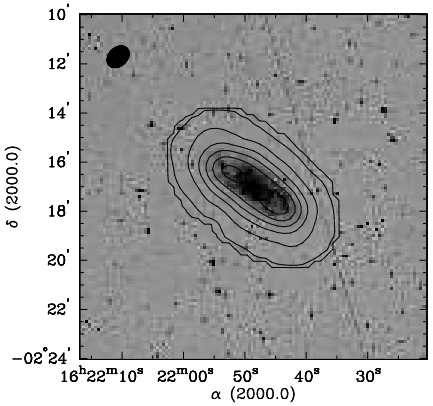


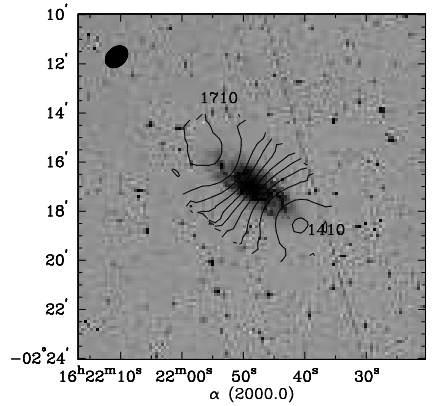

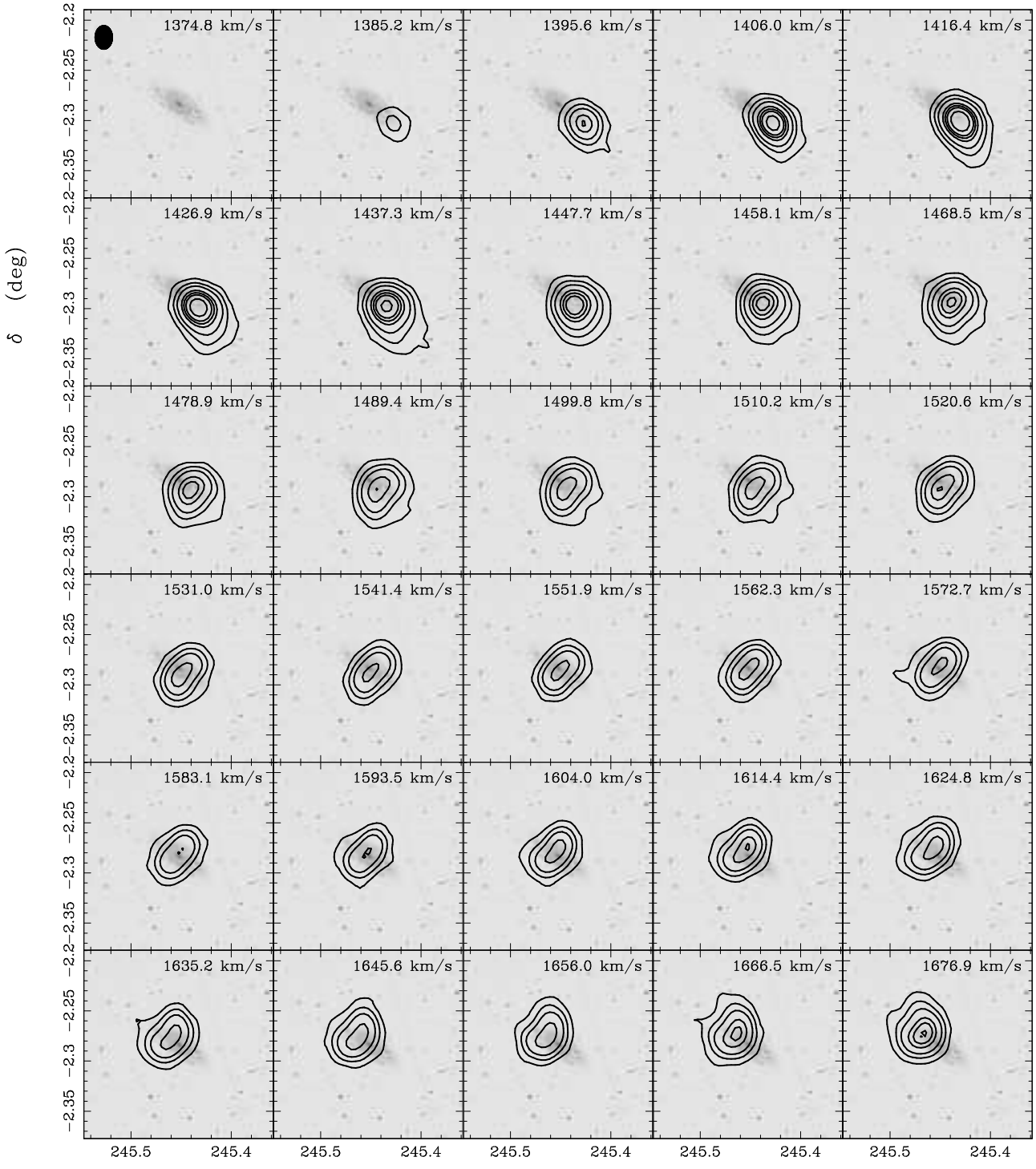
1374.8 km/s
1385.2 km/s
1395.6 km/s
1406.0 km/s
1416.4 km/s
1426.9 km/s
1437.3 km/s
1447.7 km/s
1458.1 km/s
1468.5 km/s
1478.9 km/s
1489.4 km/s
1499.8 km/s
1510.2 km/s
1520.6 km/s
1531.0 km/s
1541.4 km/s
1551.9 km/s
1562.3 km/s
1572.7 km/s
1583.1 km/s
1593.5 km/s
1604.0 km/s
1614.4 km/s
1624.8 km/s
1635.2 km/s
1645.6 km/s
1656.0 km/s
1666.5 km/s
1676.9 km/s
δ (deg)
−2.2
−2.25
−2.3
−2.35
245.5
245.4

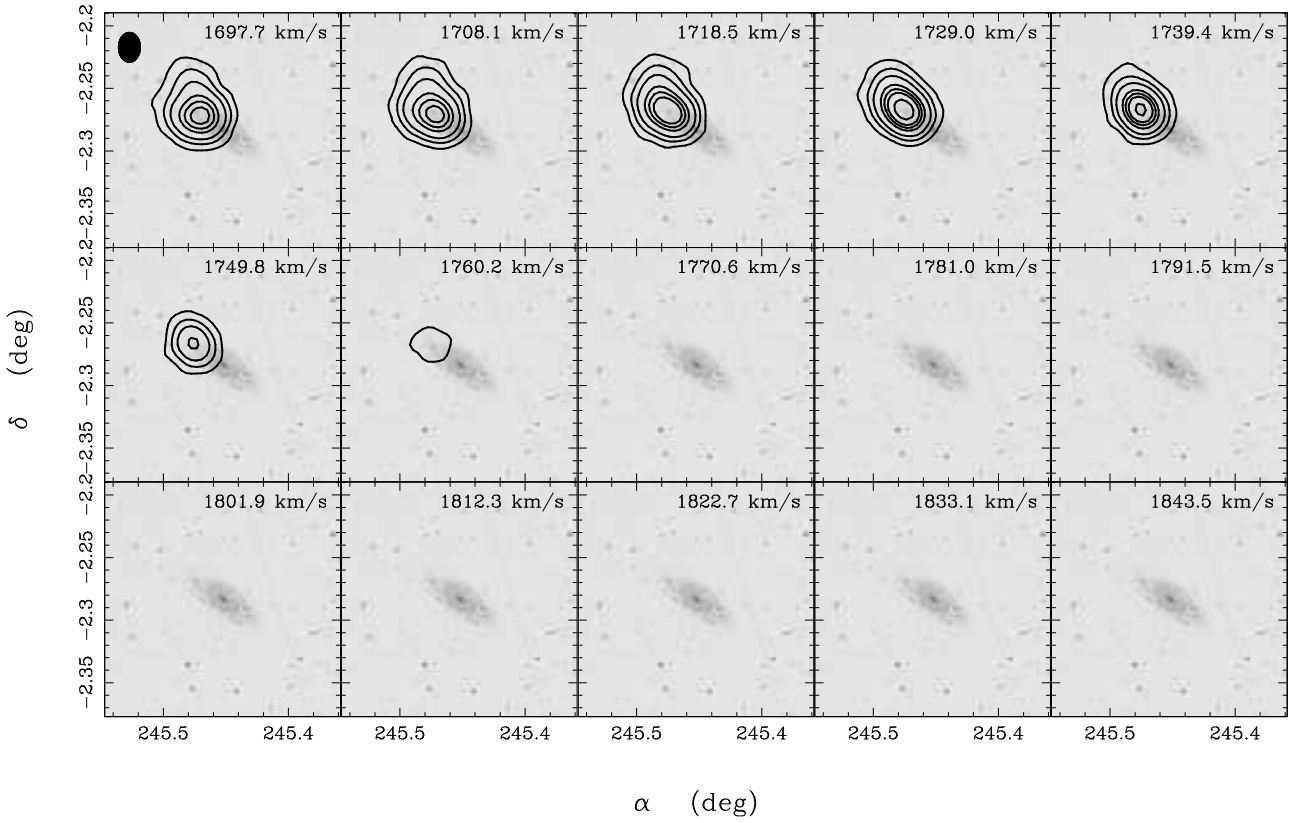
1697.7 km/s
1708.1 km/s
1718.5 km/s
1729.0 km/s
1739.4 km/s
1749.8 km/s
1760.2 km/s
1770.6 km/s
1781.0 km/s
1791.5 km/s
1801.9 km/s
1812.3 km/s
1822.7 km/s
1833.1 km/s
1843.5 km/s
−2.2
−2.25
−2.3
−2.35
245.5
245.4
δ (deg)
α (deg)

**Source: CIG 744**

| | | |
|---|---|---|
| Morphology | | Sc |
| $\alpha$(2000) | (hh:mm:ss) | 16:31:07.62 |
| $\delta$(2000) | (dd:mm:ss) | 43:20:54.5 |
| Optical field sizes | ($'\times\ '$) | 2.8 × 2.8, 14.0 × 14.0 |
| Observing time | (hours) | 3.5 |
| Central velocity | (km s$^{-1}$) | 2596 |
| Spatial resolution | ($''$) | 15 |
| Number of channels | | 64 |
| Velocity resolution | (km s$^{-1}$) | 10.4 |
| Beam size | ($\alpha \times \delta$, $''\times\ ''$) | 61.2 × 55.7 |
| Conv. beam size | ($\alpha \times \delta$, $''\times\ ''$) | 86.5 × 78.8 |
| PA (N to E) | ($^\circ$) | 75 |

**HI data parameters**

**Channel maps**

| | | |
|---|---|---|
| Field size, channels | ($\alpha \times \delta$, $'\times\ '$) | 11.4 × 11.4 , 18 - 46 |
| Velocities | (km s$^{-1}$) | 2461.6 - 2723.8 |
| rms noise channel | (mJy/beam) | 0.53 |
| Contours | (mJy/beam) | 2, 4, 8, 15, 30, 40 |

**Global HI profile**

| | | VLA — GB91m (HG91) |
|---|---|---|
| HI flux | (Jy km s$^{-1}$) | 15.01 — 13.01 |
| Heliocentric velocity | (km s$^{-1}$) | 2600 — 2598 |
| HI profile width 20% | (km s$^{-1}$) | 255 — 257 |
| $M_{HI}$ | ($10^9$ $M_\odot$) | 4.28 — 3.7 |

**HI maps**

| | | |
|---|---|---|
| Field size | ($'\times\ '$) | 8.4 × 8.4 |
| HI map contours | (mJy/beam km s$^{-1}$) | 5, 100, 250, 750, 1250, 1750, 2250, 2750, 3250 |
| | ($10^{20}$ cm$^{-2}$) | 0.3, 6, 15, 45, 75, 105, 135, 165, 195 |
| Velocity contours | ($v_{max}$ - $v_{min}$, $\delta$v) (km s$^{-1}$) | 2490 - 2700, 15 |

**Comments**

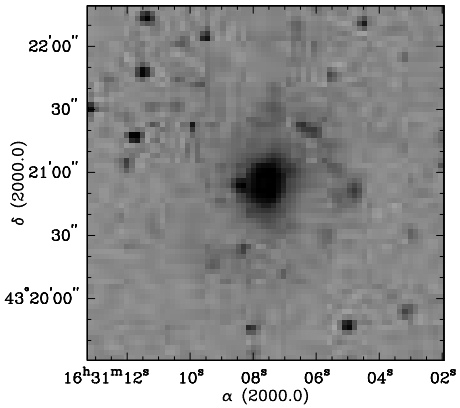


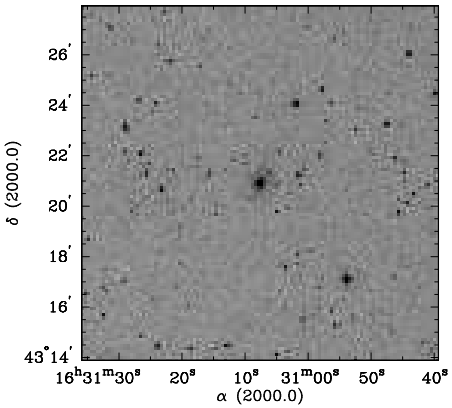


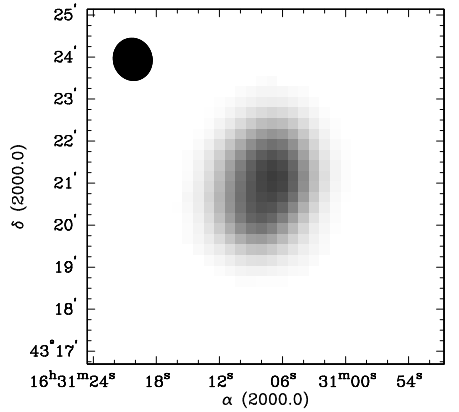


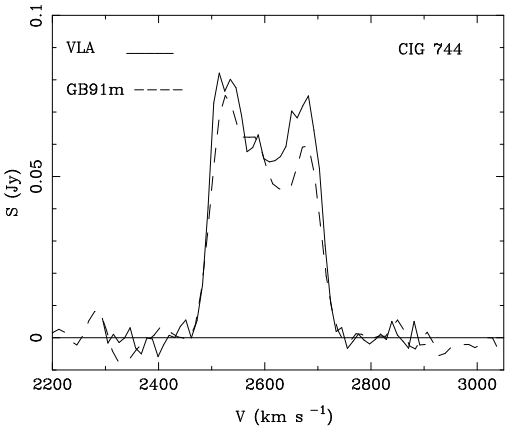


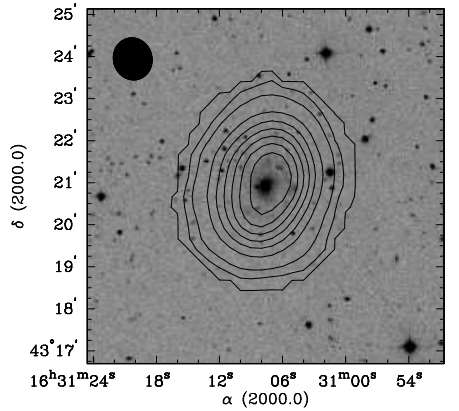


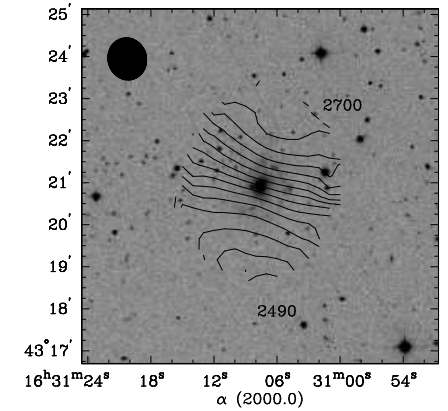

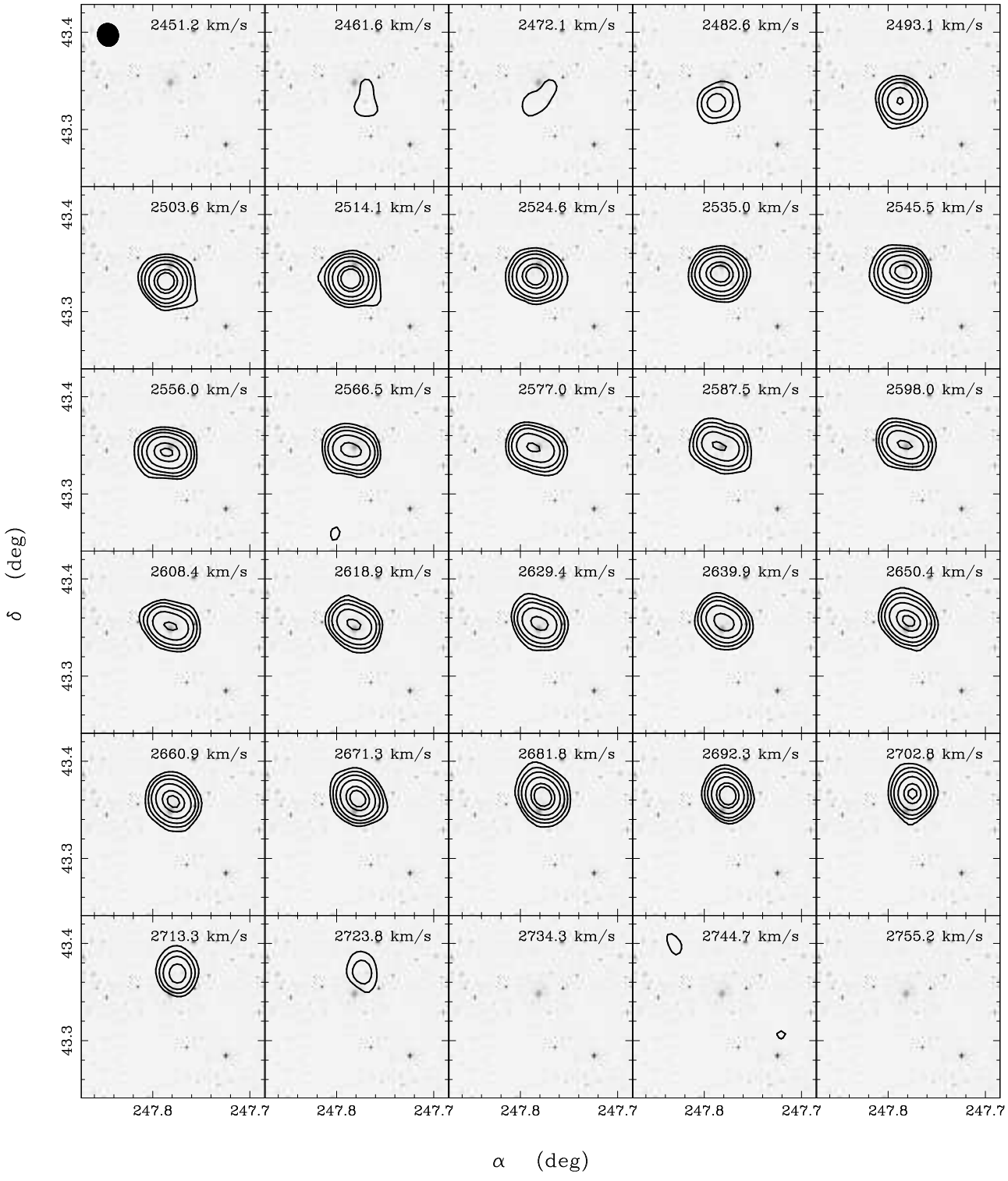


Figure 6.11: **CIG 744**

**Source: CIG 812**

| | | |
|---|---|---|
| Morphology | | Sbc |
| $\alpha$(2000) | (hh:mm:ss) | 17:32:39.78 |
| $\delta$(2000) | (dd:mm:ss) | 16:24:06.6 |
| Optical field sizes | ($'\times\ '$) | 1.4 × 1.4, 7.0 × 7.0 |
| Observing time | (hours) | 4 |
| Central velocity | (km s$^{-1}$) | 3118 |
| Spatial resolution | ($''$) | 15 |
| Number of channels | | 64 |
| Velocity resolution | (km s$^{-1}$) | 10.4 |
| Beam size | ($\alpha \times \delta$, $''\times\ ''$) | 65.1 × 58.0 |
| Conv. beam size | ($\alpha \times \delta$, $''\times\ ''$) | 92.0 × 82.0 |
| PA (N to E) | ($^o$) | 70 |
| **HI data parameters** | | |
| **Channel maps** | | |
| Field size, channels | ($\alpha \times \delta$, $'\times\ '$) | 5.7 × 5.7, 10-56 |
| Velocities | (km s$^{-1}$) | 2890.5 - 3342.9 |
| rms noise channel | (mJy/beam) | 0.58 |
| Contours | (mJy/beam) | 2, 4, 9, 17, 26, 35, 44, 48 |
| **Global HI profile** | | |
| | | VLA — GB91m (TC88) |
| HI flux | (Jy km s$^{-1}$) | 36.7 — 38.9 |
| Heliocentric velocity | (km s$^{-1}$) | 3115 — 3118 |
| HI profile width 20% | (km s$^{-1}$) | 416 — 412 |
| $M_{HI}$ | ($10^9$ $M_\odot$) | 14.55 — 15.41 |
| **HI maps** | | |
| Field size | ($'\times\ '$) | 5.7 × 5.7 |
| HI map contours | (mJy/beam km s$^{-1}$) | 50, 125, 250, 375, 750, 1250, 1750, 2250, 3250, 3750, 4250 |
| | ($10^{20}$ cm$^{-2}$) | 3, 8, 15, 23, 45, 75, 105, 135, 196, 226, 256 |
| Velocity contours | ($v_{max}$ - $v_{min}$, $\delta$v) (km s$^{-1}$) | 2945 - 3275, 30 |
| **Comments** | | |
| Companion $\alpha$=17:32:14.76 | $\delta$=16:34:50.9, v=3074 | (30-42), $M_{HI} \simeq 10^6$ |

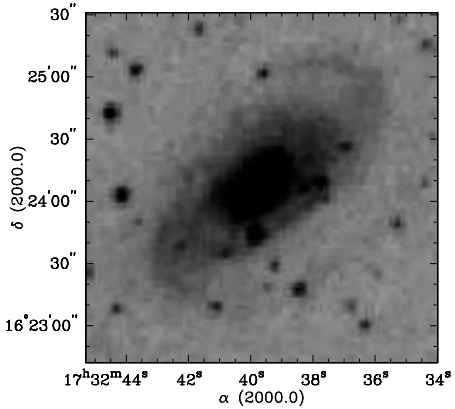


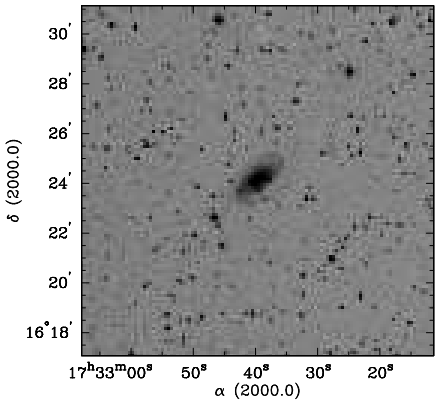


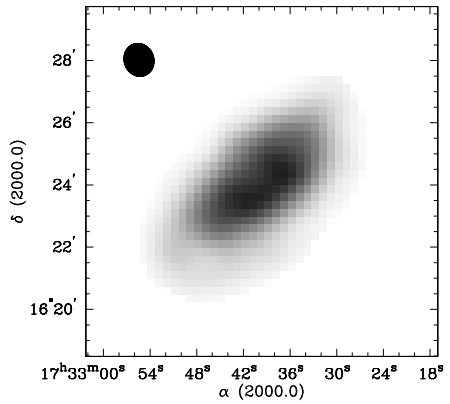


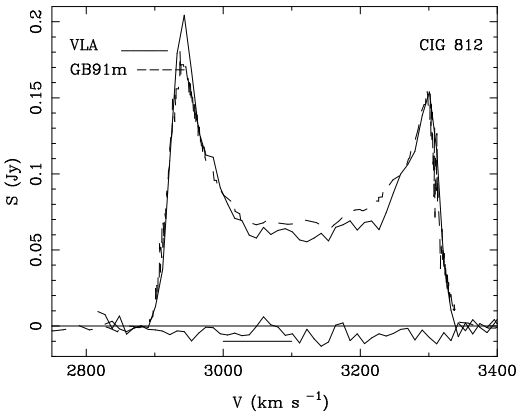


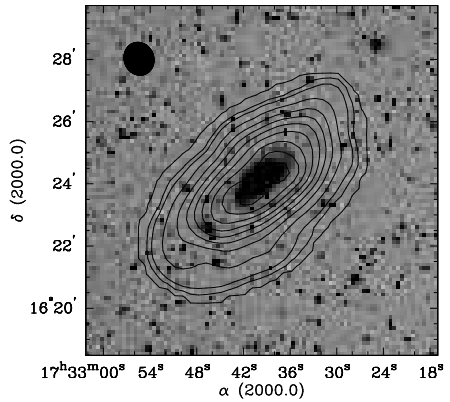


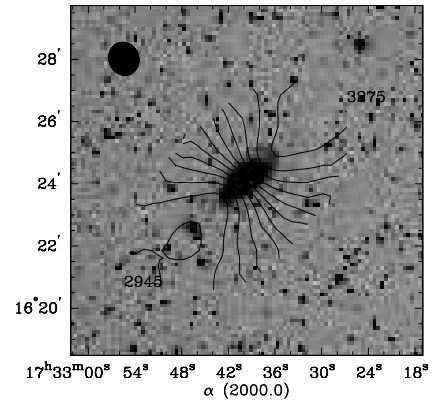

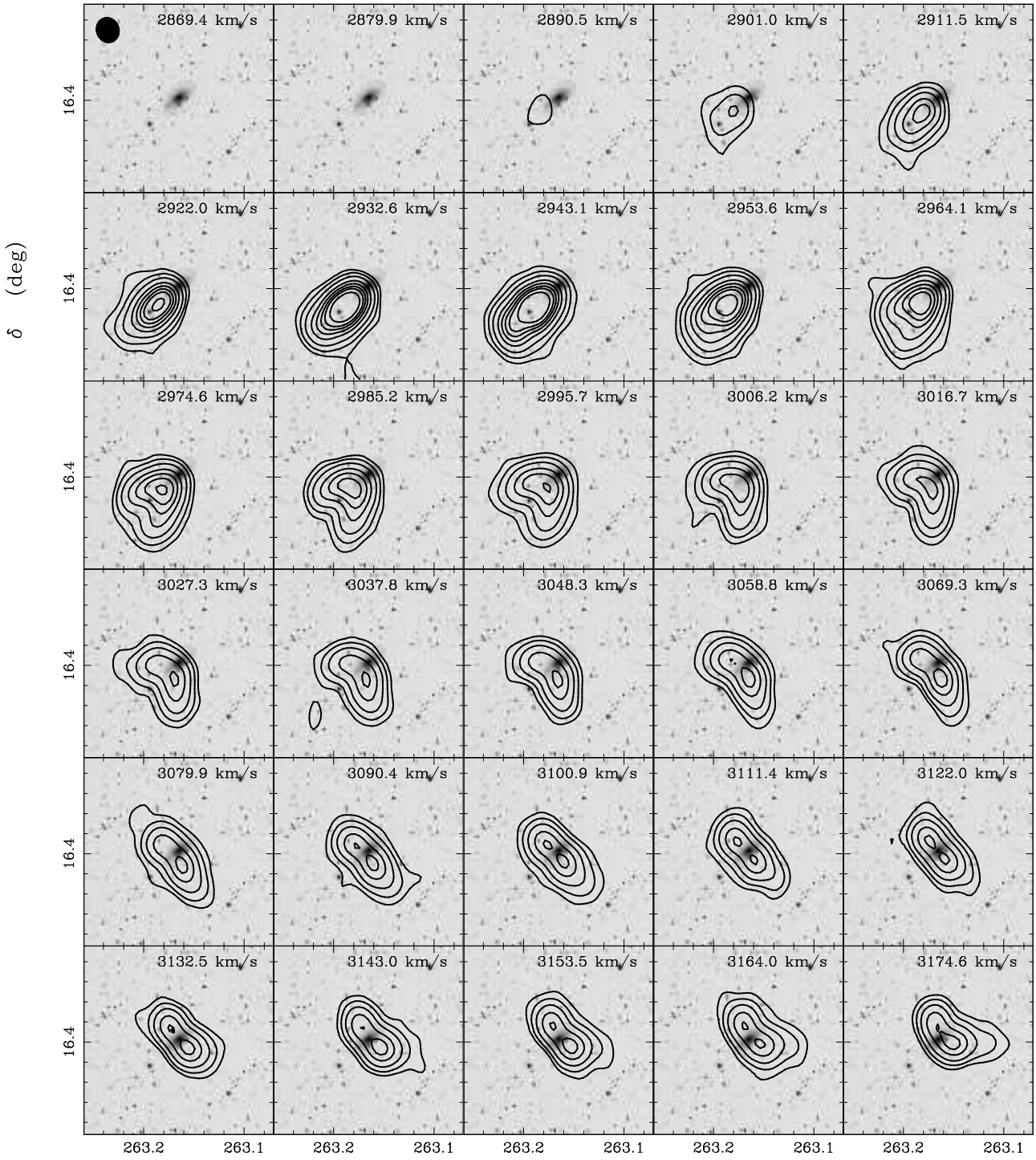


Figure 6.12: **CIG 812**

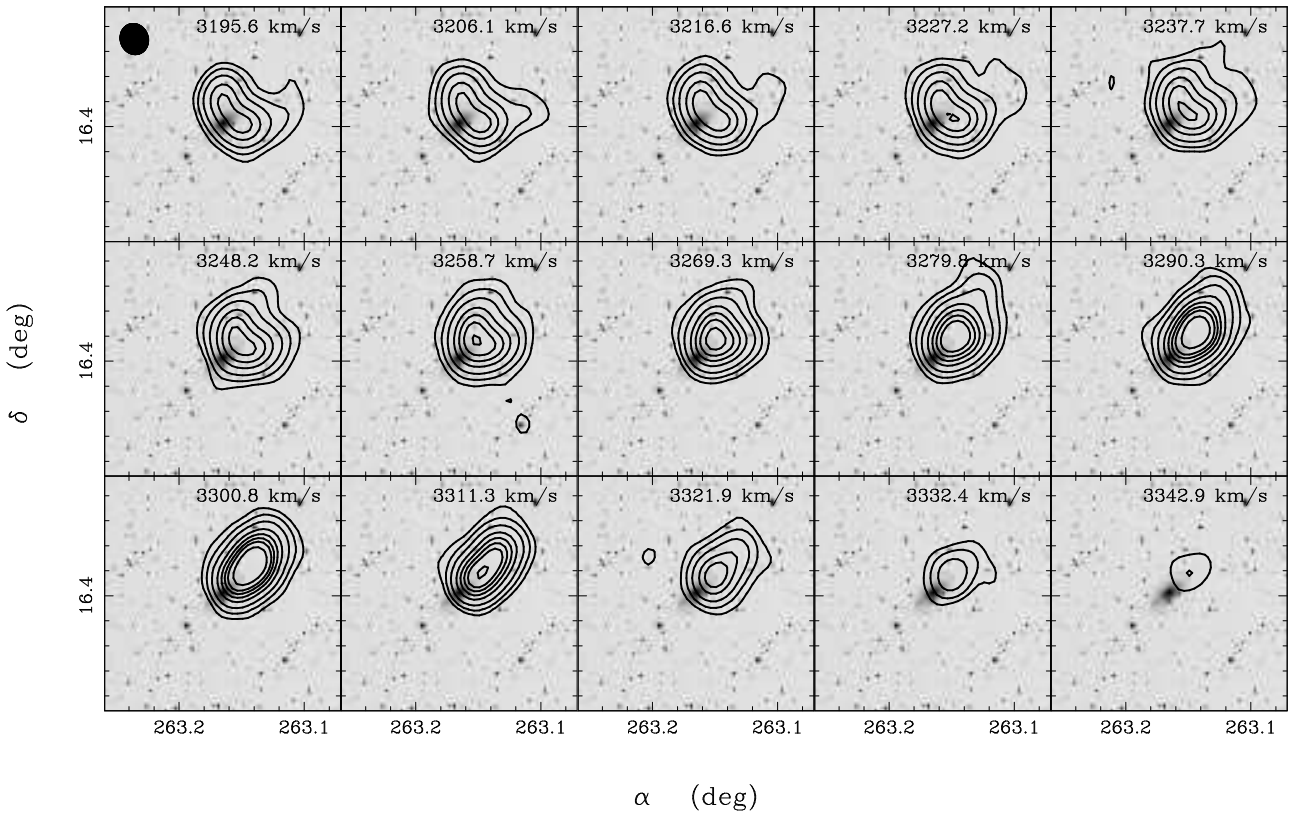
3195.6 km/s
3206.1 km/s
3216.6 km/s
3227.2 km/s
3237.7 km/s
3248.2 km/s
3258.7 km/s
3269.3 km/s
3279.8 km/s
3290.3 km/s
3300.8 km/s
3311.3 km/s
3321.9 km/s
3332.4 km/s
3342.9 km/s
16.4
16.4
16.4
263.2
263.1
263.2
263.1
263.2
263.1
263.2
263.1
263.2
263.1
δ (deg)
α (deg)

# Chapter 7

# Analysis of VLA synthesis imaging: CIG 96

**(Extracted from the paper "The large asymmetric HI envelope of the isolated galaxy NGC 864 (CIG 96)" by Espada, D.; Bosma, A.; Verdes-Montenegro, L.; Athanassoula, E.; Leon, S.; Sulentic, J.; Yun, M. S. , 2005, published in A&A)**

We present a HI synthesis imaging study of NGC 864 (CIG 96), a spiral galaxy well isolated from similarly sized companions, yet presenting an intriguing asymmetry in its integral HI spectrum. The asymmetry in the HI profile is associated with a strong kinematical perturbation in the gaseous envelope of the galaxy, where at one side the decay of the rotation curve is faster than Keplerian. We detect a small ($M_{HI}$ = 5 × $10^6$ $M_\odot$) galaxy with a faint optical counterpart at ∼ 80 kpc projected distance from NGC 864. This galaxy is probably not massive enough to have caused the perturbations in NGC 864. We discuss alternatives, such as the accretion of a gaseous companion at a radial velocity lower than the maximum.

## 7.1 Introduction

One of the most interesting galaxies in our VLA sample is NGC 864, number 96 in the CIG catalog, which, as we shall see, shows a peculiar HI envelope in our 21-cm maps. It is classified as SAB(rs)c by de Vaucouleurs et al. (1991). It has an optical size of 4′.7 x 3′.5 and an apparent magnitude $m_B$ = 11.6. It has a very asymmetric HI profile (cf. Fig. 7.1). The systemic heliocentric velocity that we have measured for this galaxy (see Sec. 7.3) is 1561.6 km $s^{-1}$ , corresponding to a distance of 17.3 Mpc ($H_0$ = 75 km $s^{-1}$ $Mpc^{-1}$) after applying the correction w.r.t. the CMB reference frame. This gives an optical luminosity of 1.1 × $10^{10}$ $L_\odot$. The closest galaxy to NGC 864 at the same redshift is a small companion that we detected in our HI observations (see Sec. 7.2) with $v_{hel}$ = 1605 km $s^{-1}$ , located at a distance d ∼ 80 kpc (15′.3) of NGC 864, visible in the POSS2 as a faint object (identified in NED as 2MASX J02162657+0556038 with a reported magnitude of $m_B$ = 16.38) with an approximate size of 0′.8 × 0′.6 (physical diameter ∼ 4 kpc). The other galaxies within a projected radius of d = 0.5 Mpc from NGC 864 are fainter by 3 to 7 magnitudes.

## 7.2 HI synthesis observations and results

The HI data were observed at the VLA in its D configuration and calibrated using the standard VLA procedure in AIPS, as explained in the previous chapter. The galaxy was detected between 1436.7 km $s^{-1}$ and 1686.6 km $s^{-1}$. The synthesized beam was 49″.8 × 46″.2 ($\alpha \times \delta$). The rms noise level achieved after 4 hours is 0.66 mJy/beam. Primary beam correction has been applied to our maps. In the composition of information and images for CIG 96 in the previous chapter we can see the channel maps smoothed to a beam size of 70″.4 × 65″.3, containing the HI emission at the observed radial

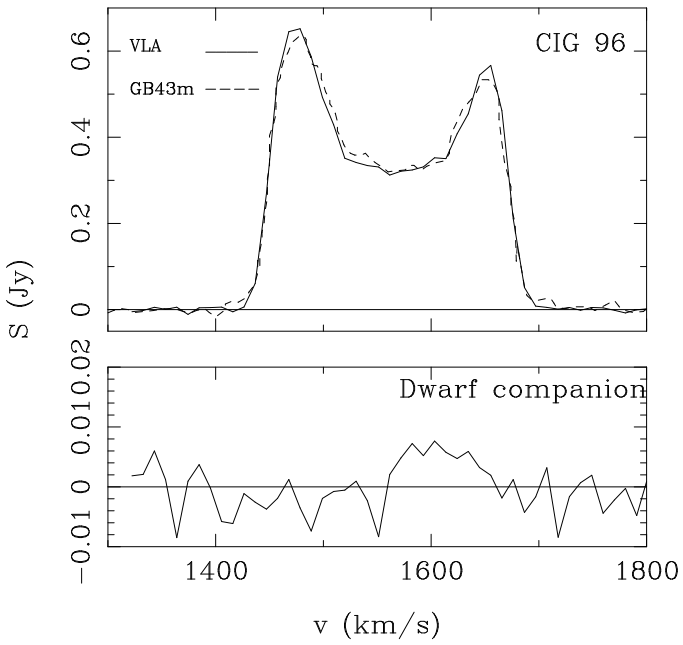


Figure 7.1: Comparison of the integrated VLA profile (solid line) and the HI profile obtained by Haynes et al. (1998) at Green Bank 43m (dots). At the bottom we show the HI profile of the dwarf companion found in the HI map.

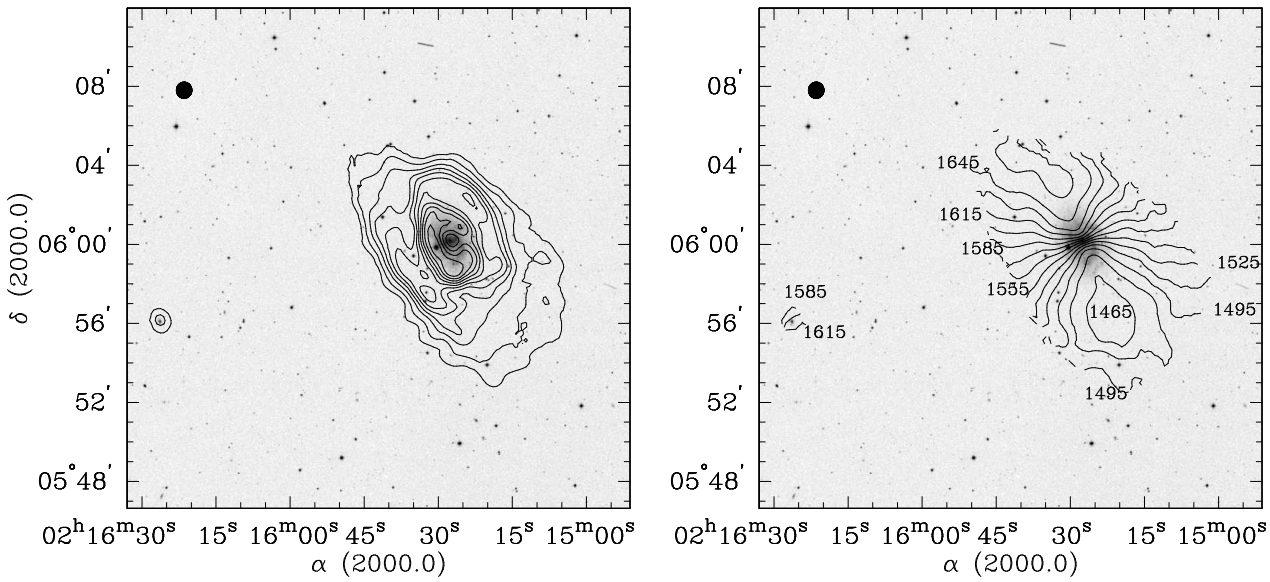


Figure 7.2: HI column density distribution (left) and velocity field (right) of NGC 864 and its companion, superimposed on the optical POSS2 red band image. The contour levels are: 5, 12, 24, 37, 49, 61, 73, 86, 98, 110 and 122 $\times$ $10^{20}$ cm$^{-2}$. The velocity contours go from 1465 to 1660 km s$^{-1}$ in intervals of 15 km s$^{-1}$, and are labeled each 30 km s$^{-1}$. The beam size of $49\farcs8 \times 46\farcs2$ is shown in the upper left of all panels.

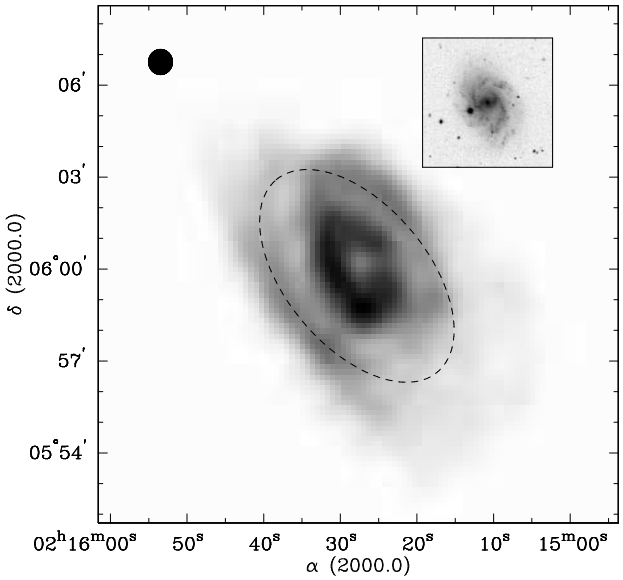


Figure 7.3: Grey scale map of the HI column density distribution of NGC 864. Darker regions correspond to higher column densities. The beam size of 49.″8 × 46.″2 is shown in the upper left part. The dashed line defines the approximate location of the pseudo-ring described in § 7.2. The insert shows the inner structure of NGC 864.

velocities, from 1426.3 to 1707.4 km s$^{-1}$ . We detect the small companion in the HI map from 1572.0 to 1655.3 km s$^{-1}$ at $\alpha(2000.0) = 02^h16^m26.^s9$ and $\delta(2000.0) = 05°56'24.''0$ .

The total spectrum has been obtained by integrating the emission in the individual channel maps (solid line in Fig. 7.1, top). We have measured a HI content of $M_{HI} = 7.53 \times 10^9$ M$_\odot$, in very good agreement with the single dish profile obtained by Haynes et al. (1998, dotted line in Fig. 7.1, top), showing that there is no loss of flux in the synthesis imaging. The profile of the small companion is shown at the bottom of the same figure. Subtraction of the flux of this dwarf galaxy from the total spectrum will not change its (asymmetric) shape.

In Fig. 7.2 we show the integrated HI column density distribution of NGC 864 (left) and the HI velocity field (right), both overlaid on a POSS2 red band image, the deepest one we found. These maps have been calculated as follows. The channel maps were smoothed with a Gaussian tapering function, and then non-signal pixels of the maps were blanked out. The channel maps where emission was detected were added up to produce the integrated emission map. The intensity weighted mean radial velocity field has been obtained in a similar way. The small companion mentioned above is clearly seen, together with its faint optical counterpart.

The integrated emission map shows an unresolved HI depression in the center of the galaxy, while the highest column densities are located in a pseudo-ring structure with a size of $\sim 90'' \times 55''$, better seen in the grey scale map shown in Fig. 7.3. This seems to trace the outer spiral structure of NGC 864, although the spatial resolution of the HI data is too small for a detailed comparison. An arm-like feature seems to join this structure at a second enhancement in the column density distribution. This enhancement has a ring-like shape with an approximate size of 8.′2 × 4.′6 (Fig. 7.2 and 7.3), nearly doubling the size of the optical disk. It is more prominent NW and SE of the optical disk and slightly closed to the NE, while undetected to the SW. The receding side of NGC 864 is narrower than the approaching one. The velocity field shows a symmetric pattern of differential rotation in the inner parts (r $\leq 300''$), while the kinematics of the outer parts is strikingly different. The outer isovelocity contours in the northern part show some twisting in the E direction, the last contour being nearly closed as a sign of a flattening rotation curve, and the southern isovelocity contours bend to the south with decreasing values characteristic of a declining rotation curve. The optical disk is reasonably symmetric in both spiral structure and angular extent, except for a slight enhancement of the southern arm, and a minor extension of the optical disk to the SE.

## 7.3 Modelling of the galaxy

We have modelled the velocity-field of NGC 864 with a least-square algorithm based on a tilted ring model (Begeman 1987; the ROTCUR task in GIPSY). By this procedure we divided the galaxy into concentric rings, each of them with a width of 20″ along the major axis. The asymmetry of the HI distribution and velocity field in the outer parts lead us to model separately the approaching and the receding part of the galaxy. Points within a sector of ± 30° from the minor axis were excluded from the fits. The center position was fixed to the position of the optical center $\alpha(2000.0) = 02^h15^m27\overset{s}{.}6$ and $\delta($ 2000.0) = 06°00′09″.1 (Leon & Verdes-Montenegro 2003). The systemic velocity of 1561.6 km s$^{-1}$ has been obtained as the central velocity of the HI spectrum at the 20% level. Expansion velocities were set to zero. In a first iteration the position angle, the inclination and rotation velocity have been left free, giving already a very satisfactory modelling of the data cube. The derived rotation curve, however, suffers from beam smoothing: since the beam is elongated along the major axis the integration effect biases the radial velocities towards values lower than the true values corresponding to the rotation curve. A second iteration has been performed, this time fixing the radial velocities at slightly higher values in order to correct for beam smearing, and leaving again the position angle and the inclination free. The modelled cubes for the redshifted and blueshifted parts of NGC 864 were combined in a single cube from which a velocity field has been obtained (Fig. 7.4). It shows a remarkable agreement with the observed one (Fig. 7.2 right), although not reproducing the asymmetries along the minor axis direction. Deriving the position angle of NGC 864 from our modelling for r ≤ 300″ we obtain a mean value of 23° ± 3, in very good agreement with the optical disk orientation. The inclination obtained as the mean between the receding and approaching sides is 43° ± 2, which is consistent to the value given by Tully & Fisher (1988) of 45°. The modelled inclinations for both sides are almost constant and their values are always close to the mean. The major axis twists both in the northern and southern part of NGC 864, although is more pronounced to the north. There it starts at r ∼ 240″ at nearly the edge of the optical disk, reaching a position angle of 39°. In the southern part it starts at r ∼ 360″ going up to 31°. In Fig. 7.5 we compare the position-velocity cut at 23° for the modelled (top) and observed (bottom) cube. Again the observations are very well reproduced. The plot also shows the projected rotation curve used. This figure contains the essential peculiarities of NGC 864: asymmetric HI distribution and kinematics, with a noticeable drop in rotation velocities. We note that the blueshifted part of the observed position-velocity diagram shows a faster than Keplerian drop in the velocity of NGC 864, with a trend to reach r$^{-0.5}$ values at larger radii, that should of course be explained by non-circular motions and/or projection effects. Such a phenomenon is extremely rare in HI envelopes.

## 7.4 Discussion and conclusions

Our results for NGC 864 have wider implications :

a) The integral HI profile is symmetric in velocity, but asymmetric in intensity. Yet the 2D-kinematics of NGC 864 show large scale asymmetries: there is a kinematic warp, and in the southern part there is an abrupt decline of the rotation velocity, as is evident in Fig. 7.5. The atomic gas here looks like a kinematically detached clump, evident as a secondary peak in the position velocity cut at radii ∼ 400″ to the SW. This region has a physical extent of around 3′×4′ in the major axis and minor axis directions, respectively. Clearly a simple integrated profile analysis will conclude that the central parts of NGC 864 are roughly symmetric, with a value of $\Delta V_{20}$ correlated with the luminosity of the galaxy, since it falls on the Tully-Fisher relation. It is the outer parts which are surprisingly asymmetric, but since the radial velocities in the approaching side are closer to the systemic velocity than those in the central parts, the asymmetry only manifests itself in a higher amplitude of the blueshifted horn of the HI profile.

b) The outer HI envelope is large, massive, very asymmetric and presents much structure. Its HI mass is about 4.5 × 10$^9$ M$_\odot$, and the HI mass associated with the steep drop of the rotation curve

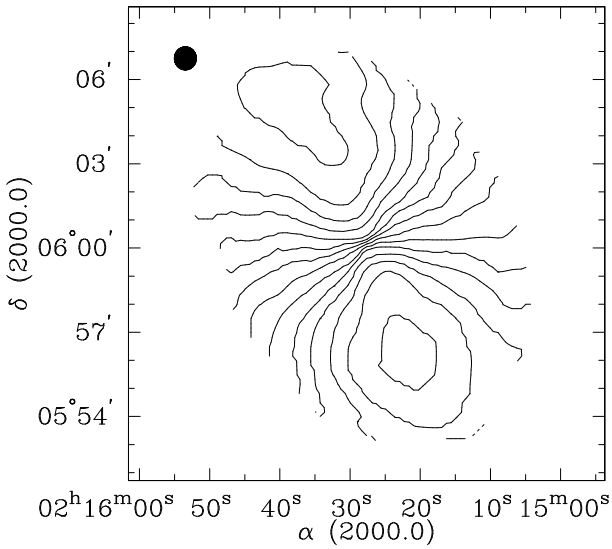


Figure 7.4: HI velocity modelled as explained in § 7.3. The velocity field contours are plotted in the map in km $s^{-1}$ from 1465 to 1660 km $s^{-1}$, in intervals of 15 km $s^{-1}$.

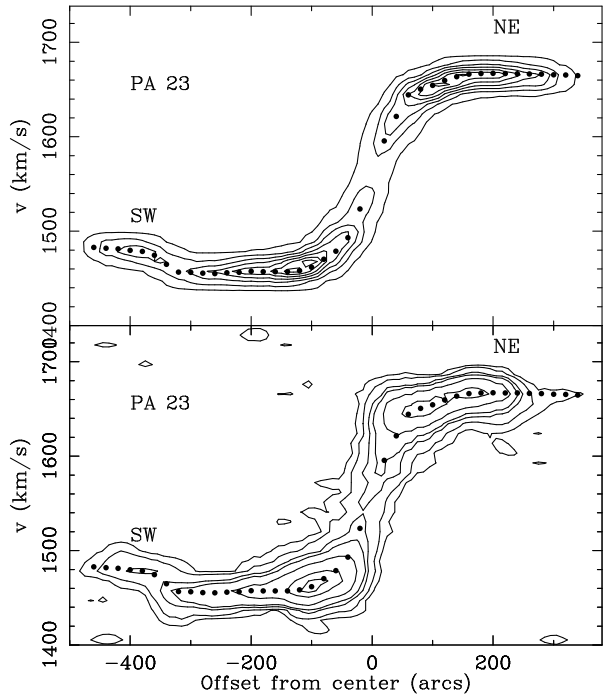


Figure 7.5: Position velocity along p.a. = 23° for the model (top), and for the observations (bottom). The projected rotation curve is also plotted (dots).

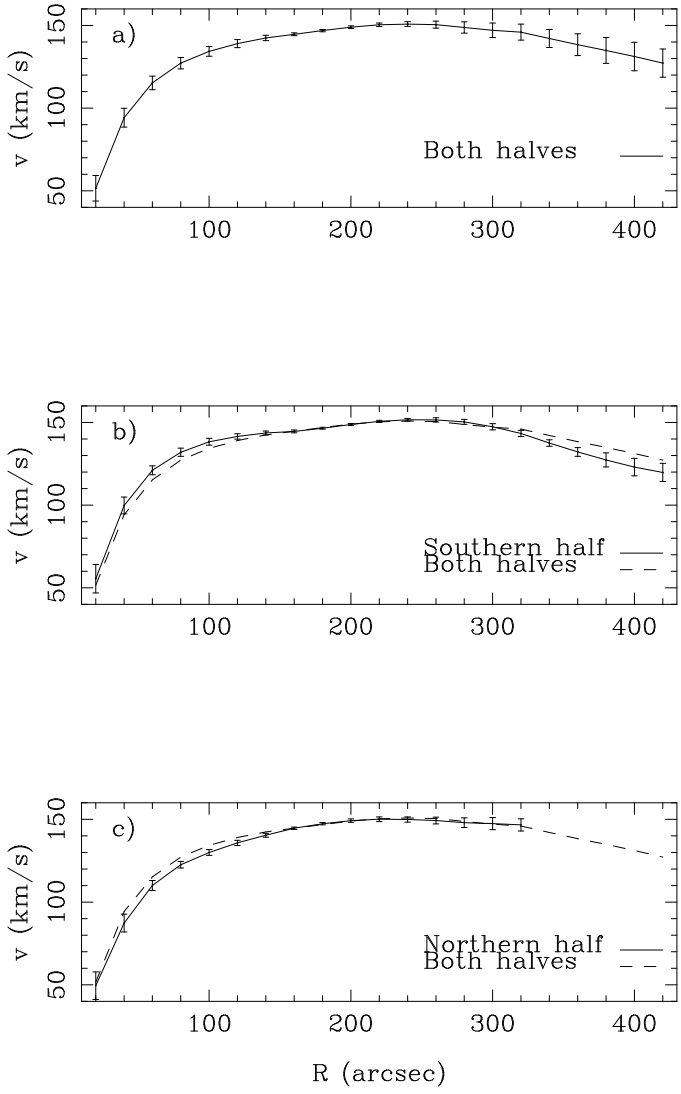


Figure 7.6: Rotation curves of NGC 864 considering: a) both the receding and approaching regions, b) the approaching half (southern region) and c) the receding half only (northern region). The dashed line represents the rotation curve in a) without error bars.

is about $2.3 \times 10^8$ $M_\odot$. No optical counterpart is found associated with the perturbed atomic gas. Warped HI envelopes are common around spirals, but few have as much structure and asymmetries as the one reported here.

c) The galaxy is isolated with respect to similarly sized galaxies by a rather strict criterion. Yet there are 5 small companions within a projected distance of 500 kpc. The closest one, detected in our maps, has a dimensionless gravitational interaction strength (Dahari 1984) of $4 \times 10^{-4}$, while for the others this parameter ranges from $1 \times 10^{-5}$ to $8 \times 10^{-7}$. They are hence too small in mass to have caused the strong perturbations in the outer envelope of NGC 864. A similar conclusion follows from considerations about spiral forcing by companions (cf. Athanassoula 1984)

We have considered several possibilities to explain the origin of these HI asymmetries. A self-induced perturbation seems highly unlikely: while the pseudo-ring is a very standard feature, the outer HI ring-like structure is too large to be a broken resonance ring, since the outer Lindblad resonance is usually located at slightly over 2 times the end of the bar (Athanassoula et al. 1982). An external perturbation by a companion, which could have interacted or even been accreted, seems likely to have caused the SW clump and the outer ring-like structure. However, we can exclude an encounter with a large pericenter distance since this would necessitate a massive companion, which is simply not there. A small companion would have to come very near NGC 864 or, even better, go through it, but a central, or near-central, passage will (cf. Athanassoula et al. 1997, Berentzen et al. 2003) yield results that do not match at all the morphology of NGC 864. The alternative left is that the companion crossed the equatorial plane of the target at an intermediate distance, e.g. just outside the optical disc and still within the extended HI disc. Such a passage could have induced the warp, and if the intruder was a loosely bound gas rich dwarf, its gas could have contributed to the SW clump, which has a similar gas mass, while its stars and dark matter could have dispersed. In order to test this interpretation and explain the form of the ring-like density enhancement, the mass of the excess gas and the velocity perturbations, full blown self-consistent simulations including both gas and stars are necessary, but beyond the scope of the present study.

We plan to perform numerical simulations of the merging of a dwarf and its host galaxy in order to determine the level at which the effects of the interaction are becoming perceptible. Results could be directly applied to CIG 96, for which the observations do not allow us to decide if its small companion can produce the degree of asymmetry observed. Although the merger of a dwarf galaxy with another galaxy has been studied in detail, simulations focused on the stellar component of the satellite galaxy, ignoring the gas and SF. Considering the quality of optical and radio observations available today, it is desirable to go a step further in terms of sensitivity.

# Chapter 8

# HI-rich early types

Most of early types are usually gas-poor systems but occasionally some of them possess a considerable amount of gas. The presence of HI in these galaxies is thought to be directly connected with the environment, from either: a) a past major merger of disk galaxies, b) recent accretions of gas-rich companions and/or c) accretion of gas from the intergalactic medium (IGM) via a cold mode. Early type isolated galaxies (ETIGs) are good candidates to be galaxies which are passively evolving, in the contrary to elliptical members of groups or clusters. In this chapter we perform a study of the properties of 31 early type isolated galaxies (12 E, 3 E/S0 and 16 S0 galaxies; Sulentic et al. 2006) which have been detected in HI ($\sim$ 27 %) from the 116 early type CIG galaxies in the AMIGA sample (with V $>$ 1500 km s$^{-1}$). We focus on the possible origin of the HI in these isolated galaxies.

## 8.1 Introduction

Early type galaxies (ETIGs) are characterized by an old stellar population, no significant star formation (SF), and very little gas. The environment plays a key role in order to understand the origin and evolution of this kind of galaxies. It is generally accepted that ETIGs can be produced by the merger of two disk galaxies [1], and that the most massive ones can be produced by the so called "dry mergers" (mergers of two cold gas poor galaxies, such as early types; e.g. Bell et al. 2006). However, the picture is much more complex if we assume a cosmological hierarchical model, since the morphologies of these galaxies would continously change as a result of the succesive interactions (minor and major mergers).

Occasionally some galaxies classified as ellipticals or lenticulars do possess a relevant amount of gas and SF activity. Whether this gas has an external origin or is a direct result of the HI content of each galaxy of the merger is an open question. Another possibility is that some of these ETIGs may have been formed in isolation via gravitational collapse of primordial protogalactic clouds, and that they may still have a relevant amount of gas. Evidences of recent merging/accretion events in the optical can be traced by: concentration of stellar light, asymmetries and clumpiness in the light distribution, total optical luminosity, peculiar colors, dust lanes, optical shells, blue cores and isophotal twists, among others (e.g. Marcum et al. 2004).

Sadler et al. (2002) classified ETIGs attending to peculiarities in the HI distribution and kinematics: i) galaxies with settled HI disks (symmetric distribution and regular velocity field, making recent merging events unlikely), ii) galaxies with high HI densities and SF in the central regions (mainly low-luminosity early types), and iii) galaxies with disturbed HI, often hosting an active nucleus. The origin of HI in i) and ii) can change from galaxy to galaxy, whereas galaxies in iii) are probably a result of a past merger. Oosterloo et al. (2002) find regular HI structures in dust lane elliptical galaxies using synthesis imaging. This suggests that mergers may lead to galaxies with extended low surface

[1] A major merger is usually defined as a merger between two galaxies with a mass ratio of 1:3 or lower. A minor merger is between systems with a mass ratio higher than 1:3.

brightness density gas disks.

It seems that optical luminosity and HI component in ETIGs are closely related. HI seems to be more usual in low-luminosity ETIGs than in bright galaxies (Lake & Schommer 1984).. Oosterloo et al. (2001) also suggest that in luminous ETIGs the HI is often irregularly distributed, while in low-luminosity ones the HI is more often located in a disk with a high central surface densities.

In § 8.2 we characterize the ETIGs in the AMIGA sample using the absolute magnitude, $M_B$, and the color $(B-V)_0$. In § **??** we present those ETIGs which have been detected in HI and compare the HI detection rate with other studies, attending to the total luminosities of the galaxies. In § **??** we investigate the origin of these objects.

## 8.2 $M_B$ and $(B-V)$ color characterization of the ETIGs

In this section we present the characterization of the ETIGs in the AMIGA sample attending to their total optical luminosities and $(B-V)$ colors. In order to see whether a recent massive SF might exist we study the absolute magnitude $M_B$ and $(B-V)$ color as in Zepf & Whitmore (1991) and Marcum et al. (2004). In this way we will identify the likely candidates to be fossil groups, to have accreted a companion, or to be primordial ETIGs.

### 8.2.1 $M_B$

A good indicator of a major past merger as origin of our early type galaxies is its total luminosity (Zepf & Whitmore 1991; Marcum et al. 2004). The prediction of the brightness for a merged group association of galaxies (i.e. fossil compact groups) is $M_B <$ -21.75 (Marcum et al. 2004). In fact, cD galaxies have characteristic luminosities of about $M_B <$ -22. This value needs to be understood only as a lower limit since light from stars which are formed via the induced starburst is not taken into account.

We have compiled $M_B$ directly from our data (Verdes-Montenegro et al. 2005). The distributions of $M_B$ for the whole AMIGA early type sample and the HI-rich ETIGs are shown in Fig. 8.1. The maximum value of $M_B$ reached for our set of galaxies is -20.86 (CIG 164), and although it is a bright elliptical, its magnitude is well bellow that of a fossil group. Therefore none of our galaxies is likely to have been formed from a past merged group of galaxies.

### 8.2.2 $(B-V)$ color

The median $(B-V)_0$ color for normal early type galaxies is $\sim$ 0.9 (Roberts & Haynes 1994), and those galaxies significantly bluer than this value (more than 0.1 mag, or 3 $\sigma$) can be good candidates to host recent massive SF, even without morphological peculiarities, since blue colors can last even for 1 - 2 Gyr (e.g. Marcum et al. 2004).

In Tab. 8.1 we present the colors available in the literature for 19 AMIGA ETIGs, compiled either from LEDA or from Marcum et al. (2004). In Fig. 8.2 we show the color distribution of all galaxies (including all morphological types) in AMIGA with available data in the literature as well as the distribution for the ETIGs (red filled histogram). We also show the histograms of the elliptical galaxies (green histogram), as well as the location of those ETIGs detected in HI (CIG numbers). The bluer early type galaxies $(B-V)_0 < 0.5$ are ellipticals (CIG 164, 393 and 870), whereas the rest of ETIGs have $(B-V)_0 > 0.7$, being mostly E/S0s and S0s.

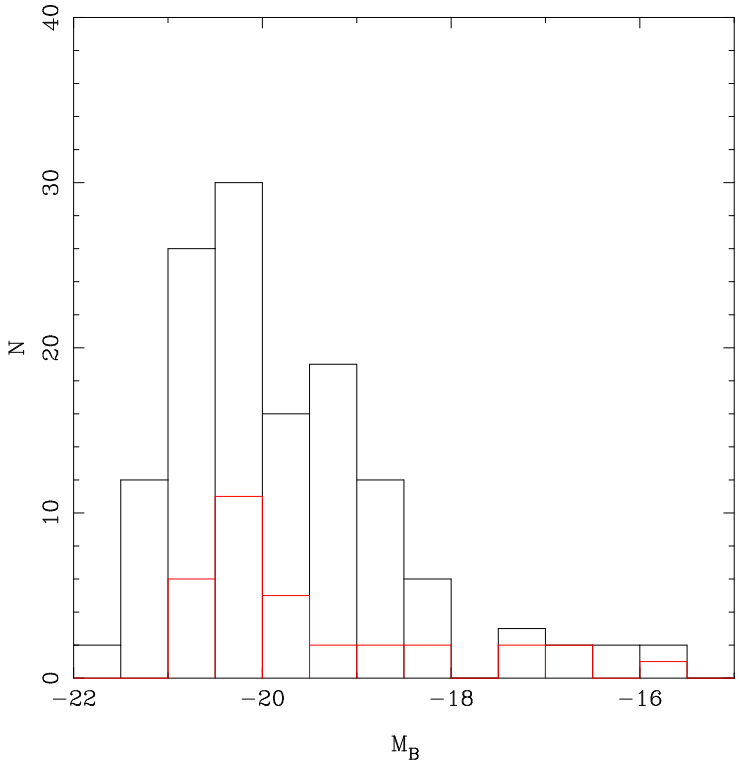


Figure 8.1: Distribution of $M_B$ for the ETIG sample (black line) and for the HI-rich ETIGs (red line).

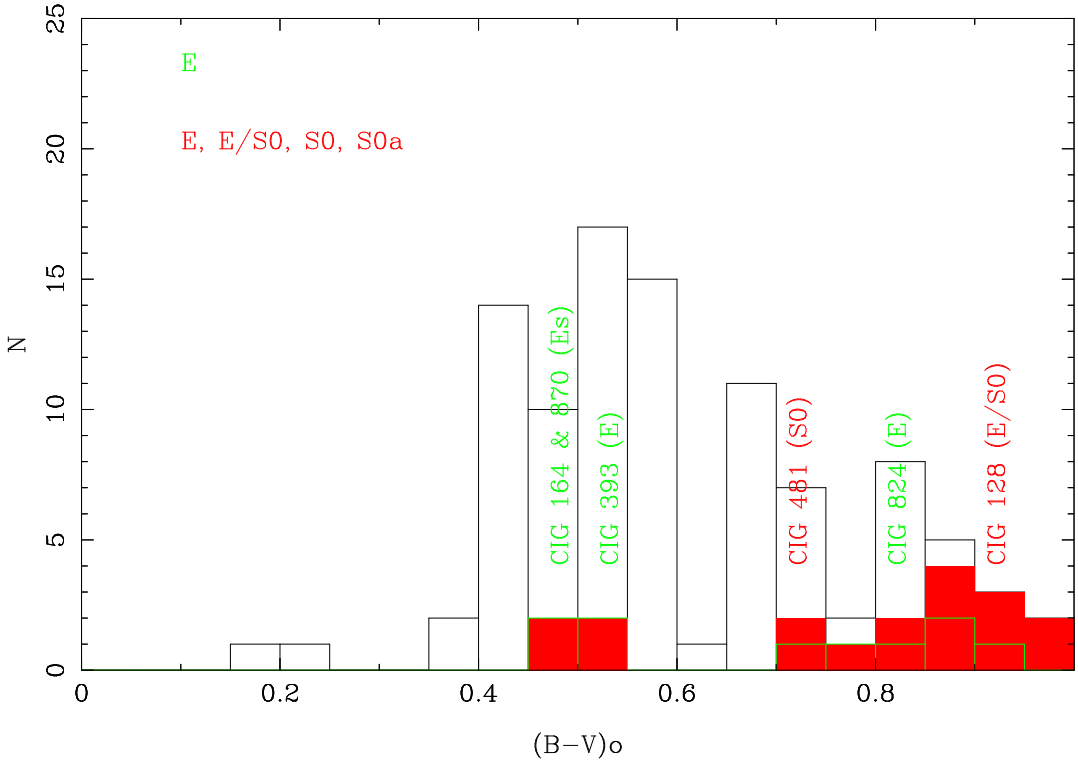


Figure 8.2: $(B-V)_0$ distribution for the whole AMIGA sample including all morphological types (non-filled black histogram). In filled red bins the early type galaxies (E, E/S0 and S0), and in green non-filled bins only the ellipticals. The location of the HI-rich early types is also shown with their CIG numbers.

Table 8.1: $(B-V)_0$ and $M_{HI}$ for early type galaxies in the CIG[1], compiled from LEDA or from Marcum et al. (2004).

| CIG | $(B-V)_0$[2] | $T_{S06}$[3] | $M_{HI}$[4] |
|---|---|---|---|
| 25 | 0.852 | E | < 5.2 e+09 |
| 89 | 0.865 | E | < 7.5 e+07 |
| 128 | 0.920 | E/S0 | 4.5 e+09 |
| 164 | 0.470(*) | E | 3.7 e+09 |
| 358 | 0.838 | S0 | < 1.9 e+08 |
| 389 | 0.770 | S0 | - |
| 393 | 0.540 | E | 1.9 e+08 |
| 412 | 0.740(*) | E | - |
| 425 | 0.960(*) | S0 | - |
| 481 | 0.720 | S0 | 2.3 e+08 |
| 557 | 0.890 (*) | E | - |
| 637 | 0.809 | S0 | - |
| 684 | 0.920(*) | S0 | < 1.7 e+09 - |
| 792 | 0.780(*) | E/S0 | - |
| 824 | 0.830(*) | E | 5.1 e+08 |
| 870 | 0.460(*) | E | 1.6 e+09 |
| 1020 | 0.923 | S0 | < 3.4 e+08 |
| 1031 | 0.498 | E | - |
| 1045 | 0.949 | S0 | < 2.6 e+08 |

[1] The full table of $(B-V)_0$ for the AMIGA sample retrieved from the literature can be downloaded from http://www.iaa.es/AMIGA.html.

[2] (*) symbol means that $(B-V)_0$ is compiled from Marcum et al. (2004).

[3] Morphological classifications by Sulentic et al. (2006).

[4] $M_{HI}$ as explained in Chapter 3 . "–" symbol means that we do not have any HI data in our database.

## 8.3 HI-rich ETIGs in AMIGA

A total of 31 ETIGs in the AMIGA sample have been detected in HI (12 are Es, 3 are E/S0 and 16 are S0s) from the 116 early type CIG galaxies with HI observations and v > 1500 km $s^{-1}$.

In order to illustrate their optical appearance, we show their optical images when available in Fig. 8.6, 8.7 and 8.8 (E, E/S0 and S0 respectively) either from POSSII or from the SDSS Data Release 4 (Adelman-McCarthy et al. 2006). We have also inspected OSN (Observatorio de Sierra Nevada) CCD optical images in order to detect any remarkable features.

The most relevant information for these galaxies is listed in Tab. 8.2 : CIG number, morphological type (revised by Sulentic et al. 2006), morphological type in NED, systemic velocity, $M_{HI}$, detection or marginal detection (det = 0 and 2 respectively), width of the HI profile at 20 % level, $M_B$, $L_B$,, $M_{HI}/L_B$, FIR luminosity (Lisenfeld et al. 2006), $M_{H_2}$(from Chapter 9), and two columns to indicate whether SDSS or OSN images were available.

Table 8.2: Morphological type (E, E/S0 or S0), HI, optical and FIR data for the HI-rich ETIG.

| CIG | T $_{S06}$ | T $_{NED}$ | V (km s$^{-1}$) | $M_{HI}$ ($10^8 M_\odot$) | det | $W_{HI}$ (km s$^{-1}$) | $M_B$ | $L_B$ ($10^8$ $L_\odot$) | $M_{HI}/L_B$ | $L_{FIR}$ ($10^8$ $L_\odot$) | $M_{H_2}$ ($10^8$ $M_\odot$) | SDSS | OSN |
|---|---|---|---|---|---|---|---|---|---|---|---|---|---|
| 14 | E | E | 5192 | 9.3 | 0 | 409 | -20.14 | 102.0 | 0.091 | < 31.3 | | | Y |
| 136 | E | E | 4849 | 20.3 | 2 | 649 | -20.05 | 93.6 | 0.21 | < 32.6 | | | |
| 164 | E | E | 9000 | 37.8 | 0 | 206 | -20.86 | 198.0 | 0.19 | 221.0 | | | Y |
| 393 | E | E | 3011 | 1.9 | 0 | 159 | -18.71 | 27.3 | 0.07 | 28.4 | < 2.3 | Y | |
| 582 | E | E | 9998 | 397.0 | 0 | 478 | -20.40 | 129.0 | 3.08 | < 55.4 | | Y | |
| 824 | E | E | 5340 | 5.12 | 0 | 277 | -19.69 | 67.0 | 0.07 | < 9.2 | | | |
| 870 | E | E | 6292 | 15.8 | 0 | 168 | -20.24 | 112.0 | 0.14 | 174 | | | Y |
| 877 | E | E | 8737 | 21.1 | 2 | 59 | -20.59 | 154.0 | 0.13 | 249 | | | Y |
| 895 | E | E | 4847 | 14.4 | 0 | 267 | -18.81 | 29.8 | 0.48 | 39.7 | 0.44 | | Y |
| 981 | E | E | 7962 | 63.2 | 2 | 349 | -20.29 | 117.0 | 0.54 | < 40.3 | | | |
| 1025 | E | E | 3403 | 45.6 | 0 | 156 | -18.3 | 20.1 | 0.22 | 10.8 | 1.21 | | |
| 1029 | E | E | 12387 | 89.8 | 0 | 282 | -20.9 | 212.0 | 0.42 | < 177.0 | | Y | |
| 128 | E/S0 | S0 | 6596 | 45.4 | 0 | 382 | -20.67 | 166.0 | 0.27 | < 44.3 | | | |
| 264 | E/S0 | E | 7624 | 31.0 | 2 | 523 | -20.31 | 119.0 | 0.26 | < 30.3 | | Y | Y |
| 811 | E/S0 | E | 7872 | 21.0 | 0 | 306 | -20.41 | 131.0 | 0.16 | 28.7 | | | |
| 83 | S0 | E | 5085 | 17.6 | 0 | 288 | -20.09 | 97.7 | 0.18 | 44.6 | | | |
| 125 | S0 | Sb | 7049 | 35.3 | 0 | 626 | -20.80 | 187.0 | 0.18 | 44.4 | | | Y |
| 134 | S0 | Sb | 5205 | 41.5 | 0 | 288 | -20.11 | 99.5 | 0.41 | < 29.5 | | | Y |
| 141 | S0 | S0? | 1714 | 1.6 | 0 | 133 | -17.49 | 8.9 | 0.17 | 5.3 | | | |
| 161 | S0 | S0? | 7991 | 156.0 | 2 | 213 | -20.41 | 131.0 | 1.19 | < 26.6 | | | |
| 295 | S0 | S0 | 5697 | 79.9 | 0 | 490 | -19.86 | 78.4 | 1.01 | 50.3 | | | |
| 332 | S0 | S0 | 4309 | 20.6 | 0 | 339 | -19.88 | 79.9 | 0.25 | 37.4 | 4.85 | Y | |
| 338 | S0 | Sb | 3494 | 18.7 | 0 | 160 | -19.35 | 49.1 | 0.38 | < 6.0 | <10.44 | Y | |
| 352 | S0 | Sb | 1680 | 0.9 | 0 | 121 | -16.80 | 4.7 | 0.18 | 43.9 | <0.81 | Y | |
| 467 | S0 | SB0 | 6393 | 10.9 | 0 | 132 | -20.30 | 118.0 | 0.09 | < 19.2 | | Y | |
| 481 | S0 | SA(s)0/a | 1508 | 2.4 | 0 | 305 | -18.45 | 21.5 | 0.10 | 34.4 | 4.30 | Y | |
| 483 | S0 | (R)SAB0 | 6710 | 29.6 | 0 | 426 | -20.71 | 172.0 | 0.17 | 26.7 | | Y | |
| 501 | S0 | E? | 6498 | 51.4 | 0 | 297 | -19.62 | 63.3 | 0.81 | - | | Y | |
| 918 | S0 | Sc | 7738 | 50.0 | 2 | 651 | -19.85 | 78.3 | 0.64 | < 41.1 | | | |
| 1015 | S0 | E? | 4437 | 8.9 | 0 | 185 | -19.44 | 53.7 | 0.16 | 10.4 | 4.44 | | |
| 1032 | S0 | S0/a | 1851 | 9.0 | 0 | 227 | -16.5 | 3.6 | 2.49 | 1.2 | | Y | |

### 8.3.1 Peculiarities in the morphologies

We give in this section some comments on the HI rich ETIGs (morphological details, star formation, etc.).We have revised SDSS, OSN and 2MASS images when available in order to check for the presence of peculiarities in the morphologies, such as dust lanes, optical shells, blue cores or SF.

**- Ellipticals (E):**

- CIG 14 : Perturbed and likely to be in minor interaction. Star projected on the galaxy.
- CIG 136: Not very well resolved. No redshift in NED.
- CIG 164: Morphological type by Marcum et al. (2004) is E, using CCD images.
- CIG 393: Morphological type by Sulentic et al. (2006) using SDSS is E/S0, with an elongated nucleus but no bar. Detected in 3 IRAS bands (25, 60 and 100$\mu$m) but not in CO. It is a HII galaxy, with a high ratio S60/S100 (HII+AGN?).
- CIG 582: Morphological type by Sulentic et al. (2006) using SDSS is S0. A bit irregular but noise in the optical image is high. Detected in IRAS (25 but not 60 and 100$\mu$m). Slight asymmetry in 2Mass-J. It may be in weak interaction and is an optically peculiar galaxy. A Dust lane is present.
- CIG 824: The centre of the galaxy is perturbed in the optical image, maybe due to a merger, although no fine structure is found in CCD images by Marcum et al. (2004).
- CIG 870: This galaxies presents tidal tails, probably as a result of a small companion. It has two nuclei plus an irregular envolope. It is detected in IRAS (25, 60 and 100), with a high ratio S60/S100 (HII+AGN?).
- CIG 877: Projected star in the field. Marcum et al. (2004) suggest that this is an active galaxy.
- CIG 895: It has a tail, suggesting that this galaxy may probably be a merger. It has been detected in IRAS (60, 100$\mu$m) and has a marginal detection in CO.
- CIG 981: It looks boxy, probably S0 instead of E.
- CIG 1025: Probably some interactions with close companions is taking place. It does not follow $r^{1/4}$, flat "bulge".
- CIG 1029: Probably S0.

**- E/S0:**

- CIG 128: No arms but spiral bulge plus disk, seen face-on.
- CIG 264: Probably E from morphological classification in SDSS and OSN image (Sulentic et al. 2006).
- CIG 811: It probably presents a dust lane and has been detected in IRAS (60, 100 but not in 25).

**- Lenticulars (S0):**

- CIG 83: Irregular halo in B, seen in POSSII image.
- CIG 141: Probably a bar is present, and arms are likely to be detected in the infrared.
- CIG 295: Maybe spiral instead of S0 considering the OSN image, warp seen in infrared and a bit irregular in red POSSII.

- CIG 332: Morphological type using SDSS image by Sulentic et al. (2006) is S0. Detected in CO, with a wide width (470 km $s^{-1}$ ) and also in IRAS (25, 60 and 100). It is probably in weak interaction since an isophote twist in 2Mass-J is seen. A small tail is found in the north direction that may be probably a merging satellite. A few projected dwarf galaxies are present in the field.

- CIG 338: Morphological type by Sulentic et al. (2006) is S0 and no bar is seen. Not detected in CO but detected in IRAS (25, 60 but not in 100). This galaxy may be in weak interaction since it has isophote twist in 2Mass-J.

- CIG 352: S0 boxy in B and warped in the outer regions. Faint spiral arms seen extending northward and southward.

- CIG 467: Classification is uncertain. it could probably be SBa instead of S0?. 2 rings.

- CIG 481: Morphological type using SDSS by Sulentic et al. (2006): S0a, with a dust lane and numerous projected dwarf satellites visible. It has been detected in CO (Wiklind & Henkel, 1989) and IRAS (25, 60 and 100).

- CIG 483: Morphological type using SDSS image by Sulentic et al. (2006): S0a, with faint arms, no bar and several projected dwarf galaxies. Probably in weak interaction. Detected in IRAS (60, 100 but not in 25), with low S60/S100 ratio.

- CIG 501: This galaxy is probably spiral with faint arm/shell and no bar.

- CIG 1015: Detected in CO and IRAS (60, 100 but not in 25), with high ratio S60/S100 and high SF in the centre.

- CIG 1032: Morphological type using SDSS image by Sulentic et al. (2006) is S0a. It is probably a merger since it seems to present a double core.

## 8.4 HI description of the HI-rich ETIGs

We show the HI profiles for the HI-rich ETIGs in Fig. 8.3, 8.4 and 8.5 for Es, E/S0s and S0s respectively. Note that some of them are marginal detections. We detail next the HI detection rate for our ETIG sample in comparison with other samples of early types found in the literature.

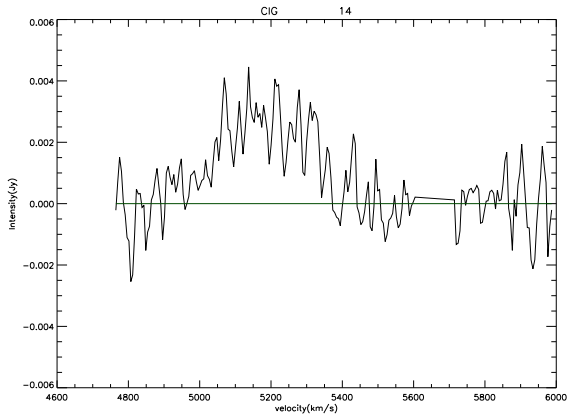


(a) CIG 14, ERT

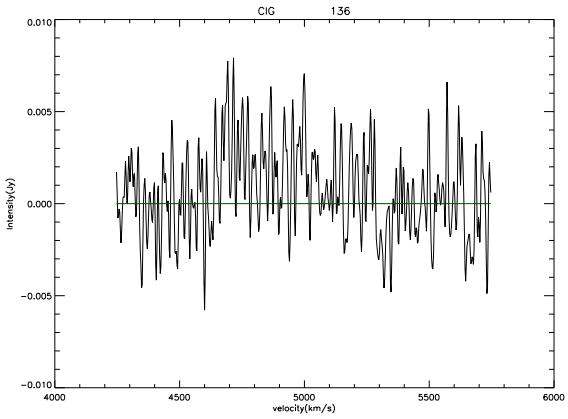


(b) CIG 136, NRT

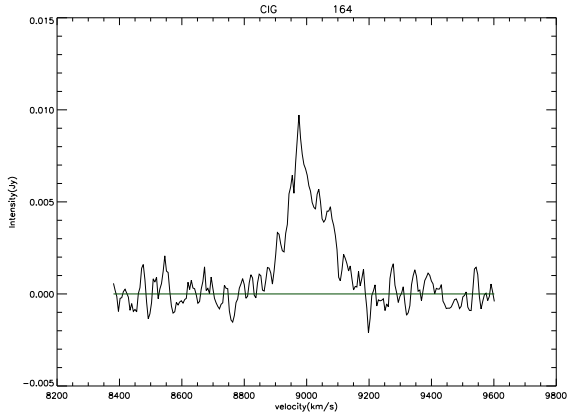


(c) CIG 164, ERT

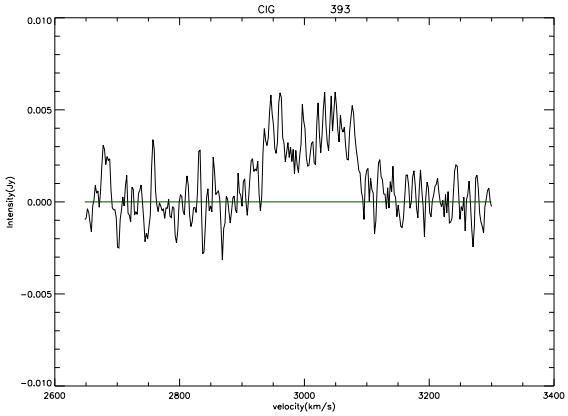


(d) CIG 393, GBT

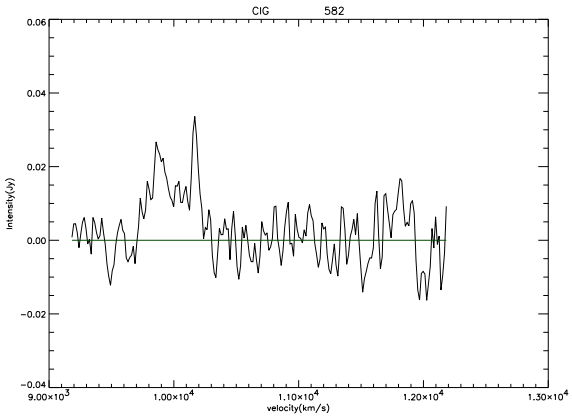


(e) CIG 582, HIP

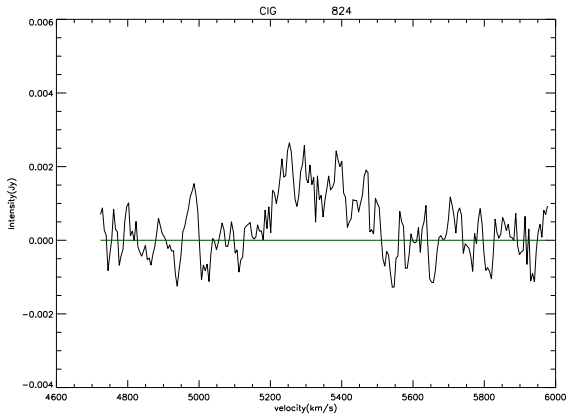


(f) CIG 824, ERT

Figure 8.3: HI profiles for the HI-rich early type subsample (see Fig. 8.6). E morphological types.

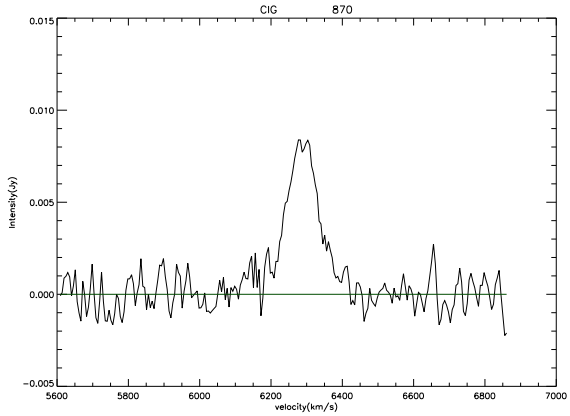


(a) CIG 870, ERT

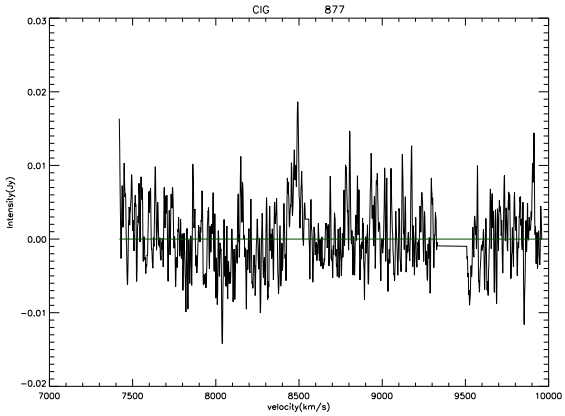


(b) CIG 877, NRT

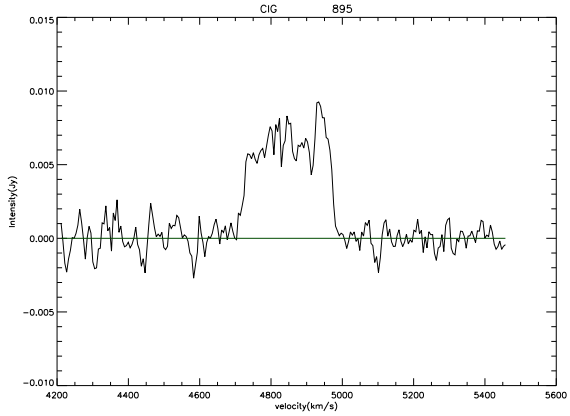


(c) CIG 895, ERT

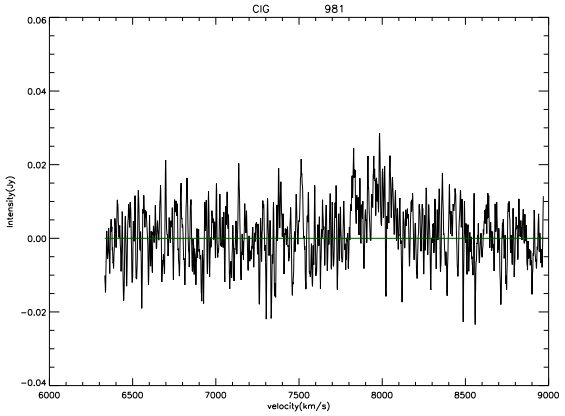


(d) CIG 981, NRT

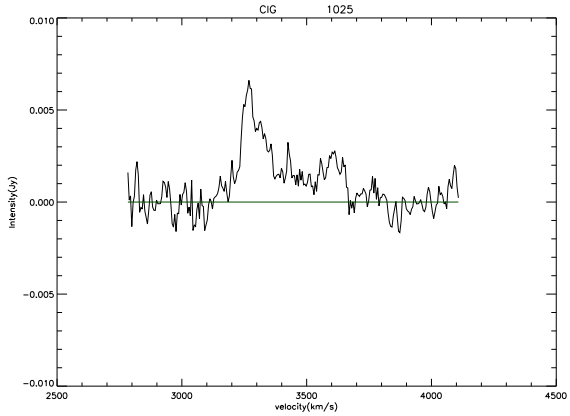


(e) CIG 1025, ERT

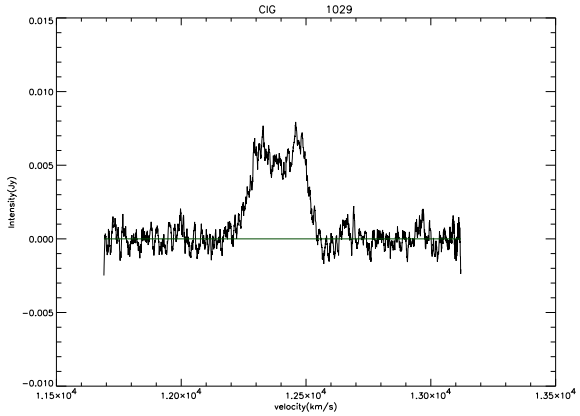


(f) CIG 1029, ART

Figure 8.3: Continued.

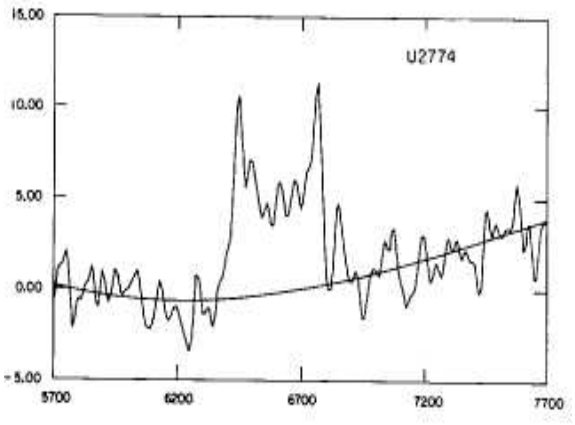


(a) CIG 128, ART, HG84

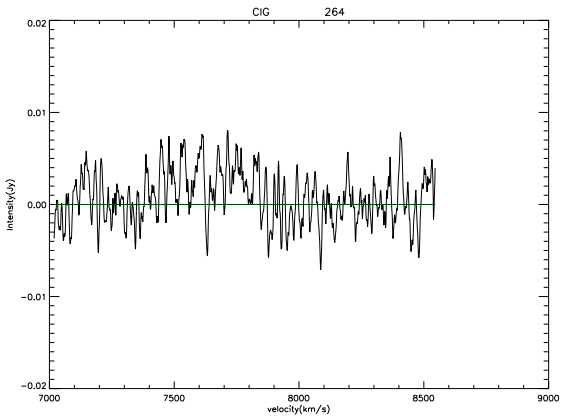


(b) CIG 264, NRT

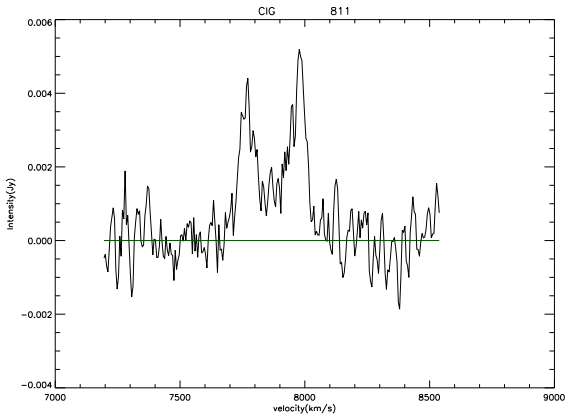


(c) CIG 811, ERT

Figure 8.4: HI profiles for the HI-rich early type subsample (see Fig. 8.7). E/S0 morphological types.

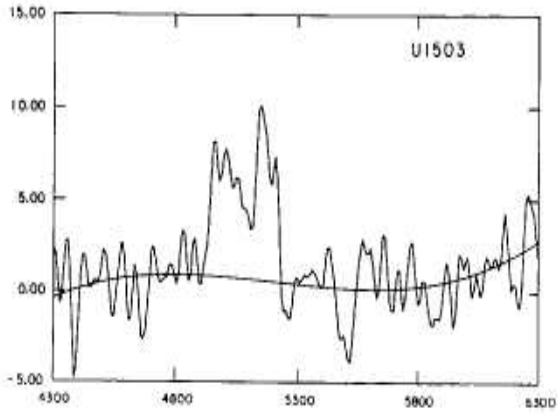


(a) CIG 83, ART, HG84

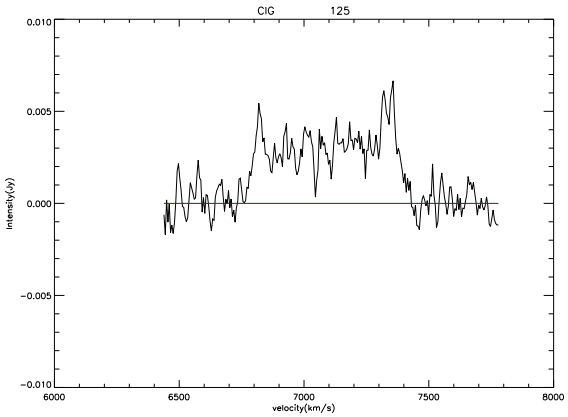


(b) CIG 125, ERT

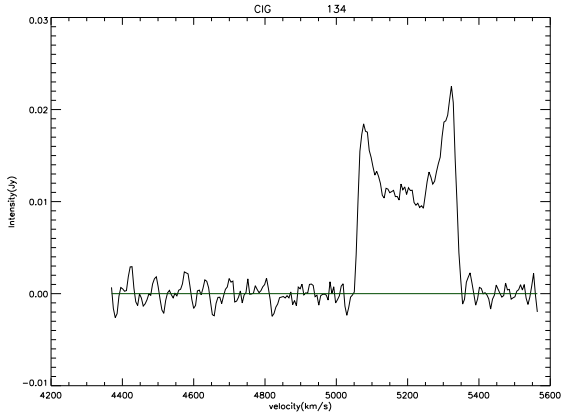


(c) CIG 134, ERT

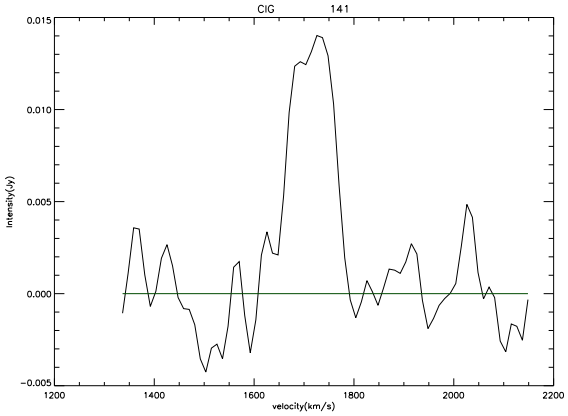


(d) CIG 141, HG

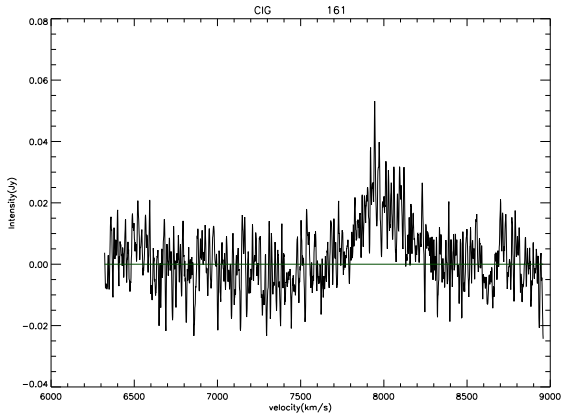


(e) CIG 161, NRT

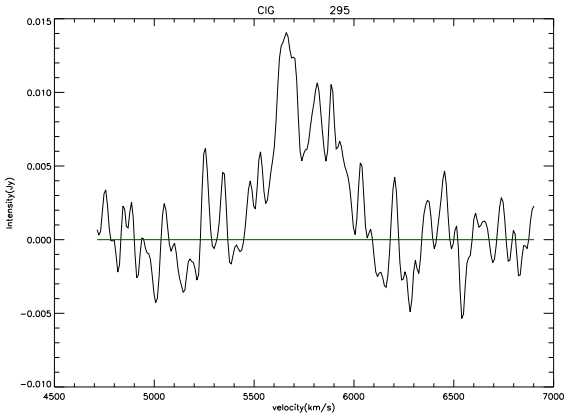


(f) CIG 295, HG

Figure 8.5: HI profiles for the HI-rich early type subsample (see Fig. 8.8). S0 morphological types.

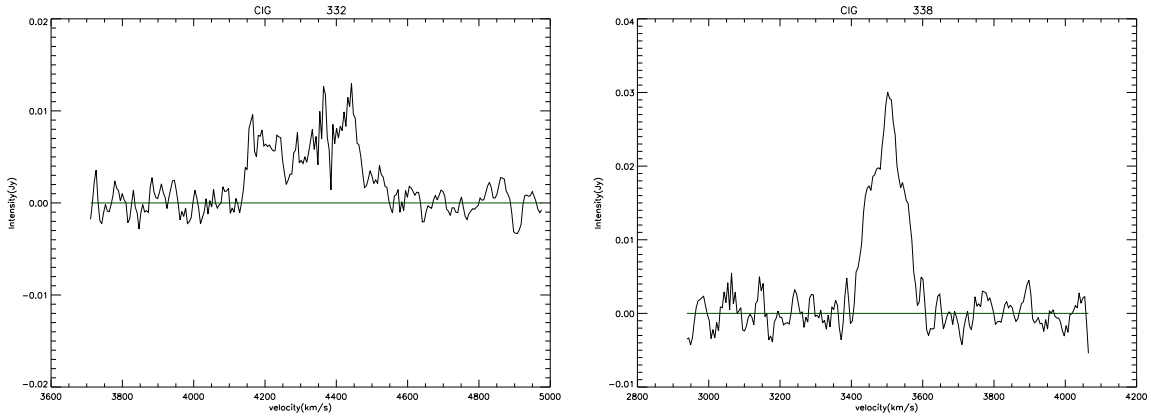


(a) CIG 332, ERT

(b) CIG 338, ERT

Figure 8.5: Continued.

### 8.4.1 HI detection rate

The HI detection rate of early type galaxies varies in the literature from 5 to 55% depending on the sample and depth of the survey. Note as well that this rate is dependent on the different morphological classifications performed from sample to sample, in the sense that one galaxy can be classified differently according to the considered images, criteria of different authors, etc. We will assume that this difference is not large and that general statistical studies can be performed.

The HI detection rate for the early type galaxies in AMIGA is $\sim$ 27% (28 % for Es, 25% for E/S0 and 27% for S0s). The detection rate does not seem to increase from ellipticals to lenticulars, as found by other authors using other samples of galaxies (e.g. Sadler et al. 2002 finds 6% detections for elliptical galaxies and 13% for S0s; a similar trend is found by Bettoni et al. 2003 and Bregman et al. 1992). This can be seen in detail in Tab. 8.3.

Low-luminosity early types seem to have a higher detection rate than bright galaxies. A total of 28 optically faint elliptical galaxies were observed by Lake & Schommer (1984) using the Arecibo radiotelescope and they found a detection rate of 39%. Sadler et al. (2001) selected the early type galaxies for which information was available in the HI Parkes All-Sky Survey (HIPASS). Their detection rate is seen significantly higher for low-luminosity E and S0 galaxies than for luminous ones (see Tab. 8.3). When sorting our sample by the same bins in $M_B$ we find 29% for -18 > $M_B$ > -20 (N = 50) and 25% for $M_B$ < -20 (N = 66). The sensitiviy is different in these studies, being the poorest sensitivity that of HIPASS, which takes into account galaxies with $M_{HI}$ between $10^9$ and $10^{10}$ $M_\odot$.

We can also discuss the effect that environment seems to cause in the detection rate of early type galaxies. The detection rate for our sample seems to be lower than for the normal galaxies considered by Bettoni et al. (2003)[1], but most of the HI data come from the literature (e.g. LEDA) and probably there is a selection effect toward HI detected galaxies. Bregman, Hogg, & Roberts (1992) find that peculiar galaxies (those with shells, dust lanes, or any other sign of interaction) are more easily detectable (45% against $\sim$ 20%). Our detection rate for a well-defined sample of isolated galaxies (although some with peculiar features too) is between both their non-peculiar and peculiar galaxies.

### 8.4.2 Shape of the HI profiles

In Tab. 8.4 we show the general information extracted from the shape of the HI profiles. We have classified them attending to the following notation: wide profile (W) if $W_{HI}$ > 400 km $s^{-1}$, very wide profile (VW) if $W_{HI}$ > 600 km $s^{-1}$, marginal if the detection is not sure for certain due to low

[1]Note that normal here means galaxies without any apparent sign of perturbed morphology and therefore they are not necessarily isolated galaxies

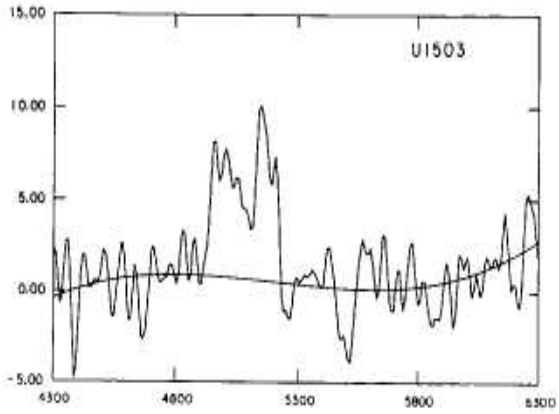


(a) CIG 83, ART, HG84

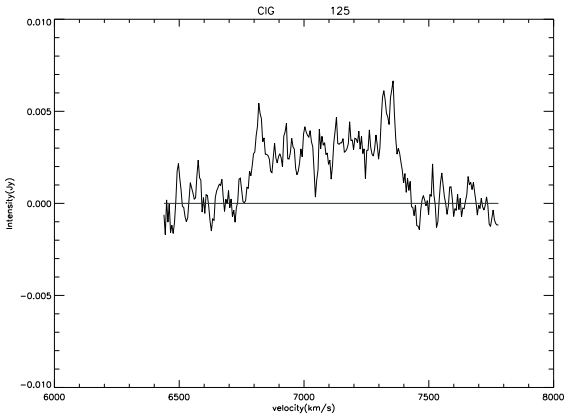


(b) CIG 125, ERT

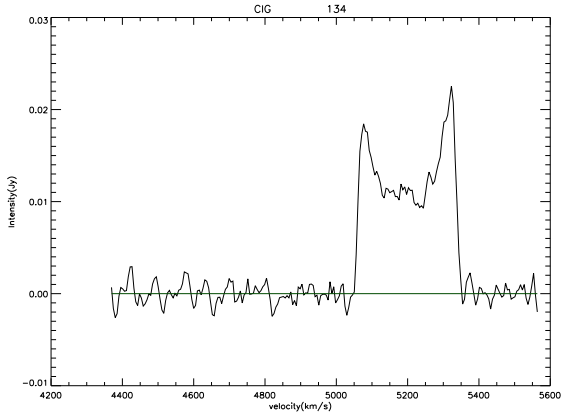


(c) CIG 134, ERT

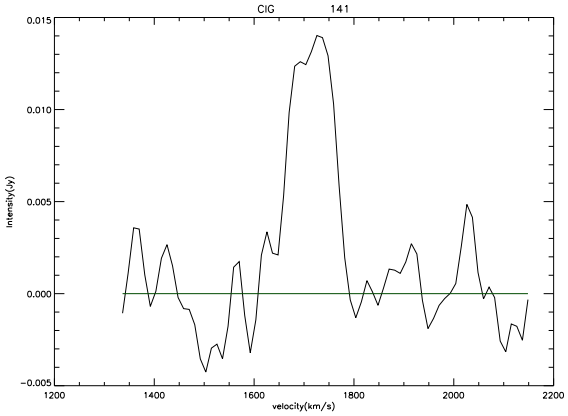


(d) CIG 141, HG

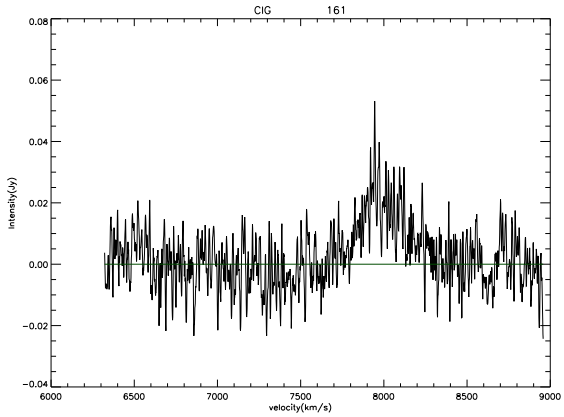


(e) CIG 161, NRT

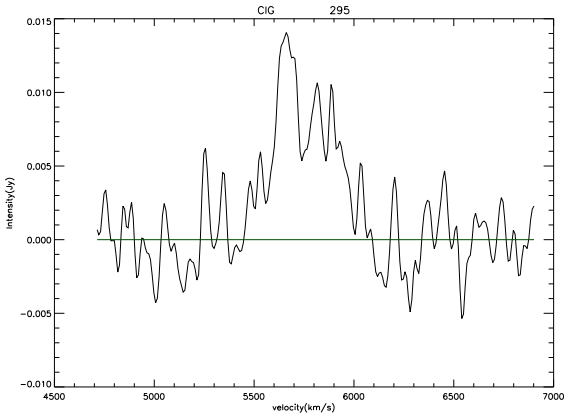


(f) CIG 295, HG

Figure 8.5: HI profiles for the HI-rich early type subsample (see Fig. 8.8). S0 morphological types.

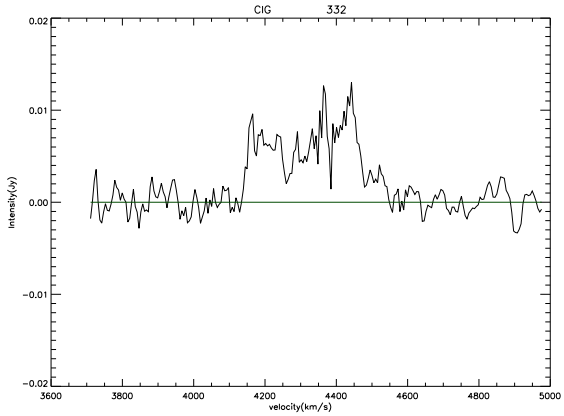


(a) CIG 332, ERT

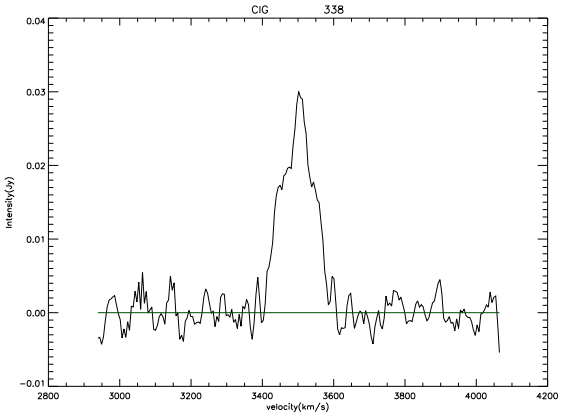


(b) CIG 338, ERT

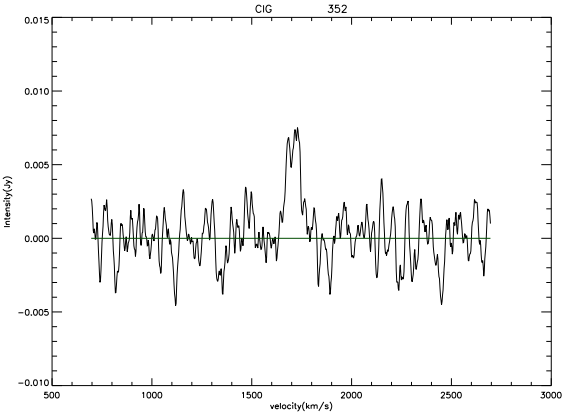


(c) CIG 352, NRT

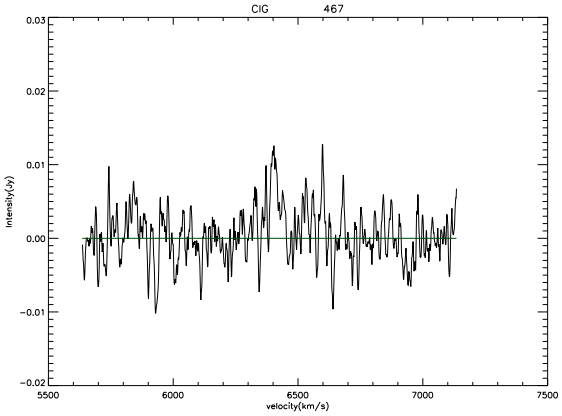


(d) CIG 467, NRT

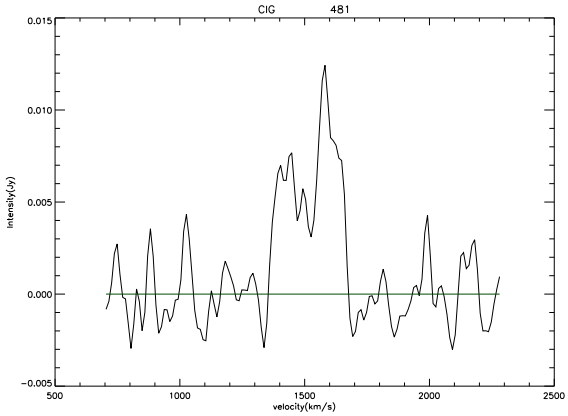


(e) CIG 481, HG

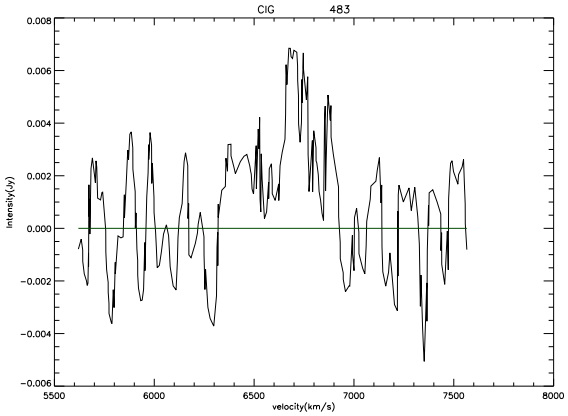


(f) CIG 483, HG84

Figure 8.5: Continued.

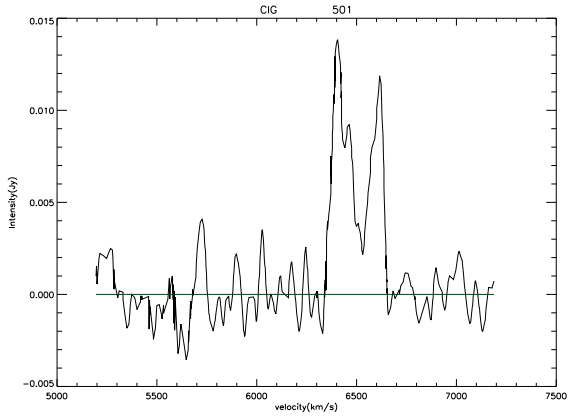


(a) CIG 501, HG80

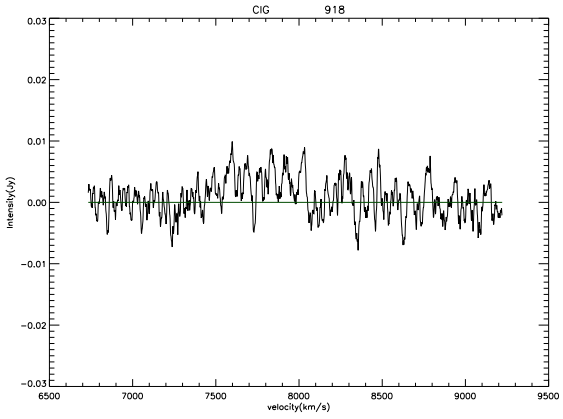


(b) CIG 918, NRT

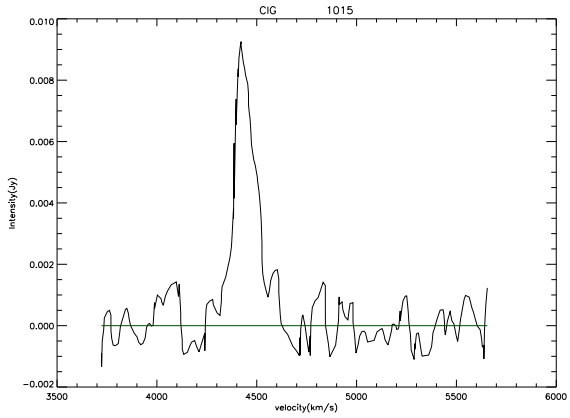


(c) CIG 1015, HG84

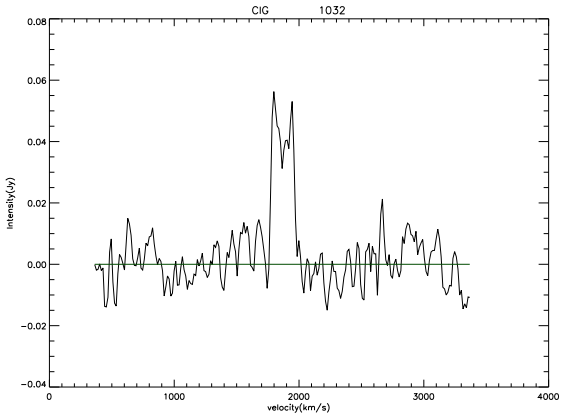


(d) CIG 1032, HIP

Figure 8.5: Continued.

Table 8.3: HI Detection rate for different samples of early type galaxies.

| Source | Type | HI detection rate | N |
|---|---|---|---|
| AMIGA | E, isolated | 28 % | 43 |
| | E/S0, isolated | 25 % | 12 |
| | S0, isolated | 27 % | 61 |
| | all ETIGs, -18 > $M_B$ > -20 | 29 % | 50 |
| | all ETIGs, $M_B$ < -20 | 25 % | 66 |
| HIPASS (Sadler et al. 2002) | E and S0 | 6% E / 13% S0 | $\sim$ 2500 |
| HIPASS (Sadler et al. 2001) | E and S0, -18 > $M_B$ > -20 | 22 $\pm$ 5 % | - |
| HIPASS (Sadler et al. 2001) | E and S0, $M_B$ < -20 | 10 $\pm$ 2 % | - |
| Lake & Schommer (1984) | low luminosity Es | 39% | 28 |
| Bettoni et al. (2003) | Es, normal[1] | 35 % | 116 |
| | E/S0, normal | 40 % | 48 |
| | S0, normal | 55 % | 307 |
| Bregman et al. (1992) | Es | 5% | 64 |
| | E/S0 | 17% | 23 |
| | S0 | 20% | 103 |
| | E, E/S0, S0 (peculiar) | 45% | 20 |

S/N ratio, and the number of horns in order to know which galaxies may have gaseous disks. We also show other relevant information as well as a visual inspection of the symmetry of the profiles (A = asymmetric, S= symmetric, ? = unknown). The latter has been performed by visual inspection because the S/N is not large enough to use our algorithm in most of the cases.

About 4 - 6 early type galaxies possess a wide profile, and 1 - 3 galaxies a very wide profile. We notice that at least 14 of the 31 HI profiles present a typical double horn in their HI profiles. These rate is as large for S0 as it is for Es. Therefore both may have gaseous disks, although it is usully thought that ellipticals do not have such property. As for the symmetry of the profiles, it seems that for those whose symmetry has been classified, at least 50% of the HI-rich ETIGs have very asymmetric profiles.

## 8.5 Origin of the HI-rich ETIGs: Minor/major mergers or primordial galaxies?

In this section we try to merge all the information that we have gathered before, in order to see whether the origin of the HI-rich ETIGs is more likely related to minor/major mergers (or gas accretion) or whether some of them are primordial galaxies.

As we have already mentioned in § 8.2.1, none of the ETIGs galaxies are likely to proceed from a past merged group since the total luminosity $M_B$ > -22 for all the galaxies. As for the $(B-V)_0$ color, several galaxies were likely to host recent SF that could be explained by minor mergers (see § 8.2.2). Most of the ETIGs detected in HI are located in the bluer regions of Fig. 8.2.

Only 6 galaxies from the HI-rich ETIGs have colors in the literature: CIG 164, 393, 824 and 870 (E); CIG 128 (E/S0); and CIG 481 (S0). In this section we focus on the properties of these galaxies since we have full information for them. It is apparent that bluer early type galaxies ($(B-V)_0 < 0.5$) are ellipticals (CIG 164, 393 and 870), and it is relevant to note that all of them have been detected

Table 8.4: Characterization of HI profiles for the HI-rich ETIG (E, E/S0 or S0).

| CIG | T $_{S06}$ | T $_{NED}$ | Width | Horns | Marginal det. | Symmetry | Other comments |
|---|---|---|---|---|---|---|---|
| 14 | E | E | ? | | Y | ? | interference |
| 136 | E | E | VW? | | Y | ? | |
| 164 | E | E | | 1 | | A | peak on one side |
| 393 | E | E | | 2 | | S | |
| 582 | E | E | W | 2 | | A? | |
| 824 | E | E | | | | ? | |
| 870 | E | E | | 1 | | S | long tails in HI profile |
| 877 | E | E | | 1 | Y | ? | |
| 895 | E | E | | 2 | | A? | |
| 981 | E | E | VW? | | Y | ? | |
| 1025 | E | E | | 2 | | A | |
| 1029 | E | E | | 2 | | A | long leften tail |
| 128 | E/S0 | S0 | | 2 | | S | |
| 264 | E/S0 | E | W | | Y | ? | |
| 811 | E/S0 | E | | 2 | | A? | no HI in the center? |
| 83 | S0 | E | | 2 | | ? | |
| 125 | S0 | Sb | VW | 2 | | S | |
| 134 | S0 | Sb | | 2 | | A | |
| 141 | S0 | S0? | | 1? | | ? | |
| 161 | S0 | S0? | W? | 1? | Y | ? | |
| 295 | S0 | S0 | W? | | | ? | |
| 332 | S0 | S0 | | 2 | | A | multicomponent? |
| 338 | S0 | Sb | | 1 | | ? | peculiar profile: 1 horn but inclined in the optical |
| 352 | S0 | Sb | | 1 | | S? | |
| 467 | S0 | SB0 | | | Y | ? | |
| 481 | S0 | SA(s)0/a | | 2 | | A? | |
| 483 | S0 | (R)SAB0 | W | | | ? | |
| 501 | S0 | E? | | 2 | | A? | no HI in the center? |
| 918 | S0 | Sc | W | | Y | ? | |
| 1015 | S0 | E? | | 1 | | ? | |
| 1032 | S0 | S0/a | | 2 | | S? | |

Table 8.5: Summary of the classification of HI profiles for the HI-rich ETIG[1].

| T | N | Two horns | One horn | Wide profile | Symmetric | Asymmetric |
|---|---|---|---|---|---|---|
| E | 12 | 5 | 3 | 1 (+2) | 2 | 3 (+2) |
| E/S0 | 3 | 2 | - | 1 | 1 | (+1) |
| S0 | 16 | 7 | 3 (+2) | 3 (+2) | 1 (+2) | 2 (+2) |
| Total | 31 | 14 | 6 (+2) | 5 (+4 ) | 4 (+2) | 5 (+5) |

[1](Numbers in parenthesis indicate the dubious classifications, which have not been added.

in HI. The rest of ETIG detected in HI have $(B-V)_0 > 0.7$.

**CIG 164** and **CIG 870** were already classified by Marcum et al. (2004) as merger remnants, due to their disturbed morphology, evident tidal features, blue colors and asymmetric nuclear morphology. CIG 164 even shows a low surface brightness bridge with a possible dwarf satellite (Marcum et al. 2004) (probably the asymmetry in its HI profile is a result of this fact). CIG 870 possibly posses a double nucleus, and presents tidal tails in the optical and is a HII with a possible AGN galaxy. Note that CIG 870 has a profile with long tails. Both galaxies are among the brightest galaxies in FIR luminosity, indicating that a high star formation is present in these galaxies. Therefore, the HI content of these galaxies could have come from the merging process. The merger ages for these two galaxies are about 1 - 2 Gyr following (Marcum et al. 2004).

**CIG 393** and **CIG 481** are also bluer than the values expected for an early type. The HII galaxy CIG 393 presents a blue asymmetric region towards the center, and CIG 481 shows a prominent dust lane. This suggest some merger event, although their HI profiles do not show a relevant lopsidedness. FIR detections are found for this galaxies, but with lower luminosities than in the case of CIG 164 and 870.

**CIG 128** and **CIG 824** are as red as expected for a normal early type galaxy. CIG 128 do not have any relevant peculiarity in their morphological properties and its HI profile is a symmetric double horn, while CIG 824 show an optical asymmetry in its nucleus that can be due to a past merger (merger age would be $>$ 2 - 3 Gyr because we see normal $(B-V)$ colors). FIR emission has not been detected in these galaxies. CIG 128 may be a good candidate to be passively evolving primordial early type galaxy.

On the other hand, we have not detected in HI another early type galaxy, CIG 684 ($M_{HI} <$ 1.7 e+09), which has normal elliptical $(B-V)$ colors ($\sim$ 0.95) and does not seem to have a past merger history (Marcum et al. 2004).

## 8.6 Conclusions and discussion

It is accepted that mergers between possibly gas-rich spiral galaxies can create spheroidal galaxies as remnants (Toomre & Toomre 1972). The HI of these galaxies may be ejected into tidal features and in principle could fall back (e.g. Hibbard 2000 and references therein). Some processes have been studied in order to explain how merger remnants remain gas poor in the presence of the continued return of HI from the created tidal features (e.g. superwinds and ionization by continued star formation). Assuming that the merger escenario is the main mechanism to produce early type galaxies, we can imagine that different kind of mergers can produce different products, depending on the impact properties and the properties of the objects.

The number of ETIGs depend on the environment. In fact, the population of ETIGs (Es to S0s) in the AMIGA sample is about 14 % (N = 138), percentage which is below the rate in denser environments. This may be interpreted in the sense that we have a sample of galaxies minimized in terms of major interactions. In this Chapter we study the nature of these early type galaxies. To do so we consider all the relevant data which we have obtained for the sample, that is, $M_B$ for all the ETIGs, HI for 116 ETIGs and FIR for 137 of them. A total of 31 of these galaxies have been detected in HI and the same number have been detected in FIR. About half of the galaxies detected in HI is also detected in FIR.

From the luminosities we find that none of the galaxies in our sample is expected to be a fossil group, since the typical $M_B$ value for early type galaxies is about $M_B$ = -20.5. There is a very low probability of two spiral galaxies in our sample (with $M_B$ = -20.8 mean value of types Sa - Sc for our sample) to produce early type galaxies since it would result in a more luminous system.

We detect 31 ETIGs in HI (27%). The morphological classification may be wrong in individual cases, but not in all the cases that we have shown. From these, 12 are ellipticals, 3 E/S0 and 16 lenticulars. The detection rate between E and S0 is very similar, result which is in disagreement with other ETIG samples in the literature. The non-dependence of the HI detection rate on the morphological type found by us for our early type objects could be an evidence of the different nature

of the galaxies with respect to other samples. Note that in our sample of isolated galaxies we do not have very luminous early type galaxies (Sulentic et al. 2006), but on the other hand, it is likely that other samples include very luminous elliptical galaxies typical of high density environments (which could look like not peculiars in the case of Bettoni et al. 2003). These are usually gas-poor and thus can decrease their detection rate.

The shape of the HI profiles can give us information about the origin of the HI-rich ETIGs: half of the galaxies present double horn profiles (even ellipticals galaxies), which is typical of gaseous disksThe existence of gaseous disks is in agreement with numerical simulations of the merger of two gas-rich spiral galaxies performed by Barnes (2002). Some of the gas loses its angular momentum due to shocks and falls to the nucleus, but about half of the gas contained in the progenitors can form a rotationally supported disk. In our sample one third of the HI-rich ETIGs present asymmetric profiles or some kind of peculiarity (e.g. CIG 870) and only a 20% present symmetric profiles. For the rest the low S/N does not allow us to classify the HI profiles, although we see that in some cases the HI profiles are very wide ($\sim$ 500 km s$^{-1}$).

Attending to the HI information, our galaxies in the HI-rich sample are members of three different groups: 1) HI profiles with one horn (e.g. CIG 164, 338, 352, 870 and 877), without any gaseous disks in principle; 2) asymmetric HI profiles with two horns (e.g. CIG 134, 332, 1025 and 1029), where the gas may proceed from minor mergers and is not settled yet; and 3) symmetric HI profiles with two horns (e.g. 128 and 393). Probably galaxies in group 3) come from group 2) but with the HI already settled. Another possibility is that symmetric and asymmetric profiles have different origins: taking into account that the asymmetric profiles are 1 mag brighter than the symmetric ones ($M_B$ -19.8 to -18.9), the former could be originated with mergers of low-luminosity spirals while the latter may be due to minor accretions.

Now we discuss the 6 galaxies for which we have full information, including $(B-V)$ colors, although it does not allow us to obtain general conclusions. We inspect $(B-V)$ colors, peculiarities in the optical images, HI information and FIR luminosities in order to check their origin. From this set of galaxies, we have detected HI in two ellipticals (CIG 164 and 870), with colors bluer than the usual values found in these galaxies, with morphological peculiarities and the largest values in FIR luminosity. Therefore they could have been formed as a result of a past minor merger (or merger of low-luminosity spiral galaxies). CIG 393 and CIG 481 are also bluer (but redder than the former group), with smaller FIR luminosities than CIG 164 and 870 and have some optical peculiarities (asymmetry in the center and dust lane). For galaxies with normal colors, upper limits in FIR and without any morphological peculiarities, we find early type galaxies with and without HI. For example one early type is detected: CIG 128, and another is not: CIG 684 (the upper limit is large though). CIG 128 could be a primordial elliptical galaxy with its own HI which have been evolving relatively isolated from the protogalactic formation, or probably it has obtain their HI via accretion of gas from the IGM.

## 8.7 Future work

We would need optical images with good spatial resolution in order to: 1) improve the morphological classifications and check possible fine structure such as shells, dust lanes, etc., 2) obtain colors that allow us to distinguish the possibility of a merger event, and 2) have information about SF. With a similar analysis to that done in this study, we will select the most representative cases in order to perform HI observations with high spatial resolution (e.g. VLA). This will allow us to better understand the origin of the HI in these galaxies, since we would have information about the HI distribution (tidal tails, ring structures, etc.) and its kinematics, in addition to the optical one.

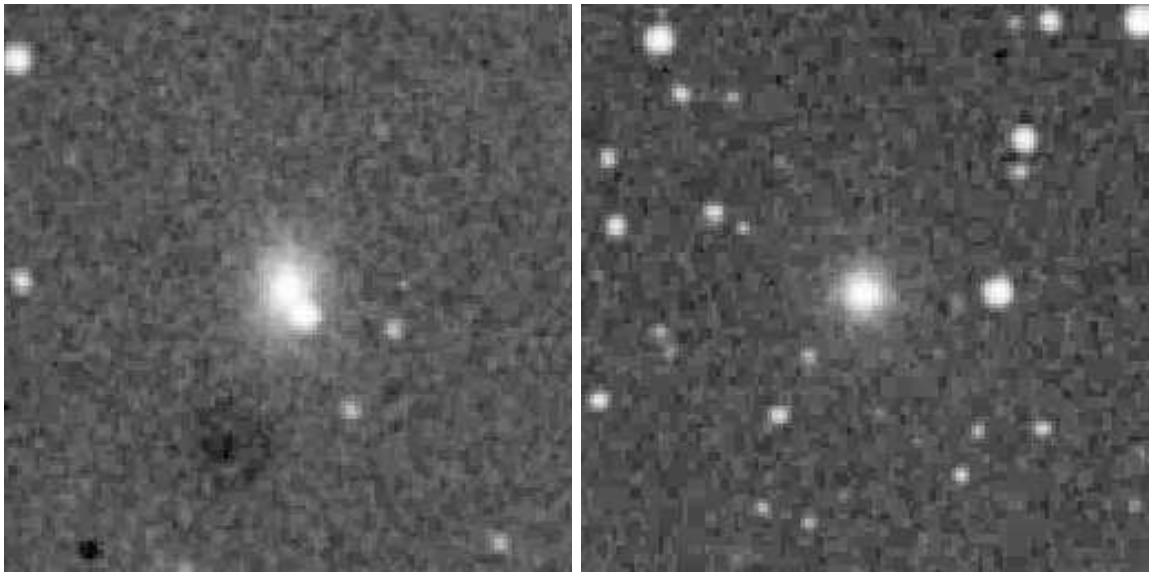

(a) CIG 14, POSSII

(b) CIG 136, POSSII

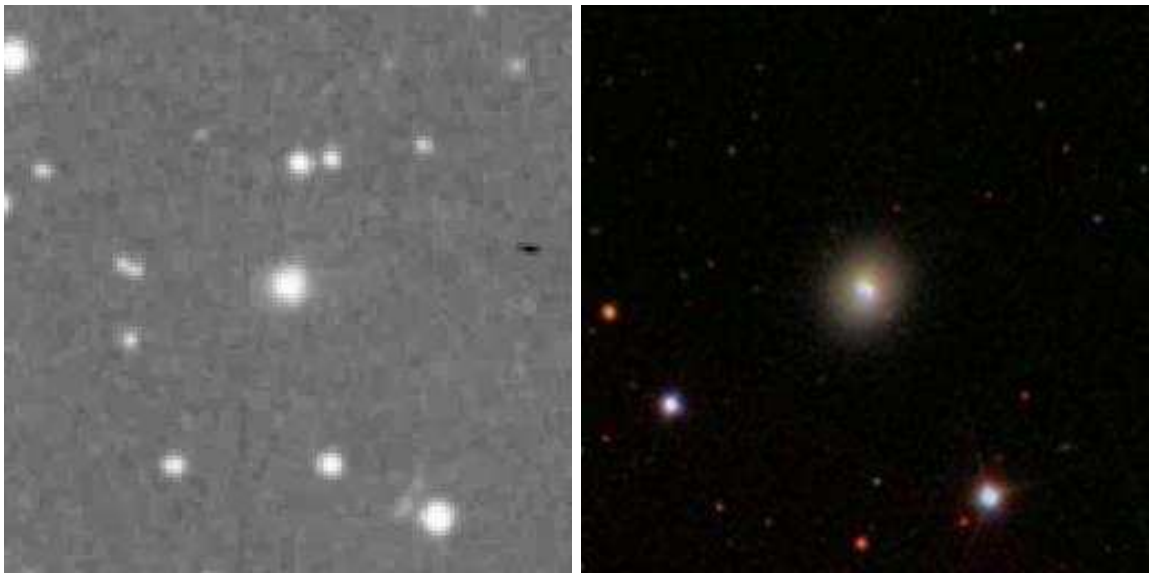

(c) CIG 164, POSSII

(d) CIG 393, SDSS

Figure 8.6: Optical images for the HI-rich early type subsample, from POSSII (Palomar Sky Survey) or from SDSS (Sloan Digitized Sky Survey ) when avalaible. E morphological types. The field is 3.4 $\times$ 3.4 $'$(256 $\times$ 256 pixels, with 0.8 $''$/pixel resolution for SDSS).

(a) CIG 582, SDSS

(b) CIG 824, POSSII

(c) CIG 870, POSSII

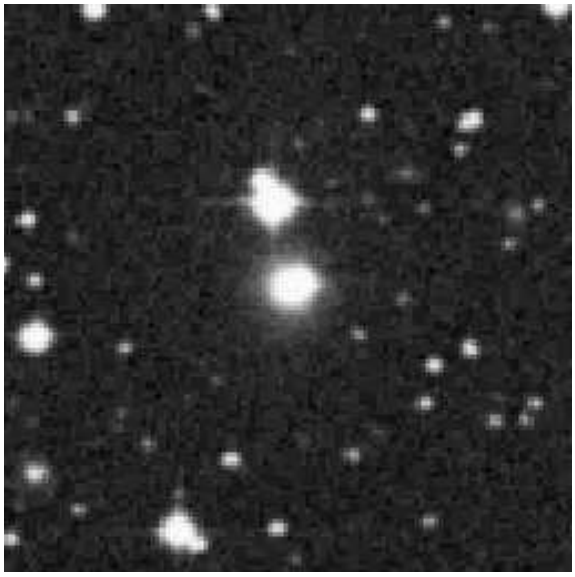

(d) CIG 877, POSSII

Figure 8.6: Continued.

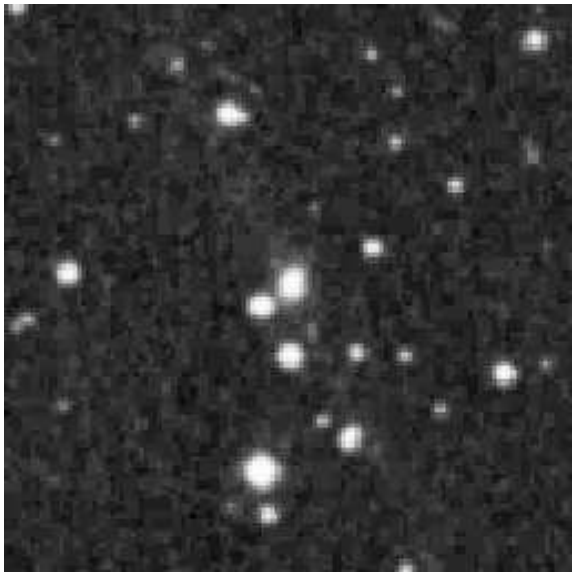

(a) CIG 895, POSSII

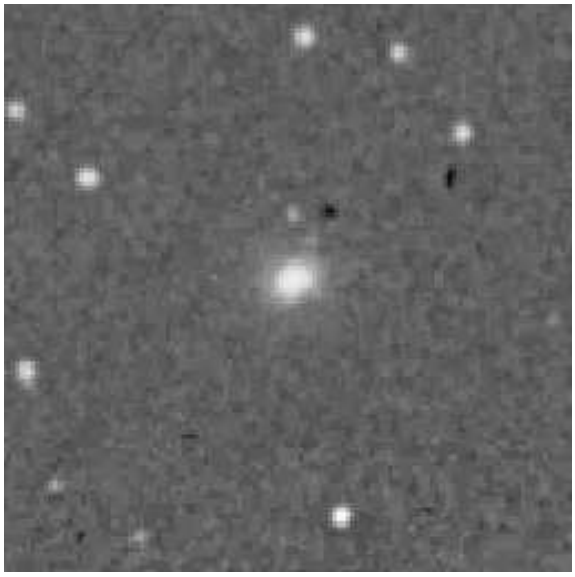

(b) CIG 981, POSSII

(c) CIG 1025, POSSII

(d) CIG 1029, SDSS

Figure 8.6: Continued.

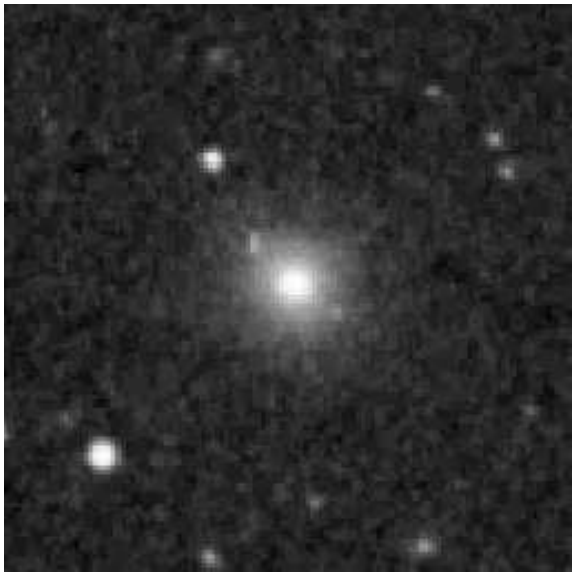

(a) CIG 128, POSSII

(b) CIG 264, SDSS

(c) CIG 811, POSSII

Figure 8.7: Optical images for the HI-rich early type subsample. E/S0 morphological types.

(a) CIG 83, POSSII

(b) CIG 125, POSSII

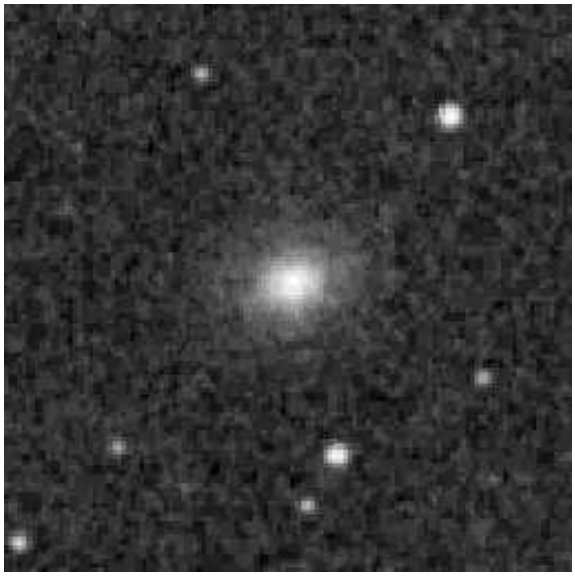

(c) CIG 134, POSSII

(d) CIG 141, POSSII

Figure 8.8: Optical images for the HI-rich early type subsample. S0 morphological types.

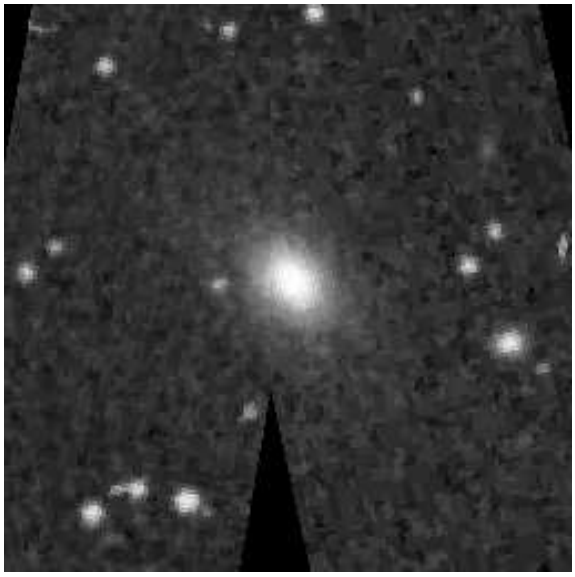

(a) CIG 161, POSSII

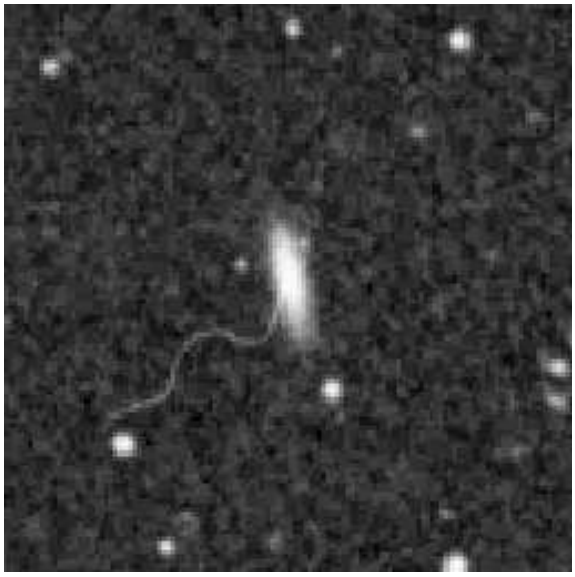

(b) CIG 295, POSSII

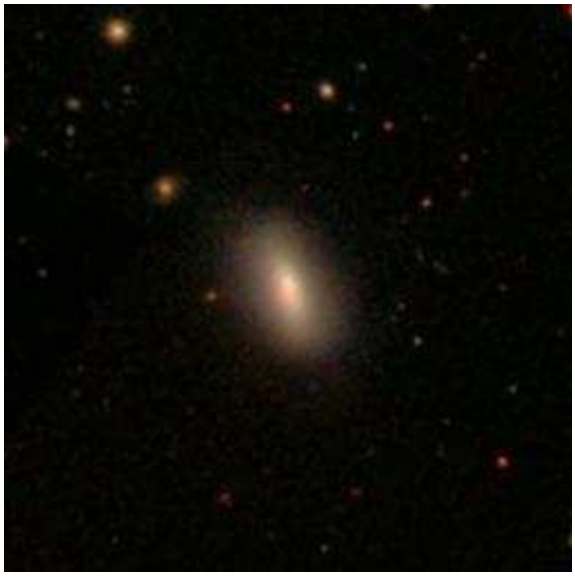

(c) CIG 332, SDSS

(d) CIG 338, SDSS

Figure 8.8: Continued.

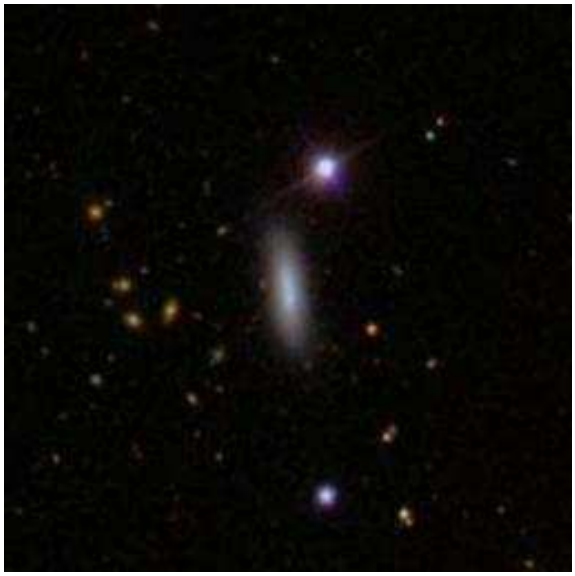

(a) CIG 352, SDSS

(b) CIG 467, SDSS

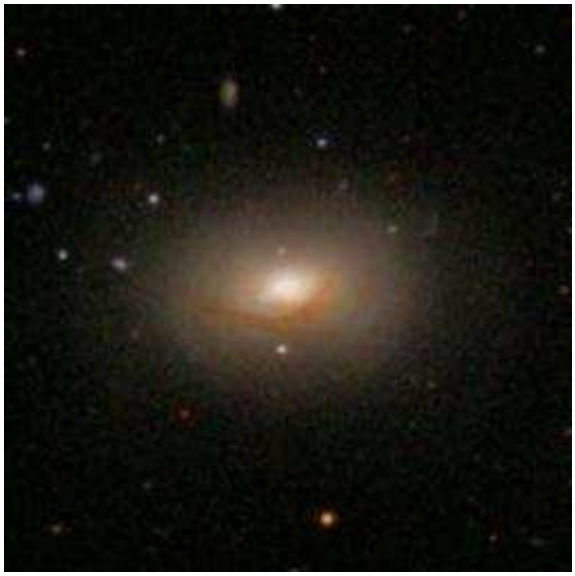

(c) CIG 481, SDSS

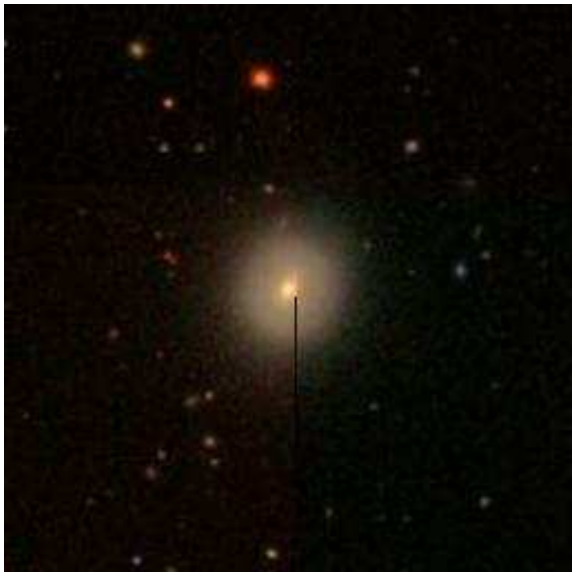

(d) CIG 483, SDSS

Figure 8.8: Continued.

(a) CIG 501, SDSS

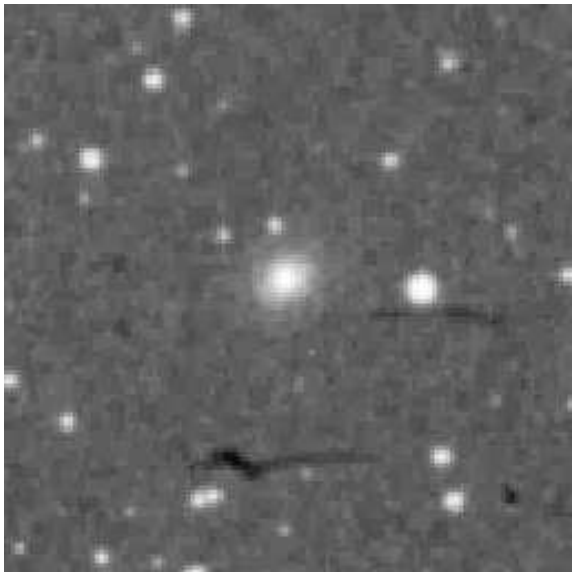

(b) CIG 918, POSSII

(c) CIG 1015, POSSII

(d) CIG 1032, SDSS

Figure 8.8: Continued.

# Part III

# Molecular gas

# Chapter 9

# CO in the AMIGA sample

In this chapter we present the single-dish 3mm CO(1-0) molecular emission survey of the AMIGA project, including 278 galaxies. We have observed 201 galaxies at FCRAO, IRAM 30m or Nobeyama and compiled the rest from the literature. We consider a redshift selected subsample between 1500 < v <5000 (N = 204 galaxies). We will refer to this sample as the CO(1-0) subsample. The CO(1-0) subsample is used in this Chapter to perform a statistical characterisation of the $M_{H_2}$ for a well-defined sample of isolated galaxies. We inspect the relationships between $M_{H_2}$, optical luminosity ($L_B$), linear optical diameter ($a$), Hubble type and atomic gas content ($M_{HI}$). We also check the influence of the environment on the $M_{H_2}$ in galaxies.

## 9.1 Introduction

While studies of HI have established that deficiencies of atomic gas are present in galaxies located in dense environments, the situation of the $H_2$ content ($M_{H_2}$) is somewhat unclear yet. There might be however a relationship between HI (which is the gas reservoir) and the $H_2$ (molecular clouds) of a galaxy. At the same time, star formation should be linked to $H_2$ since stars are formed by collapse of the molecular clouds. Although galaxies in high density regions usually have less $M_{HI}$ than isolated galaxies of the same Hubble type (e.g. Verdes-Montenegro et al. 2001a), their $M_{H_2}$ seem to be approximately normal for their Hubble type (Kenney & Young 1989; Stark et al. 1986).

A problem in the understanding of the $M_{H_2}$ as a function of the environment arises from the fact that the studied samples are very closeby galaxies and/or bright in the FIR, which are usually dominated by strongly interacting systems ( e.g. Solomon & Sage 1988). Therefore a biased detection rate is expected to be found since only this kind of galaxies is considered (e.g. Boselli et al. 1997).

It is therefore needed to consider a well-defined sample isolated galaxies in order to disentangle the role of the environment on the galaxy $M_{H_2}$. Only a few studies about the $M_{H_2}$ focusing on samples of normal galaxies have been performed so far: Solomon & Sage (1988), Sage (1993), Boselli et al. (1997), Perea et al. (1997) and Sauty et al. (2003a).

Except the latter reference, most of the isolation criteria used by the rest of studies are not as strict as that of the CIG, and may include interacting galaxies. Solomon & Sage (1988) consider galaxies with no companions at velocities $v < 1000$ km s$^{-1}$ with respect to the main galaxy at an extension of $10 \times D_{25}$, or showing no signs of morphological disturbance. Sage (1993) considers a distance-limited (D $\leq$ 10 Mpc) survey of nearby systems which "are not strongly interacting with their neighbours". As a result, only 6 out of their 50 galaxies were catalogued in the CIG. Boselli et al. (1997) observe 37 galaxies in the Coma/A1367 supercluster region without companions at a distance lower than 300 kpc. Perea et al. (1997) consider a sample of N = 68 (6 out of them were upper limits) normal galaxies which are not included in the CIG. Most of these galaxies had $v < 1000$ km s$^{-1}$. Therefore the isolation is difficult to check due to the large number of plates that need to be revised, so isolation is not completely guaranteed. The largest compilation of isolated galaxies is that by Sauty et al. (2003a),

Table 9.1: Properties of molecular gas regions.

| | |
|---|---|
| Density | n $\simeq 10^3$ - $10^5$ (cm$^{-3}$) |
| Temperature | T $\simeq$ 5-30 (K) |
| Pressure | P $\simeq 3 \times 10^{-12}$ - $3 \times 10^{-11}$ (dyn cm$^{-2}$) |

who observed a total of 99 CIG galaxies, although it suffers from not being complete since considers galaxies with v $<$ 14000 km s$^{-1}$.

In this Chapter we present the characterisation of the molecular gas for a subsample of CIG galaxies that will serve as reference of normalcy of the $M_{H_2}$ to be compared with that of galaxies in denser environments. Due to the reduced number of isolated galaxies found in the literature, we have chosen to focus on a redshift-limited subsample 1500 $<$ v $<$ 5000 (N = 204 CIG galaxies, the same subsample used in the H$_\alpha$ study by Verley 2006). CO(1-0) information have been obtained from our new observations or directly extracted from the literature.

The outline of this Chapter is very similar to that of the HI presentation. In § 9.2 we present the general properties of the CO(1-0) emission in galaxies (from which an estimation of $M_{H_2}$ is derived later). In § 9.3 we show the characteristics of the considered CO(1-0) sample as we did for the HI sample (radial velocities, morphologies, optical luminosities and diameters). In § 9.4 we include a description of the observations performed by us and the search for single-dish CO(1-0) data in the literature. The data reduction of the CO profiles, calculation of useful parameters, and the final presentation of the CO(1-0) data is included in § 9.4.5. The total CO(1-0) (from different pointings) and $M_{H_2}$ are calculated in § 9.5. We include in § 9.7 correlations between $M_{H_2}$, morphology, $L_B$, linear size $a$ and $M_{HI}$. Once the normalcy reference of isolated galaxies is built, we present in § 9.8 the comparison with other galaxies in denser environments.

## 9.2 Introduction to the $H_2$ properties in galaxies

The neutral gas is mainly composed by HI and H$_2$, which in normal spiral galaxies amounts on average to a 20% (Boselli et al. 1997). No H$_2$ rotational emission lines can be studied directly because it has no permanent electric dipole moment and its lowest energy rotational transition lie in the infrared ($\lambda$ = 24 $\mu$m), which is not easily observable. Nevertheless, $H_2$ can be traced by means of the most abundant molecule after it, the CO, through its rotational transition (1-0) at $\lambda$ = 3 mm, with an energy level of 5.2 K. Therefore this molecule is excited even in cold gas and CO is found to be optically thick in molecular clouds. We assume that clouds can be considered to be virialized so that the integrated brightness temperature, $I_{CO}$, is proportional to $M_{H_2}$.

The CO(1-0) transition was discovered by Wilson et al. (1970) in the Orion Nebula, and since then it has become one of the most powerful tools for the study of the cold and dense ISM (H$_2$) in galaxies. The properties of the molecular regions traced by this emission line are expressed in Tab. 9.1.

The fist successful detection of a galaxy in CO(1-0) was performed by Rickard et al. (1975) towards the galaxies NGC 253 and M 82. Since HI is the reservoir for $H_2$, any perturbation or deployment in the HI can lead to a different evolution of the galaxy, producing changes in its $H_2$ component and therefore in the SF. The molecular gas content is seen to increase from early to late type spirals (Sauty et al. 2003a), being the ISM of the former types mainly molecular while the latter ones possess an ISM richer in atomic gas (e.g. Young et al. 1995).

### 9.2.1 CO to H$_2$ ratio

The $M_{H_2}$ is usually calculated assuming a constant ratio X = $N_{H_2}/I_{CO}$. Several values for X are considered, for example Strong et al. (1988) find X = 2.3 $\times$ 10$^{20}$ cm$^{-2}$ (K km s$^{-1}$)$^{-1}$, while Young & Scoville (1991) consider X = 3 $\times$ 10$^{20}$ cm$^{-2}$ (K km s$^{-1}$)$^{-1}$. In order to compare with other samples in the

literature, we will consider along this work the latter value. This factor is obtained from a rough empirical comparison of dynamical masses of resolved molecular clouds and CO emission in our Galaxy and nearby galaxies.

This conversion factor is expected to depend on density and temperature (from the virial theorem) and metallicity. In particular, one would expect X to increase with metallicity and observations seem to confirm this expectation (Wilson 1995):

$$X \simeq 3 \times 10^{24} \ [(6 \pm 0.9) - (0.7 \pm 0.1)[12 + \log(O/H)]]$$

which means a five-fold decrease in X for a tenfold decrease in metallicity. X is found to increase with increasing radius in our galaxy and other galaxies (e.g. IC310) (Wilson 1995; Sodroski et al. 1995; Strong et al. 2004). However, no evidence of radial variation is found in M31 (Nieten et al. 2005).

Therefore, the assumption of a constant conversion factor between CO and $H_2$ can lead in some cases to wrong results, especially in those galaxies where the molecular gas clouds properties are not similar to those in our Galaxy or other nearby galaxies (e.g. dwarf galaxies).

### 9.2.2 $H_2$ distribution

Considering the radial density profiles of $H_2$ and HI we can see several differences. Whereas the distribution of HI often shows a depression in the center and its distribution is more extended than the distribution of star-light, $H_2$ is seen to be much more strongly concentrated towards the center of the galaxy (Binney & Merrifield 1998).

Young et al. (1995) find that the distribution of the CO(1-0) emission is often concentrated in the center: Only 15% of the 193 galaxies observed at multiple positions with a 45″ resolution showed molecular distributions that lacked a central peak, within 0.5 the optical extent more or less and with an exponential decay as in the optical. Recent synthesis imaging of 44 galaxies by Helfer et al. (2003) with a 6″ resolution show that about half of the galaxies did not exhibit central peaks, but other structures such as rings and bars.

### 9.2.3 $M_{H_2}$, $L_{FIR}$ and $L_B$

$L_{FIR}$ is usually used as tracer of star formation (in fact, it is produced by dust heated by young OB stars). It is seen that the correlation between $L_{FIR}$ and $M_{H_2}$ is linear (e.g. Perea et al. 1997). We can use $L_{FIR}/M_{H_2}$ as an indicator of the efficiency of SF. This ratio depends strongly on the temperature of the dust, which is determined as the ratio of emission in the 60 and 100 microns (higher for interacting galaxies). In normal spirals this ratio varies from 1 to 3; in starburst galaxies the ratio is 20-30, and is 100-200 in ULIRGs (Combes et al. 1995).

On the other hand, Perea et al. (1997) find a non-linear dependence is found between $M_{H_2}$ (or $L_{FIR}$) versus $L_B$ for a wide range in $L_B$. When comparing $M_{H_2}$ versus $L_B$ and FIR with galaxies in denser environments they do not find an enhancement in $M_{H_2}$ , and only find a weak trend of higher FIR luminosities for strongly interacting galaxies. They also claim that they do not find any dependence in the linear regression fits as a function of morphological type.

## 9.3 The CO sample

We have CO(1-0) data for 278 members of the CIG. The heliocentric velocities distribution for these galaxies are shown in Fig. 9.1. Most of these galaxies (N = 182) have been observed by us at the IRAM 30m, FCRAO 14m or Nobeyama 45m radio-telescopes, and the rest of data were compiled from a search in the bibliography. We have observed 103 galaxies at the FCRAO radio-telescope, 101 at the IRAM 30m and 9 at Nobeyama, and found CO(1-0) data from the literature for 74 galaxies in the CIG sample. The CO(1-0) study focus on a redshift-limited subsample ($1500 < v < 5000$ km s$^{-1}$) of those isolated galaxies which had been classified as strictly isolated following the Karatchenseva's criteria, including a total of 204 CIG galaxies.

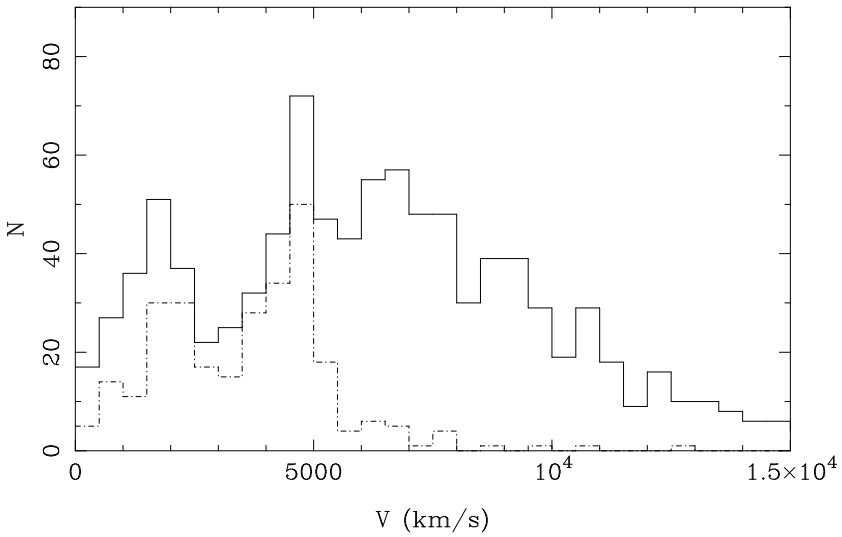


Figure 9.1: Histogram of optical heliocentric velocities for those CIG galaxies with CO(1-0) data (dashed-pointed line) versus the 989 CIG galaxies with redshift data (solid line).

By using this sample we are considering a wide range of luminosities and morphologies. The galaxies cover a range in luminosities from $L_B \simeq 9$ - 11 $L_\odot$, as shown in Fig. 9.2(a). The mean value of $L_B$ is 9.9 $\pm$ 0.4. In Fig. 9.2(b) we show the number of galaxies with $M_{H_2}$ data for a given morphological type. This will allow us to make statistical studies as a function of the morphological type, except for early type galaxies since the AMIGA sample contains only a 14% of this kind of galaxies.

## 9.4 CO(1-0) data

Our data come mainly from observations performed by us at the IRAM 30m and FCRAO 14m radio-telescopes from 2002 to 2004 (N = 204 galaxies). A total of 9 galaxies were observed at Nobeyama but we had bad weather and pointing problems. These data have not been included in the study. Data for 74 galaxies have been also obtained from the literature, 40 of them with v > 1500 km $s^{-1}$. In Tab. 9.2 we show the antenna size, the half power beam width (HPBW) and the conversion factor Jy/K at the CO(1-0) frequency for the main millimetre radio-telescopes where CO(1-0) surveys have been performed.

Table 9.2: Main parameters of millimetre single-dish radio-telescopes.

| code | Radio-Telescope | Diameter | $\theta_{HPBW}$ (115 GHz) | Jy/K |
|---|---|---|---|---|
| 1 | Nobeyama | 45m | 10″ | 4.2 |
| 2 | IRAM | 30m | 22″ | 4.95 |
| 3 | FCRAO | 14m | 45″ | 42 |
| 4 | SEST | 15m | 44″ | 27 |
| 5 | Onsala | 20m | 33″ | 19 |
| 6 | NRAO | 12m | 55″ | 33 |

### 9.4.1 Compilation of CO(1-0) data

There are very few CO(1-0) studies on isolated galaxies, most of them with no special care in the sample definition. Most of the CO surveys focus in the brightest IRAS sources ($S_{60\mu}$ > several Jy), on

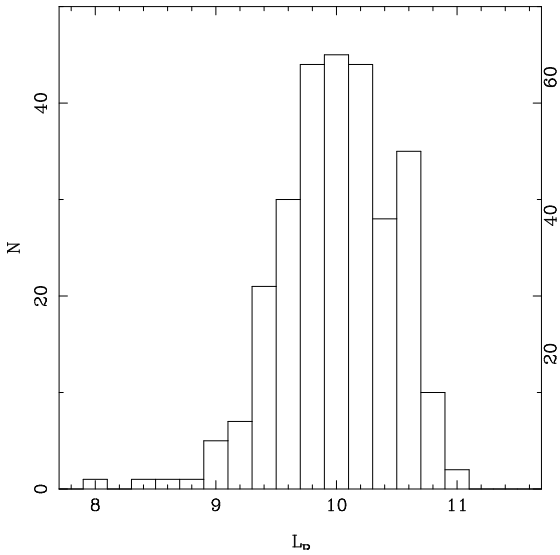


(a) $L_B$ distribution for the CIG galaxies with CO(1-0) data (N = 278).

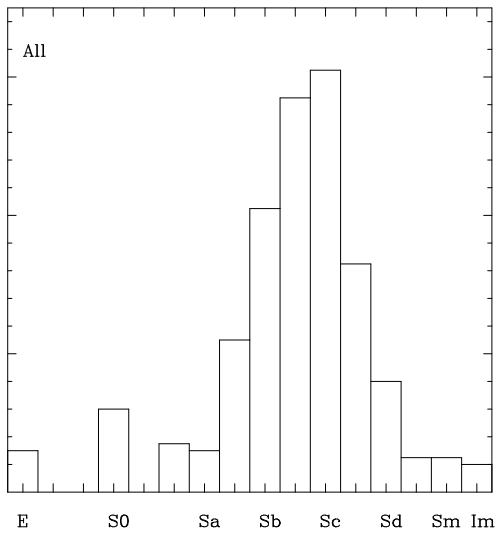


(b) Distribution of morphologies for the CIG galaxies with CO(1-0) (N = 278).

Table 9.3: List of papers from which we have compiled the CO data.

| Bibl. code | | Article | Telescope | N |
|---|---|---|---|---|
| 1 | Yo95 | Young et al. (1995) | 3, 6 | 34 |
| 2 | Br93 | Braine & Combes (1993) | 2 | 12 |
| 3 | Sa03 | Sauty et al. (2003a) | 2, 4, 6 | 99 |
| 4 | El96 | Elfhag et al. (1996) | 4, 5 | 15 |
| 5 | SS88 | Solomon & Sage (1988) | 3, 6 | 7 |
| 6 | Sa93 | Sage (1993) | 6 | 7 |
| 7 | Ch96 | Chini et al. (1996) | 2 | 4 |

the contrary to the majority of our sources ($S_{60\mu} < 1$ Jy). The only survey focused on CIG galaxies is Sauty et al. (2003a) with N = 99 galaxies, although it suffers from not being complete since includes galaxies within a wide range of velocities ($0 < v < 14000$ km s$^{-1}$ ), and it does not consider any isolation criterion. We include all of their galaxies in our compilation.

In Tab.9.3 we show the articles where we have found single-dish CO(1-0) data for our whole sample of isolated galaxies. The telescopes codes are as in Tab. 9.2.

### 9.4.2 Description of the observations

We sorted the galaxies according to the ratio of the radio-telescope beam to the optical size: galaxies with $D_{25} < 45''$ were observed at Nobeyama 45m, those with $45'' < D_{25} < 100''$ at IRAM 30m and the rest at FCRAO 14m. Since the sensitivity of each radio-telescope is very different, we tried to obtain the same upper limit to have useful statistics. This upper limit has been fixed to be $6 \times 10^8$ $M_\odot$, assuming a typical width of 200 km s$^{-1}$ and a $3\sigma$ level of the emission of the source. At the Nobeyama radio-telescope we observed 9 galaxies and we only marginally detected 2 of the galaxies due to bad weather conditions and bad pointing. We therefore do not include these observations in the study, but we have re-observed these galaxies with IRAM 30m.

A total of 13 galaxies have been observed both at FCRAO 14m and IRAM 30m to check the consistency of the calibration at different telescopes. Since the CO(1-0) emission is usually confined

Table 9.4: Summary of our CO(1-0) observations.

| Radio-telescope | N | Det. | Resolution (km s$^{-1}$) | Bandwidth (km s$^{-1}$) | Observing dates |
|---|---|---|---|---|---|
| FCRAO 14m | 103 | 55% | 13.1 | 825 | 200h (3 blocks), Dec 2002 to May 2003 |
| IRAM 30m | 102 | 78% | 2.6 | 1250 | 170h, Nov 2002 to Jan 2004 |

within the 70% of the optical diameter, our strategy suggests that we are not losing most of the CO(1-0) emission. Some of our galaxies subtend several arcminutes in size, much larger than any of the considered single dish radio-telescopes, and therefore a mapping of the galaxy is needed if we do not want to lose a considerable amount of the flux. At IRAM 30m 19 galaxies were mapped along the major axis with offsets of 15″, until the detection limit was reached. Data observed at Nobeyama (only 2 detections) have not been considered in the current study.

In Tab. 9.4 we present the general summary of the observations performed by us, as well as the configuration of the backend (used resolution and bandwidth).

### 9.4.3 IRAM 30m

A total of 102 galaxies were observed at the IRAM 30m radio-telescope.The beam size of this antenna at CO(1-0) is 22″, which corresponds to 3.5 kpc at a distance of 2500 km s$^{-1}$, assuming a Hubble constant H$_0$ = 75 km s$^{-1}$ Mpc$^{-1}$. The 3mm heterodyne receiver HERA was used for these observations. The detection rate for this radio-telescope was around 78%, for the 102 observed galaxies. A total of 19 galaxies with the strongest emission at the center have been mapped using 5 positions along their major axis with a spacing of 15″, until the detection limit was reached. The galaxies were grouped into seven ranges of velocity with a width of 500 km s$^{-1}$ to avoid losing time for tuning. The integration time was 7 minutes for pointing (scan + calibration), and a maximum time of around 1.5 hours. The flux density scale for this antenna is 6.3 Jy/K for the 115 GHz band.

### 9.4.4 FCRAO 14m

Observations were also carried out with the FCRAO 14m radio-telescope. The beam size of the radio-telescope at this frequency to observe CO(1-0) is 47″ (88″ between pixels), which corresponds to 7.5 kpc at a distance of 2500 km s$^{-1}$ (again considering H$_0$ = 75 km s$^{-1}$ Mpc$^{-1}$). The used heterodyne receiver was SEQUOIA, which is a 4 × 4 pixels array operating from the 85 to 115 GHz. We used the so called "beam switching" mode, by considering the information in one pixel when it is ON source and the signal in the opposite pixel when it is OFF source. With this mode we double the effective integration time.

We have observed 102 galaxies in this radio-telescope, being the detection rate 52%. We performed observations of around one hour for each galaxy (or 2 hours with this method), so we can have upper limits of $10^8 M_\odot$. The flux density scale is 42 Jy/K for this antenna.

### 9.4.5 Final presentation of the CO(1-0) data

The data was reduced in the standard way (similar to that in HI profiles), using the CLASS package. The spectra were added and a constant continuum level was subtracted. All the CO spectra and luminosities are presented on the main beam temperature scale which is defined as

$$T_{mb} = (F_{eff}/B_{eff}) \times T_A^*$$

. The HI profiles observed by us at FCRAO 14m and IRAM 30 are shown in Appendix **??**.

In Tab. 9.5 we show the obtained data. The list of calculated parameters is the following:

1) CIG : Entry number in the Catalog of Isolated Galaxies.

2) Off. $\alpha$: offset position in R.A., in arcsec.

3) Off. $\delta$: offset position in declination, in arcsec.

4) $\alpha$: R.A., in hh:mm:ss.s

5) $\delta$: declination in (-)dd:mm:ss.s.

6) Det: detection code (0 = detection, 1 = non-detection, 2 = marginal)

7) rms: root main square in mK.

8) $I_{CO}$: integrated flux intensity $\int T_{\rm mb}\ {\rm d}v$, in K km s$^{-1}$, and its error, calculated as:

$$\text{error } (I_{CO}) = \sigma(W_{CO}\ \delta V_{CO})^{1/2}\ [\text{K km s}^{-1}]$$

For undetected galaxies, the reported value is an upper limit determined as:

$$I_{u.l.}(\text{CO}) = 3 \times \sigma(W_{HI}\ \delta V_{CO})^{1/2}\ [\text{K km s}^{-1}]$$

where $\sigma$ is the rms noise of the spectrum, $W_{\rm HI}$ is the HI line width, and $\delta V_{\rm CO}$ is the spectral resolution. Note that for galaxies with unknown $W_{\rm HI}$ the HI width was considered to be 300 $\times$ sin($i$) km s$^{-1}$, where $i$ is the galaxy inclination, or 50 km s$^{-1}$ if $i = 0^{\rm o}$. Each $I_{CO}$ was converted into the $T_{mb}$ scale.

9) $V_{CO}$: mean velocity of the CO profile, in km s$^{-1}$.

10) $W_{CO}$: width of the profile, in km s$^{-1}$.

11) Tel: radio-telescope code, as shown in Tab. 9.2.

12) Bib: bibliographic code, as in Tab. 9.3.

Table 9.5: CO(1-0) data for the CIG galaxies.

| CIG (1) | Off. $\alpha$ (2) | Off. $\delta$ (3) | $\alpha$ (4) | $\delta$ (5) | Det. (6) | rms (7) | $I_{CO}$ (8) | $V_{CO}$ (9) | $W_{CO}$ (10) | Tel. (11) | Bib. (12) |
|---|---|---|---|---|---|---|---|---|---|---|---|
| 1 | 0 | 0 | 00:03:05.6 | -01:54:49.0 | 0 | 4.1 | 1.99 ± 0.55 | 7322 | 302 | 32 | 58 |
| 4 | 0 | 0 | 00:01:24.9 | 20:28:18.0 | 0 | 2.0 | 5.22 ± 0.79 | 2324 | 480 | 1 | 7 |
| 4 | 32 | 32 | 00:01:24.9 | 20:28:18.0 | 1 | 0.0 | 1.04 ± 0.39 | 0 | 0 | 1 | 7 |
| 4 | -32 | -32 | 00:01:24.9 | 20:28:18.0 | 0 | 3.0 | 1.62 ± 0.39 | 2433 | 130 | 1 | 7 |
| 4 | 0 | 0 | 00:03:58.7 | 20:45:03.0 | 0 | 2.7 | 5.71 ± 0.36 | 2345 | 292 | 33 | 58 |
| 6 | 0 | 0 | 00:08:54.7 | 23:49:04.0 | 1 | 2.1 | 0.21 ± 0.00 | 0 | 0 | 33 | 58 |
| 10 | 0 | 0 | 00:13:00.6 | 39:14:45.9 | 2 | 2.1 | 0.97 ± 0.20 | 5070 | 400 | 2 | 1 |
| 11 | 0 | 0 | 00:14:31.8 | -00:44:15.0 | 1 | 3.9 | 0.51 ± 0.00 | 0 | 0 | 32 | 58 |
| 22 | 0 | 0 | 00:27:35.4 | 08:52:38.0 | 0 | 3.1 | 0.94 ± 0.31 | 13131 | 166 | 32 | 58 |
| | ... | ... | ... | ... | ... | ... | ... | | | | |

### 9.4.6 Detection rate

Since we have not selected our CO(1-0) sample (N = 278) attending to FIR luminosity but to an isolation criteria, it is of interest to see what the detection rate is. The detection rate taking into

Table 9.6: Detection rate as a function of the morphology.

| Type | T | N | Det. | Non-det. | CO Detection rate | HI Detection rate |
|---|---|---|---|---|---|---|
| E | -5 | 6 | 2 | 4 | 33% | 50% (3/6) |
| S0 | -2 | 12 | 4 | 8 | 33% | 42% (5/12) |
| S0/a | 0 | 7 | 3 | 4 | 43% | 57% (4/7) |
| Sa | 1 | 6 | 5 | 1 | 83% | 100% (6/6) |
| Sab | 2 | 22 | 19 | 3 | 89% | 89% (16/18) |
| Sb | 3 | 42 | 32 | 10 | 75% | 95% (38/40) |
| Sbc | 4 | 57 | 41 | 16 | 70% | 98% (52/53) |
| Sc | 5 | 62 | 48 | 14 | 74% | 98% (53/54) |
| Scd | 6 | 33 | 17 | 16 | 46% | 100% (26/26) |
| Sd | 7 | 16 | 8 | 8 | 50% | 100% (12/12) |
| Sdm, Sm, Im, Pec. | 8,9,10,998 | 15 | 2 | 13 | 13% | 100% (12/12) |
| E,S0,SO/a | -5,-2,0 | 25 | 9 | 16 | 36% | 48% (12/25) |
| All | | 278 | 181 | 97 | 65% | 91% (227/246) |

account data from our observations and the literature is the following: 65% are detections or marginal detections and 35% upper limits. When we compare our global CO detection rate of 65% with other sources in the literature we find that our percentage is lower. For example, Young et al. (1995) detect 236 out of the 300 galaxies in their survey (80%).

An interesting issue is to see the detection rate as a function of morphology. The number of non-detected galaxies is higher for early type galaxies and T > Sd. The HI detection rate considering the same sample is larger for all the morphological bins, 72% are detections (including marginal detections) and 24% non-detections. In Tab. 9.6 and Fig. 9.3 we can see the CO(1-0) and HI detection rate as a function of the morphology. It is especially remarkable that the detection rate as a function of morphology is always higher in HI than in CO (in total, 91% to 65% respectively). Especially interesting is the fact that the CO detection rate distribution has a peak for Sa/Sab galaxies (85%) while the HI detection rate is maintained to around 90% for all spirals, from Sa to Sd. Half of the Scd or Sd galaxies are not detected in CO but all of them are detected in HI. A total of 7 galaxies are not detected in HI but have been detected in CO: CIG 153 (T = -2), 1013 (T = 2), 160 (T = 2), 306 (T = 5), 678 (T = 0), 733 (T = 3), 886 (T = 0). In Fig.9.2 we show the distribution of detections and non-detections as a function of the morphology for the CO(1-0) sample (N = 278).

The detection rate is larger for Sa to Sc ($\sim$ 80 %). Although the types from Sa to Sd have similar distributions of velocities, the galaxies in Sa - Sc have larger $L_B$ (see Fig. 9.4), and since $M_{H_2}$ correlate with $L_B$, they are expected to be easier to detect.

## 9.5 $M_{H_2}$ derivation

The molecular hydrogen content (or its upper limit value), $M_{H_2}$, was determined with the derived $I_{CO}$ and adopting a constant conversion factor X = 3 $\times$ $10^{20}$ mol cm$^{-2}$ (K km s$^{-1}$)$^{-1}$ (see discussion in Sect. 9.1). Then, $M_{H_2}$ is derived by the following equation:

$$M_{H_2} = 86 \times D[Mpc]^2 I_{CO}\ [K\ km\ s^{-1}]\ \Omega$$

where $\Omega$ is the area covered by the obseravtions in arcsec$^2$ (i.e. $\Omega = 1.13\ \Theta^2$ for a single pointing with a Gaussian beam where the HPBW = $\Theta$)

As explained in § 9.1 the CO(1-0) emission extent is smaller than the optical one (Young et al. 1995). The CO emission in spiral galaxies is in average centrally peaked within the central 5 kpc (see §. 9.1), that can be roughly modelled by an exponential distribution with a scale length $\sim$1.5. We

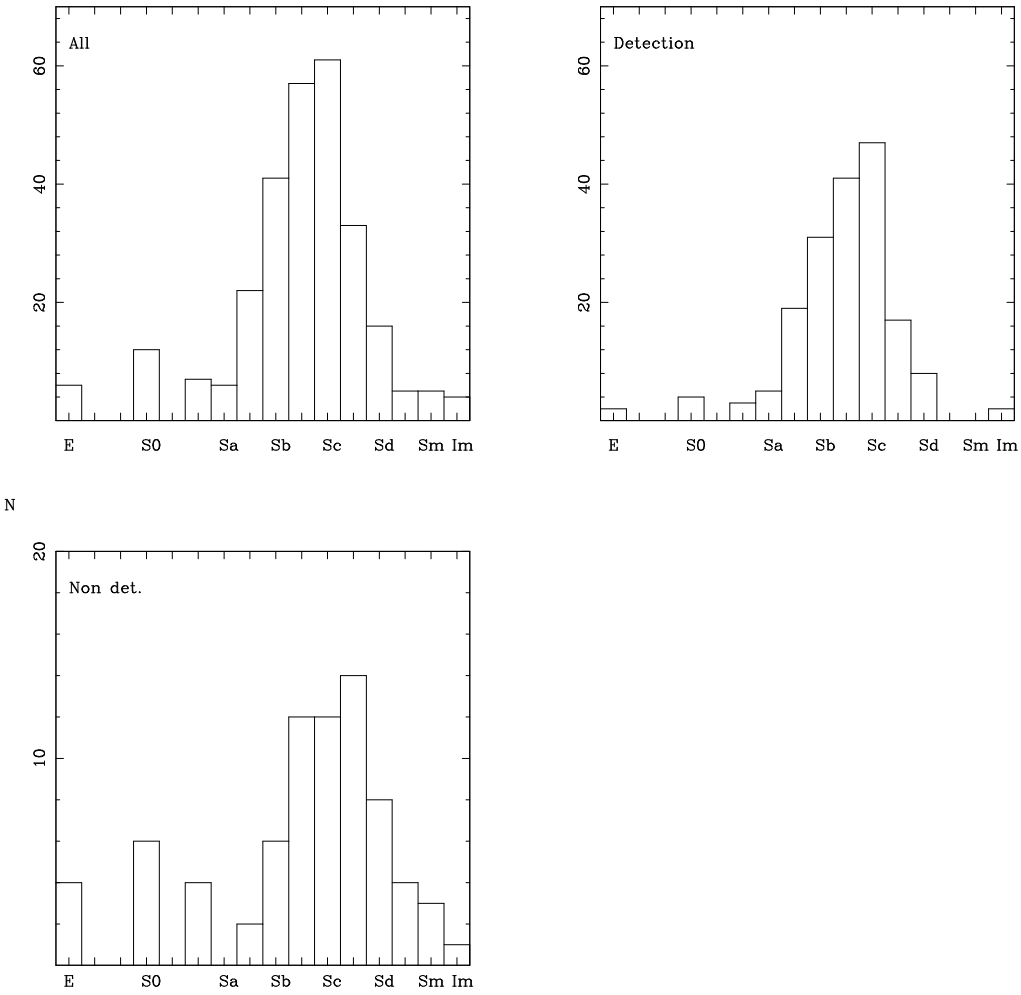


Figure 9.2: Histogram of detections and non-detections as a function of morphology for the CO(1-0) sample (N = 278).

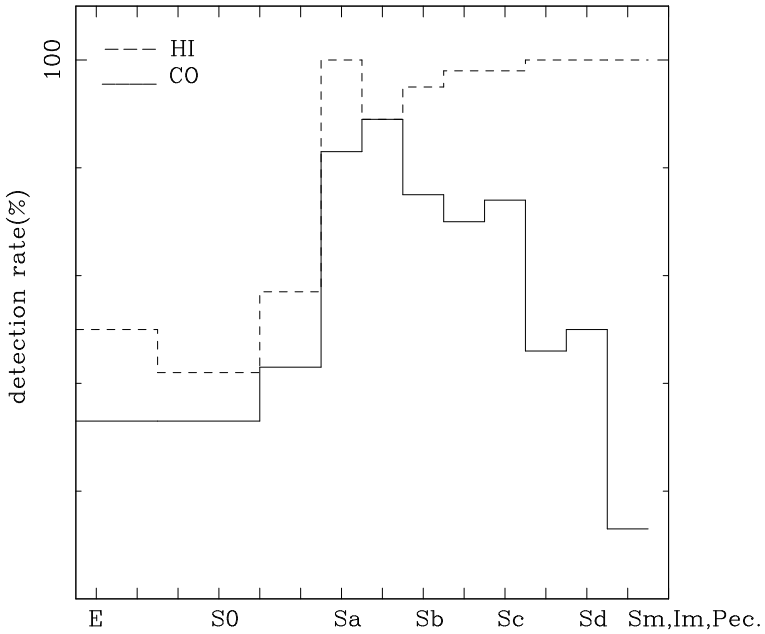


Figure 9.3: CO(1-0) and HI detection rate as a function of morphology for the CO(1-0) sample (N = 278).

Figure 9.4: $L_B$ distribution sorting by morphological type: Sa - Sab, Sb - Sc and Scd - Sdm.

Figure 9.5: $M_{H_2}$ distribution. Red filled histogram correspond to the redshift limited sample (N = 204), in comparison with the sample containing all the galaxies with CO(1-0) data (N = 278).

take into account a correction as follows (Elfhag et al. 1996):

$$I_{CO\ corr} = I_{CO\ obs} \times f \tag{9.1}$$

where $I_{CO\ obs}$ is the observed central brightness temperature, and $f$ the correction factor:

$$f = ([1 + (\frac{\Theta}{D_{CO}})^2][1 + (cos(i)\frac{\Theta}{D_{CO}})^2)])^{\frac{1}{2}} \tag{9.2}$$

In this equation $D_{CO}$ is the expected isophotal diameter for the CO surface distribution, $\Theta$ is the HPBW of the radio-telescope and $i$ the inclination. The expected $D_{CO}$ has been calculated following Young et al. (1995): $D_{CO} = w\ D_{25}$, where $w = 0.35$ for T $\leq$ Sab, $w = 0.55$ for T = Sb, Sc and $w = 0.45$ for T $\geq$ Scd. On the other hand, if a galaxy was not detected, then the upper limit at the central position is considered as explained in Sect. 9.4.6.

The distribution of $M_{H_2}$ is plotted in Fig. 9.5. We find a mean value of the distribution of about 8.6 $\pm$ 0.6. We see that the redshift limited sample (N = 204) have fewer galaxies with large $M_{H_2}$ contents than the sample with all the galaxies with CO(1-0) data (N = 278).

## 9.6 Ratios between $L_B$, $M_{H_2}$, $M_{HI}$, and $M_{gas}$

In this section we study the ratios between $L_B$, $M_{H_2}$, $M_{HI}$, and $M_{gas}$, and compare with the results found in the literature, in especial with the results obtained by Young et al. (1989). We consider the

Figure 9.6: $M_{H_2}/L_B$ distribution as a function of the morphological type.

corrected $M_{H_2}$ as explained in the former section, and the redshift limited sample.

### 9.6.1 $M_{H_2}$ / $L_B$

Young et al. (1989) find a ratio of $M_{H_2}/L_B$ = -0.77 ± 0.05 (decimal logarithmic scale), and de Mello et al. (2001) a value equal to $M_{H_2}/L_B$ = -0.91 ± 0.24 (only Sb and Sbc). The sample used by Kenney & Young (1989) was a biased sample towards bright FIR galaxies. The sample in de Mello et al. (2001) was selected with an isolation criterion, but they only require that they are located in low density regions without looking to the presence of companion galaxies. As a result of using an isolation criteria their galaxies have lower $M_{H_2}$. Braine & Combes (1993) find $M_{H_2}/L_B$ = -0.11 for mergers, -0.43 for disturbed galaxies and -0.66 for close/isolated galaxies. The latter class contains galaxies in which no companions are seen, or if there is a close companion they include the galaxy if they do not find signatures of any possible perturbation. Therefore many of their galaxies are likely to be interacting, and then it is normal that they find larger values of $M_{H_2}/L_B$ than the one by de Mello et al. (2001).

Our $M_{H_2}/L_B$ mean value is -1.3 ± 0.4. We find a lower value for $M_{H_2}/L_B$ that these three references, as we expected since we have minimized possible interactions in the galaxies of our sample.

In Fig. 9.6 we see the distribution of $M_{H_2}/L_B$ in three morphological bins: Sa-Sab, Sb-Sc and Scd-Sdm. The difference between their mean values is not relevant: -1.3 ± 0.4, -1.3 ± 0.4 and -1.4 ± 0.5 (decimal logarithmic scale), respectively. As a function of the morphology, Young et al. (1989) find that the ratio $M_{H_2}/L_B$ is essentially constant for types Sa - Sc and then decreases for later types, Scd - Sdm. In Tab. 9.7 we show the comparison of $M_{H_2}/L_B$ by Young et al. (1989) with respect to our values. Note that we have translated all the results to X = $2.8 \times 10^{20}$, as in Young et al. (1989), in order to allow a direct comparison between their values and ours.

Table 9.7: $M_{H_2}/L_B$ comparison with Young et al. (1989)[1].

| Type | $M_{H_2}/L_B$ (Young & Knezek 1989) | N | $M_{H_2}/L_B$ AMIGA | N |
|---|---|---|---|---|
| S0-Sa | 0.26 ± 0.10 | 11 | 0.04 ± 0.05 | 21 |
| Sab | 0.07 ± 0.02 | 14 | 0.07 ± 0.05 | 13 |
| Sb | 0.14 ± 0.03 | 27 | 0.12 ± 0.12 | 28 |
| Sbc | 0.14 ± 0.02 | 35 | 0.08 ± 0.08 | 42 |
| Sc | 0.13 ± 0.02 | 27 | 0.08 ± 0.11 | 42 |
| Scd | 0.07 ± 0.02 | 14 | 0.07 ± 0.08 | 23 |
| Sd-Sm | 0.04 ± 0.01 | 13 | 0.07 ± 0.08 | 16 |
| S0-Sm | 0.12 ± 0.01 | 142 | 0.08 ± 0.09 | 185 |

[1]The errors listed in the (Young & Knezek 1989) column are the ±1 $\sigma$ uncertainty in the mean value, while our errors indicate the standard deviation.

Table 9.8: Same as Tab. 9.7 but for $M_{HI}/L_B$.

| Type | $M_{HI}/L_B$ (Young & Knezek 1989) | N | $M_{HI}/L_B$ AMIGA | N |
|---|---|---|---|---|
| S0-Sa | 0.30 ± 0.21 | 11 | 0.2 ± 0.2 | 21 |
| Sab | 0.08 ± 0.02 | 14 | 0.2 ± 0.2 | 13 |
| Sb | 0.13 ± 0.02 | 27 | 0.3 ± 0.2 | 28 |
| Sbc | 0.22 ± 0.02 | 35 | 0.4 ± 0.3 | 42 |
| Sc | 0.27 ± 0.03 | 27 | 0.6 ± 0.5 | 42 |
| Scd | 0.34 ± 0.06 | 14 | 0.8 ± 0.6 | 23 |
| Sd-Sm | 0.53 ± 0.11 | 13 | 0.5 ± 0.3 | 16 |
| S0-Sm | 0.24 ± 0.02 | 142 | 0.4 ± 0.4 | 185 |

It is remarkable to note that for our sample $M_{H_2}/L_B$ remains constant, even for T= Scd - Sdm, within the errors. It is also interesting that $M_{H_2}/L_B$ for T= S0 - Sa in our sample is considerably smaller. This support the idea that the environment plays a key role in order to understand the origin of gas in lenticulars. A possible explanation is that lenticulars in denser environments accrete gas from the environment and become richer in HI.

### 9.6.2 $M_{HI}$ / $L_B$

Although the scatter is large, it is apparent that $M_{HI}/L_B$ increases among spirals from Sa to Scd (see Tab. 9.8). This trend was already found by Roberts (1969), and is partially due to the contribution of the bulge to the $L_B$ in early type galaxies. It is also relevant to note that there is a weak trend of lower $M_{HI}$ in lenticulars. These two trends support again the isolation of our sample, for in denser environments galaxies tend to be deficient in HI, and S0 in isolation may have lower HI contents for the reason given before.

### 9.6.3 $M_{H_2}$ / $M_{HI}$

The $M_{H_2}/M_{HI}$ ratio for our redshift limited sample is shown in Fig. 9.7. The ISM of an early-type spiral tends to be predominantly molecular, while that of a late-type spiral tends to be atomic. The main difference between the distribution by Young & Knezek (1989) and ours is that our $M_{H_2}/M_{HI}$ are systematically lower. In Tab. 9.10 we show the $M_{H_2}/M_{HI}$ obtained by Young & Knezek (1989) in comparison with ours. Young & Knezek (1989) find a decrease of a factor 20 in the $M_{H_2}/M_{HI}$ ratio as a function of morphological type, while our decrease is much lower, of about 6. Their average of

Table 9.9: Same as Tab. 9.7 but for $M_{H_2}/M_{HI}$.

| Type | $M_{H_2}/M_{HI}$ (Young & Knezek 1989) | N | $M_{H_2}/M_{HI}$ AMIGA | N |
|---|---|---|---|---|
| S0-Sa | 4.0 ± 1.9 | 11 | 1.0 ± 2.3 | 21 |
| Sab | 2.2 ± 0.6 | 14 | 1.2 ± 1.4 | 13 |
| Sb | 1.8 ± 0.3 | 27 | 0.6 ± 0.5 | 28 |
| Sbc | 1.4 ± 0.3 | 35 | 0.4 ± 0.5 | 42 |
| Sc | 0.73 ± 0.13 | 27 | 0.3 ± 0.4 | 42 |
| Scd | 0.29 ± 0.07 | 14 | 0.2 ± 0.5 | 23 |
| Sd-Sm | 0.19 ± 0.10 | 13 | 0.2 ± 0.3 | 16 |
| S0-Sm | 1.4 ± 0.2 | 142 | 0.5 ± 1.0 | 185 |

Table 9.10: Same as Tab. 9.7 but for $M_{gas}/L_B$.

| Type | $M_{gas}/L_B$ (Young & Knezek 1989) | N | $M_{gas}/L_B$ AMIGA | N |
|---|---|---|---|---|
| S0-Sa | 0.62± 0.35 | 11 | 0.2 ± 0.2 | 21 |
| Sab | 0.16± 0.04 | 14 | 0.3 ± 0.2 | 13 |
| Sb | 0.27± 0.04 | 27 | 0.4 ± 0.2 | 28 |
| Sbc | 0.39± 0.03 | 35 | 0.5 ± 0.3 | 42 |
| Sc | 0.42± 0.04 | 27 | 0.6 ± 0.6 | 42 |
| Scd | 0.42± 0.06 | 14 | 0.8 ± 0.6 | 23 |
| Sd-Sm | 0.57± 0.11 | 13 | 0.5 ± 0.3 | 16 |
| S0-Sm | 0.39± 0.03 | 142 | 0.5 ± 0.4 | 185 |

early type had four times more $M_{H_2}$ than $M_{HI}$, while in our sample the ratio is much smaller.

Assuming that the $L_B$ distributions in both samples are similar, we see that our sample may contain galaxies with more $M_{HI}$ and a less $M_{H_2}$. Since their galaxies may be in principle interacting galaxies this difference may be interpreted in the following way: maybe there is an enhanced conversion of atomic to molecular gas due to the interactions, or maybe the MHI has been removed, or probably a combination of both.

### 9.6.4 $M_{gas}$ / $L_B$

Our results for the total gas ($M_{gas} = M_{HI} + M_{H_2}$) are the following. There is a lower content of gas in isolated lenticulars, and a total gas content equal or larger for the rest of morphological types. Again, this seems to confirm that galaxies in denser environments are exposed to interactions which causes HI deficiencies. Other than that, we do not find any other relevant deviations between both samples.

In summary, in general the total gas content is a fundamental component of galaxies which mainly depend on the morphological type, and which is affected only in second order by the environment. Nevertheless, as Young & Knezek (1989) suggested, the relative contents of neutral gas in their different phases, that is atomic or molecular, changes when a galaxy suffers a perturbation. Therefore, we see that in isolated galaxies the relative content of atomic gas is larger with respect to the molecular gas, while in denser environments is the opposite because interactions between galaxies are more likely and more atomic gas is turned to molecular.

Figure 9.7: $\log(M_{H_2}/M_{HI})$ distribution as a function of the morphological type.

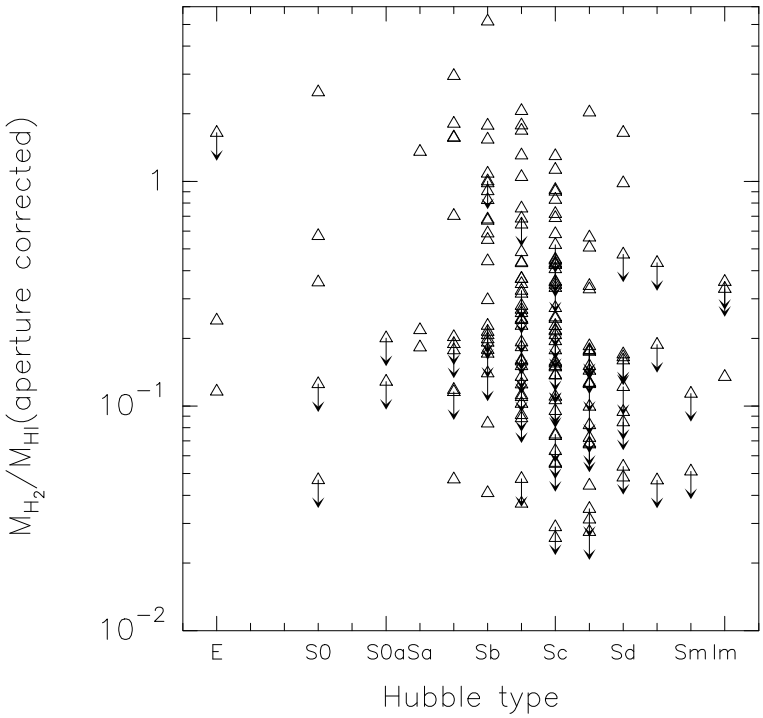


Figure 9.8: The $M_{H_2}/M_{HI}$ as a function of the morphological type. Arrows denote galaxies with only upper limits in CO(1-0).

## 9.7 $M_{H_2}$ as a function of $L_B$, linear diameter $a$ and morphological type

We consider the redshift limited sample of isolated galaxies (N = 204). In Fig. 9.9 and 9.10 we plot the linear regressions of $M_{H_2}$ as a function of $L_B$ and $a^2$. In Tab. 9.12 we present the coefficients of the fits using OLS($M_{H_2}$—$L_B$). Upper limits have been taken into account by using survival analysis (with the Schmitt method in ASURV). The bisector method has been considered to calculate the linear regression fits. For comparison, the linear regression OLS($L_B$—$M_{H_2}$) calculated by Perea et al. (1997) is also presented in Tab.9.12. Note that although they have used ASURV, their fit is calculated considering $L_B$ as dependent variable, which in principle is not well justified. Therefore we obtain a smaller slope in $L_B$ versus $M_{H_2}$. The same trend is seen when considering $a^2$.

Table 9.11: Correlation $M_{H_2}$ - $L_B$ with and without survival analysis, and bisector fit.

| Correlation | Intercept | Slope | N (N upper limits) |
|---|---|---|---|
| **CO(1-0) redshift limited sample** | | | |
| $M_{H_2}$ - $L_B$ (AMIGA fit, survival) | -2.3 ± 1.1 | 0.77 ± 0.08 | 204 (74) |
| $M_{H_2}$ - $L_B$ (AMIGA fit, only det) | -1.3 ± 1.0 | 1.00 ± 0.10 | 204 (74) |
| Bisector (AMIGA fit, survival) | -6.32 | 1.50 | 204 (74) |
| **Perea et al. 1997** | | | |
| $M_{H_2}$ - $L_B$ (survival) | -8.59 | 1.75 | 68 (6) |

Table 9.12: Correlation $M_{H_2}$ - $a^2$ , with and without survival analysis, and bisector fit.

| Correlation | Intercept | Slope | N (N upper limits) |
|---|---|---|---|
| **Redshift limited sample** | | | |
| $M_{H_2}$ - $a^2$ (AMIGA fit, survival) | -2.3 ± 1.1 | 0.77 ± 0.08 | 204 (74) |
| $M_{H_2}$ - $a^2$ (AMIGA fit, only det) | -1.3 ± 1.0 | 1.00 ± 0.10 | 204 (74) |
| Bisector (AMIGA fit, survival) | -6.32 | 1.50 | 204 (74) |

In Fig. 9.11 and Fig. 9.12 we see the $M_{H_2}$ as a function of $L_B$ and $a^2$ for the detected galaxies, showing the procedence of the CO data. No trend is found with respect to the radio-telescopes from which the data have been observed.

The linear regression coefficients for $M_{H_2}$ versus $L_B$ and $a^2$ as a function of morphology are presented in Tab. 9.13 and 9.14 respectively, and the fits are plotted in Fig. 9.13 and 9.14.

## 9.8 $M_{H_2}$ and the environment

In this section we compare the $M_{H_2}$ of our redshift limited CO(1-0) sample with respect to other samples in denser environments. We revise former works on this issue (e.g. Perea et al. 1997). Boselli et al. (1997) show that the frequency distributions of the CO deficiency parameter, defined as the difference between the expected and the observed molecular gas content of a galaxy of given luminosity (or

Table 9.13: Correlation $M_{H_2}$ - $L_B$ as a function of the morphology for the redshift limited sample (N = 204, 74 non-detections).

| Types | Correlation | Intercept | $\sigma$(Intercept) | Slope | $\sigma$(Slope) | N |
|---|---|---|---|---|---|---|
| -5, -3, -2, 0 | survival | 1 | 2 | 0.8 | 0.2 | 23 |
| | only det | 6 | 3 | 0.2 | 0.2 | 9 |
| | survival, bisector | -4 | | 1.2 | | |
| 1, 2 | survival | -4 | 3 | 1.2 | 0.3 | 18 |
| | only det | -1 | 4 | 0.9 | 1.0 | 14 |
| | survival, bisector | -9 | | 1.8 | | |
| 3 | survival | -3 | 2 | 1.2 | 0.2 | 28 |
| | only det | 0 | 2 | 0.8 | 0.8 | 23 |
| | survival, bisector | -8 | | 1.7 | | |
| 4 | survival | -2 | 2 | 1.0 | 0.2 | 42 |
| | only det | -2 | 3 | 1.1 | 1.1 | 28 |
| | survival, bisector | -6 | | 1.5 | | |
| 5 | survival | -1 | 2 | 1.0 | 0.2 | 42 |
| | only det | -1 | 2 | 1.0 | 1.0 | 32 |
| | survival, bisector | -6 | | 1.5 | | |
| 6, 7 | survival | -1 | 2 | 1.0 | 0.2 | 34 |
| | only det | -0 | 4 | 0.8 | 0.9 | 14 |
| | survival, bisector | -5 | | 1.4 | | |
| 8, 9, 10, 998 | survival | -1 | 2 | 1.0 | 0.3 | 16 |
| | only det | -1 | 10 | 1.0 | 1.0 | 7 |
| | survival, bisector | -4 | | 1.3 | | |

Table 9.14: Correlation $M_{H_2}$ - $a^2$ as a function of the morphology for the redshift limited sample (N = 204, 74 non-detections).

| Types | Correlation | Intercept | $\sigma$(Intercept) | Slope | $\sigma$(Slope) | N |
|---|---|---|---|---|---|---|
| -5, -3, -2, 0 | survival | 7.5 | 0.4 | 0.2 | 0.2 | 23 |
| | only det | 7.8 | 0.5 | 0.2 | 0.3 | 9 |
| | survival, bisector | 6.2 | | 0.8 | | |
| 1, 2 | survival | 7.0 | 0.9 | 0.6 | 0.4 | 18 |
| | only det | 7.6 | 1.2 | 0.4 | 0.4 | 14 |
| | survival, bisector | 5.0 | | 1.3 | | |
| 3 | survival | 6.5 | 0.4 | 0.8 | 0.1 | 28 |
| | only det | 7.5 | 0.4 | 0.5 | 0.6 | 23 |
| | survival, bisector | 5.4 | | 1.3 | | |
| 4 | survival | 6.3 | 0.4 | 0.8 | 0.2 | 42 |
| | only det | 6.8 | 0.9 | 0.7 | 0.7 | 28 |
| | survival, bisector | 4.9 | | 1.4 | | |
| 5 | survival | 5.5 | 0.6 | 1.1 | 0.3 | 42 |
| | only det | 5.8 | 0.9 | 1.0 | 1.1 | 32 |
| | survival, bisector | 3.9 | | 1.7 | | |
| 6, 7 | survival | 6.3 | 0.4 | 0.7 | 0.2 | 34 |
| | only det | 7.1 | 0.5 | 0.5 | 0.6 | 14 |
| | survival, bisector | 5.2 | | 1.1 | | |
| 8, 9, 10, 998 | survival | 5.7 | 0.4 | 1.0 | 0.2 | 16 |
| | only det | 6.0 | 0.7 | 0.9 | 0.9 | 7 |
| | survival, bisector | 5.2 | | 1.2 | | |

Figure 9.9: OLS ($M_{H_2}$—$L_B$) for the CO(1-0) redshift limited sample (N = 204), using survival analysis (green line) and and only detections (blue).

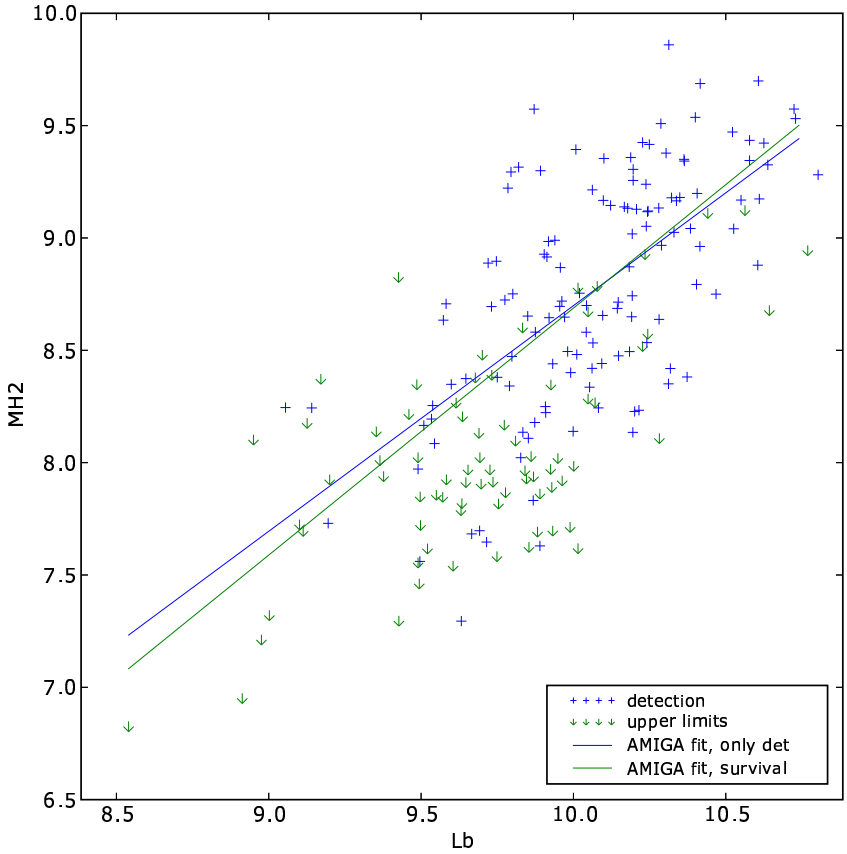


linear diameter), computed separately for cluster and isolated galaxies, are not significantly different, indicating that the environment does not considerably affect the molecular gas content of spiral discs.

## 9.9 Conclusions

As part of the multiwavelength study of the AMIGA project, we have observed and compiled CO(1-0) single dish for 205 of the most isolated galaxies in the nearby universe, being a reasonably complete sample between 1500 and 5000 km/s. We have calculated the $M_{H_2}$(or upper limits for those undetected galaxies), including an aperture correction for the beam attenuation.

We have studied the ratios $L_B$, $M_{H_2}$, $M_{HI}$, and $M_{gas}$, and compared with the results by Young & Knezek (1989) for a sample containing in general interacting galaxies. It seems that the total gas content is a fundamental component of galaxies which mainly depend on the morphological type, and which is affected only in second order by the environment. Nevertheless, as Young & Knezek (1989) suggested, the relative contents of neutral gas in their different phases, that is atomic or molecular, changes when a galaxy suffers a perturbation. Therefore, we see that in isolated galaxies the relative content of atomic gas is larger with respect to the molecular gas, while in denser environments is the opposite because interactions between galaxies are more likely and more atomic gas is turned to molecular.

The distribution of points $M_{H_2}$ versus $L_B$ for our isolated galaxies is similar to that for the galaxies used in Perea et al. (1997). Note however that the fit used by them is the OLS($L_B$—$M_{H_2}$) instead

Figure 9.10: Fit $M_{H_2}$ - $a^2$ for the CO(1-0) redshift limited sample (N = 204), using survival analysis (green line) and and only detections (blue).

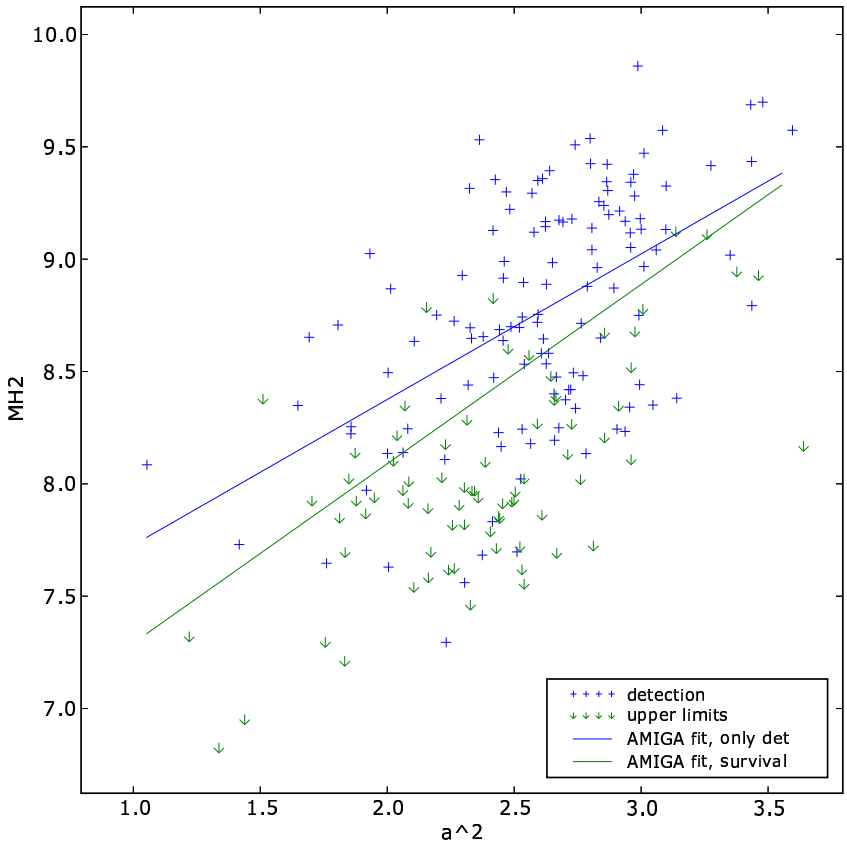


of OLS($M_{H_2}$—$L_B$), which in principle is not well justified. We have considered our OLS($M_{H_2}$—$L_B$) fit, but the fit to the data is not very well reproduced due to the scatter of the data points. Using the bisector line may be a better approach. We have found that in general it seems that there is no excess or deficiency in the $M_{H_2}$ of strongly interacting galaxies, as suggested by Verdes-Montenegro et al. (1998), although some galaxies probably show certain degree of deficiency.

## 9.10 Future work

Once we have the reference of $M_{H_2}$ from a our sample of isolated galaxies, we will compile for comparison all the information available in the literature for galaxies in different environments, including pairs, groups and clusters. In particular we have recently been granted with observing time at the IRAM 30m to observe the CO(1-0) emission line of a complete and statistically significant sample of 22 Hickson Compact Groups (HCGs) which have been already mapped in HI with the VLA.

The multiwavelength information that we have obtained/compiled will allow us to select the best targets for a follow up at sub-mm wavelengths. In our future work we plan to carry out high resolution observations of CO(1-0), CO(2-1) (PdB, NRT) and CO(3-2) (SMA) of selected regions in the disks of some isolated galaxies characterised by unusually high or low star formation, and of isolated galaxies with a high nuclear star formation. These observations will allow us to study the detailed distribution and kinematics of the molecular gas, necessary to identify feature relevant for the onset of star formation (as molecular outflows from the center or instabilities). The analysis of the different excitation

Figure 9.11: $M_{H_2}$ - $L_B$, showing the procedence of the CO(1-0) data (only detections in the redshift limited sample, N = 186).

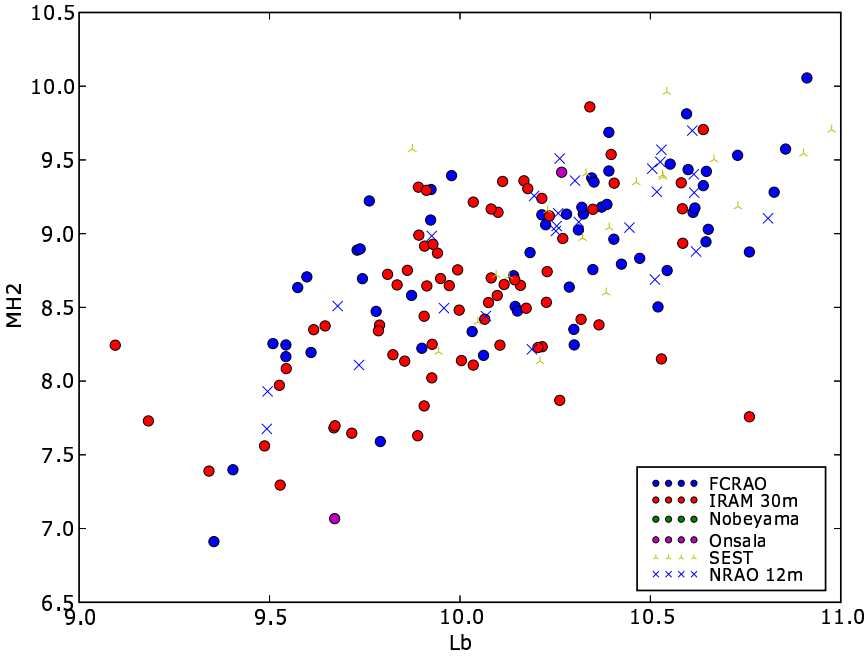


Figure 9.12: Same as Fig. 9.11, but for $M_{H_2}$ - $a^2$.

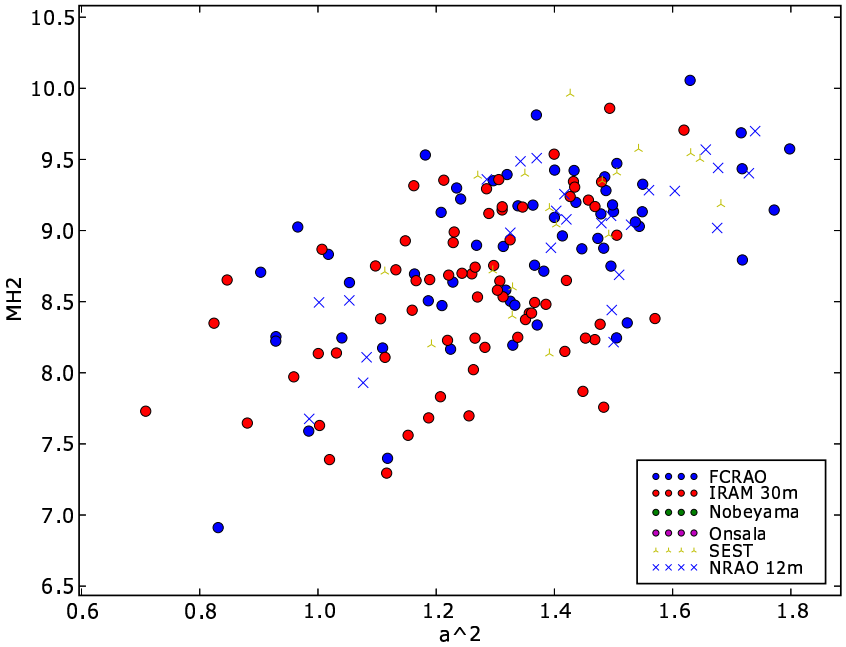

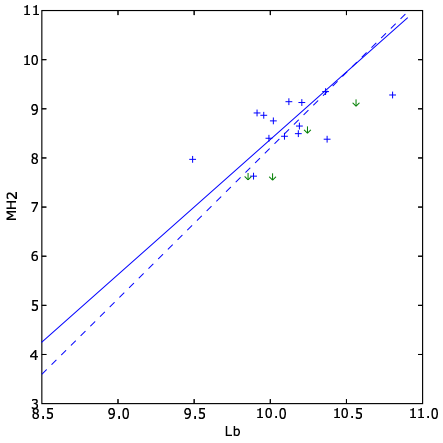


(a) T = (1,2)

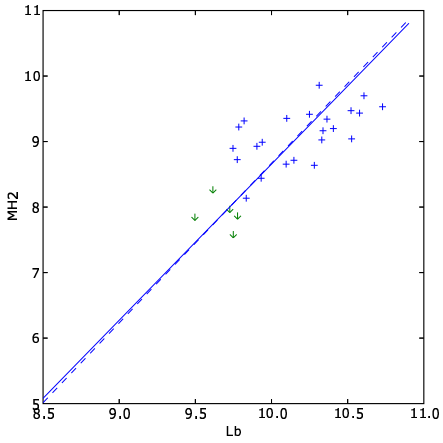


(b) T = 3

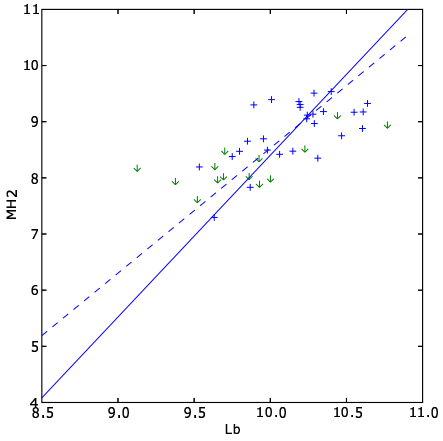


(c) T = 4

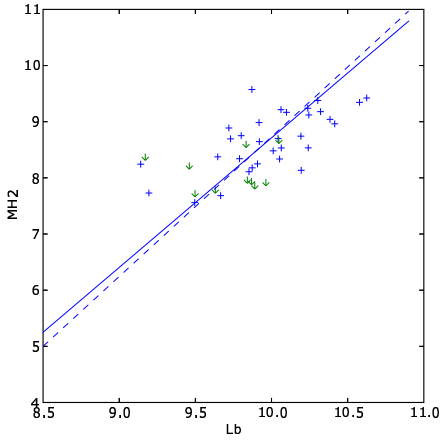


(d) T = 5

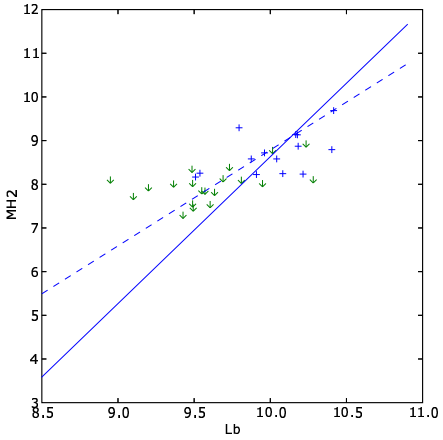


(e) T = (6,7)

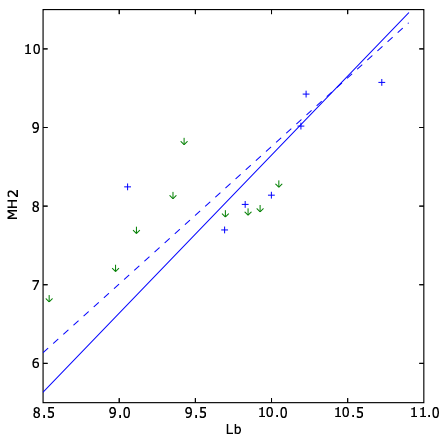


(f) T = (8,9,10,998)

Figure 9.13: $M_{H_2}$ - $L_B$ as a function of morphology. Dashed line represents the fit to the detected galaxies and the full line corresponds to the fit using survival analysis.

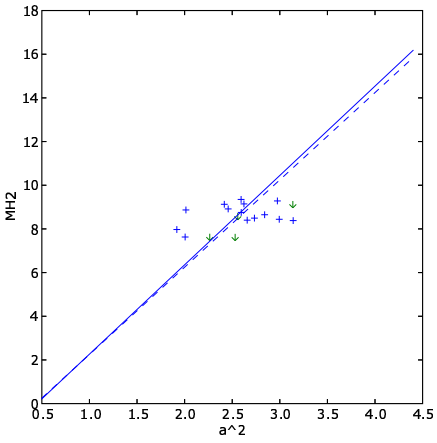


(a) T = (1,2)

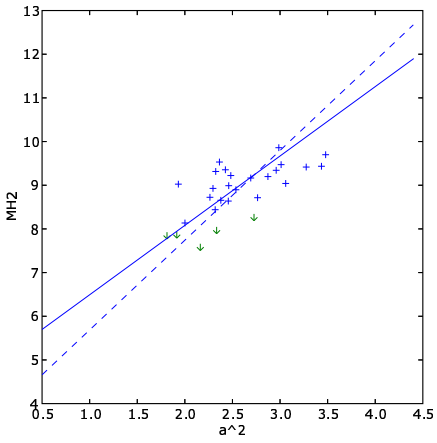


(b) T = 3

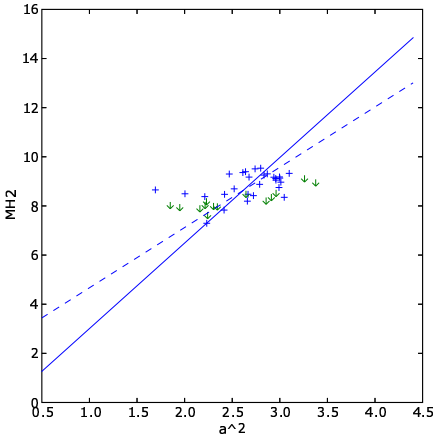


(c) T = 4

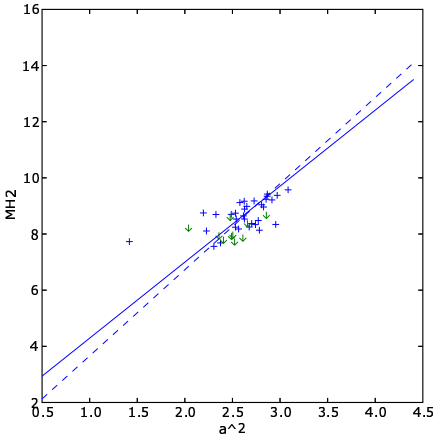


(d) T = 5

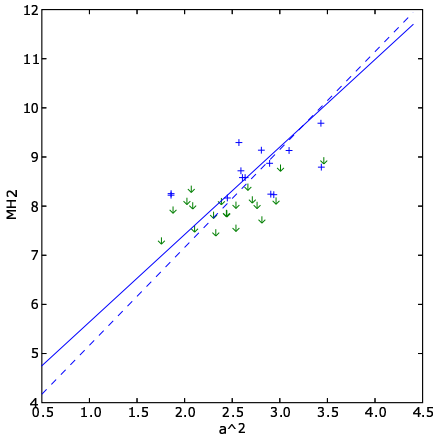


(e) T = (6,7)

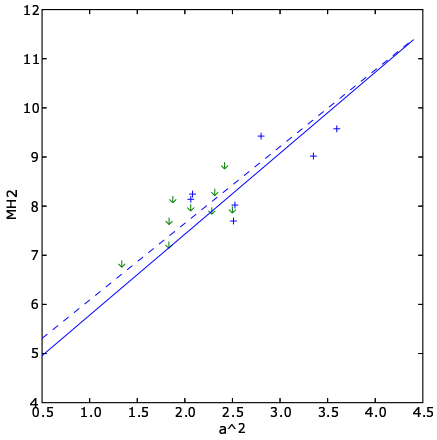


(f) T = (8,9,10,998)

Figure 9.14: $M_{H_2}$ - $a^2$ as a function of morphology. Dashed line represents the fit to the detected galaxies and the full line corresponds to the fit using survival analysis.

Figure 9.15: Comparison of the relation between $L_B$ and $M_{H_2}$ for isolated galaxies (blue dots) and different types of interacting galaxies (black dots). The interacting galaxies are separated into HCG galaxies (left) and other interacting galaxies (right, including weakly perturbed, strongly perturbed, and Virgo Cluster galaxies, Perea et al. 1997). The black line is the fit to the sample of isolated galaxies used by Perea et al 1997. The blue line is the OLS($M_{H_2}$|L$_B$) linear regression obtained using only the detected galaxies and the black one is fit calculated by Perea et al. (1997) using OLS($L_B$—$M_{H_2}$).

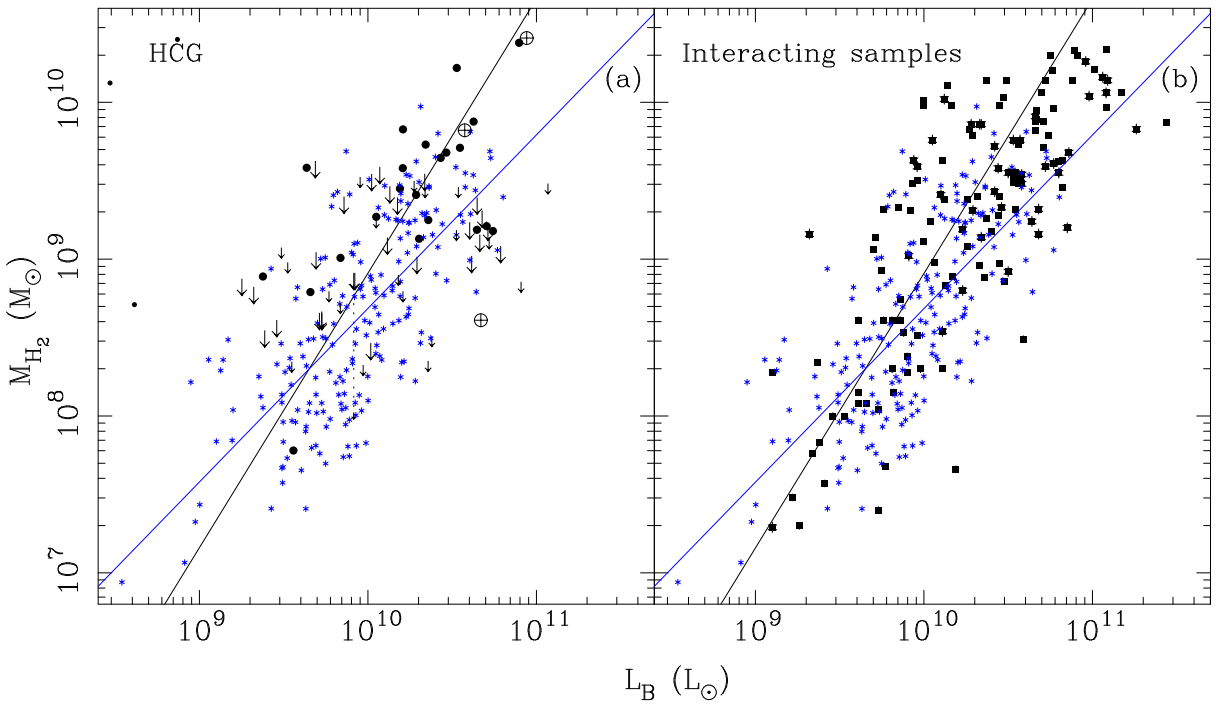

levels of CO will permit to characterize the physical conditions (as temperature and density) of the molecular gas.

# Chapter 10

# Final conclusions

In this Thesis we have studied the properties of neutral gas in both its atomic and molecular phases for galaxies in a low-density environment, as part of the AMIGA project. This is done in order to minimize the probability of contamination of the intrinsic galaxy properties by possible interactions with companions.

To do so we have observed the HI and CO(1-0) (tracing $H_2$) emission lines or compiled their main parameters from the bibliography. In total we have information for N = 910 in HI and N = 278 for the CO(1-0). In order to avoid biases in our study, we have considered all the galaxies with v > 1500, to allow us check the environment of the galaxies.

We have derived $M_{HI}$ and $M_{H_2}$ from these emission lines, by taking into account corrections by beam attenuation and pointing offsets. In order to avoid biases in their characterization, we have consider samples which are as complete as possible: in the case of the HI sample, we have considered those galaxies with HI in the optically complete sample derived by Verdes-Montenegro et al. (2005); and in the case of the CO(1-0) sample, due to the reduced number of galaxies observed, we have considered a cut in velocity at 5000 km $s^{-1}$.

We have revised previous studies (e.g. Haynes & Giovanelli 1984 and Perea et al. 1997) including correlations between $M_{HI}$ or $M_{H_2}$ and $L_B$, optical sizes and morphology. Our correlations are statistically more meaningful due to the higher number of galaxies, that allow us to sort by morphological bins. No major differences are found between our correlations and those found in the literature. With the references of normalcy here presented further studies can be performed by comparing the predicted and observed $M_{HI}$ and $M_{H_2}$ for galaxies in different environments. We illustrate this kind of comparison for the $M_{H_2}$. We confirm that interacting galaxies seems to have normal $M_{H_2}$ contents, but given the scatter of the data points, the results depends much on the kind of correlation considered (e.g. OLS(Y—X), OLS(X—Y) or bisector).

We have studied the ratios $L_B$, $M_{H_2}$, $M_{HI}$, and $M_{gas}$, and compared with the results by Young & Knezek (1989) for a sample of galaxies with interacting members. Our data confirm that the total gas content is a fundamental component of galaxies which mainly depend on the morphological type, and which is affected only in second order by the environment. Moreover, as Young & Knezek (1989) suggested, the relative contents of neutral gas in their different phases, that is atomic or molecular, changes when a galaxy suffers a perturbation. We see that in isolated galaxies the relative content of atomic gas is larger with respect to the molecular gas, while in denser environments occurs the opposite.

We have also studied the rate of isolated spiral galaxies with HI lopsidedness. To do so a good approach is to use the HI profiles, since it contains information about both the velocity field and the HI distribution. We took care not to include in our statistics artificial lopsidedness in the HI profiles due to bad pointing or beam attenuation. We have found that our rate of symmetric profiles is larger than previously thought. Almost 80% of the galaxies in our sample shows a difference lower than 15% between the flux at the receding and the approaching halves of the HI profile. This support the idea that one-on-one interaction plays a key role on the HI in isolated galaxies, and that probably there is no need for other ways to produce lopsided disks such as cosmological gas accretion (Bournaud et al.

2005) or distorted disks in lopsided halos (Levine & Sparke 1998; Noordermeer et al. 2001), although they may contribute.

In order to elucidate what the origin of HI lopsidedness in isolated galaxies is, we have mapped at the VLA 8 CIG galaxies which are among the most extreme cases of galaxies showing significant asymmetries in their HI profiles, while being in the low density end of our sample of isolated galaxies. We have also observed 4 symmetric profiles for comparison. For three galaxies we detect three companions in the primary beam but they are probably too small to produce such perturbations in the HI. The asymmetries in the HI profiles can not be explained by confusion with HI-rich companions either. The field galaxies included in Pisano et al. (2002) present in general more irregular HI distributions than in our sample, which supports again our better isolation selection. In our subsample, if a galaxy presents irregularities in the HI distribution then its velocity field also suffers of some kind of irregularity, but the opposite is not always true. Then the event that produced the asymmetry still remains visible in the velocity field for a longer time than for the HI distribution, and this is what maintains the lopsidedness in the HI profiles. This is probably the reason why we still see a considerable amount of asymmetric profiles in our sample of isolated galaxies.

As for the early type galaxies in our sample, we find that our galaxies are different to those in denser environments. None of the galaxies in our sample are expected to be a fossil group, attending to the low luminosities of our galaxies. We detect 31 ETIGs in HI (27%), being the detection rate between E and S0 very similar, result which is in disagreement with other ETIG samples in the literature. This is probably due to the fact that ellipticals in dense environments are luminous systems which do not possess a relevant amount of cold gas. We also find that half of the galaxies present double horn profiles, which is typical of gaseous disks, which may be in agreement with the standard merger scenario (Toomre & Toomre 1972). We have also studied the colors, which may indicate a minor merger event in case the early type galaxy is bluer than expected. We find different types of HI-rich ETIGs that may indicate different stages of an evolutive sequence: 1) galaxies with one horn HI profile (no gaseous disk in principle), blue colors, peculiarities in the optical, and high SF (CIG 164 and 870); 2) galaxies not as blue as in the first group, with gaseous disks (two horn HI profiles), with some peculiarities in the optical, and much lower SF than the former group (CIG 393 and 481); and finally 3) galaxies with typical red colors, not disturbed in the optical, with symmetric gaseous disks and no relevant SF.

# Part IV

# Appendices

# Appendix A

# Corrections to $m_B$

In this appendix we present the procedure to correct the apparent magnitudes contained in the Catalog of Galaxies and Cluster of Galaxies (CGCG, Zwicky et al. 1961) for the galaxies in CIG. All the CIG galaxies are contained in this catalog so they have direct photographic calculations for the blue magnitude. Although photographic plates lacks of the linearity that offer the CCD images, the number of galaxies with photographic information is much larger than that obtained with CCDs. Moreover, the large number of photographic data available in this catalog makes it suitable in order to perform statistical studies in an homogeneous way. Using this catalog we can have uniform optical information not only for a large sample of isolated galaxies but also for other galaxies in denser environments. These apparent magnitudes need to be corrected for systematic errors in the catalog, for internal absorption due to the dust of the galaxy, for Galactic extinction and finally for the shift on the SED due to the velocity of the galaxy (K correction). This work has been partially published in Verdes-Montenegro et al. (2005, § 4.2).

## A.1 Correction by CGCG volume

Systematic errors in Volume I of the CGCG (basically galaxies with $\delta < 15^o$, covering the Palomar survey fields of the declination zones 0, +6, +12° , and $7^h < \alpha < 18^h$) have been reported by Kron & Shane (1976). For Volume I they found that there were important systemic errors in comparison with other sources in the literature (Stebbins et al 1952; Pettit 1954; Bigay et al 1954, 1964; de Vaucouleurs 1972, Kron & Shane unpublished; and Holmberg 1958). The difference is typically ± 0.5. Volumes II to VI presented only a mean dispersion of typically 0.05 and therefore no correction is needed.

The correction is performed by substracting the mean offset values of $m_{B\ Zw}$, sorting in intervals up to $m_{B\ Zw} \simeq 15.7$ mag. The offsets are detailed in Kron & Shane (1976). Therefore, it yields that this correction depends on the Volume where the $m_{B\ Zw}$ was published ($\alpha$ and $\delta$) as well as the magnitude of the galaxy. We have applied these corrections ($A_v$) to the CIG galaxies which are contained in Volume I. We show some examples in Tab. A.1, where we include: $\alpha$ and $\delta$ (2000) in hh:mm:ss, the $m_{B\ Zw}$ as compiled from the CGCG catalog and the final correction that should be taken into account, $A_V$.

## A.2 Correction for Galactic extinction

In this section we deal with the Galactic extinction correction, which in principle depends on the Galactic coordinates ($l$,$b$). The galactic extinction in a given filter can be calculated as a constant times the reddening, e.g. $A_g = 4.3 \times E(B\text{-}V)$. Two approaches to the correction for Galactic extinction can be used, 1) using HI column densities and galaxy counts; and 2) using IRAS/DIRBE data.

First we explain that using HI information and galaxy counts. Burstein & Heiles (1982, BH) produced reddening maps for almost the entire sky with -10 < $b$ < 10 degrees having into account

Table A.1: Examples for the corrections by CGCG Volume.

| CIG | $\alpha$ (2000) | $\delta$ (2000) | $m_{B\ Zw}$ (mag) | $A_V$ (mag) |
|---|---|---|---|---|
| 279 | 08:23:52.06 | 14:45:11.7 | 13.4 | -0.520 |
| 309 | 08:41:31.92 | 04:58:49.8 | 11.4 | -0.460 |
| 626 | 09:10:20.22 | 07:02:15.3 | 12.8 | -0.460 |
| 247 | 14:22:23.67 | -00:23:14.1 | 14.4 | -0.170 |

Table A.2: Examples for the corrections by Galactic extinction.

| CIG | $m_{B\ Zw}$ (mag) | $A_{BH}$ (mag) | $A_{Sch}$ (mag) |
|---|---|---|---|
| 1 | 14.300 | -0.150 | -0.176 |
| 2 | 15.700 | -0.150 | -0.247 |
| 3 | 15.700 | -0.190 | -0.244 |
| 4 | 12.700 | -0.130 | -0.250 |

$N_{gal}$ (galaxy counts) and $N_H$ (HI column densities). In some regions (e.g. within a few degrees of the south galactic pole) reddenings are calculated by extrapolating or interpolating values from nearby regions with HI data. For the remaining galaxies (all within 9° of the galactic plane) a mean relation to convert RC2 absorption estimates into the BH system is considered. The mean precision for BH for reddening is 20%. It is also assumed that $A_g = 0$ where E(B-V) $\leq 0$. The way of calculating the reddening is the following (BH): $E(B\text{-}V) = y_1 + y_2 \times N_H + y_3 \times N_H^2 + y_4 \times N_H \log(N_{gal})$ (for the northern sky). Accurate to 0.02 mag (Burstein & Heiles 1978) where $y_i$ are parameters of the fit. The data are given in pixels of size 0.3 × 0.6 degrees in ($l$,$b$). We compiled the data from NED, where a small adjustment to the zero point is performed (Burstein, 1988, private communication; NED): $A_g = 4 \times E(B\text{-}V) + 0.005$.

The other approach is to use Galactic extinction corrections derived from the IRAS/DIRBE measurements of diffuse IR emission by Schlegel et al. (1998). According to the NED notes, they consider the estimate of E(B-V) calculated from COBE and IRAS maps as well as the Leiden-Dwingeloo maps of HI emission and using the Landolt UBVRI filters for the optical total absorptions.

The zero points of these two reddening laws differ by 0.02 magnitudes in E(B-V), with Schlegel et al. adopting a higher zero point than BH (Burstein's note in NED).

We have decided to consider the Schlegel et al. (1998) instead of BH values, since reddening is based directly on dust emission and have a much higher spatial resolution. In addition there is no restriction in latitude as in BH (b < 10° , galactic disk) and other regions (-135 < l < 21 degrees, b < -62 degrees). For our sample we see a mean difference of $A_{g\ Sch}$ - $A_{g\ BH} = 0.10$ and a standard deviation equal to 0.15, for a mean value of $A_{g\ Sch} = 0.26$ and $A_{g\ BH} = 0.16$. We show some examples containing the BH and Schlegel et al. (1998) values in Tab. A.2.

## A.3 Correction for internal absorption

Now we correct by dust extinction in the galaxy itself. The internal dust correction ($A_i$) has been calculated as a function of inclination and morphological type. Inclinations were estimated from the ratio of major to minor axes as explained in §.2.3.5. We used our revised morphologies (see § 2.3.3).

$A_i$ is a function of inclination, which can be expressed as a linear function of log $R_{25}$ (de Vaucouleurs et al. 1991):

$$A_i = \alpha(T) log R_{25} \tag{A.1}$$

Table A.3: Examples for the corrections by internal extinction.

| CIG | $m_{B\ Zw}$ (mag) | T (RC3) | incl(° ) | $A_i$ (mag) |
|---|---|---|---|---|
| 5 | 15.500 | 4 | 68 | -0.510 |
| 8 | 15.400 | 6 | 71 | -0.669 |
| 9 | 15.400 | 5 | 72 | -0.630 |
| 4 | 12.700 | 5 | 80 | -0.914 |
| 1 | 14.300 | 5 | 65 | -0.479 |
| 2 | 15.700 | 5 | 46 | -0.213 |

Table A.4: Examples to the K correction.

| CIG | $m_{B\ Zw}$ (mag) | T (RC3) | z | $A_i$ (mag) |
|---|---|---|---|---|
| 1 | 14.300 | 5 | 0.0243 | -0.038 |
| 4 | 12.700 | 5 | 0.0077 | -0.012 |
| 5 | 15.500 | 4 | 0.0262 | -0.055 |
| 7 | 15.600 | 4 | 0.0425 | -0.088 |

where $\alpha$ is a function of the morphological type T:

$$\alpha(T) = \begin{array}{ll} 1.5 - 0.03(T-5)^2 & T \geq 0 \\ 0 & T < 0 \end{array}$$

In Tab. A.3 we show the internal extinction corrections, as a function of the morphological type (following the RC3 system) and inclination.

## A.4 K correction

In this section we consider corrections due to the change in the spectral energy distribution of our galaxies due to redshift. Since our sample of isolated galaxies is nearby, the corrections are small. The application of the K-correction for galaxies at our distances: 1500-15000 km $s^{-1}$ is about 0 - 0.1 mag, depending on the morphological type.

K correction ($A_K$) has been calculated as in Pence (1976) (see also Giovanelli et al. 1981). The following fits to Pence's tabulation of K-correction for the B magnitudes were applied:

$$A_K = \begin{array}{ll} 4.69 \times z & \text{E, S0, S0a} \\ 3.50 \times z & \text{Sa, Sab} \\ 2.08 \times z & \text{forSb, Sbc} \\ 1.55 \times z & \text{forSc, Scd, Sd} \\ 0.62 \times z & \text{forSdm, Irr} \\ 3.50 \times z & \text{forPec} \end{array}$$

where z is the redshift of the galaxy. We show some examples in Tab. A.4.

Table A.5: Apparent blue magnitudes (Zwicky and corrected one) and the considered corrections[1].

| CIG | $m_{B\ Zw}$ | $m_{B\ corr}$ | A | $A_V$ | $A_{g\ Sch}$ | $A_i$ | $A_K$ |
|---|---|---|---|---|---|---|---|
| 1 | 14.3 | 13.608 | -0.692 | 0.000 | -0.176 | -0.479 | -0.038 |
| 2 | 15.7 | 15.204 | -0.496 | 0.000 | -0.247 | -0.213 | -0.036 |
| 3 | 15.7 | 15.141 | -0.559 | 0.000 | -0.244 | -0.315 | 0.000 |
| 4 | 12.7 | 11.525 | -1.175 | 0.000 | -0.250 | -0.914 | -0.012 |
| 5 | 15.5 | 14.712 | -0.788 | 0.000 | -0.223 | -0.510 | -0.055 |
| 6 | 14.5 | 14.092 | -0.408 | 0.000 | -0.408 | 0.000 | 0.000 |
| 7 | 15.6 | 15.166 | -0.434 | 0.000 | -0.099 | -0.247 | -0.088 |
| 8 | 15.4 | 14.212 | -1.188 | 0.000 | -0.486 | -0.669 | -0.033 |
| 9 | 15.4 | 14.624 | -0.776 | 0.000 | -0.102 | -0.630 | -0.044 |
| ... | | | ... | | | | ... |

[1] The full table can be downloaded from http://www.iaa.es/AMIGA.html.

Table A.6: Mean and standard deviation of each correction

| Correction | Mean | Standard dev. |
|---|---|---|
| $A_V$ | -0.001 | 0.0831 |
| $A_{g\ Sch}$ | -0.264 | 0.2370 |
| $A_i$ | -0.316 | 0.3103 |
| $A_K$ | -0.048 | 0.0436 |
| A | -0.630 | 0.4016 |

## A.5 Final corrected $m_B$

Once all the corrections were obtained for the galaxies in the CIG sample, $m_B$ was calculated as follows:

$$m_{B-corr} = m_B + A = m_B + A_V + A_{g\ Sch} + A_i + A_K \tag{A.2}$$

In Tab. A.5 we detail the different corrections which have been taken into account to calculate the corrected blue magnitudes. In Tab. A.6 we show the mean and standard deviation of the sample. The most important contribution to the correction is due to the internal extinction $A_i$ , followed by the Galactic extinction $A_{g\ Sch}$. As expected $A_K$'s mean value is low, $\sim 0.05$ mag and ranging from 0 to 0.3 mag depending on the morphological type. $A_V$ is important only in those cases where the galaxies are in Volume I but, the contribution in terms of the total sample are not relevant.

# Appendix B

# Optical diameters

We have performed a compilation of the angular diameters available in the literature, especially taking into account catalogs such as LEDA, NED, the Third Reference Catalog of Bright Galaxies (de Vaucouleurs et al. 1991, RC3), the Uppsala general catalogue of galaxies (Nilson 1973, UGC), and those apparent diameters given by Karatchenseva in the CIG itself (Karachentseva 1973, K73). These are the catalogues where the overlapping with the CIG galaxies is larger.

Different kind of diameters are given in the archives, being the most relevant the visual (or apparent) diameters, and diameters calculated with respect to a surface brightness level (e.g. the so-called de Vaucouleurs diameter to a level of 25 B-mag arcsec$^{-2}$, usually expressed as $D_{25}$, RC2 de Vaucouleurs et al. 1976) or Holmberg diameters ($D_H$, Holmberg 1958). The diameter system that we will use is $D_{25}$, since it is the most used one.

Basically all the diameters in the literature have been derived from visual measurements on the POSS plates (blue or red). There are other works, like Paturel et al. (2000), where they consider the $D_{25}$ using the digitised DSS images. However, measuring the diameters on the DSS is not the best idea due to the scale and the uncertainty of calibrating Schmidt plates photometrically. For some catalogues (like UGC, RC3, etc.) there are formulae available allowing the transfer from one system into the other.

## B.1 Diameters for the CIG galaxies in catalogues

We detail the different considered catalogues as follows:

**K73**: the whole set of isolated galaxies had apparent diameters in the CIG catalogue (Karachentseva 1973). The cutoff for completeness in terms of diameter is seen to be around $1'.2$.

**UGC**: this catalogue is based on the Palomar Sky Survey, and was designed to be complete to the limiting diameter of $1'$ on the blue prints. It also contains all galaxies to limiting magnitude 14.5 mag (even those with a diameter less than 1.0) in the CGCG (Zwicky & et al. 1961). Apparent major and minor axis were found for a total of 524 CIG galaxies. For example this is the catalogue that HG84 used to obtain their visual diameters of their isolated galaxies.

**RC3**: it includes information mainly for galaxies having apparent diameters larger than $1'$ at the $D_{25}$ isophotal level and total B-band magnitudes $B_T$ brighter than about 15.5, with v $<$ 15000 km s$^{-1}$. Apparent major diameter, axis ratio and its errors were compiled for a total of 596 CIG galaxies. Three primary sources were used as standards: a) 407 galaxies derived from photoelectrically calibrated photographic and/or CCD surface photometry (see references in RC3), b) 652 galaxies whose diameters were derived by R. Buta from the photoelectric "growth curves", B(A), by interpolation near the 25 B-mag arcsec$^{-2}$ determined by numerical differentiation, and c) diameters of 11876 southern galaxies ($\delta <$ -17) derived from photoelectrically calibrated photographic surface photometry by Lauberts & Valentijn (1989, ESO-LV). Northern sources of UGC where reduced to these set of

measurements, building in this way a larger standard reference (only those galaxies with log $D_{UGC}$ $\geq$ 1 were taken into account). Consistency was checked with the ESGC catalogue (Corwin & Skiff 1995) which has some overlapping of both the north and the south, finding that there is no significant difference between the diameters of both hemispheres. In Tab. 6 of RC3 we can see the slope and intercept a and b of the fit: log $D_{25}$ =a log $D_i$ + b, in order to convert the diameter for the most relevant catalogues into the RC3 system (ESGC, ESO-B, ESO-LV, HOLM, K73, KUG, MCG, RC1, SGC, UGC, UGCA, VCC). The slope a was considered to be the unity in almost all cases.

In particular we have extracted the transformation for the diameters in the K73 and UGC catalogues:

$$\begin{aligned} logD_{RC3} = \quad & logD_{K73} - 0.005(\pm 0.004) && (\mathrm{N} = 372,\ \sigma = 0.070) \\ logD_{RC3} = \quad & logD_{UGC} - 0.038(\pm 0.020) && T \geq 0\ (\mathrm{N} = 411,\ \sigma = 0.086) \\ & logD_{UGC} + 0.006(\pm 0.008) && T < 0\ (\mathrm{N} = 159,\ \sigma = 0.098) \end{aligned}$$

where $\sigma$ is the standard deviation and N is the number of considered galaxies.

**LEDA**: this archive has merged and made uniform former compilations of apparent diameters, by including their information and adding data from some other recent compilations as well (see Tab. B.1 where we show a list of individual articles from where diameter data of CIG galaxies are available). Several corrections were done to the dataset: First a correction of the visual diameters was performed to convert each catalogue into a uniform $D_{25}$ system (Paturel et al. 1991a, 1997). Basically they fit a linear regression to the diameter taking into account a cut off since all catalogs are not complete up to a certain diameter (1' is the cut off for UGC, for example). The regression coefficients can be found in Paturel et al. (1991b). Finally the compiled apparent diameters were corrected for inclination and galactic extinction.

Another relevant source of diameters which is included in LEDA is Paturel et al. (2000), where they used the DSS to electronically extract diameters. They calibrated the apparent blue diameters $D_{25}$ and the major to minor axis ratio $R_{25}$ by reducing them to the RC3 system using the already compiled diameters in the LEDA database (after a 3-$\sigma$ rejection).

$$\begin{aligned} logD_{25} = \quad & logD_{\mathrm{DSS}} + 0.09 && (N = 5619)\ \sigma = 0.06 \\ logR_{25} = \quad & logR_{\mathrm{DSS}} + 0.00 && (N = 5555)\ \sigma = 0.07 \end{aligned}$$

It seems that the most homogeneous way to compile the data is to take LEDA data, since they have reduced all the catalogs to be in the $D_{25}$ system. We will consider this catalogue as our source of diameters.

## B.2 Comparison between diameters from different catalogues

We present in Tab. B.2 and B.3 the compilation of $D_{25}$ and $R_{25}$ contained in the former catalogues. We inspect the different correlations in order to check systematic problems that may be present in the LEDA database.

When representing apparent diameters from two different catalogues for the same set of galaxies, we need to take care of two effects: a) there is a higher dispersion for smaller diameters and b) cutoffs or limits in apparent diameter of the catalogues (reason why sometimes the slope is different than unity, see Paturel et al. 1991a). Fits of $D_{25}$ and $R_{25}$ for LEDA with respect to the values in NED, UGC, K73 and RC3 are shown in Tab. B.4 and B.5. These correlations are shown in Fig. B.1 (K73 and UGC), Fig. B.2 (RC3 and LEDA 2006) and Fig. B.3 (NED). RC3 shows the best correlation of all

Table B.1: Sources from the bibliography where 25 B-mag $''^{-2}$ isophote diameters of the CIG galaxies are found[1].

| Code | Reference |
|---|---|
| 1 | de Vaucouleurs et al. (1991), RC3 |
| 2 | Karachentseva (1973), K73 |
| 3 | Nilson (1973), UGC |
| 4 | Paturel et al. (2000) |
| 5 | Vorontsov-Velyaminov & Krasnogorskaya (1974), MCG |
| 6 | Takase & Miyauchi-Isobe (1988), KUG |
| ... | ... |

[1] Compiled using the LEDA catalogue. The full list can be downloaded from http:/www.iaa.es/AMIGA.html

Table B.2: Compiled $D_{25}$ from LEDA (old and new ones), NED, K73, UGC and RC3[1].

| CIG | LEDA (old) | NED | K73 | UGC | RC3 | LEDA (2006) |
|---|---|---|---|---|---|---|
| 1 | 1.214 | 1.255 | 1.380 | 1.114 | 1.2500 | 1.135 |
| 2 | 0.868 | 0.903 | 0.845 | 1.041 | 0.900 | 0.828 |
| 3 | 0.609 | 0.602 | 0.477 | - | 0.600 | 0.575 |
| 4 | 1.534 | 1.544 | 1.556 | 1.602 | 1.550 | 1.517 |
| 5 | 0.844 | 0.778 | 0.778 | - | - | 0.861 |
| 6 | 0.922 | 1.113 | 0.903 | 1.114 | 1.100 | 0.868 |
| 7 | 0.834 | 0.778 | 0.778 | - | 0.790 | 0.809 |
| 8 | 0.998 | 1.079 | 1.041 | 1.114 | 1.070 | 0.881 |
| 9 | 0.965 | 0.954 | 0.903 | 1.079 | 0.960 | 0.924 |
| ... | | | | | ... | |

of them. In Fig. B.1 we show the apparent diameters of LEDA versus those in K73, where the cutoff at 1.2 can be easily seen. This is similar to what is seen in the comparison of diameters in LEDA versus those in NED.

While the evaluation of diameters for the CIG galaxies, we found that there were suspicious outliers in the fits LEDA - NED. We reported this fact to P. Prugniel. He communicated us that this was a bug in the last release of HyperLeda, which was probably due to a problem in a new procedure to compute the homogenized $D_{25}$. The diameters were biased toward larger values by in average 20%. The new release of the diameters (available just 1 month ago!, LEDA 2006 in Tab. B.2 and B.3) is the one that we have taken into consideration along this Thesis work. The difference between former LEDA diameters and corrected ones is shown in Fig. B.2 b).

### B.2.1 Comparison with CIG diameters from SExtractor

We have compared the diameters in NED and LEDA and the diameters calculated using SExtractor by Verley (2006). Fits between D SExtractor and $D_{25}$ LEDA y $D_{25}$ NED are very similar, although it seems that LEDA is better reproduced (see Tab. B.6). The correction factor to convert the values given by SExtractor to the $D_{25}$ system is around 2.3. The fit is shown in Fig. B.4. The agreement between the different catalogues is very satisfactory, and with this correction factor the diameters extracted with SExtractor can be used for galaxies where no diameters are found in the archives (e.g. to calculate the $D_{25}$ of the companions for the isolation revision of the CIG galaxies by Verley 2006 ).

Table B.3: Compiled $R_{25}$ from LEDA (old and new ones), NED, K73, UGC and RC3[1].

| CIG | LEDA (old) | NED | K73 | UGC | RC3 | LEDA (2006) |
|---|---|---|---|---|---|---|
| 1 | 0.319 | 0.301 | 0.602 | 0.210 | 0.290 | 0.343 |
| 2 | 0.142 | 0.124 | 0.200 | 0.087 | 0.100 | 0.155 |
| 3 | 0.228 | 0.301 | 0.236 | - | 0.300 | 0.222 |
| 4 | 0.609 | 0.589 | 0.721 | 0.560 | 0.580 | 0.587 |
| 5 | 0.347 | 0.477 | 0.397 | - | - | 0.367 |
| 6 | 0.34 | 0.268 | 0.366 | 0.268 | 0.240 | 0.357 |
| 7 | 0.168 | 0.079 | 0.124 | - | 0.080 | 0.166 |
| 8 | 0.455 | 0.477 | 0.721 | 0.511 | 0.500 | 0.451 |
| 9 | 0.42 | 0.477 | 0.710 | 0.380 | 0.460 | 0.441 |
| ... | | | | | ... | |

[1] The full tables can be downloaded from http://www.iaa.es/AMIGA.html.

Table B.4: Linear fits to compare $D_{25}$ of various catalogues (NED, UGC, K73, RC3 and LEDA).

| Catalogues | N | Slope | Intercept | $\rho$ |
|---|---|---|---|---|
| LEDA - NED | 1050 | 0.774 ± 0.011 | 0.176 ± 0.012 | 0.89 |
| LEDA - UGC | 523 | 0.93 ± 0.01 | 0.140 ± 0.019 | 0.93 |
| LEDA - K73 | 1040 | 1.07 ± 0.01 | -0.090 ± 0.013 | 0.94 |
| LEDA - RC3 | 595 | 0.97 ± 0.01 | 0.048 ± 0.015 | 0.95 |
| LEDA - LEDA (2006) | 1050 | 0.952 ± 0.005 | 0.035 ± 0.005 | 0.99 |

Table B.5: Linear fits to compare $R_{25}$ of various catalogues (NED, UGC, K73, RC3 and LEDA).

| Catalogues | N | b | a | $\rho$ |
|---|---|---|---|---|
| LEDA - NED | 1050 | 0.70 ± 0.01 | 0.055 ± 0.004 | 0.89 |
| LEDA - UGC | 523 | 1.10 ± 0.01 | -0.019 ± 0.005 | 0.96 |
| LEDA - K73 | 1040 | 1.21 ± 0.01 | 0.010 ± 0.005 | 0.93 |
| LEDA - RC3 | 595 | 1.06 ± 0.01 | -0.015 ± 0.004 | 0.97 |
| LEDA - LEDA (2006) | 1050 | 0.943 ± 0.005 | 0.015 ± 0.002 | 0.98 |

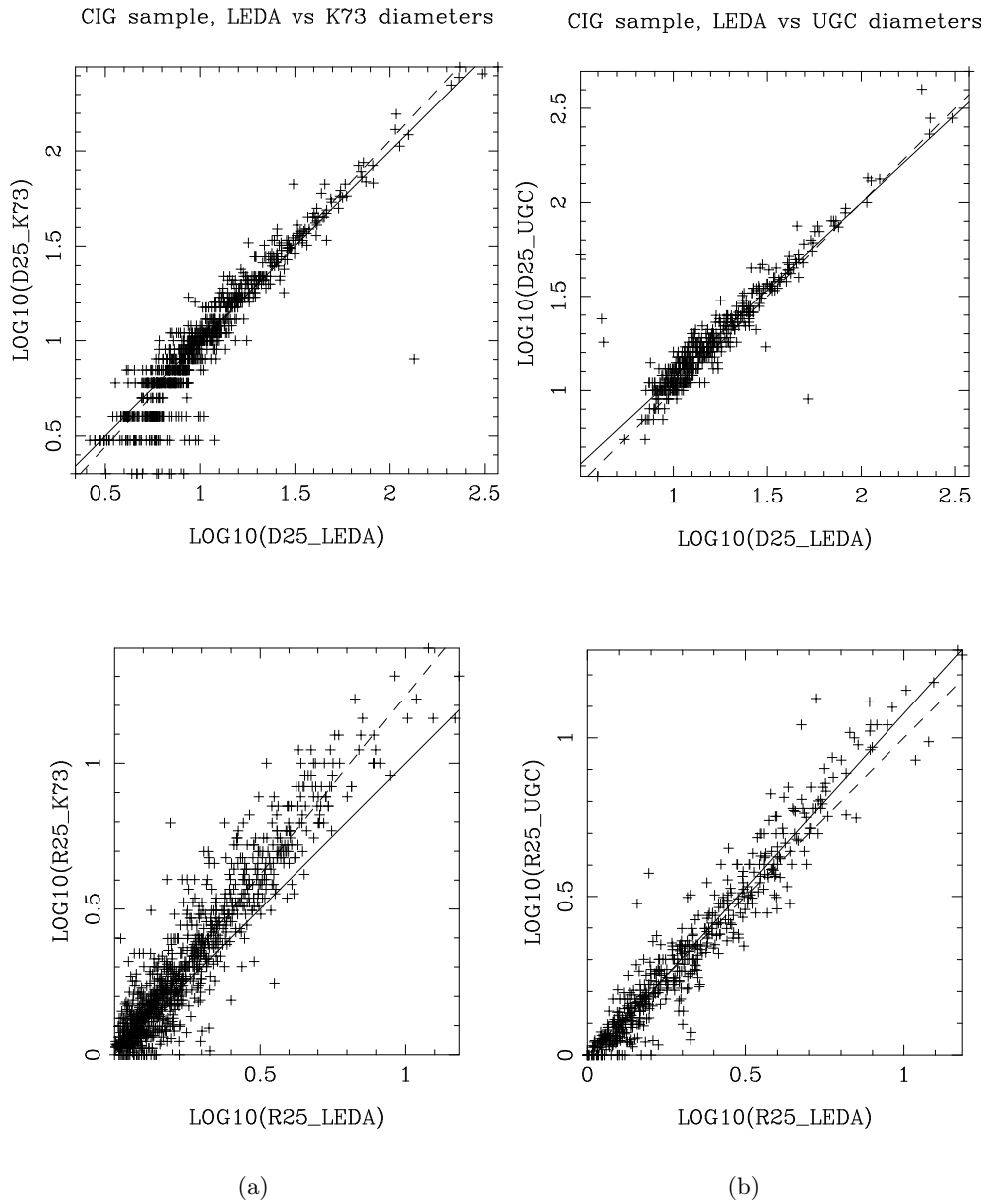


Figure B.1: a) Comparison of the diameters in LEDA with respect to those in K73. Full line represents y = x, and the fit to the points is the dashed line. b) Same as a) but for UGC.

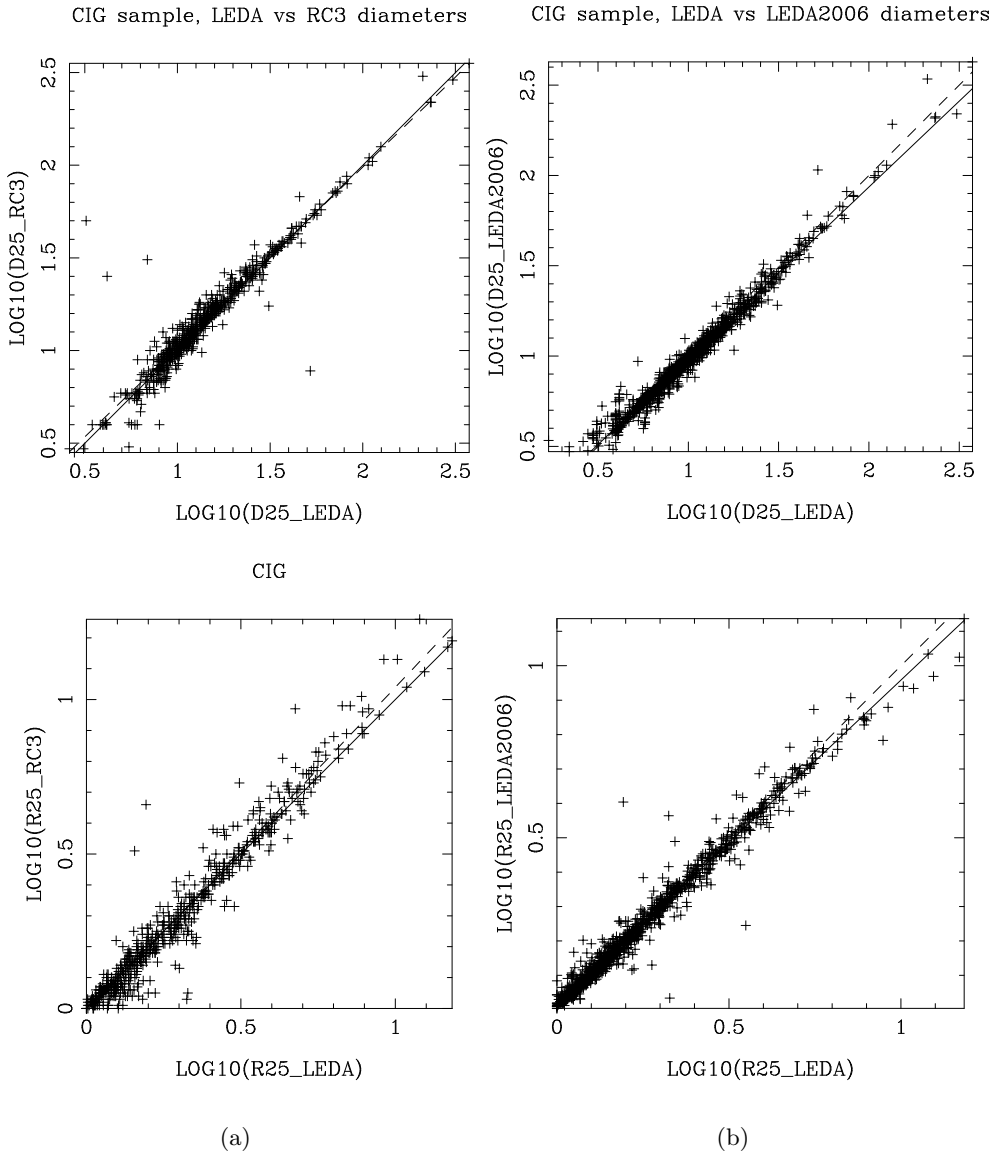


(a) (b)

Figure B.2: a) Same as Fig. B.1 but RC3 versus LEDA. b) Comparison of old LEDA diameters with the corrected ones.

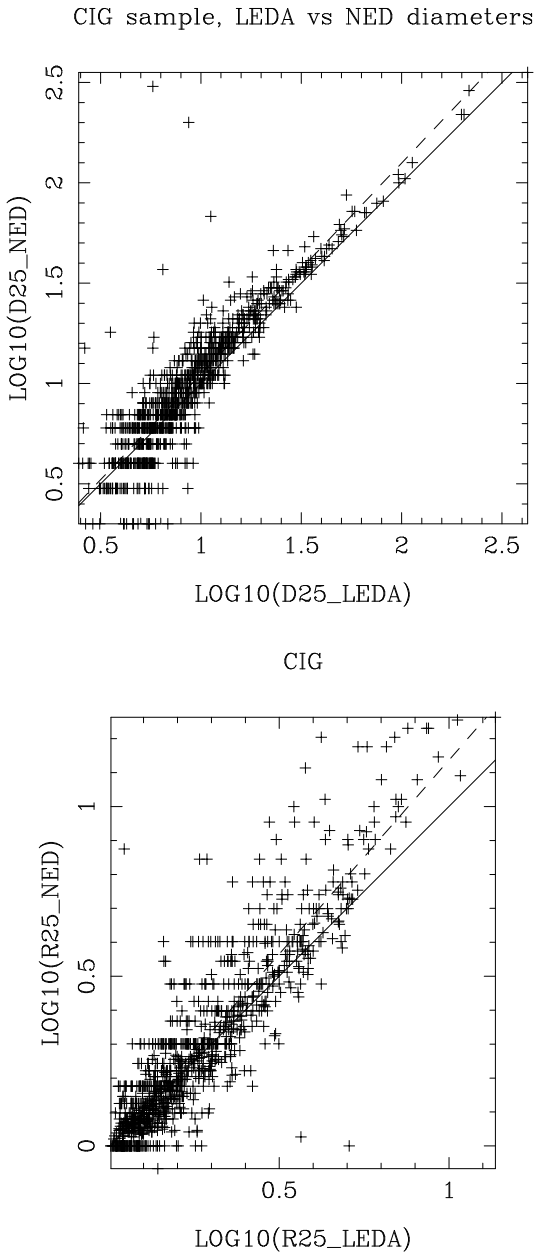


Figure B.3: Same as Fig. B.1 but NED versus LEDA.

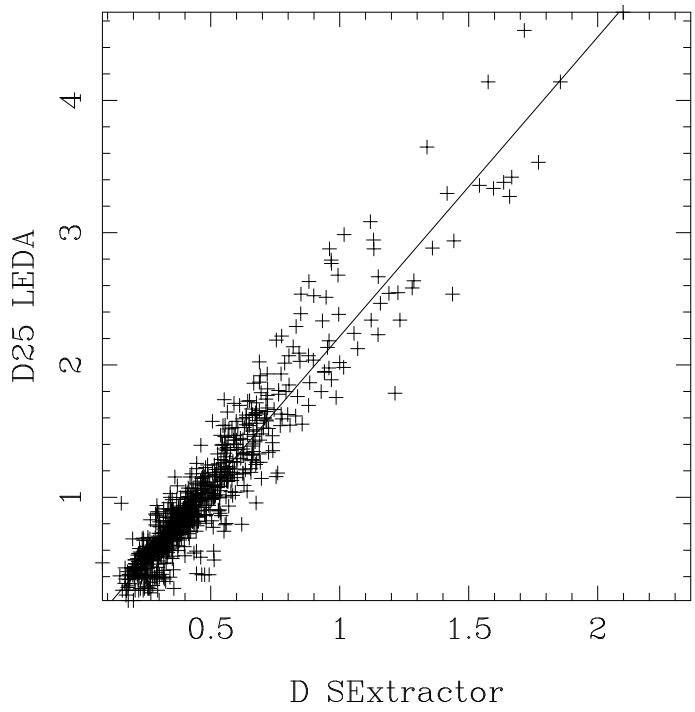


Figure B.4: Comparison of diameters in LEDA with SExtractor. The line represents the linear regression.

## B.3 Corrected apparent diameters

We correct the diameters by inclination and galactic extinction, but not for redshift, as in RC3:

$$logD_C = logD_{25} - C \times logR_{25} + A_{g\ Sch} K_d \tag{B.1}$$

where C = 0.3 for the E class (T $\leq$ -4), C = 0.15 for -3 $\leq$ T $\leq$ -1, 0.05 for T = 0, and C = 0.04 if T > 1, $A_{g\ Sch}$ is the galactic extinction (Schlegel et al. 1998) and $K_d$ is given by Fouque & Paturel (1985) as 0.094 for spiral galaxies (T > 0) and 0.081 - 0.016 × T for early type galaxies (T < 0). Note that in some references (e.g. LEDA) C is usually considered to be constant over all morphologies and equal to 0.04. This consideration is not very important: a comparison of diameters corrected by us by inclination and extinction with respect to the corrected $D_{25}$ in LEDA yields to the same result within less than 0.1 (logarithmic scale, see Fig.B.5). Considering that errors arise only from errors in $D_{25}$ and $R_{25}$, typical errors for log $D_C$ are always lower than 0.2. However, errors in the coefficient fits (LEDA) and bad morphological classification could be introducing larger uncertainties.

Finally, the linear (or physical) diameter in kpc can be calculated using the following equation:

$$a[kpc] = 1000 \times D \tan(\frac{D_C[']}{60} \frac{\pi}{180} \frac{1}{1+z})$$

Table B.6: Linear fits to compare $D_{25}$ of LEDA and NED with those extracted with SExtractor by Verley 2006.

| Catalogues | N | b | a | $\rho$ |
|---|---|---|---|---|
| SExt-LEDA | 864 | 2.26 ± 0.02 | -0.04 ± 0.01 | 0.95 |
| SExt-NED | 864 | 2.32 ± 0.03 | -0.06 ± 0.016 | 0.93 |

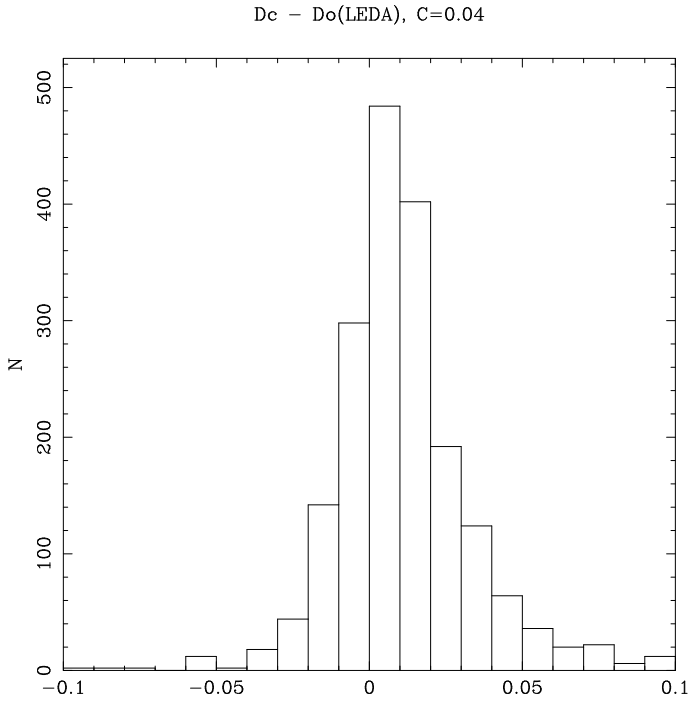


Figure B.5: Histogram showing log $D_C$ calculated by us (C dependent on the morphology) minus log $D_{CLEDA}$ (C = 0.04 constant)

where D is the distance defined as $D = V_{3K}/H_0$ ($H_0$=75 km $s^{-}1$ $Mpc^{-1}$).

# Appendix C

# Peculiar cases in the selection of HI data

In order to illustrate the criteria used to select a final HI datum in those cases where several HI data were available in the archives for a given galaxy, we present in this Appendix several galaxies which are especially representative and can serve as examples. In particular, we show the following cases: a) confusion with a HI-rich dwarf galaxy within the beam size, b) some HI data are clearly wrong, c) HI integrated density flux calculated using mapping, d) pointing problems and e) HI data selected from one source in the literature and one HI profile from a different one.

### C.0.1 a) Case with confusion with a HI-rich dwarf galaxy within the beam size: CIG 4

The major and minor axis of the galaxy CIG 4 is $3.5'$ and $0.9'$ respectively, and its heliocentric velocity is V $\simeq$ 2300 km s$^{-1}$. In Tab. C.1 we list all the available HI data in the bibliography. We detail in this table the integrated density flux (S) and if this value is corrected or not (Correction equal to 1 or 0 respectively), the radio-telescope used and the reference of the HI data. The table is ordered by beam size.

All the compiled HI data come from profiles which show good quality without apparent problems (e.g. baseline problems or interferences). As we can see directly from a simple inspection to the table, the flux increases with the beam size. If we take into account that the optical extent is double the atomic extent (as was shown in Chapter 2), we can infer that both the Arecibo ($\theta$ =3.4$'$) and Nancay radio-telescopes($\theta$=4$'\times$ 22$'$) are likely to be losing flux. Therefore the integrated density flux may be underestimated. Some of these values are corrected by beam attenuation but these corrections are based on approximations trying to reproduce the HI distribution using optical information. We do not consider these values for S since they may be not accurate.

The rest of radio-telescopes are not likely to lose flux, but those whose beam is very large may be introducing some HI-rich dwarf galaxy. In fact, this is what happens in CIG 4. Following Tab. C.1 we can classify the measurements into:
1) 10 - 13 Jy km s$^{-1}$, in observations at Arecibo and Nançay radio-telescopes,
2) 14 - 16 Jy km s$^{-1}$, in two out of the 3 observations in Green Bank 91m ($\theta \simeq 11'$), and
3) 18 - 19 Jy km s$^{-1}$, Green Bank 43m($\theta \simeq 22'$) and one observation at Green Bank 91m.

Using Aladin we found at $7'$a HI-rich dwarf galaxy, F538-02, which possess a integrated density flux S = 2 Jy km s$^{-1}$ and a velocity of 2175 km s$^{-1}$. Therefore the flux of this dwarf galaxy is likely to be included in the group 3) of measurements, and then we discard these group as well.

Finally, we will select a measurement from one of the members of group 2). In this case we select the observation presented in TC88 since it has the best signal to noise ratio.

Table C.1: HI data in the archives for CIG 4: Example where we find confusion with a HI-rich dwarf galaxy within the beam size.

| S (Jy km $s^{-1}$) | Correction | Radio-telescope | Reference[1] |
|---|---|---|---|
| 10.09 | 0 | Arecibo | Ch93 |
| 11.37 | 0 | Arecibo | No98 |
| 13.42 | 1 | Arecibo | He83 |
| 13.80 | 0 | Arecibo | Kr80 |
| 13.80 | 1 | Nançay | Bo82 |
| 14.19 | 1 | G91m | TC88 |
| 15.84 | 1 | G91m | FT81 |
| 18.70 | 0 | G91m | DS83 |
| 16.59 | 1 | J76m | St87 |
| 18.87 | 0 | G43m | HG99 |
| 14.72 | 0 | J26x38m | Ro91 |
| 16.59 | 0 | Westerbork | Oo93 |
| 16.90 | 0 | Westerbork | Rh96 |

[1] References codes as in Tab. 3.4

### C.0.2 b) Case where some HI data are clearly wrong: CIG 18

In Tab. C.2 we list the available data found in the literature. The size of the galaxy is $0.9' \times 0.5'$. In this case the extent of the source with respect to the beam size is not a problem. The HI data in HG84 is slightly larger than that in HG99. If we observe the profile in HG99 we can see that there is an interference just in the centre of the HI profile, modifying in this way the integrated flux density. We therefore select the data in HG84.

Table C.2: HI data in the archives for CIG 18: Case where some HI data is clearly wrong.

| S (Jy km $s^{-1}$) | Correction | Radio-telescope | Reference |
|---|---|---|---|
| 2.94 | 0 | Arecibo | HG84 |
| 2.3 | 0 | Arecibo | HG99 |

### C.0.3 c) Case where the HI integrated density flux is calculated using mapping: CIG 59

In Tab. C.3 we show the two HI observations that we have found in the bibliography for CIG 59. The optical diameters are $2.7' \times 2.1'$. The observation in HG99 was performed with Arecibo and then it is likely that these HI profiles are losing flux. The other HI data come from the same radio-telescope but this time was obtained by mapping the source along its major axis (He83), so the integrated flux is expected to be more accurate. We therefore select the mapping observation.

Table C.3: HI data in the archives for CIG 59: Case where the HI integrated density flux is calculated using mapping.

| S (Jy km s$^{-1}$) | Correction | Radio-telescope | Reference |
|---|---|---|---|
| 11.48 | 0 | Arecibo | He83 |
| 9.5 | 0 | Arecibo | HG99 |

### C.0.4 d) Case with pointing problems: CIG 319 and CIG 661

In the case of CIG 319 the optical extent of the source is $1.8' \times 0.6'$. The observations were performed with Arecibo and therefore we are in the limit to be affected by beam attenuation. In Tab. C.4 we show the data available in the literature, as Tab. C.1. If we only consider the signal to noise ratio, we can see that the best profile is that of HG84, but in both cases we find a pointing problem. The baseline seems to be fine but both profiles are lopsided. In HG84 the approaching horn is higher whereas in Bi86 is the opposite. This clearly means that in both cases there is a loss of flux. We select Bi86 because although it is slightly worse in terms of signal to noise than HG84, the former is losing less flux than the latter. The global profile is expected to be more symmetric that it actually is.

Table C.4: HI data in the archives for CIG 319: Case with pointing problems.

| S (Jy km s$^{-1}$) | Correction | Radio-telescope | Reference |
|---|---|---|---|
| 6.91 | 1 | Arecibo | HG84 |
| 7.73 | 1 | Arecibo | Bi86 |

Now we describe the second case, CIG 661, which has been observed with Nancay (Th98) and the GBT (observed by us). The optical extent is $1.3' \times 0.9'$ so no loss is expected from either radio-telescope. The integrated density flux is indicated in Tab. C.5. GBT integrated density flux is larger than the one obtained with Nancay. This can be visually seen in Fig. C.1. Two possibilities can explain the flux loss in Nancay: either the HI extent of this galaxy is larger than the $4'$ of the minor axis of the Nancay radio-telescope or this is a pointing problem. We have selected obviously the GBT HI data.

Table C.5: HI data in the archives for CIG 661: Case with pointing problems.

| S (Jy km s$^{-1}$) | Correction | Radio-telescope | Reference |
|---|---|---|---|
| 6.91 | 1 | Nancay | Th98 |
| 7.73 | 1 | GBT | AMIGA |

### C.0.5 e) Case where we have selected one HI data from one source in the literature and one HI profile from another: CIG 71.

The optical extent in this galaxy is $1.6' \times 0.2'$. Again, in Tab. C.6 we list the data found in the literature. Both HI integrated density flux are very similar, so we decide according to signal to noise ratio. The noise of the baseline for the former is 1.2 mJy while in the latter is 0.9 mJy. We therefore

(a) Th98, Nancay (b) AMIGA, GBT

Figure C.1: HI data in the archives for CIG 661: Case with pointing problems.

select the integrated density flux in GH97, but no HI profile was available in this article, so we gathered the HI profile in HG84 because both data are consistent.

Table C.6: HI data in the archives for CIG 71: Case where we have selected one HI data from one source in the literature and one HI profile from another.

| S (Jy km $s^{-1}$) | Correction | Radio-telescope | Article |
|---|---|---|---|
| 2.66 | 0 | Arecibo | HG84 |
| 2.75 | 0 | Arecibo | GH97 |

# Appendix D

# Corrections to the HI integrated flux density and width

In this appendix we present a summary of the corrections to the HI integrated flux density and width.

## D.1 HI integrated flux density

Due to the extent of the HI distribution of galaxies, the point source approximation is not valid and we have to apply a correction to the measured HI flux (e.g. Shostak 1978):

$$S_c \; = \; f \; S \tag{D.1}$$

where f is the beam filling correction factor, calculated as follows:

$$f = \frac{\int \sigma_{HI}(x,y) G(x,y) dxdy}{\int \sigma_{HI}(x,y) dxdy} \tag{D.2}$$

In this equation x and y are angular Cartesian coordinates, $\sigma_{HI}$ is the hydrogen surface-density distribution and B(x,y) is the beam response of the telescope. We consider $\sigma_{HI}$ and B(x,y) in a first order approximation to be Gaussian functions. The correction factor f is always larger than 1 and approaches the unity when the size of the source is negligible in comparison with the beam of the telescope.

In case the beam is circular then f can be expressed as:

$$f = [[1 + (pD_{25}/\theta_{HPBW})^2][1 + (pd_{25}/\theta_{HPBW})^2]]^{\frac{1}{2}} \tag{D.3}$$

where $D_{25}$ and $d_{25}$ are respectively the major and minor axis diameter at a level of 25 B-mag arcsec$^{-2}$ in arcmin ($'$) and $\theta_{HPBW}$ is the beam size of the radio-telescope (expressed here in $'$as well), which are shown in Tab. 3.6. The coefficient p is a constant depending on the adopted diameter system and set to p=0.85 in this case, as in Bottinelli et al. (1990). We have calculated in this way the correction factor for the following radio-telescopes: Arecibo, Effelsberg, GBT, 76m Jodrell Bank, Green Bank 43m and 91m. For Nançay the beam response is not circular and therefore the correction is more complicated. In this case, the following equation have to be use in order to calculate f:

$$T_1 = (D_{25} sin(\beta))^2 + (d_{25} cos(\beta))^2$$
$$T_2 = (D_{25} cos(\beta))^2 + (d_{25} sin(\beta))^2$$

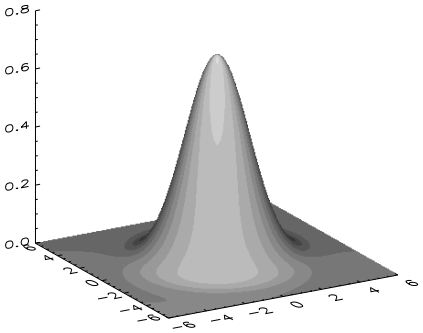

(a) Radio-telescope beam (beam size $\simeq 5\ '$)

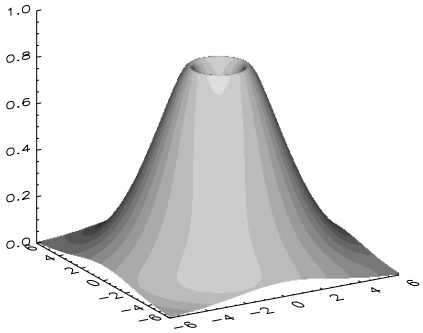

(b) HI surface of a typical face-on galaxy.

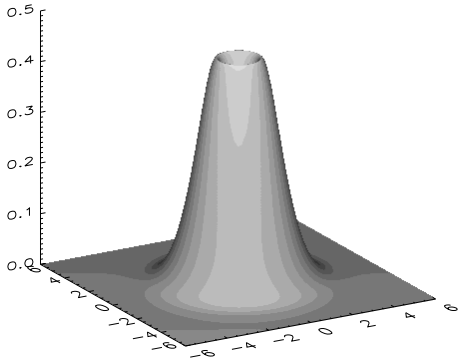

(c) Result of the observation with beam attenuation.

Figure D.1: Illustration of the HI surface model and the result from beam attenuation when the HI of the galaxy has a comparable size to the beam.

$$f = [[1.d0 + (p^2 T_1/\theta^2_{E-W})][1.d0 + (p^2 T_2/\theta^2_{N-S})]]^{\frac{1}{2}} \tag{D.4}$$

where $\beta$ is the position angle of the considered galaxy from N-E and $\theta_{E-W}$ and $\theta_{N-S}$ are the HPBW in each direction. We do not consider possible random pointing errors in the calculations of the corrections to S. Internal HI auto-absorption correction (Appendix B in Haynes & Giovanelli 1984) are usually small, unless the inclination of the galaxy is high (2%, 6%, 19% respectively at 60° , 75° and 85° , Heidmann et al. 1972a). The calculation of this type of correction suffers of much uncertainty due to the dependence on the morphological type and the modelling of the gas distribution, and therefore it has not been taken into account in this work.

## D.2 Corrections to the line width (W)

Corrections by resolution effect, internal velocity dispersion and by inclination have been taken into account. For resolution effect, the correction is (Bottinelli et al. 1990):

$$W_c^{re} = W_l + (0.014 \times l - 0.83) * \delta \tag{D.5}$$

where $W_l$ is the observed line width at a certain level with respect to the peak (l = 20,30 or 50 %) and $\delta$ is the resolution of the spectra. This correction has been applied only for $\delta$ values lower than 40 km s$^{-1}$ , in order to avoid large extrapolations (as in Bottinelli et al. 1990).

For internal velocity dispersion:

$$W_c^{re\&vd} = [W_c^{re2} + W_t^2(1 - 2exp(\frac{-W_c^{re2}}{W_o(l)^2}) - 2W_c^{re}W_t(1 - exp(\frac{-W_c^{re2}}{W_o(l)^2})]^{\frac{1}{2}} \tag{D.6}$$

where $W_o$(l) is a characteristic velocity parameter needed to convert the correction for a simple Gaussian profiles to a double horn distribution. In our case we have considered $W_o$(20%) = 120, $W_o$(30%) = 120 and $W_o$(50%) = 100 km s$^{-1}$ (Tully & Fouque 1985). $W_t$ is defined as:

$$W_t = 2.0 \times \sigma_z \; k(l) \tag{D.7}$$

where $\sigma_z = 12.0$ and k(l) is a parameter set to k(20%) = 1.96, k(30%) = 1.9, k(50%)=1.13, considering an isotropic distribution of non-circular motions and nearly a Gaussian velocity distribution.

Finally the correction to the width of the HI profile is:

$$W_c^{tot} = \frac{W_c^{re\&vd}}{sin(i)} \tag{D.8}$$

where i is the inclination of the galaxy presented in Chapter 2.

# Appendix E

# Bivariate analysis

## E.1 Introduction

Here we discuss the use of bivariate analysis in order to make linear regressions between pairs of variables. Different kind of fits are considered and are illustrated with some examples ($M_{HI}$ - $L_B$ , $M_{H_2}$- $L_B$ and $L_{FIR}$- $L_B$ ). The use of survival techniques is needed if one wants to take into account the important information contained in the so-called censored data (upper or lower limits). We consider the use of bivariate correlation tests (Kendall's tau and Spearman's rho) and linear regression analysis (Schmitt's method) in ASURV to perform bivariate statistical studies with survival analysis. In the AMIGA project is important to obtain accurate linear regressions between two variables (e.g. $M_{HI}$ vs $L_B$ or size), since one of the aims of the project is to obtain accurate measures of normalcy over the properties of galaxies in denser environments (e.g. possible deficiencies in $M_{HI}$ and/or enhancement in the $M_{H_2}$of interacting galaxies with respect to isolated ones).

## E.2 Bivariate analysis

A fit to a set of bidimensional points basically depends on:

- 1) the model that we consider to represent our data (for example, y = a + b x for linear regression),
- 2) the way the distance to the fit is measured and minimize (the most used is the least-squares minimization, or sum of the squares of the residuals),
- 3) the nature of the dataset. The nature of the problem needs to be known in advance in order to decide the kind of fit to do (for example, whether we expect intrinsic scatter between two variables, even if there is no error in the measurement of them; or the errors that arise from the measurement, etc.)
- 4) the scientific purpose of the linear regression (prediction or comparison with a physical theory, etc.).

Given a dataset for which we want to obtain a parametrization (in probabilistic terms), different results can arise just from the consideration of different ways of calculating distances to the fit. The selection of the best way of calculating depends on the nature of the variables. The use of different linear regressions is studied in detail in Isobe et al. (1990). They study five kinds of fits:

- **OLS(Y—X)**: ordinary least-squares (OLS) regression of Y on X,
- **OLS(X—Y)**: ordinary least-squares (OLS) regression of X on Y,
- **OLS(bisector)**: line that bisects OLS(Y—X) and OLS(X—Y) (has been used for example in Tully-Fisher and Faber-Jackson relations to estimate galaxy distances),

- **Orthogonal regression**: line minimizing the perpendicular distance to the points (and not distance in the Y-axis like in the ordinary least-squares method), and
- **"Reduced major-axis" regression**: geometric mean of the slopes of OLS(Y—X) and OLS(X—Y)

Variables can be in principle independent one with respect to the other, have their own errors in the measurement, have its own intrinsic scatter and contain censored data.

The scientific question give us an idea of what kind of linear regression should be used. If we need to treat both variables X and Y symmetrically, then we can choose between OLS(bisector), Orthogonal regression or the "Reduced major-axis"regression, although they yield in principle to completely different regression lines. Isobe et al. (1990) stated that OLS(Y—X) is appropriate when we just want to make a prediction of Y given the X value, but if we want to establish the underlying relationship between X and Y for comparisons with an astrophysical theory then a method treating both variables symmetrically is more appropriate.

Akritas & Bershady (1996) shows how to accomodate scatter in addition to the measurement error of each variable. Another method is derived by them, the BCES estimator (for Bivariate Correlated Errors and intrinsic Scatter), allowing measurements of errors in both variables, even if they are dependent, as well as magnitudes of the measurement errors depending on the measurements. We will not consider this by now.

We find in the literature that OLS(Y—X) is the standard way used in most of the studies to calculate linear regressions (e.g. Haynes & Giovanelli 1984, where Y= $M_{HI}$, X= $L_B$ ), although in some cases the bisector line is used as the most representative fit (e.g. Shapley et al. 2001).

### E.2.1 Correlation tests

For the bivariate analysis, we can use the package BIVAR in ASURV Rev 1.1 (Lavalley et al. 1992), which provides three methods to test the presence of a correlation between two variables containing upper limits:

- the **Cox hazard model**, a parametric method which requires certain assumptions with respect to the underlying distribution of the sampled data points. It can be only used when there is one type of censoring (upper or lower limits), and when the censoring only occurs in the dependent variable.
- the **generalized Kendall's tau**, a non-parametric method (operating on the basis of the sample values alone, without any assumptions regarding the underlying population). It can handle censoring in both the independent and dependent variable.
- the **Spearman's rho**, another non-parametric method that can handle censoring in both variables.

Many of the pairs of variables under consideration in the AMIGA project contain upper limits in both variables, and therefore we could not apply the Cox method, but we can still use the Kendall and Spearman correlation tests. Wherever applicable, the Cox method gives results consistent with those of the other two methods.

### E.2.2 Linear regressions

Linear regression analysis can be applied to bivariate correlations to estimate the functional relations between the variables. ASURV's BIVAR package offers three routines for linear regression analysis of censored data:

- the **estimation-maximization (EM) method**,
- the **Buckley-James method**, and

- the **Schmitt's binning method** (Schmitt 1985).

We select the Schmitt's method because it can handle censoring in both variables, while the first two methods only can do it in the dependent variable alone. We calculate OLS (ordinary least squares) in both (X—Y) and (Y—X). We also calculate the bisector line of these two regressions (see Isobe et al. (1990) for details about bisector fits and Appendix B in Shapley et al. (2001) for a discussion of the derivation of these bisectors).

### E.2.3 Examples using bivariate statistics for AMIGA.

In this section we illustrate with some examples ($M_{HI}$, $L_B$, optical size, $M_{H_2}$ and $L_{FIR}$) the use of different linear regressions depending on the nature of the dataset and the scientific question to address.

The characteristics of the considered variables is summarized as follows. $M_{HI}$ and $M_{H_2}$ are both dependent on the distance of the galaxy and corrected by beam attenuation (angular diameter to beam of the radio-telescope). $M_{HI}$ corrections for internal HI auto-absorption is also taken into account in some works, which depends on morphological type and inclination. On the other hand, $L_B$ and $a^2$ depends on distance, galactic extinction, morphological type and inclination. Therefore it is expected errors of $M_{HI}$, $L_B$ and $a^2$ to be correlated among them since they all depend on distance, morpholocical type and inclination errors. The BCES method should be taken into account if we want to consider the effect of the measurement errors on the linear regression. Note however that BCES and OLS are not immune to: 1) biases that arise from data truncation (i.e., a magnitude-limited sample), and 2) changes in the scatter along the regression.

The Kendall tau and the Spearman's rho are calculated for several pairs of variables ($M_{HI}$ vs $L_B$, $L_{FIR}$ vs $L_B$, etc.). All correlations are characterized by the probability $P < 10^{-6}$ that the null hypothesis of no correlation is true. Then we calculatethe linear regressions obtained from the Schmitt's method using survival analysis and compare it with respect to those calculated with exclusively non-censored data.

#### Case 1: $M_{HI}$ versus $L_B$

The main (and rough) assumption here is that in nearby galaxies only $M_{HI}$ changes as a function of the environment from the set of variables $M_{HI}$, $L_B$ and morphological type. We can not forget however that morphology is also another quantity that extremely depends on the environment, and we are considering that there is no error in the estimation of it. Certainly this, together with the uncertainty in $L_B$, introduces a large intrinsic scatter to the fits even if we sort by morphological type. Having this problem in mind we can consider $Y = M_{HI}$ and $X = L_B$ for a given morphology and the following scientific question: make a prediction of $M_{HI}$ given the $L_B$ of the galaxy (e.g. Haynes & Giovanelli 1984). Since we are predicting Y from X then it seems that OLS(Y—X) is the most appropriate way for our scientific question, attending to the statement given by Isobe et al. (1990). In this sense $L_B$ would be the independent variable from which we would predict the expected HI content of a given galaxy.

On the other hand, from a scientific point of view it can be argued that using $M_{HI}$ as dependent makes sense because $L_B$ is a more stable quantity than $M_{HI}$ in terms of the environmental density where the galaxy resides (galaxies in denser environments are seen to be HI-deficients). It seems that $M_{HI}$ is not as fundamental as $L_B$ because it depends strongly on the environment and we want to predict $M_{HI}$ for galaxies in denser environments. However, to calculate the deficiencies, we calculate the predicted $M_{HI}$ always in the "isolated galaxies" space, and we do not have to worry about the environment. That is, we suppose that the interacting galaxy has a given $L_B$ independent on the environment, and we calculate the $M_{HI}$ as it were an isolated galaxy. From this point of view, in the "isolated galaxies" space (where the $M_{HI}$ is not affected by interactions) both $L_B$ and $M_{HI}$ could be treated symmetrically in the sense that we could obtain $L_B$ from the $M_{HI}$ to. None of these two variables would be more fundamental than the other in this regime. However, note that this is only

Table E.1: Coefficients for the different linear regressions of $M_{HI}$ vs $L_B$ using non-censored data both in SLOPES and ASURV-python. Other fits (orthogonal, reduced major axis, mean OLS) are also included.

| Package | Linear regression | Intercept | Slope |
|---|---|---|---|
| SLOPES | | | |
| | OLS(Y—X) | 2.1 ± 0.4 | 0.74 ± 0.04 |
| | OLS(X—Y) | -6.3 ± 0.9 | 1.56 ± 0.08 |
| | OLS(bisector) | -1.3 ± 0.4 | 1.07 ± 0.04 |
| | Orthogonal | -1.7 ± 0.6 | 1.10 ± 0.06 |
| | Reduced major-axis | -1.3 ± 0.4 | 1.07 ± 0.04 |
| ASURV-python (N = 463) | | | |
| | OLS(Y—X) | 2.2 ± 0.4 | 0.73 ± 0.04 |
| | OLS(X—Y) | -6.4 ± 0.4 | 1.57 ± 0.09 |
| | OLS(bisector) | -1.3 | 1.07 |

important to address the scientific question, it would not make sense to predict $L_B$ from $M_{HI}$ for denser environments, because the trend of $M_{HI}$ depends strongly on environmental density. As we said, the scientific purpose of this linear regression is to predict the $M_{HI}$ and therefore we should use OLS(Y—X), but since we wish to compare it with the real observed value it yields that the bisector line is probably a good option. For this reason we calculate both OLS(Y—X) and the bisector fit along this work.

In Tab. E.1 we see the different coefficients (intercept and slopes) calculated using SLOPES for the detections (Isobe et al. 1990) and using ASURV for survival analysis. With SLOPES we see that the errors for the intercept and the slope of the fits are very symilar for OLS(Y—X) and OLS(bisector) using ASURV. A direct comparison with ASURV-python (ASURV-python is an implementation of ASURV in the Python programming language by J. Sabater) using the Schmitt's method shows that the coefficients and errors are consistent with those calculated with SLOPES. The fits are shown in Fig. E.2.3 for the detected galaxies in HI using SLOPES; and Fig. E.2.3 for all the galaxies using ASURV, including censored data.

### Case 2: $M_{HI}$ vs linear diameter ($a^2$)

A direct comparison of the coefficients and errors using SLOPES and ASURV-python for the detected galaxies in HI show that they are in agreement. See Tab. E.2 to see the details of the linear fits. In Fig. E.3 we present the fits for the detections using SLOPES and in Fig. E.4 all the HI data using ASURV-python. In this case we can see that the OLS(X—Y) does not fit properly, and therefore the OLS(bisector) is not recommendable to be used either.

### Case 3: $L_{FIR}$vs $L_B$

In this case we consider FIR versus optical luminosities for the galaxies in AMIGA with morphological types $3 < T < 5$.

First we use the three methods in ASURV to test the presence of a correlation between two variables containing censored data points (125 upper limits in the dependent variable). The probability that a correlation is not present in this dataset is null, considering both the Cox hazard model (global chi square = 155.346, 1 degree of freedom with a probability of 100%) and the kendall's tau (z-value =13.396 and probability of a correlation not present equal to 0.00001).

Once we have shown that a correlation is present we can calculate the linear regression. First we compare the results of linear regression considering only detections, and later we extend the problem to the use of ASURV in the case of survival analysis.

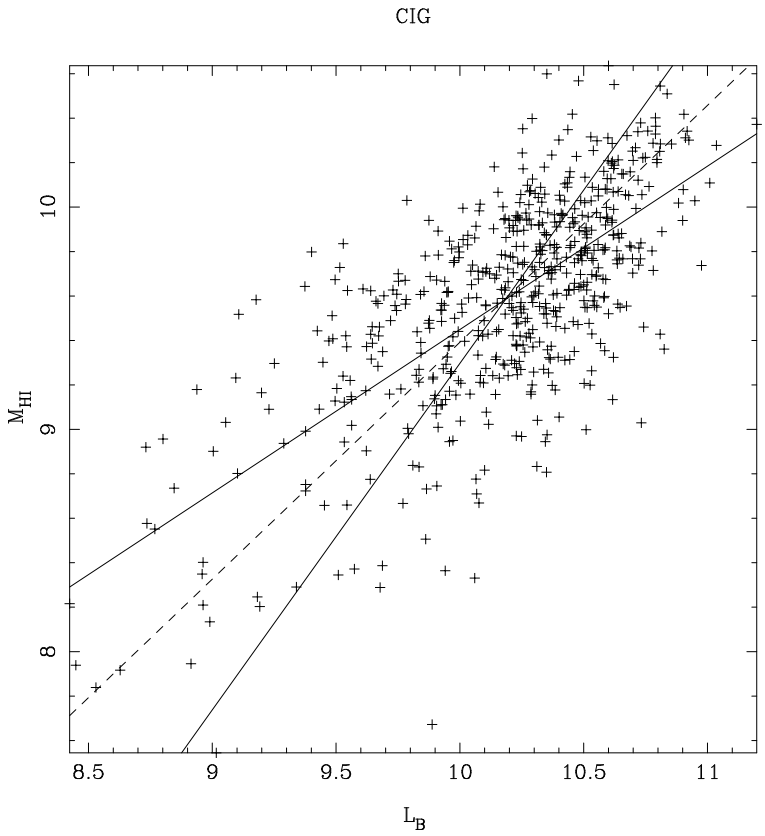


Figure E.1: OLS(X—Y), OLS(Y—X) (full lines) and OLS(bisector) (dashed line) for the linear regression $M_{HI}$ - $L_B$ , without survival analysis (N = 463).

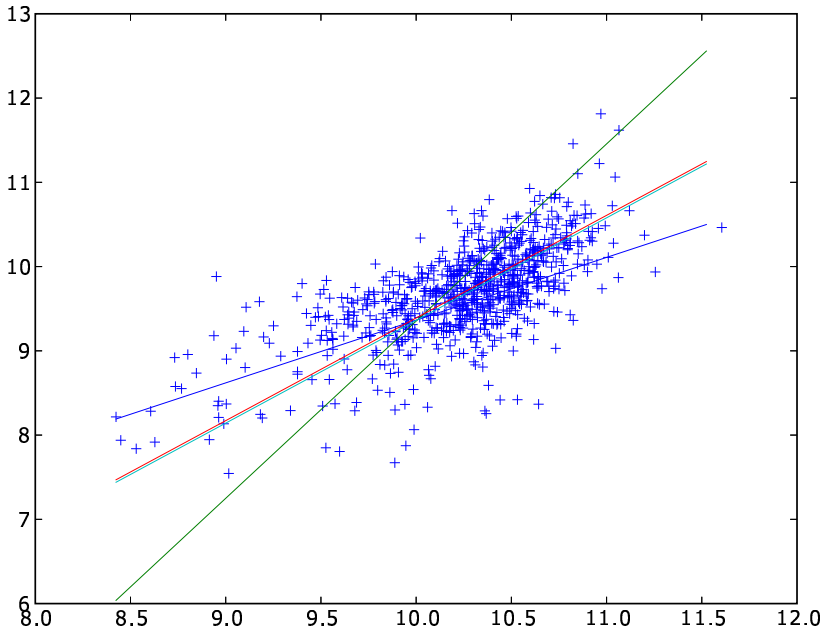


Figure E.2: OLS(X—Y), OLS(Y—X) and OLS(bisector) for the linear regression $M_{HI}$ - $L_B$ , considering survival analysis.

Table E.2: Coefficients for the different linear regressions of $L_{FIR}$vs $L_B$ using SLOPES and ASURV-python. No survival analysis is taken into account (N= 463).

| Package | Linear regression | Intercept | Slope |
|---|---|---|---|
| SLOPES | | | |
| | OLS(Y—X) | 7.40 ± 0.08 | 0.81 ± 0.03 |
| | OLS(X—Y) | 6.27 ± 0.14 | 1.22 ± 0.05 |
| | OLS(bisector) | 6.89 ± 0.08 | 0.99 ± 0.03 |
| | Orthogonal | 6.90 ± 0.10 | 0.99 ± 0.04 |
| | Reduced major-axis | 6.90 ± 0.08 | 0.99 ± 0.03 |
| ASURV-python | | | |
| | OLS(Y—X) | 7.41 ± 0.07 | 0.80 ± 0.04 |
| | OLS(X—Y) | 6.23 ± 0.35 | 1.24 ± 0.06 |
| | OLS(bisector) | 6.88 | 1.00 |

Figure E.3: OLS(X—Y), OLS(Y—X) and OLS(bisector) for the linear regression $M_{HI}$ - $a^2$, using SLOPES.

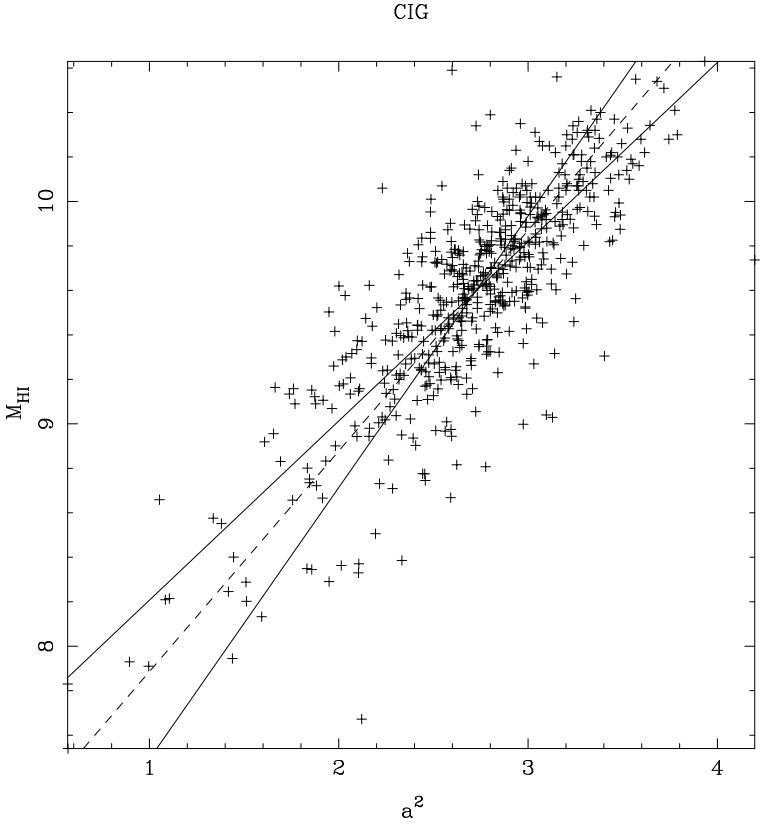

Figure E.4: OLS(X—Y), OLS(Y—X) and OLS(bisector) for the linear regression $M_{HI}$ - $a^2$. Survival analysis have been considered, using ASURV-python.

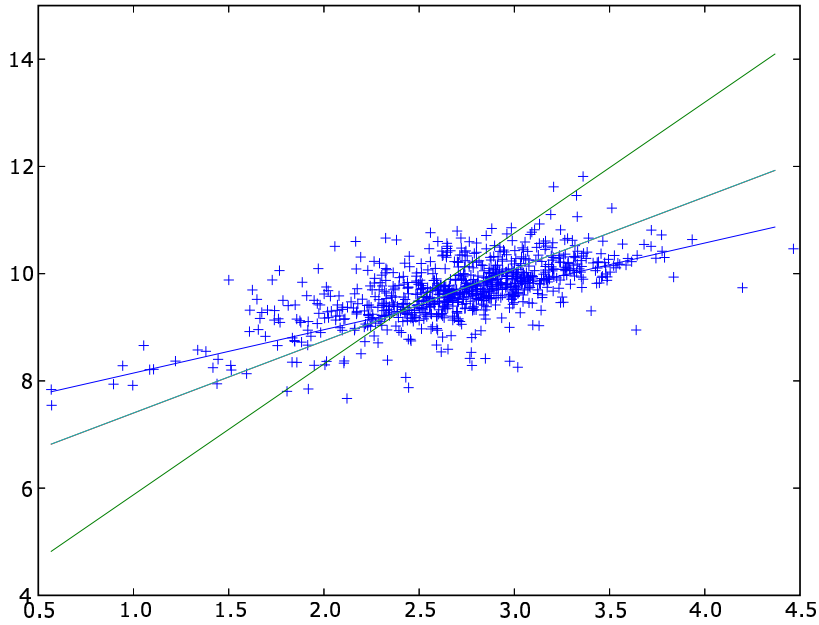


The coefficients and errors using SLOPES and ASURV-python for the detected galaxies are in agreement. See Tab. E.3, Fig. E.5 and Fig. E.6. We can compare results obtained by means of the three different routines for linear regression analysis of censored data in ASURV. Note that only OLS(Y—X) can be calculated for the first two methods (EM and Buckley-Jeans methods) since they only allow censored data in the independient variable. Results for the linear regression coefficients with upper limits are in agreement.

We find a problem when calculating OLS(X—Y), and probably in the bisector line since it is calculated from both OLS(Y—X) and OLS(X—Y) (see Fig. E.6). Upper limits are mostly located in the region $L_B$ (10,11) and $L_{FIR}$(9,10), but they are distributed almost uniformly along the dataset if we take into account the percentage of them. In this case, the effect of these upper limits is to decrease the slope a bit and also the intercept of the the regression line. This effect is seen with all the three methods for censored data (again, only OLS(Y—X)).

But this is not true for OLS(X—Y): surprisingly the effect seems to be just the opposite. No problems have been found in the code of ASURV when doing the censoring identification (-1 if it is upper limit in the dependient variable and -2 if it is in the independient). X and Y seems to be treated symmetrically up to the linear regression to the bin probabilites. In part it could be caused by the use of an arbitrary binning (see discussion about this in Schmitt 1985 and Isobe et al. 1990). However, it remains unclear what is the best size for the cell in order to have the most accurate linear regression. When increasing the binning OLS(X—Y) decreases its slope and intercept. By considering 20 cells in X and Y it yields to a slope of 2.3 while for 50 it is reduced to 1.8 . At any rate this does not solve the whole problem because we expect a lower slope to be consistent with the values without using survival analysis and OLS(Y—X) with survival. The effect seen with OLS(X—Y) should be pretty similar to OLS(Y—X) in principle. This trend is also seen in other fits belonging to this study (see for ex. $M_{HI}$ - $L_B$ ), as well as in fits of some papers (e.g. Shapley et al. (2001), where they used the Schmitt's method in ASURV to calculate the bisector line, see for ex. page 159). At any rate, in this case seems that the bisector is pretty the same for 25 bins.

Other effect that is introducing a bias in the calculation of OLS(X—Y) is due intrisicly to the

Table E.3: Coefficients for the different linear regressions of $L_{FIR}$vs $L_B$ using SLOPES and ASURV-python (with and without survival analysis -N= 463 and N=338 respectively-.

| Linear regression | Intercept | Slope |
|---|---|---|
| SLOPES | | |
| OLS(Y/X) | -1.1 ± 0.5 | 1.11 ± 0.04 |
| OLS(X/Y) | -6.6 ± 0.7 | 1.58 ± 0.07 |
| OLS(bisector) | -3.5 ± 0.4 | 1.29 ± 0.04 |
| Orthogonal | -4.3 ± 0.5 | 1.37 ± 0.05 |
| Reduced Major-Axis | -3.6 ± 0.4 | 1.29 ± 0.04 |
| ASURV-python, only det. N= 338 | | |
| OLS(Y—X) | -0.9 ± 0.5 | 1.04 ± 0.05 |
| OLS(X—Y) | -6.4 ± 0.3 | 1.56 ± 0.08 |
| OLS(bisector) | -3.310 | 1.267 |
| ASURV-python, survival analysis, N=463 | | |
| OLS(Y—X) | -0.4 ± 0.5 | 0.97 ± 0.05 |
| OLS(X—Y) | -11.5 ± 0.3 | 2.04 ± 0.12 |
| OLS(bis) | -4.5 | 1.38 |
| ASURV, survival analysis, N=463 (17 u.l. taken as detections) | | |
| OLS(Y—X) | -0.3 | 0.95 |
| ASURV, survival analysis, EM method, N=463 | | |
| OLS(Y—X) | -0.6 ± 0.5 | 0.99 ± 0.05 |
| ASURV, survival analysis, BJ method, N=463 | | |
| OLS(Y—X) | -0.6 | 0.99 ± 0.04 |

Schmitt's method. A re-definition of the lowest upper limits to detections in each bin is needed when no detections are found below it (Schmitt 1985, see). In other words, upper limits introduce biases when they are not constrained by surrounding detections. In this case, $L_{FIR}$over $L_B$ do not introduce much difference because of the long tail in the faint $L_B$ end, where upper limits are actually bordered by detections, but for $L_B$ vs $L_{FIR}$upper limits in the brighter $L_B$ end become important and introduce bias.

Therefore one need to be very careful when applying the Schmitt's method for survival techniques, especially in those cases where detection points and upper limits are not uniformly distributed. In these cases it will be worthy to consider higher values for the upper limits so they are constrained by detections.

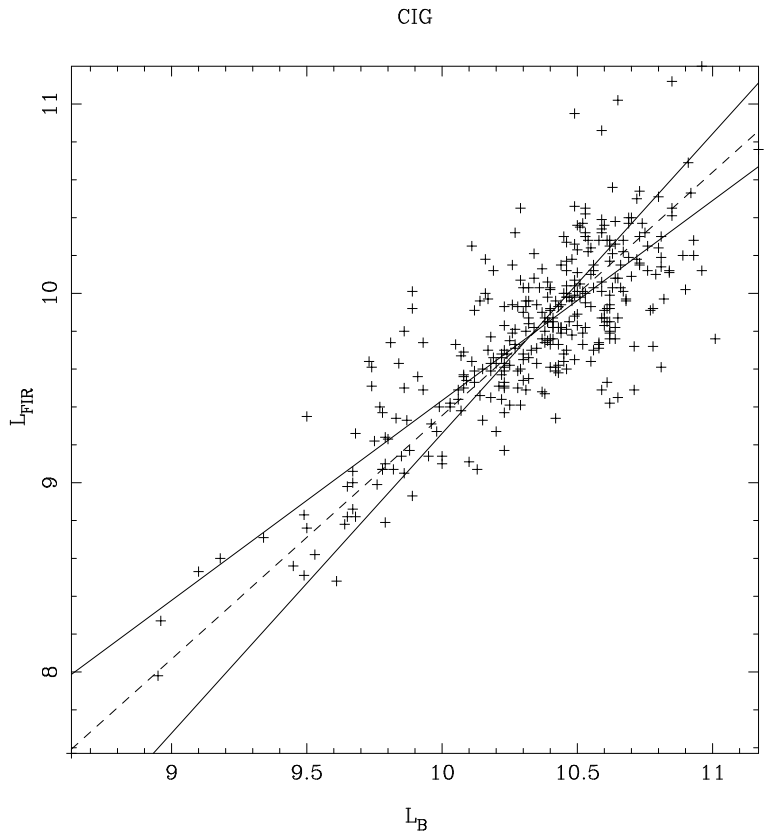


Figure E.5: OLS(X—Y), OLS(Y—X) (full lines) and OLS-bisector (dashed line) for the linear regression $L_{FIR}$- $L_B$ to test what method should be used. SLOPES was used to obtain the coefficients, survival analysis was not considered.

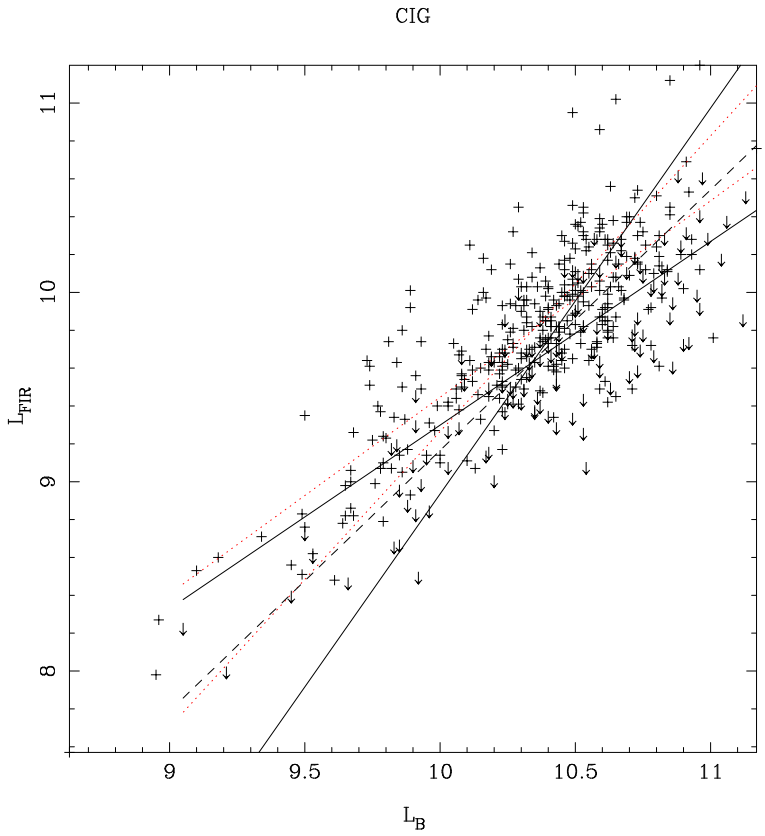


Figure E.6: OLS(X—Y), OLS(Y—X) (full lines) and OLS-bisector (dashed line) for the linear regression $L_{FIR}$- $L_B$ with ASURV-python, in comparison to OLS(Y—X) and OLS(X—Y) made with ASURV-python only for the non-censored data (point line).

# Bibliography


Abell, G. O. 1958, ApJS, 3, 211

Adams, M. T., Jensen, E. B., & Stocke, J. T. 1980, AJ, 85, 1010

Adelman-McCarthy, J. K., Agüeros, M. A., Allam, S. S., et al. 2006, ApJS, 162, 38

Akritas, M. G. & Bershady, M. A. 1996, ApJ, 470, 706

Athanassoula, E. 1984, Phys. Rep., 114, 321

Athanassoula, E., Bosma, A., Creze, M., & Schwarz, M. P. 1982, A&A, 107, 101

Athanassoula, E., Puerari, I., & Bosma, A. 1997, MNRAS, 286, 284

Baldwin, J. E., Lynden-Bell, D., & Sancisi, R. 1980, MNRAS, 193, 313

Barnes, D. G., Staveley-Smith, L., de Blok, W. J. G., et al. 2001, MNRAS, 322, 486

Barnes, J. E. 2002, MNRAS, 333, 481

Begeman, K. G. 1987, Ph.D. Thesis

Bell, E. F., Naab, T., McIntosh, D. H., et al. 2006, ApJ, 640, 241

Berentzen, I., Athanassoula, E., Heller, C. H., & Fricke, K. J. 2003, MNRAS, 341, 343

Bergvall, N., et al., & et al. 1996, in IAU Symp. 171: New Light on Galaxy Evolution, ed. R. Bender & R. L. Davies, 344–+

Bertin, E. & Arnouts, S. 1996, A&AS, 117, 393

Bettoni, D., Galletta, G., & García-Burillo, S. 2003, A&A, 405, 5

Bicay, M. D. & Giovanelli, R. 1986, AJ, 91, 705

Binney, J. & de Vaucouleurs, G. 1981, MNRAS, 194, 679

Binney, J. & Merrifield, M. 1998, Galactic astronomy (Galactic astronomy / James Binney and Michael Merrifield. Princeton, NJ : Princeton University Press, 1998. (Princeton series in astrophysics) QB857 .B522 1998 ($35.00))

Boselli, A., Gavazzi, G., Donas, J., & Scodeggio, M. 2001, AJ, 121, 753

Boselli, A., Gavazzi, G., Lequeux, J., et al. 1997, A&A, 327, 522

Bottinelli, L., Gouguenheim, L., Fouque, P., & Paturel, G. 1990, A&AS, 82, 391

Bottinelli, L., Gouguenheim, L., Paturel, G., & Teerikorpi, P. 1995, A&A, 296, 64

Bournaud, F., Combes, F., Jog, C. J., & Puerari, I. 2005, A&A, 438, 507

Braine, J. & Combes, F. 1993, A&A, 269, 7

Bravo-Alfaro, H., Cayatte, V., van Gorkom, J. H., & Balkowski, C. 2000, AJ, 119, 580

Bravo-Alfaro, H., Cayatte, V., van Gorkom, J. H., & Balkowski, C. 2001, A&A, 379, 347

Bravo-Alfaro, H., Szomoru, A., Cayatte, V., Balkowski, C., & Sancisi, R. 1997, A&AS, 126, 537

Bregman, J. N., Hogg, D. E., & Roberts, M. S. 1992, ApJ, 387, 484

Broeils, A. H. & van Woerden, H. 1994, A&AS, 107, 129

Burstein, D. & Heiles, C. 1978, ApJ, 225, 40

Burstein, D. & Heiles, C. 1982, AJ, 87, 1165

Bushouse, H. A. 1987, ApJ, 320, 49

Cayatte, V., Kotanyi, C., Balkowski, C., & van Gorkom, J. H. 1994, AJ, 107, 1003

Cayatte, V., van Gorkom, J. H., Balkowski, C., & Kotanyi, C. 1990, AJ, 100, 604

Chamaraux, P., Balkowski, C., & Gerard, E. 1980, A&A, 83, 38

Chini, R., Kruegel, E., & Lemke, R. 1996, A&AS, 118, 47

Chung, A. 2005, American Astronomical Society Meeting Abstracts, 207,

Colbert, J. W., Mulchaey, J. S., & Zabludoff, A. I. 2001, AJ, 121, 808

Combes, F., Boisse, P., Mazure, A., Blanchard, A., & Seymour, M. 1995, Galaxies and Cosmology (Galaxies and Cosmology, XVI, 407 pp. 192 figs.. Springer-Verlag Berlin Heidelberg New York. Also Astronomy and Astrophysics Library)

Corwin & Skiff. 1995, in prep.

Dahari, O. 1984, AJ, 89, 966

Davis, L. E. & Seaquist, E. R. 1983, ApJS, 53, 269

de Mello, D., Wiklind, T., & Maia, M. A. G. 2001, Astrophysics and Space Science Supplement, 277, 67

de Vaucouleurs, G., de Vaucouleurs, A., Corwin, H. G., et al. 1991, Third Reference Catalogue of Bright Galaxies (Volume 1-3, XII, 2069 pp. 7 figs.. Springer-Verlag Berlin Heidelberg New York)

de Vaucouleurs, G., de Vaucouleurs, A., & Corwin, J. R. 1976, in Second reference catalogue of bright galaxies, 1976, Austin: University of Texas Press., 0–+

Demleitner, M., Accomazzi, A., Eichhorn, G., et al. 2001, in ASP Conf. Ser. 238: Astronomical Data Analysis Software and Systems X, ed. F. R. Harnden, F. A. Primini, & H. E. Payne, 321–+

Dickey, J. M. 1997, AJ, 113, 1939

Dressler, A. 1980, ApJ, 236, 351

Dressler, A., Oemler, A. J., Couch, W. J., et al. 1997, ApJ, 490, 577

Elfhag, T., Booth, R. S., Hoeglund, B., Johansson, L. E. B., & Sandqvist, A. 1996, A&AS, 115, 439

Espada, D., Bosma, A., Verdes-Montenegro, L., et al. 2005, A&A, 442, 455

Falco, E. E., Kurtz, M. J., Geller, M. J., et al. 1999, PASP, 111, 438

Fisher, J. R. & Tully, R. B. 1981, ApJS, 47, 139

Fouque, P. & Paturel, G. 1985, A&A, 150, 192

Fouqué, P., Durand, N., Bottinelli, L., Gouguenheim, L., & Paturel, G. 1990, A&AS, 86, 473

Giovanelli, R. & Haynes, M. P. 1985, AJ, 90, 2445

Giovanelli, R. & Haynes, M. P. 1993, AJ, 105, 1271

Giovanelli, R., Haynes, M. P., Herter, T., et al. 1997, AJ, 113, 22

Haynes, M. P. & Giovanelli, R. 1980, ApJ, 240, L87

Haynes, M. P. & Giovanelli, R. 1984, AJ, 89, 758

Haynes, M. P. & Giovanelli, R. 1991, ApJS, 77, 331

Haynes, M. P., Giovanelli, R., Chamaraux, P., et al. 1999, AJ, 117, 2039

Haynes, M. P., Giovanelli, R., & Chincarini, G. L. 1984, ARA&A, 22, 445

Haynes, M. P., Magri, C., Giovanelli, R., & Starosta, B. M. 1988, AJ, 95, 607

Haynes, M. P., van Zee, L., Hogg, D. E., Roberts, M. S., & Maddalena, R. J. 1998, AJ, 115, 62

Heidmann, J., Heidmann, N., & de Vaucouleurs, G. 1972a, MmRAS, 75, 85

Heidmann, J., Heidmann, N., & de Vaucouleurs, G. 1972b, MmRAS, 75, 105

Helfer, T. T., Thornley, M. D., Regan, M. W., et al. 2003, ApJS, 145, 259

Hernández Toledo, H. M. 1999, in ASP Conf. Ser. 163: Star Formation in Early Type Galaxies, ed. P. Carral & J. Cepa, 279–+

Hewitt, J. N., Haynes, M. P., & Giovanelli, R. 1983, AJ, 88, 272

Hibbard, J. E. 2000, in ASP Conf. Ser. 197: Dynamics of Galaxies: from the Early Universe to the Present, ed. F. Combes, G. A. Mamon, & V. Charmandaris, 285–+

Hickson, P. 1982, ApJ, 255, 382

Hickson, P., Mendes de Oliveira, C., Huchra, J. P., & Palumbo, G. G. 1992, ApJ, 399, 353

Holmberg, E. 1958, Meddelanden fran Lunds Astronomiska Observatorium Serie II, 136, 1

Huchra, J. & Thuan, T. X. 1977, ApJ, 216, 694

Huchtmeier, W. K. 1997, A&A, 325, 473

Huchtmeier, W. K. & Richter, O.-G. 1989, A General Catalog of HI Observations of Galaxies. The Reference Catalog. (A General Catalog of HI Observations of Galaxies. The Reference Catalog, XIX, 350 pp. 8 figs.. Springer-Verlag Berlin Heidelberg New York)

Isobe, T., Feigelson, E. D., Akritas, M. G., & Babu, G. J. 1990, ApJ, 364, 104

James, P. A., Shane, N. S., Beckman, J. E., et al. 2004, A&A, 414, 23

Jore, K. P. 1997, Ph.D. Thesis

Karachentsev, I. D. 1972, Soobshcheniya Spetsial'noj Astrofizicheskoj Observatorii, 7, 1

Karachentseva, V. E. 1973, Astrofizicheskie Issledovaniia Izvestiya Spetsial'noj Astrofizicheskoj Observatorii, 8, 3

Karachentseva, V. E., Karachentsev, I. D., & Shcherbanovskii, A. L. 1979, Astrofizicheskie Issledovaniia Izvestiya Spetsial'noj Astrofizicheskoj Observatorii, 11, 3

Kenney, J. D. P. & Young, J. S. 1989, ApJ, 344, 171

Kennicutt, R. C. & Kent, S. M. 1983, AJ, 88, 1094

Kornreich, D. A., Haynes, M. P., Jore, K. P., & Lovelace, R. V. E. 2001, AJ, 121, 1358

Kornreich, D. A., Haynes, M. P., Lovelace, R. V. E., & van Zee, L. 2000, AJ, 120, 139

Kornreich, D. A., Lovelace, R. V. E., & Haynes, M. P. 2002, ApJ, 580, 705

Kron, G. E. & Shane, C. D. 1976, Ap&SS, 39, 401

Lake, G. & Schommer, R. A. 1984, ApJ, 280, 107

Lauberts, A. & Valentijn, E. A. 1989, The Messenger, 56, 31

Lavalley, M., Isobe, T., & Feigelson, E. 1992, in ASP Conf. Ser. 25: Astronomical Data Analysis Software and Systems I, 245–+

Leon, S. & Verdes-Montenegro, L. 2003, A&A, 411, 391

Leon, S., Verdes-Montenegro, L., Sabater, J., et al. 2006, A&A, submitted

Levine, S. E. & Sparke, L. S. 1998, ApJ, 496, L13+

Lewis, B. M. 1987, ApJS, 63, 515

Lewis, B. M., Helou, G., & Salpeter, E. E. 1985, ApJS, 59, 161

Lisenfeld, U., Verdes-Montenegro, L., Espada, D., et al. 2006, A&A, submitted

Magri, C. 1994, AJ, 108, 896

Marcum, P. M., Aars, C. E., & Fanelli, M. N. 2004, AJ, 127, 3213

Márquez, I., Durret, F., Masegosa, J., et al. 2000, A&A, 360, 431

Márquez, I. & Moles, M. 1999, A&A, 344, 421

Matthews, J. 1998, Bulletin of the American Astronomical Society, 30, 1153

Matthews, L. D., van Driel, W., & Gallagher, J. S. 1998, AJ, 116, 1169

McMahon, P. M. 1993, Ph.D. Thesis

Nieten, C., Neininger, N., Guelin, M., et al. 2005, ArXiv Astrophysics e-prints

Nilson, P. 1973, Uppsala general catalogue of galaxies (Acta Universitatis Upsaliensis. Nova Acta Regiae Societatis Scientiarum Upsaliensis - Uppsala Astronomiska Observatoriums Annaler, Uppsala: Astronomiska Observatorium, 1973)

Noordermeer, E., Sparke, L. S., & Levine, S. E. 2001, MNRAS, 328, 1064

Odewahn, S. C. 1995, PASP, 107, 770

Oemler, A. J. 1974, ApJ, 194, 1

Oosterloo, T. A., Morganti, R., Sadler, E. M., Vergani, D., & Caldwell, N. 2002, AJ, 123, 729

Paturel, G., Andernach, H., Bottinelli, L., et al. 1997, A&AS, 124, 109

Paturel, G., Fang, Y., Petit, C., Garnier, R., & Rousseau, J. 2000, A&AS, 146, 19

Paturel, G., Fouque, P., Bottinelli, L., & Gouguenheim, L. 1989, A&AS, 80, 299

Paturel, G., Garcia, A. M., Fouque, P., & Buta, R. 1991a, A&A, 243, 319

Paturel, G., Petit, C., Kogoshvili, N., et al. 1991b, A&AS, 91, 371

Paturel, G., Petit, C., Prugniel, P., et al. 2003a, VizieR Online Data Catalog, 7237, 0

Paturel, G., Theureau, G., Bottinelli, L., et al. 2003b, A&A, 412, 57

Pence, W. 1976, ApJ, 203, 39

Perea, J., del Olmo, A., Verdes-Montenegro, L., & Yun, M. S. 1997, ApJ, 490, 166

Pisano, D. J., Wilcots, E. M., & Liu, C. T. 2002, ApJS, 142, 161

Postman, M. & Geller, M. J. 1984, ApJ, 281, 95

Rhee, M.-H. & van Albada, T. S. 1996, A&AS, 115, 407

Richter, O.-G. & Huchtmeier, W. K. 1987, A&AS, 68, 427

Richter, O.-G. & Sancisi, R. 1994, A&A, 290, L9

Rickard, L. J., Palmer, P., Morris, M., Zuckerman, B., & Turner, B. E. 1975, BAAS, 7, 529

Roberts, M. S. 1969, AJ, 74, 859

Roberts, M. S. & Haynes, M. P. 1994, ARA&A, 32, 115

Ryder, S. D. & Dopita, M. A. 1993, ApJS, 88, 415

Sabater, J., Leon, S., Verdes-Montenegro, L., et al. 2006, A&A, submitted

Sadler, E. M., Oosterloo, T., & Morganti, R. 2001, in ASP Conf. Ser. 230: Galaxy Disks and Disk Galaxies, ed. J. G. Funes & E. M. Corsini, 285–288

Sadler, E. M., Oosterloo, T., & Morganti, R. 2002, in ASP Conf. Ser. 273: The Dynamics, Structure History of Galaxies: A Workshop in Honour of Professor Ken Freeman, ed. G. S. Da Costa & H. Jerjen, 215–+

Sage, L. J. 1993, A&AS, 100, 537

Sauty, S., Casoli, F., Boselli, A., et al. 2003a, A&A, 411, 381

Sauty, S., Casoli, F., Boselli, A., et al. 2003b, A&A, 411, 381

Schlegel, D. J., Finkbeiner, D. P., & Davis, M. 1998, ApJ, 500, 525

Schmidt, M. 1968, ApJ, 151, 393

Schmitt, J. H. M. M. 1985, ApJ, 293, 178

Schneider, S. E., Thuan, T. X., Mangum, J. G., & Miller, J. 1992, ApJS, 81, 5

Shapley, A., Fabbiano, G., & Eskridge, P. B. 2001, ApJS, 137, 139

Shostak, G. S. 1978, A&A, 68, 321

Shostak, G. S., Allen, R. J., & Sullivan, W. T. 1984, A&A, 139, 15

Shu, F. H., Tremaine, S., Adams, F. C., & Ruden, S. P. 1990, ApJ, 358, 495

Smoker, J. V., Davies, R. D., Axon, D. J., & Hummel, E. 2000, A&A, 361, 19

Sodroski, T. J., Odegard, N., Dwek, E., et al. 1995, ApJ, 452, 262

Solanes, J. M., Giovanelli, R., & Haynes, M. P. 1996, ApJ, 461, 609

Solanes, J. M., Manrique, A., García-Gómez, C., et al. 2001, ApJ, 548, 97

Solomon, P. M. & Sage, L. J. 1988, ApJ, 334, 613

Springob, C. M., Haynes, M. P., Giovanelli, R., & Kent, B. R. 2005, ApJS, 160, 149

Stark, A. A., Knapp, G. R., Bally, J., et al. 1986, ApJ, 310, 660

Staveley-Smith, L. & Davies, R. D. 1987, MNRAS, 224, 953

Staveley-Smith, L. & Davies, R. D. 1988, MNRAS, 231, 833

Staveley-Smith, L., Wilson, W. E., Bird, T. S., et al. 1996, Publications of the Astronomical Society of Australia, 13, 243

Strong, A. W., Bloemen, J. B. G. M., Dame, T. M., et al. 1988, A&A, 207, 1

Strong, A. W., Moskalenko, I. V., Reimer, O., Digel, S., & Diehl, R. 2004, A&A, 422, L47

Sulentic, J. W. 1989, AJ, 98, 2066

Sulentic, J. W. & Arp, H. 1983, AJ, 88, 489

Sulentic, J. W., Verdes-Montenegro, L., Bergond, G., et al. 2006, A&A, 449, 937

Swaters, R. A., van Albada, T. S., van der Hulst, J. M., & Sancisi, R. 2002a, A&A, 390, 829

Swaters, R. A., van Albada, T. S., van der Hulst, J. M., & Sancisi, R. 2002b, A&A, 390, 829

Syer, D. & Tremaine, S. 1996, MNRAS, 281, 925

Szomoru, A., van Gorkom, J. H., & Gregg, M. D. 1996, AJ, 111, 2141

Takase, B. & Miyauchi-Isobe, N. 1988, Annals of the Tokyo Astronomical Observatory, 22, 41

Theureau, G., Bottinelli, L., Coudreau-Durand, N., et al. 1998, A&AS, 130, 333

Theureau, G., Coudreau, N., Hallet, N., et al. 2005, A&A, 430, 373

Tifft, W. G. & Cocke, W. J. 1988, ApJS, 67, 1

Tifft, W. G. & Huchtmeier, W. K. 1990, A&AS, 84, 47

Toomre, A. & Toomre, J. 1972, ApJ, 178, 623

Tully, R. B. & Fisher, J. R. 1988, Catalog of Nearby Galaxies (Catalog of Nearby Galaxies, by R. Brent Tully and J. Richard Fisher, pp. 224. ISBN 0521352991. Cambridge, UK: Cambridge University Press, April 1988.)

Tully, R. B. & Fouque, P. 1985, ApJS, 58, 67

van Driel, W., van den Broek, A. C., & Baan, W. 1995, ApJ, 444, 80

van Gorkom, J. H., Bravo-Alfaro, H., Dwarakanath, K. S., et al. 2003, Ap&SS, 285, 219

Varela, J., Moles, M., Márquez, I., et al. 2004, A&A, 420, 873

Verdes-Montenegro, L., Sulentic, J., Lisenfeld, U., et al. 2005, A&A, 436, 443

Verdes-Montenegro, L., Yun, M. S., Perea, J., del Olmo, A., & Ho, P. T. P. 1998, ApJ, 497, 89

Verdes-Montenegro, L., Yun, M. S., Williams, B. A., et al. 2000, in ASP Conf. Ser. 209: IAU Colloq. 174: Small Galaxy Groups, ed. M. J. Valtonen & C. Flynn, 167–+

Verdes-Montenegro, L., Yun, M. S., Williams, B. A., et al. 2001a, A&A, 377, 812

Verdes-Montenegro, L., Yun, M. S., Williams, B. A., et al. 2001b, A&A, 377, 812

Verheijen, M. A. W. 1997, Ph.D. Thesis

Verley, S. 2006, PhD Thesis

Vettolani, G., de Souza, R., & Chincarini, G. 1986, A&A, 154, 343

Vorontsov-Velyaminov, B. & Krasnogorskaya, A. A. 1974, Morphological catalogue of galaxies (Trudi Gosudarstvennovo Astronomicheskogo Instituta (Sternberg), Moscow: State University, 1962-1974)

Walker, I. R., Mihos, J. C., & Hernquist, L. 1996, ApJ, 460, 121

Warmels, R. H. 1988, A&AS, 72, 427

Weinberg, M. D. 1994, ApJ, 421, 481

Wilcots, E. M. & Prescott, M. K. M. 2004, AJ, 127, 1900

Williams, B. A., McMahon, P. M., & van Gorkom, J. H. 1991, AJ, 101, 1957

Williams, B. A. & van Gorkom, J. H. 1988, AJ, 95, 352

Williams, B. A. & van Gorkom, J. H. 1995, in ASP Conf. Ser. 70: Groups of Galaxies, ed. O.-G. Richter & K. Borne, 77–+

Williams, B. A., van Gorkom, J. H., Yun, M., & Verdes-Montenegro, L. 1999, in IAU Symp. 186: Galaxy Interactions at Low and High Redshift, ed. J. E. Barnes & D. B. Sanders, 375–+

Wilson, C. D. 1995, ApJ, 448, L97+

Wilson, R. W., Jefferts, K. B., & Penzias, A. A. 1970, ApJ, 161, L43+

Xu, C. & Sulentic, J. W. 1991, ApJ, 374, 407

Young, J. S., Kenney, J. D., Tacconi, L., et al. 1986, ApJ, 311, L17

Young, J. S. & Knezek, P. M. 1989, ApJ, 347, L55

Young, J. S. & Scoville, N. Z. 1991, ARA&A, 29, 581

Young, J. S., Xie, S., Kenney, J. D. P., & Rice, W. L. 1989, ApJS, 70, 699

Young, J. S., Xie, S., Tacconi, L., et al. 1995, ApJS, 98, 219

Yun, M. S., Ho, P. T. P., & Lo, K. Y. 1994, Nature, 372, 530

Zaritsky, D. & Rix, H.-W. 1997, ApJ, 477, 118

Zasov, A. V. & Sulentic, J. W. 1994, ApJ, 430, 179

Zepf, S. E. & Whitmore, B. C. 1991, ApJ, 383, 542

Zwicky, F. & et al. 1961, in California Inst. Techn., 1 (1961), 0–+

Zwicky, F., Herzog, E., & Wild, P. 1961, Catalogue of galaxies and of clusters of galaxies (Pasadena: California Institute of Technology (CIT), —c1961)